THE ENTANGLED UNIVERSE

BENJAMIN MOSK

# THE ENTANGLED UNIVERSE

BENJAMIN MOSK

# The entangled universe

This work has been accomplished at the Institute for Theoretical Physics (ITFA) of the University of Amsterdam (UvA) and is part of the research programme of the Foundation for Fundamental Research on Matter (FOM), which is part of the Netherlands Organisation for Scientific Research (NWO).

# The entangled universe

## Academisch Proefschrift

ter verkrijging van de graad van doctor

aan de Universiteit van Amsterdam

op gezag van de Rector Magnificus

prof. dr. D. C. van den Boom

ten overstaan van een door het College voor Promoties ingestelde

commissie, in het openbaar te verdedigen in de Agnietenkapel

op dinsdag 8 september 2015, te 10:00 uur

door

Benjamin Mosk

geboren te Wageningen

# Promotiecommissie

Promotor

| | |
|---|---|
| prof. dr. J. de Boer, | Universiteit van Amsterdam |

Co-Promotores

| | |
|---|---|
| dr. B. W. Freivogel, | Universiteit van Amsterdam |
| dr. J. P. van der Schaar, | Universiteit van Amsterdam |

Overige leden

| | |
|---|---|
| prof. dr. E. P. Verlinde, | Universiteit van Amsterdam |
| prof. dr. C. J. M. Schoutens, | Universiteit van Amsterdam |
| prof. dr. A. Achúcarro, | Universiteit Leiden |
| prof. dr. T. Hertog, | Katholieke Universiteit Leuven |
| dr. A. Castro Anich, | Universiteit van Amsterdam |
| dr. D. Roest, | Rijksuniversiteit Groningen |

Faculteit der Natuurwetenschappen, Wiskunde en Informatica

# Publications

This thesis is based on the following publications:


[1] F. V. Dimitrakopoulos, L. Kabir, B. Mosk, M. Parikh and J. P. van der Schaar
*Vacua and correlators in hyperbolic de Sitter space*
Journal of High Energy Physics **1506**, 095 (2015), arXiv:1502.00113 [hep-th].

[2] B. Freivogel, R. A. Jefferson, L. Kabir, B. Mosk and I. S. Yang
*Casting Shadows on Holographic Reconstruction*
Physical Review D **91**, 086013 (2015), arXiv:1412.5175 [hep-th].

[3] B. Mosk and J.P. van der Schaar
*Chaotic inflation limits for non-minimal models with a Starobinsky attractor*
Journal of Cosmology and Astroparticle Physics **1412**, 022 (2014), arXiv:1407.4686 [hep-th].

[4] B. Freivogel and B. Mosk
*Properties of Causal Holographic Information*
Journal of High Energy Physics **1309**, 100 (2013),
arXiv:1304.7229 [hep-th].

# Preface

## Guide for the reader

This doctoral thesis is based on the scientific endeavors undertaken by myself and my collaborators over the past four years. Two main lines of research can be distinguished, which are presented in the two parts of this thesis. Even though these lines of research are largely independent, the reader will also find that there is an intimate entanglement between the two parts.

This thesis is written from the first person plural (we) perspective, which is common practice in the field of theoretical physics. The only exceptions to this convention are this preface, the chapter discussing my contributions to previously published work and the acknowledgments, where I write in first person singular. The work presented in this thesis was done in collaborations. My individual contribution to these published works will be clarified after the bibliography.

In the sub-fields that correspond to the two parts of this thesis, the commonly used conventions are different. At the first page of each part, the conventions used in that part will be clarified.

The level of exposition in this thesis is such that a starting PhD-candidate should be able to read and understand it. The introductory chapters of part I and part II are suitable for those who have at least some familiarity with the topics at hand. In these chapters I will refer to lecture notes that give a more extensive treatment of the introductory topics.

# Introduction

This thesis consists of two parts. The first part is dedicated to topics in holography and the second part is devoted to topics in cosmology. Both parts will have their proper introductions. The purpose of this introduction is hence not to explain concepts in either of these fields. In this introduction we first give a general context of these two fields. Subsequently we make the reader aware of the overlap between the two parts.

The first model of gravity appeared in 1687 in Newton's famous Philosophiæ-Naturalis Principia Mathematica. It was superseded a hundred years ago, with Einstein's article Die Feldgleichungen der Gravitation. In the same period of time, quantum mechanics was being discovered. The combination of special relativity and quantum mechanics led to the development of quantum field theory and the standard model of particle physics. A quantum theory of *general* relativity proved to be much harder to construct. So far, string theory, which originally emerged from the study of hadronic interactions, is the only theory that successfully incorporates gravity and quantum mechanics.

The study of black holes, which are special solutions of general relativity, made apparent that black holes have an entropy that scales with the area of the surface that encloses it. This led to the conjecture that the number of physical degrees of freedom in a volume of space in a theory of gravity does not scale with the volume, but with the area of the surface that encloses it. This realization led to the formulation of the holographic principle: in a theory of gravity, the degrees of freedom associated to a volume of space can be described by a model with one dimension less. The study of string theory gave an explicit realization of holography, by means of the AdS/CFT-correspondence. Holography allows the study of gravity from a different perspective; that of the holographic screen. In part I we discuss topics in the field of holography.

The study of general relativity led, in combination with the observation of cosmological redshifts, to the idea of an expanding universe. Friedmann realized that general relativity admits solutions that describe an expanding universe. For a number of reasons, which we elaborate on in part II, it is believed that our universe went through a period of accelerated expansion, or inflation. The classical evolution of a simple model involving just the metric and a single scalar field already admits the phenomenon of inflation. Quantization of the perturbations around the classical evolution of such a model brought forth a set of predictions that are remarkably well in accordance with observations. In part II we discuss topics in the field of cosmological inflation.

Apart from the fact that general relativity and quantum field theory form the building blocks of both parts of this thesis, there are many other similarities. For example, quantum entanglement appears as an important concept in both parts. If the entanglement between two boundary regions is removed, then the corresponding bulk space tends to pinch of [5] (we will not go into the details here, see chapter 1 of Part I). This seems to be related to another phenomenon: when one tries to define a vacuum state for the Rindler wedge, the energy momentum tensor becomes divergent at the boundary of the Rindler wedge (see chapter 1 of Part I and chapter 5 of Part II for details). Something similar appears when we try to define a vacuum state for the hyperbolic patch of de Sitter spacetime, as described in chapter (5) of part II.

The spacetimes we consider in part I and part II also show similarities; they are both maximally symmetric solutions of the Einsteins equations with a cosmogical constant and they are related to each other by a double analytic continuation. In part I we consider Anti de Sitter (AdS) spacetime in the context of the AdS/CFT-correspondence, whereas in part II we consider de Sitter (dS) spacetime in the context of inflation. In fact, attempts have been made to construct a dS/CFT-correspondence, but much remains to be clarified in this topic.

We invite the reader to discover these and other links in the next chapters.

# Contents

# Part I

# Holography

# Notes for the reader

## Conventions

| | |
|---|---|
| Planck units | $\hbar = c = 1$ |
| Minkowski metric | $\eta_{\mu\nu}$=diagonal(-1,+1,...,+1) |
| Bulk indices | capital letter indices $M, N, ...$ |
| Boundary indices | Greek letter indices $\mu, \nu, ...$ |
| Number of bulk dimensions | D=d+1 |
| Number of boundary dimensions | d |

**Anti de Sitter radius $L_{\text{AdS}}$:** in chapter (1) we will consistently write $L_{\text{AdS}}$ where it is appropriate, since this is an introductory chapter. In chapters (2) and (3) we will not explicitly write $L_{\text{AdS}}$ and quantities with unit length should be considered to be stated in units of $L_{\text{AdS}}$.

## Published work

This part of the thesis is based on (parts of) our work presented in the following articles:

[4] B. Freivogel and B. Mosk
*Properties of Causal Holographic Information*
JHEP **1309**, 100 (2013), arXiv:1304.7229 [hep-th].

[2] B. Freivogel, R. A. Jefferson, L. Kabir, B. Mosk and I. S. Yang
*Casting Shadows on Holographic Reconstruction*
Phys.Rev.D **D 91**, 086013 (2015), arXiv:1412.5175 [hep-th].

In particular, elements of [4] will be presented in chapter (3), (sub-) sections (3.1), (3.5) and (3.6). Elements of [2] can be found in chapters (2) and (3), (sub-) sections (2.2), (2.3) and (3.4). Chapter (1) is introductory and does not contain products of our scientific endeavors.

# Chapter 1

# Introducing holography

## 1.1 The holographic principle and the AdS/CFT-correspondence

In this section we will introduce the *holographic principle*, the conjecture that under certain conditions the degrees of freedom in a volume of space, "the bulk", can be described by a theory defined on a surface with one dimension less, "the boundary", where the bulk degrees of freedom include gravity, whereas the boundary degrees of freedom do not. Holography provides an example of a duality. A duality is the equivalence of two different models, which describe the same physical system. In recent years, a particular realization of such a holographic duality has been of central interest in theoretical physics: the AdS/CFT-correspondence. We will describe the key ingredients of this conjectured duality. The AdS/CFT-correspondence relates a conformal field theory (CFT) living on a $d$ dimensional spacetime to a theory of gravity in a $(d+1)$-dimensional spacetime. The information of the gravitational dynamics are hence encoded in the non-gravitational description of the CFT, which allows us to study gravity from a completely different perspective. We will first describe the developments that led to the idea of holography and then we will give a heuristic derivation of the most famous example of the AdS/CFT-correspondence.

In the seventies it was realized for the first time that black holes can emit radiation and that this radiation exhibits a thermal spectrum [6–9], where the temperature is proportional to the surface gravity of the black hole. Furthermore, an entropy can be assigned to a black hole, which satisfies laws similar to those of thermodynamics

[10–12]. The black hole entropy was found to be proportional to the area of the event horizon $A_H$:

$$S_{\mathrm{BH}} = \frac{k_b A_H c^3}{4G\hbar}, \tag{1.1}$$

where $G$ is Newton's gravitational constant, $k_b$ is Boltzmann's constant, $c$ is the speed of light in vacuum and $\hbar$ is Planck's constant. Naively, one would expect the entropy to behave extensively and to scale with system volume. However, for black holes the entropy is proportional to the area of the event horizon. The area of the event horizon of a black hole was shown to satisfy the *area law* or *second law of black hole thermodynamics*:

$$\frac{dA_H}{dt} \geq 0, \tag{1.2}$$

where $A_H$ is the size of the black hole horizon. This suggests that the black hole entropy (1.1) can increase *only* by increasing the size of the black hole.

The *generalized second law* states that the total entropy (black hole entropy and matter entropy) increases with time. If the total entropy is not allowed to decrease by dropping matter into the black hole, then the entropy of matter enclosed by a surface should not be allowed to exceed (1.1), thus providing a bound on the maximum entropy of a system [13, 14].

The *covariant entropy bound*, put forward in [15], provides a more concrete formulation of the entropy bounds that were formulated in the context of black holes.

> ***Covariant entropy bound [15, 16]***
> *Let $A_B$ be the area of an arbitrary $d$-dimensional spatial surface $B$ (which need not be closed). A $D$-dimensional hyper surface $L$ is called a light-sheet of $B$ if $L$ is generated by light rays which begin at $B$, extend orthogonally away from $B$, and have non-positive expansion,*
>
> $$\theta \leq 0, \tag{1.3}$$
>
> *everywhere on $L$. Let $S$ be the entropy on any light-sheet of $B$. Then*
>
> $$S \leq \frac{A_B}{4G}. \tag{1.4}$$

The observation that entropy scales with area instead of volume led to the holographic principle. The *holographic principle* as formulated by Susskind and 't Hooft (based on unitarity) can suggestively be formulated:

> *The combination of quantum mechanics and gravity requires the three dimensional world to be an image of data that can be stored on a two dimensional projection much like a holographic image [14].*

In the nineties a new conjecture provided a realization of the holographic principle. The AdS/CFT-correspondence states that under certain conditions, a gravitational theory on a $(d+1)$-dimensional (asymptotically-) Anti de Sitter background can be described by a conformal field theory (CFT) on a $d$-dimensional background (without gravity) and vice-versa.

The AdS/CFT-correspondence arises naturally in the context of string theory. In particular, the most important realization of the AdS/CFT-correspondence is the equivalence of Type IIB string theory on $AdS_5 \times S^5$ and $\mathcal{N} = 4$ supersymmetric $U(N)$ Yang Mills theory in $(3 + 1)$ dimensions [17]. Certain types of supersymmetric string theories contain stable objects called $Dp$-branes, which are $(p+1)$-dimensional objects on which open strings can end [18–20]. Type IIB string theory, a maximally supersymmetric string theory in $(9 + 1)$ dimensions, contains $D3$-branes. A stack of $N$ $D3$-branes can have open strings that end either on the same brane, or on different branes.

Type IIB string theory with a stack of $D3$-branes contains open strings that end on the $D3$-branes and closed strings. We consider the low energy limit in combination with two different limits, $g_sN \ll 1$ and $g_sN \gg 1$, where $g_s$ is the string coupling.

At small $g_sN \ll 1$, the low energy description decomposes into two decoupled sectors: the massless excitations of the closed strings far away from the branes and the massless excitations of the open strings, which have a (perturbative) description in terms of a $\mathcal{N} = 4$, $U(N)$ $\mathcal{SYM}$ gauge theory *on* the branes.

An alternative description, in terms of closed strings can be given at large $g_sN \gg 1$ and low energies. The massless excitations of the closed strings "far away from the branes" decouple again. The $D3$-branes have a large backreaction, couple to closed string modes and deform the spacetime into a "throat", which can be thought of as a potential well. Now the massive closed string modes deep inside the deformed "throat" also survive the low energy limit.

In both the $g_sN \ll 1$ and $g_sN \gg 1$ the closed string modes far away decouple, leaving us with $\mathcal{N} = 4$, $U(N)$ $\mathcal{SYM}$ gauge theory in $(3 + 1)$ dimensions for $g_sN \ll 1$ and Type IIB string theory on the "near horizon" region, which can be shown to have $AdS_5 \times S^5$ geometry. These observations led to the conjecture that Type IIB string theory on $AdS_5 \times S^5$ is dual to $\mathcal{N} = 4$, $U(N)$, $\mathcal{SYM}$ gauge theory in $(3 + 1)$ dimensions.

The classical supergravity description of the theory on $AdS_5 \times S^5$ is good for large $N$ (small $g_s \ll 1$) and large $g_sN$, which corresponds to large coupling in the gauge theory. In this thesis we will assume a strong version of the conjecture, where the duality holds for all $g_sN$ and not exclusively in the $N \to \infty$ limit. The combination $g_sN \equiv \lambda$ is also called the 't Hooft coupling and is the effective coupling in the

gauge theory. The supergravity description is well known and can teach us about the description of strongly coupled gauge theories. Vice-versa, the gauge theory description at weak coupling can teach us about non-perturbative string theory.

But first we need to know how laws of physics and physical quantities in one theory translate to the dual theory, that is, we need to develop a *dictionary*. A lot of work has been done in recent years to make this *holographic dictionary*. The fundamental statement of the duality is

$$Z_{\text{CFT}}[\phi_0(x)] = Z_{\text{IIB string}}[\phi_0(x)], \tag{1.5}$$

where $Z_{\text{CFT}}$ is the CFT partition function. The sources $\phi_0$ serve as boundary conditions for the string theory partition function $Z_{\text{IIB string}}$, as will be explained in the next section. In the supergravity limit $g_s N \gg 1, g_s \ll 1$, a saddle point approximation of the string partition function can used and the statement (1.5) becomes

$$W[\phi_0(x)] = -S_{\text{SUGRA,on shell}}[\phi_0(x)], \tag{1.6}$$

where $W = \log Z$ is the generating functional of connected CFT correlation functions, also known as the quantum effective action with a source and $S_{\text{SUGRA,AdS}}$ is the $IIB$ on shell supergravity action.

## 1.2 Elements of the dictionary

In this section we will introduce elements of the holographic dictionary necessary in later chapters. First, we introduce Anti de Sitter (AdS) spacetime. Subsequently we will make the fundamental statement (1.6) more precise for the toy model of a single bulk scalar field. Then we will discuss Wilson loops on the boundary and its holographic bulk dual. Lastly, we will introduce boundary entanglement entropy and its holographic dual, which is a crucial ingredient for chapter (2) and (3).

### 1.2.1 AdS spacetime

In this subsection we introduce Anti de Sitter (AdS) spacetime. Anti de Sitter (AdS) spacetime is a maximally symmetric spacetime with negative constant curvature. Anti de Sitter spacetime can be embedded in flat space with signature $(--+\cdots+)$. The embedding equation is given by

$$-X_0^2 - X_{d+1}^2 + \sum_{i=1}^{d-1} X_i^2 = -L_{\text{AdS}}^2 \tag{1.7}$$

$$ds^2 = -dX_0^2 - dX_{d+1}^2 + \sum_{i=1}^{d} dX_i^2. \tag{1.8}$$

The embedding equation (1.7) as well as the metric (1.8) are invariant under $O(2,d)$ transformations. The pullback of the metric (1.8) onto the surface defined by (1.7) gives an AdS spacetime.

AdS spacetime is a solution of the Einstein equations with negative cosmological constant. The Einstein Hilbert action with cosmological constant is given by:

$$S = \frac{1}{16\pi G} \int d^{d+1}x \sqrt{-g} \left(R - \Lambda\right). \tag{1.9}$$

The Einstein equations that follow from extremizing the Einstein Hilbert action with cosmological constant (1.9) are given by

$$R_{\mu\nu} - \frac{R}{2} g_{\mu\nu} = -\frac{\Lambda}{2} g_{\mu\nu}. \tag{1.10}$$

There exists a maximally symmetric solution of (1.10), with vanishing Weyl tensor. In a $(d+1)$-dimensional maximally symmetric spacetime, the Riemann tensor is given by:

$$R_{\mu\nu\rho\sigma} = \frac{R}{d(d+1)} \left(g_{\mu\rho} g_{\nu\sigma} - g_{\mu\sigma} g_{\nu\rho}\right). \tag{1.11}$$

From the Einstein equations (1.10) it follows that

$$R = \frac{(d+1)\Lambda}{d-1}. \tag{1.12}$$

The curvature in terms of $L_{\text{AdS}}$ is given by

$$R = -\frac{d(d+1)}{L_{\text{AdS}}^2}. \tag{1.13}$$

Two coordinate charts for the $(d+1)$-dimensional subspace defined by (1.7) are frequently used in this thesis: Poincaré coordinates and global coordinates.

### Poincaré patch

Poincaré coordinates only cover a part of Anti de Sitter space, the Poincaré patch. A set of coordinates on the Poincaré patch is given by

$$\begin{aligned} X_0 &= \frac{z}{2}\left(1+\frac{1}{z^2}\left(L_{\text{AdS}}^2+\sum_i x_i^2-t^2\right)\right), \\ X_{d+1} &= \frac{L_{\text{AdS}}t}{z}, \\ X_i &= \frac{L_{\text{AdS}}x_i}{z} \qquad \text{for } i=1,\ldots,d-1, \\ X_d &= \frac{z}{2}\left(1-\frac{1}{z^2}\left(L_{\text{AdS}}^2-\sum_i x_i^2+t^2\right)\right), \end{aligned} \tag{1.14}$$

which brings the metric into the form

$$ds^2 = L_{\text{AdS}}^2\left(\frac{dz^2}{z^2}+\frac{dx^\mu dx^\nu \eta_{\mu\nu}}{z^2}\right). \tag{1.15}$$

The *conformal boundary*, defined by $\lim_{z\to 0} z^2 ds^2$ is $d$-dimensional Minkowski space.

### Global AdS

There are several commonly used global coordinate systems for the global cover of AdS spacetime, here we present one that is used in later chapters. The coordinates are defined by

$$\begin{aligned} X_0 &= L_{\text{AdS}}\sqrt{1+\frac{r^2}{L_{\text{AdS}}^2}}\sin\frac{t}{L_{\text{AdS}}} \\ X_{d+1} &= L_{\text{AdS}}\sqrt{1+\frac{r^2}{L_{\text{AdS}}^2}}\cos\frac{t}{L_{\text{AdS}}} \\ \sum_{i=1}^{d} X_i &= r^2, \end{aligned} \tag{1.16}$$

where the last line implicitly defines a set of $d-1$ angular coordinates. The metric in global coordinates defined by (1.16) is given by:

$$ds^2 = -\left(1+\frac{r^2}{L_{\text{AdS}}^2}\right)dt^2+\left(1+\frac{r^2}{L_{\text{AdS}}^2}\right)^{-1}dr^2+r^2 d\Omega_{d-1}^2. \tag{1.17}$$

This coordinate set is sometimes called the "hyper-polar" coordinate set.

### Causal structure of AdS

Another set of coordinates for global AdS makes the causal structure explicit. The defining equation are given by:

$$\begin{aligned} X_0 &= L_{\text{AdS}} \cosh\rho \cos t \\ X_{d+1} &= L_{\text{AdS}} \cosh\rho \sin t \\ \sum_{i=1}^{d} X_i^2 &= L_{\text{AdS}}^2 \sinh^2\rho, \end{aligned} \tag{1.18}$$

where the last line implicitly defines $(d-1)$ angular coordinates on $S^{d-1}$. The pullback of the metric on surface (1.7) in these coordinates is given by

$$ds^2 = L_{\text{AdS}}^2 \left(-\cosh^2\rho dt^2 + d\rho^2 + \sinh^2\rho d\Omega_{d-1}^2\right). \tag{1.19}$$

Now a coordinate transformation $\sinh\rho = \tan R$ with $R \in [0, \frac{\pi}{2}]$ brings the metric (1.19) in the form

$$ds^2 = \frac{L_{\text{AdS}}^2}{\cos^2 R}\left(-dt^2 + dR^2 + R^2 d\Omega_{d-1}^2\right), \tag{1.20}$$

which makes the conformal structure of global AdS explicit. The metric $d\tilde{s}^2 = L_{\text{AdS}}^{-2}\cos^2 R ds^2$ is that of a solid cylinder $(R, \theta_1, t)$ where every point still represents a $(d-2)$-sphere. In figure 1.1 the conformal structure of global AdS is illustrated.

### Asymptotically AdS-spaces

Asymptotically Anti de Sitter (AAdS) spacetimes have a conformal structure similar to AdS spacetime. For a formal definition, see [22], or [23] for a pedagogical discussion. The metric of an AAdS spacetime can be written as [24, 25]

$$\begin{aligned} ds^2 &= G_{MN} dX^M dX^N \\ &= \frac{dz^2}{z^2} + \frac{1}{z^2} g_{\mu\nu}(z,x) dx^\mu dx^\nu \\ g_{\mu\nu}(z,x) &= g_{\mu\nu}^{(0)}(x) + z^2 g_{\mu\nu}^{(2)}(x) + ... + z^d \left(g_{\mu\nu}^{(d)}(x) + \log z\ h_{\mu\nu}(x)\right) + O(z^{d+1}). \end{aligned} \tag{1.21}$$

$g_{\mu\nu}^{(0)}(x)$ is the metric on the conformal boundary:

$$\lim_{z\to 0} z^2 ds^2 = g_{\mu\nu}^{(0)} dx^\mu dx^\nu. \tag{1.22}$$

In Einstein gravity with cosmological constant (1.9), the $g_{\mu\nu}^{(2i)}$ $(1 \le i \le \frac{d}{2} - 1)$ and $h_{\mu\nu}$ are fully determined in terms of $g_{\mu\nu}^{(0)}$, by the gravitational equations of motion (1.10).

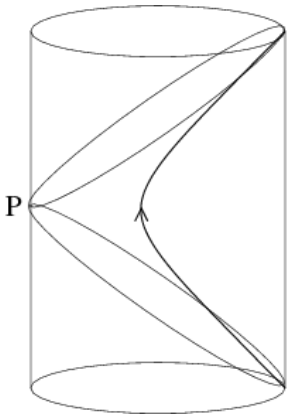


***Figure 1.1:*** *The conformal structure of global AdS is that of a* solid *cylinder. In this picture, the planar patch is a wedge covering only part of the cylinder. Planar AdS can be thought of as the part of AdS that is accessible to certain accelerated observers (indicated). A planar patch of AdS can also be associated to a point on the conformal boundary (P), consisting of the points that are spacelike separated from P. Source: [21].*

### AdS-Schwarzschild

A particular *AAdS* metric is the AdS-Schwarzschild, which has the conformal structure of AdS spacetime, but with a black hole in the centre. The Schwarzschild black hole metric in $(d+1)$ dimensions is given by

$$\begin{aligned} ds^2 &= -f(r)dt^2 + \frac{dr^2}{f(r)} + r^2 d\Omega_{d-1}^2, \\ f(r) &= 1 - \frac{2GM}{r^{d-2}}. \end{aligned} \tag{1.23}$$

The metric of the AdS-Schwarzschild black hole in $(d+1)$ dimensions is given by

$$\begin{aligned} ds^2 &= -f(r)dt^2 + \frac{dr^2}{f(r)} + r^2 d\Omega_{d-1}^2, \\ f(r) &= 1 + \frac{r^2}{L_{\text{AdS}}^2} - \frac{GM}{r^{d-2}} \\ &= 1 + \frac{r^2}{L_{\text{AdS}}^2} - \frac{r_H^{d-2}}{r^{d-2}}\left(1 + \frac{r_H^2}{L_{\text{AdS}}^2}\right). \end{aligned} \tag{1.24}$$

The AdS-Schwarzschild black hole in $(2+1)$ dimensions is called the static BTZ black hole [26]. It is special because one does not recover pure $AdS_{2+1}$ as $GM \to 0$. The geometry with $-1 < GM < 0$ corresponds to a geometry with a conical defect at the origin.

### 1.2.2 Emergence of the radial direction

Now that we have introduced several coordinate sets for AdS spacetime, we can present an intuitive argument for the emergence of the radial (bulk) dimension in the AdS/CFT-correspondence. Subsequently, we will briefly discuss the idea that the radial (bulk) direction can be seen as the RG-scale of the boundary theory.

The first argument is heuristic and it is based on the matching of the bulk and boundary symmetries. We already noted that AdS spacetime has a $SO(2,d)$-symmetry group (1.7,1.8). Furthermore, it can be shown that the conformal group in $d$ dimensions is also given by $SO(2,d)$. A particular conformal transformation, the scaling of the boundary coordinates $x^\mu \to \lambda x^\mu$ can be associated to a $SO(2,d)$-transformation of the bulk. In the Poincaré coordinates given by (1.14,1.15), the corresponding isometry is given by $x^\mu \to \lambda x^\mu$, $z \to \lambda z$. This allows an identification of the (inverse) radial direction as the energy scale:

$$z^{-1} \equiv u \propto E. \tag{1.25}$$

If this interpretation is to be taken seriously, then the near-boundary region would describe the full UV-complete boundary theory, while the Poincaré horizon $z \to \infty$ would correspond to the deep IR-sector of the boundary theory.

These ideas have been made precise in [27–29], where it is shown that, in the supergravity limit, the radial direction can be interpreted as the renormalization group (RG) scale of the theory. The renormalization group equations describe how the theory behaves as a function of the energy scale. In the bulk, the radial evolution of the fields is specified by the (gravitational) equations of motion, whereas the renormalization group behavior in the boundary theory is determined by the RG or Callan-Symanzik equations. These two prescription are shown to be equivalent.

### 1.2.3 Scalar field

The analysis of a single bulk scalar field and its dual boundary operator exemplifies the underlying principles of the AdS/CFT-correspondence. Generally, the equations of motion for a bulk scalar field couple to the gravitational equations of motion through the energy momentum tensor, but in this case the gravitational equations decouple near the boundary [30] such that we can study the Klein Gordon equation solely. We assume large $N$ and a classical geometry. The Euclidean action for a massive free bulk scalar field is given by

$$S = \frac{1}{2}\int d^{d+1}x\sqrt{g}\left(g^{MN}(\partial_M\Phi)(\partial_N\Phi) + m^2\Phi^2\right). \tag{1.26}$$

In Poincaré coordinates (1.141.15) the equation of motion is

$$z^2\partial_z\partial_z\Phi - (d-2)z\partial_z\Phi + z^2\eta^{\mu\nu}\partial_\mu\partial_\nu\Phi = m^2L^2_{\text{AdS}}\Phi. \tag{1.27}$$

The ansatz $\Phi(z, x^\mu) = z^\Delta$ can be solved by

$$\Delta\left(\Delta - d\right) = m^2L^2_{\text{AdS}}, \qquad \Delta_\pm \quad = \frac{d}{2} \pm \sqrt{\left(\frac{d}{2}\right)^2 + m^2L^2_{\text{AdS}}}. \tag{1.28}$$

These two solutions capture the leading near boundary behavior of the scalar field. The $\Delta_+$ solution is normalizable, that is, we can calculate its Klein Gordon norm. The $\Delta_-$ mode is non-normalizable and is associated to the source of the boundary operator $\mathcal{O}_\Phi$ that is dual to the bulk field $\Phi$.[1]

The near boundary behavior of a general solution of the equation of motion (1.27) is given by

$$\Phi(z, x) = \phi_+(x)z^{\Delta_+}(1 + O(z)) + \phi_-(x)z^{\Delta_-}(1 + O(z)), \tag{1.29}$$

where $\phi_-(x)$ is interpreted as a boundary source; in equation (1.6) we can make the identification $\phi_{(0)} = \phi_-$:

$$\begin{aligned} W[\phi_-] &= -Z_{\text{AdS,on shell}}[\phi_-] \\ &= \langle e^{-\int d^dx\mathcal{O}_\Phi\phi_-}\rangle, \end{aligned} \tag{1.30}$$

where $\mathcal{O}_\Phi$ is the boundary dual operator of the bulk field $\Phi$.

Below, we will further illustrate the AdS/CFT-correspondence by deriving the two-point function of an (primary) operator $\mathcal{O}_\Phi$ in a CFT calculation as well as with a bulk calculation via its dual field $\Phi$. The derivation will be heuristic: for the sake of simplicity we will not work out all the details. A detailed treatment can be found in [23].

**Two point functions in a CFT**

First we will "derive" an expression for the two-point function of a primary operator in a conformal field theory. If a theory is invariant under conformal transformations, then its two-point functions must be invariant under these transformations; this requirement constrains the correlation functions in a conformal field theory. A conformal transformation is a coordinate transformation $\tilde{x}(x)$ such that the line element $ds^2$ transforms as

$$d\tilde{s}^2 = \Omega^2(x)ds^2. \tag{1.31}$$

[1] The choice where $\phi_-(x)$ has the interpretation of source is called the "standard" boundary condition. One can also consider the "alternate" boundary condition where the roles of $\phi_-$ and $\phi_+$ are reversed [31].

These transformations are generated by translations, scaling, Lorentz transformations and special conformal transformations. A conformal field theory is a field theory that is invariant under such transformations.

We will consider two-point functions of *primary operators*. A *primary* operator $\mathcal{O}$ with *dimension* $\Delta$ transforms under scaling $x \to \lambda x$ as

$$\mathcal{O}(\lambda x) = \lambda^{\Delta}\mathcal{O}(x). \tag{1.32}$$

Now consider the two-point function

$$\langle \mathcal{O}(x)\mathcal{O}(y)\rangle \equiv f(x,y). \tag{1.33}$$

Invariance under translations requires $f(x,y) = f(|x-y|)$. Invariance under scaling requires that

$$\langle \mathcal{O}(x)\mathcal{O}(y)\rangle \propto \frac{1}{|x-y|^{2\Delta}}. \tag{1.34}$$

Conformal invariance completely fixes not just the coordinate dependence of the two-point functions, but also of the one and three point functions in the CFT, given the spectrum $\{\mathcal{O}_i, \Delta_i\}$, which is the set of primary operators and their dimensions.

**Bulk to boundary propagator**

Below we will try to recover the CFT result for the two-point function of a primary operator (1.34), using the bulk field $\Phi$ that is dual to $\mathcal{O}$. The bulk field with nonzero source can be reconstructed in terms of a bulk to boundary propagator $K(z, x-y)$ [32] [33]:

$$\Phi(x,z) = \int d^d y K(z, x-y)\phi_-(x), \tag{1.35}$$

where $K$ has to satisfy the equation of motion. One can show that the $SO(2,d)$ transformation $z \to \frac{z}{z^2+x_\nu x^\nu}, x^\mu \to \frac{x^\mu}{z^2+x^\nu x_\nu}$ of the $\Delta_+$ solution (1.28) yields the bulk to boundary propagator:

$$K(z, x-y) = c_{\Delta+}\left(\frac{z}{z^2+(x-y)^2}\right)^{\Delta_+}, \qquad c_{\Delta_+} = \frac{\Gamma[\Delta_+]}{\pi^{\frac{d}{2}}\Gamma[\Delta_+ - \frac{d}{2}]}. \tag{1.36}$$

In the small $z \to 0$ limit we can compare (1.29) and (1.35) order by order. At order $z^{\Delta_+}$ we find:

$$\phi_+(x) = c_{\Delta_+}\int d^d y \frac{1}{|x-y|^{2\Delta_+}}\phi_-(y). \tag{1.37}$$

Using the fundamental statement (1.30) and the identification of the source $\phi_{(0)} = \phi_-$, we can calculate connected n-point functions using the on shell gravitational action:

$$\begin{aligned}\langle \mathcal{O}(x_1)\dots\mathcal{O}_n\rangle_{\text{connected}} &= \frac{(-1)^{n+1}\delta^n}{\delta\phi_-(x_1)\dots\delta\phi_-(x_n)} W[\phi_-] \\ &= \frac{(-1)^{n}\delta^n}{\delta\phi_-(x_1)\dots\delta\phi_-(x_n)} S_{\text{AdS,on shell}}[\phi_-].\end{aligned} \tag{1.38}$$

The on shell action $S_{\text{AdS,on shell}}[\phi_-]$ is divergent for $z \to 0$ and must be regulated by a small parameter $z = \epsilon$. The regulated action can be evaluated on the equation of motion:

$$\begin{aligned}S &= -\frac{1}{2}\int d^{d+1}x\sqrt{g}\Phi\left(\Box - m^2\right)\Phi + L_{\text{AdS}}^{d-1}\int_{z=\epsilon} d^dx\ \frac{\Phi\partial_z\Phi}{z^{d-1}}\bigg|_{z=\epsilon} \\ &= L_{\text{AdS}}^{d-1}\int_{z=\epsilon} d^dx\ \frac{\Phi\partial_z\Phi}{z^{d-1}}\bigg|_{z=\epsilon}.\end{aligned} \tag{1.39}$$

We really should have added counter terms to the action to make it finite, but the result obtained by using the finite part of (1.39) turns out to be proportional to the answer obtained by properly renormalizing the action. Substituting (1.29) into (1.39) and keeping the finite part, we obtain using (1.37)

$$S \propto \int d^dx \int d^dy \frac{\phi_-(x)\phi_-(y)}{|x-y|^{2\Delta_+}}. \tag{1.40}$$

From this result we find

$$\begin{aligned}\langle \mathcal{O}(x)\rangle_{\text{connected}} &= \frac{-\delta}{\delta\phi_-(x)} S_{\text{AdS,on shell}} && \propto \phi_+(x), \\ \langle \mathcal{O}(x)\mathcal{O}(y)\rangle_{\text{connected}} &= \frac{\delta^2}{\delta\phi_-(x)\delta\phi_-(y)} S_{\text{AdS,on shell}} && \propto \frac{1}{|x-y|^{2\Delta_+}}.\end{aligned} \tag{1.41}$$

Note that the two-point function of the operator dual to $\Phi$ satisfies the constraints of the conformal group (1.34). The CFT analysis and the bulk calculation give the same result, illustrating that the holographic dictionary allows us to do calculations in either the boundary theory, or the bulk theory. Also note that we have

$$\langle \mathcal{O}(x)\rangle_{\text{connected}} = 0 \tag{1.42}$$

from the first line of (1.41) when the source term is set to zero. From the point of view of the CFT, this is required by translation invariance.

### 1.2.4 Wilson loop

The $ADS/CFT$-correspondence is sometimes called a gauge-gravity duality, because the examples derived from string theory involve boundary gauge theories. In a gauge theory, the gauge invariant operators are the so called Wilson loops. For a loop $\mathcal{C}$, the wilson loop $W_\mathcal{C}$ for a gauge field $A$ in representation $R$ is given by

$$W_\mathcal{C} = \frac{1}{\mathcal{N}} \mathrm{Tr}_R\{P[e^{i \oint_\mathcal{C} A}]\}, \tag{1.43}$$

where $P$ stands for "path ordered" and $\mathcal{N}$ is a normalization constant. The trace is taken over the representation of the gauge group. Note: in the context of $\mathcal{N} = 4$ $\mathcal{SYM}$ theory the Wilson loop also involves the scalar fields $X^I$ [34], which also transform in the adjoint representation.

The bulk dual of the expectation value of a Wilson loop $\mathcal{W}(\mathcal{C})$ evaluated in the supergravity limit is proposed to be [34, 35]:

$$\mathcal{W}(\mathcal{C}) \sim e^{-S} \tag{1.44}$$

where $S$ is the proper area of a fundamental string ending on the boundary loop $\mathcal{C}$ (see figure 1.2).

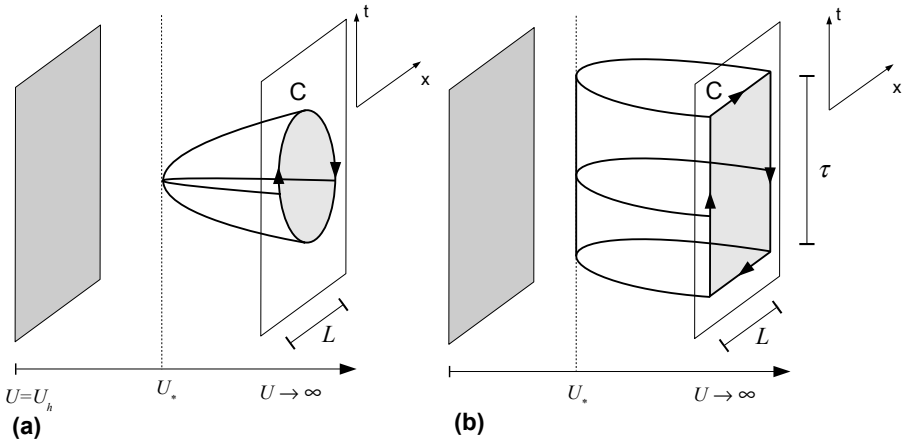


***Figure 1.2:*** *Circular (a) and (long) rectangular (b) Wilson loops $\mathcal{C}$ and their corresponding world sheets. In these pictures, the bulk is the area "on the left" of the boundary surface at $U \to \infty$. The coordinate $U$ is associated to the Poincaré coordinate $z$ by $U = z^{-1}$ and the Poincaré horizon, indicated by the gray planes at $U = U_h$ correspond to $z \to \infty$. The deepest point to which the world sheets reach is indicated by $U_*$. (Source: [36])*

The expectation value of a rectangular Wilson loop extending far into the past and future, is associated to the potential of a quark anti-quark pair with the same

separation. The action of a fundamental string, $S$, ending on a loop $\mathcal{C}$ on the boundary is divergent, where the leading divergence is proportional to the length of the loop $\mathcal{C}$. The divergence is interpreted as the unrenormalized self energy of massive quarks. Proper renormalization is necessary, but simple subtraction of the area of a string world sheet that goes "straight" into the bulk yields finite results [34].

## 1.3 Entanglement entropy

In this section, we will introduce holographic entanglement entropy and its bulk dual, which are crucial ingredients for chapter (2) and (3). First we will introduce the Von Neumann entropy. Then we will explain what the entanglement entropy of a subregion is, in the context of quantum field theory. Subsequently we will discuss several proposals for the bulk dual of boundary entanglement entropy.

### 1.3.1 Von Neumann entropy and entanglement

A quantum system can be described by a density matrix $\rho$, which is a linear operator on the Hilbert space. A density matrix is hermitian, semi-positive definite and has $\mathrm{Tr}\{\rho\} = 1$. The expectation value of an operator $\mathcal{O}$ can be calculated by evaluating:

$$\langle \mathcal{O} \rangle = \mathrm{Tr}\{\rho \mathcal{O}\}. \tag{1.45}$$

When the system is in a pure state $|\psi\rangle$, the density matrix has the form

$$\rho = |\psi\rangle\langle\psi|, \tag{1.46}$$

which implies that the eigenvalue spectrum contains $\lambda = 1$ with multiplicity one and the other eigenvalues are all zero. Non-pure states are called mixed. For a pure state $\rho = |\psi\rangle\langle\psi|$, the expectation value of an operator $\mathcal{O}$ (1.45) simply reduces to:

$$\langle \mathcal{O} \rangle = \mathrm{Tr}\{\rho \mathcal{O}\} = \sum_n \langle n|\psi\rangle\langle\psi|\mathcal{O}|n\rangle = \sum_n \langle\psi|\mathcal{O}|n\rangle\langle n|\psi\rangle = \langle\psi|\mathcal{O}|\psi\rangle, \tag{1.47}$$

where we have used that the trace is over a complete basis of orthonormalized states, such that $\sum_n |n\rangle\langle n| = \mathbf{I}$.

A general density matrix can be diagonalized and decomposed with respect to an orthonormalized eigenbasis:

$$\rho = \sum_i p_i |i\rangle\langle i|, \qquad \langle i|j\rangle = \delta_{ij}. \tag{1.48}$$

The Von Neumann entropy is a measure for the mixedness of a state:[2]

$$S_{\mathrm{VN}} = -\mathrm{Tr}\{\rho \log \rho\}. \tag{1.49}$$

When we decompose $\rho$ as in (1.48), we find:

$$S_{\mathrm{VN}} = -\sum_i p_i \log p_i, \tag{1.50}$$

which is always positive by virtue of the semi-positive definiteness of the density matrix and the property $\mathrm{Tr}\{\rho\} = 1$, because all eigenvalues are in the range $[0, 1]$. For a pure state the eigenvalue spectrum is $\{1, 0, \dots\}$ and the Von Neumann entropy vanishes.

If a quantum system consists of two (or more) separable parts $A$ and $B$ and if we can decompose the Hilbert space as

$$\mathcal{H} = \mathcal{H}_A \otimes \mathcal{H}_B, \tag{1.51}$$

then we can define a *reduced density matrix* $\rho_A$:

$$\rho_A = \mathrm{Tr}_{\mathcal{H}_B}\{\rho\}. \tag{1.52}$$

The reduced density matrix reproduces all expectation values of operators that have support on $\mathcal{H}_A$. The Von Neumann entropy is now called the entanglement entropy and is a measure of entanglement. It can be proved that the entanglement entropy satisfies the following properties [37](pages $515 - 521$):

$$\begin{aligned} S_{A\cup B} &\leq S_A + S_B && \text{subadditivity} \\ S_{A\cup B\cup C} + S_B &\leq S_{A\cup B} + S_{B\cup C} && \text{strong subadditivity.} \end{aligned} \tag{1.53}$$

Related quantities are the mutual information and the relative entropy. The *mutual information* of two subsystems $A$ and $B$ is given by

$$I(A, B) = S_A + S_B - S_{A\cup B} \tag{1.54}$$

and satisfies

$$I(A, B) \geq 0 \tag{1.55}$$

by virtue of the subadditivity of the Von Neumann entropy. The mutual information also sets an upper bound for correlations between operators $\mathcal{O}_A$ and $\mathcal{O}_B$ with support on $A$ and $B$ respectively [38]:

$$\left( \frac{\langle \mathcal{O}_A \mathcal{O}_B \rangle - \langle \mathcal{O}_A \rangle \langle \mathcal{O}_B \rangle}{\|\mathcal{O}_A\| \|\mathcal{O}_B\|} \right)^2 \leq 2I(A, B)\,. \tag{1.56}$$

[2]Sometimes, the Von Neumann entropy is defined with the base two $\log_2$. We will use the the natural logarithm log throughout this thesis, which differs by a multiplicative factor of $\log 2$.

The *quantum relative entropy* is a measure of the difference between two states. For two density matrices $\rho_0$ and $\rho_1$ the quantum relative entropy is defined as:

$$S(\rho_1|\rho_0) = \mathrm{Tr}\{\rho_1 \log \rho_1\} - \mathrm{Tr}\{\rho_1 \log \rho_0\}. \tag{1.57}$$

It can be be shown to satisfy the following property [39](page 511-513):

$$S(\rho_1|\rho_0) \geq 0 \qquad \forall \rho_1, \rho_0, \tag{1.58}$$

which is called the *positivity of relative entropy*. One can show that for a small change of the state parametrized by $\lambda$, of the form $\rho_\lambda = \rho + \lambda\delta\rho$ with $\delta\rho$ traceless (up to order $O(\lambda)$),

$$S(\rho_\lambda|\rho) = O(\lambda^2). \tag{1.59}$$

We will use property (1.59) in the statement of the first law of entanglement entropy (1.62), but first we need to define the *modular Hamiltonian*. The modular Hamiltonian $H_0$ of $\rho_0$ is defined by

$$\rho_0 = \frac{e^{-H_0}}{\mathrm{Tr}\{e^{-H_0}\}}. \tag{1.60}$$

Using (1.60), the quantum relative entropy can be written as:

$$S(\rho_1|\rho_0) = \Delta\langle H_0\rangle - \Delta S, \tag{1.61}$$

where $\Delta\langle H_0\rangle = \mathrm{Tr}\{H_0(\rho_1 - \rho_0)\}$ and $\Delta S = S(\rho_1) - S(\rho_0)$. Using the positivity of the quantum relative entropy and (1.59) we find up to first order:

$$\delta S = \delta\langle H\rangle. \tag{1.62}$$

This is called the first law of entanglement entropy [40]. Indeed, when the density matrix is thermal, we find the first law of thermodynamics.

### 1.3.2 Entanglement entropy in field theory

In the previous subsection we introduced the concept of entanglement entropy for quantum systems. Consider a quantum field theory defined on a (globally hyperbolic) spacetime $\mathcal{M}$. A spacelike Cauchy surface $\Sigma$ now comprises the "full system" and a subset $\mathcal{A} \subset \Sigma$ can be considered as a "subsystem". For $\mathcal{A}$, a reduced density matrix can be constructed by tracing over the degrees of freedom in the Hilbert space $\mathcal{H}_{\mathcal{A}^c}$ of $\mathcal{A}^c$, the complement of $\mathcal{A}$ in $\Sigma$:

$$\rho_{\mathcal{A}} = \mathrm{Tr}_{\mathcal{H}_{\mathcal{A}^c}}\{\rho\}. \tag{1.63}$$

Here we will derive a formal expression for the reduced density matrix $\rho_{\mathcal{A}}$ in terms of wave functionals and path integrals, in the vacuum state of the "full system", for the simple setup with a quantum field theory on $(1+1)$-dimensional flat space and with $\mathcal{A}$ equal to half-space: $\mathcal{A} = \{(x,t) : x \geq 0\, t = 0\}$. The techniques used in this example generalize to more complicated setups. The material covered below can be found largely in [41, 42]. We will use coordinates $(x,t)$ with $ds^2 = -dt^2 + dx^2$ or in Euclideanized coordinates $(x, \tau = it)$, $ds^2 = d\tau^2 + dx^2$.

First we will introduce the *replica trick*, a trick used to simplify the calculation of entanglement entropy:

$$\begin{aligned} S(\rho) &= -\mathrm{Tr}\{\rho \log \rho\} \\ &= -\frac{\partial}{\partial n}\mathrm{Tr}\{\rho^n\}\Big|_{n=1}. \end{aligned} \tag{1.64}$$

Another version of the replica trick, that also works for non-normalized $\rho$ is given by

$$S(\rho) = -\lim_{n\to 1}(n\partial_n - 1)\mathrm{Tr}\{\rho^n\}. \tag{1.65}$$

If the replica trick can be used, then the computation of the entanglement entropy reduces to the computation of $\mathrm{Tr}\{\rho^n\}$. The replica trick can be used under the assumption that the analytic continuation $n \to \mathbb{R}$ is correct. To check whether the answers obtained with the replica trick are correct, one can compare the obtained results to a lattice calculation in the limit where the lattice size goes to zero.

We assume that the replica trick can be used, and proceed to the calculation of $\mathrm{Tr}\{\rho^n\}$, for which we will derive a formal expression below.

For a theory with a scalar field $\phi(x)$ a complete set of states is given by

$$\{|\tilde{\phi}, t\rangle : \hat{\phi}(x)|\tilde{\phi}, t\rangle = \tilde{\phi}(\vec{x})|\tilde{\phi}, t\rangle\}, \tag{1.66}$$

where the operator $\phi(x)$ is time independent and the time dependence is carried by the states (Schrödinger picture). The wave functional for a general state $|\Psi\rangle$ can formally be defined as

$$\Psi(\phi, t) = \langle \phi, t|\Psi\rangle. \tag{1.67}$$

The Euclidean wave functional of the vacuum state is given by:

$$\Psi(\phi, \tau) = \int_{\tau\to-\infty}^{\tilde{\phi}(\tau)=\phi} D[\tilde{\phi}]e^{-S[\tilde{\phi}]}. \tag{1.68}$$

Now we divide the $x$-axis into two "subsystems" with the origin as boundary: $\mathcal{A} = \{(x,\tau) : x > 0, \tau = 0\}$. Supposing that we can further decompose the

eigenstates of $\hat{\phi}$ (1.66)[3]

$$|\phi, \tau\rangle \sim |\phi_L, \tau\rangle \otimes |\phi_R, \tau\rangle, \tag{1.69}$$

where $L$ (R) refers to the interval $x < 0$ ($x > 0$), we can see that the components of the *reduced density matrix* for the region $x > 0$ can be obtained by integrating over all field configurations on the "left" ($x < 0$):

$$\begin{aligned}\langle \phi_{R,+}, 0_+| \ \rho \ |\phi_{R,-}, 0_-\rangle &= \langle \phi_{R,+}, 0_+|\Psi\rangle\langle\Psi|\phi_{R,-}, 0_-\rangle \\ &= \int D[\tilde{\phi}_L] \int_{\tilde{\phi}_R(0_-)=\phi_{R,-}}^{\tilde{\phi}_R(0_+)=\phi_{R,+}} D[\tilde{\phi}_R] e^{-S[\tilde{\phi}_L, \tilde{\phi}_R]}.\end{aligned} \tag{1.70}$$

An alternative and equivalent formulation of equation (1.70) is given by [43]

$$\begin{aligned}&\langle \phi_{R,+}, 0_+| \ \rho \ |\phi_{R,-}, 0_-\rangle = \langle \phi_{R,+}, 0_+|\Psi\rangle\langle\Psi|\phi_{R,-}, 0_-\rangle \\ &= \int_{\tau\to\infty}^{\tau\to-\infty} D[\tilde{\phi}] e^{-S[\tilde{\phi}]} \Pi_{x>0} \delta\left(\tilde{\phi}(0_+) - \phi_{R,+}\right) \delta\left(\tilde{\phi}(0_-) - \phi_{R,-}\right).\end{aligned} \tag{1.71}$$

The expressions (1.70) and (1.71) contain path integrals with fixed field values along the cut $x > 0, \tau = 0$, with $\phi = \phi_{R,\pm}$ as constraint value at $\tau = 0\pm$. The "product" of $n$ reduced density matrices can be constructed by matching the field values of $\phi^i_{R,+}$ with $\phi^{i+1}_{R,-}$, followed by integration over the matched field value (this is the analog of matrix multiplication for density matrices of Hilbert spaces with finite dimension):

$$\begin{aligned}&\langle \phi_{R,+}, 0 + |\rho^2|\phi_{R,-}, 0_-\rangle \propto \\ &\langle \phi_{R,+}, 0 + |\Psi\rangle\langle\Psi|\Psi\rangle\langle\Psi|\phi_{R,-}, 0_-\rangle = \\ &\int D[\bar{\tilde{\phi}}_R] \int D[\tilde{\phi}_L] \int_{\tilde{\phi}_R(0-)=\bar{\tilde{\phi}}_R}^{\tilde{\phi}_R(0+)=\phi_{R,+}} D[\tilde{\phi}_R] e^{-S[\tilde{\phi}]} \int D[\tilde{\phi}'_L] \int_{\tilde{\phi}'_R(0-)=\phi_{R,-}}^{\tilde{\phi}'_R(0+)=\bar{\tilde{\phi}}_R} D[\tilde{\phi}_R] e^{-S[\tilde{\phi}']}\end{aligned} \tag{1.72}$$

Repeating this "sewing" procedure and taking an overall trace, one obtains a path integral over a conical defect space with a defect angle of $2\pi(n-1)$.

Hence, calculating $\mathrm{Tr}\{\rho^n\}$ amounts to the calculation of the partition function $Z_n$ on the conical defect space. In the above discussion we did not take into account the normalization of $\rho$ in order to make sure that $\mathrm{Tr}\{\rho\} = 1$. The full expression for $\mathrm{Tr}\{\rho^n\}$ is given by

$$\mathrm{Tr}\{\rho^n\} = \frac{Z_n}{Z_1^n}, \tag{1.73}$$

where $Z_n$ is the partition function on the conical defect space and $Z_1$ is the partition function on $\mathscr{R}^2$.

[3]This is a matter of debate, but for a theory on a lattice it is certainly true.

**Example: Rindler wedge**

We just derived an important expression that allows us to calculate the entanglement entropy of a subregion by calculating the partition function on a conical defect space (if the replica trick can be used). Now we will use a slightly different technique to derive an expression for the reduced density matrix of half-space, for a field theory on (1+1)-dimensional Minkowski spacetime. This is an important example, that has many applications in later chapters.

First we introduce the *Rindler wedge*, the subset $\{(x,t) : |t| \leq x, x \geq 0\}$ of Minkowski space. This wedge can be covered by Rindler coordinates $T, R$ defined by

$$\begin{aligned} x &= R\cosh T, \\ t &= R\sinh T, \\ ds^2 &= -R^2 dT^2 + dR^2. \end{aligned} \tag{1.74}$$

An observer at fixed $R$ can be associated to an accelerated observer in Minkowski space. Consider the example of a scalar field in $(1+1)$ dimensions.

Half-space, $\{(x,t) : x > 0, t = 0\}$, is a Cauchy surface for the Rindler wedge. In Lorentzian signature, boosts are generated by $\xi = x\partial_t + t\partial_x$. One can check that observers with constant acceleration $a$, that come in from infinity and turn at $x = \frac{1}{a}$ and go back to infinity, move on trajectories generated by $\xi$, satisfying

$$\xi^\mu \nabla_\mu \xi^\nu = a\xi^\nu. \tag{1.75}$$

The boosts generated by $\xi$ are a symmetry of a Lorentz invariant theory and the generator is given by

$$K = \int_\Sigma d\Sigma^\mu T_{\mu\nu}\xi^\nu, \tag{1.76}$$

where $T$ is the energy momentum tensor and $\Sigma$ is a Cauchy slice.

In the Euclidean picture $\tau = it$, $\xi$ becomes the generator of rotations:

$$x\partial_t + t\partial_x \to -i\left(x^1\partial_\tau - \tau\partial_x\right). \tag{1.77}$$

The expression for the components of $\rho_R$ (1.70) is given in the Euclidean picture and is a path integral with fixed field values along the cut $x > 0, t = 0$. The path integral can be calculated by slicing the Euclidean plane in angular sections. But the Euclideanized theory is invariant under rotations which are generated by the Euclideanized $K$ (1.76):

$$\begin{aligned} \langle \phi_{R,+}, 0+|\Psi\rangle\langle\Psi|\phi_{R,-}, 0_-\rangle &= \int D[\tilde{\phi}_L] \int_{\tilde{\phi}_R(0-)=\phi_{R,-}}^{\tilde{\phi}_R(0+)=\phi_{R,+}} D[\tilde{\phi}_R] e^{-S[\tilde{\phi}_L, \tilde{\phi}_R]} \\ &= \langle \phi_{R,+}, 0+|e^{-2\pi K}|\phi_{R,-}, 0_-\rangle. \end{aligned} \tag{1.78}$$

We conclude that

$$\rho_{\mathcal{A}} = \frac{e^{-2\pi K}}{\mathrm{Tr}\{e^{-2\pi K}\}}, \tag{1.79}$$

where $K$ is the generator of Euclidean boosts. This is an example of a thermal density matrix. The associated temperature depends on the normalization of $K$, or equivalently, it depends on the choice of accelerated observer. For an observer with constant acceleration $a$, translations in proper time are generated by $\tilde{K} = aK$ and the density matrix is thermal with $T = \frac{a}{2\pi}$:

$$\rho_R = \frac{e^{-\frac{2\pi}{a}\tilde{K}}}{\mathrm{Tr}\{e^{-\frac{2\pi}{a}\tilde{K}}\}}. \tag{1.80}$$

### 1.3.3 A bulk dual for entanglement entropy

#### Ryu-Takayanagi proposal and beyond

The boundary entanglement entropy of a subregion $\mathcal{A}$ of a Cauchy slice $\Sigma$ has been conjectured to be equal to the area of a surface $\mathfrak{E}_{\mathcal{A}}$, which is a bulk extremal surface with minimal area that ends on $\partial\mathcal{A}$ and is homologous to $\mathcal{A}$ [44, 45]:

$$S_{\mathcal{A}} = \frac{A_{\mathfrak{E}_{\mathcal{A}}}}{4G}, \tag{1.81}$$

where $G$ is Newton's gravitational constant. This formula is referred to as the HRT formula or HRT proposal (Hubeny, Rangamani, Takayanagi). The expression (1.81) is thought to hold to leading order in $\frac{1}{N}$. Recently a limited proof for static spacetimes of (1.81) was given in [46].[4] There is also surmounting evidence for the HRT formula; it gives results that are consistent with field theory calculations and it also automatically satisfies nontrivial properties such as strong subadditivity (1.53), which we discuss below.

The formula (1.81) was originally formulated by Ryu and Takayanagi for static spacetimes. In a static spacetime, one can consider a constant time slice $\Sigma_t$ in the bulk. When the boundary entanglement surface $\partial\mathcal{A}$ lies on (the boundary restriction of) the constant time slice, the extremal surface ending on $\partial\mathcal{A}$ lies completely on the bulk constant time slice and is simply the minimal surface on $\Sigma_t$.

The Ryu-Takayanagi prescription is believed to hold at leading order in large $N$. In the $AdS_5 \times S^5$ example, this means the formula (1.81) holds at order $N^2$. The

[4] Fursaev made an early attempt to prove (1.81) [47], but in [48] it was argued that this proof is incorrect.

subleading correction in $N^{-1}$ is proposed to be given by the *bulk* entanglement entropy across the bulk extremal surface defined by (1.81) [49]:

$$S_{\mathcal{A}} = \frac{A_{\mathfrak{E}_{\mathcal{A}}}}{4G} + S_{\text{bulk}}(\mathfrak{E}_{\mathcal{A}}), \tag{1.82}$$

where the leading order contribution is given by (1.81) and $S_{\text{bulk}}(\mathfrak{E}_{\mathcal{A}})$ is the bulk entanglement entropy across the extremal surface $\mathfrak{E}_{\mathcal{A}}$ defined by (1.81). Another proposal was given by Wall and Engelhardt [50]:

$$S_{\mathcal{A}} = \frac{A_{\mathfrak{F}_{\mathcal{A}}}}{4G} + S_{\text{bulk}}(\mathfrak{F}_{\mathcal{A}}), \tag{1.83}$$

where $\mathfrak{F}_{\mathcal{A}}$ is determined by extremizing the sum of *both* terms in (1.83) instead of just the term corresponding to (1.81). The surface $\mathfrak{F}_{\mathcal{A}}$ is called a quantum extremal surface. Note that both quantities (1.82,1.83) involve counter terms necessary to normalize the bulk entanglement entropy. Details can be found in [49, 50].

**Strong subadditivity**

The strong subadditivity property is an important feature of the Von Neumann entropy. The holographic entanglement entropy satisfies the strong subadditivity property. The fact that it *does* is nontrivial and provides evidence for the HRT proposal (1.81). Below we briefly illustrate the strong subadditivity property of holographic entanglement entropy in the case of static spacetimes and constant time slices, following [51].

The Von Neumann entropy of subsystems $A, B, C$ always satisfies the highly nontrivial strong subadditivity property (1.53):

$$S_{A\cup B\cup C} + S_B \leq S_{A\cup B} + S_{B\cup C}. \tag{1.84}$$

In a quantum field theory we can recast the strong subadditivity property for subregions $A, B$ as

$$S_{A\cup B} + S_{A\cap B} \leq S_A + S_B. \tag{1.85}$$

For static bulk spacetimes, we can introduce constant time slices. If $A$ and $B$ are both subregions of the boundary restriction of a constant timeslice, then their associated minimal surfaces $\mathfrak{E}_A$ and $\mathfrak{E}_B$ also lie on that constant timeslice. A pictorial argument now shows that the surface $\mathfrak{E}_A \cup \mathfrak{E}_B$ can be decomposed into a surface that ends on $\partial(A \cup B)$ and a surface that ends on $\partial(A \cap B)$. If these happen to coincide with the minimal surfaces ending on $\partial(A \cup B)$ and $\partial(A \cap B)$ respectively, then (1.53) is satisfied and the bound is saturated. If these surfaces do not correspond to the minimal surfaces ending on $\partial(A \cup B)$ and $\partial(A \cap B)$, then the associated entanglement entropies will satisfy (1.53), since the true minimal

surfaces ending on $\partial(A \cup B)$ and $\partial(A \cap B)$ will yield a smaller area and hence smaller associated entanglement entropy [51].

In [52], strong subadditivity is also shown to hold for non-static bulk spacetimes. The fact that the HRT proposal satisfies the nontrivial strong subadditivity property provides evidence for its correctness.

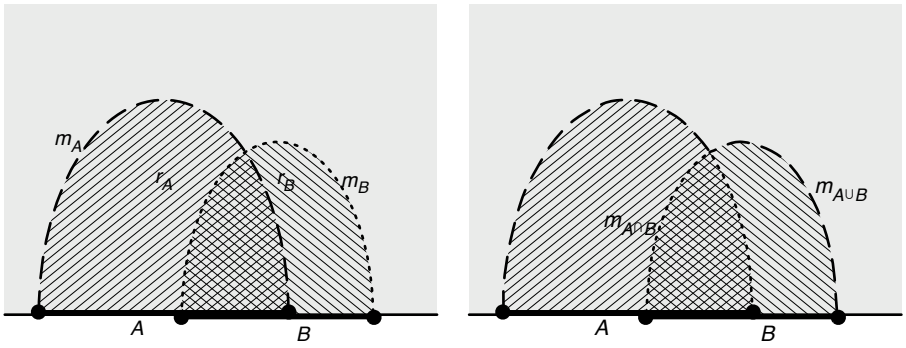


***Figure 1.3:*** *Heuristic visual proof of (1.85). The union $m_A \cup m_B$ of the minimal surfaces $m_A$ and $m_B$, which are associated to the two partially overlapping boundary subregions $A$ and $B$ respectively, can be decomposed into two surfaces $r_{A\cup B}$ and $r_{A\cap B}$ which end on $\partial(A \cup B)$ and $\partial(A \cap B)$ respectively. The area of the minimal surfaces $m_{A\cup B}$ and $m_{A\cap B}$ is generally smaller than or equal to the area of $r_{A\cup B}$ and $r_{A\cap B}$ respectively, with equality if $m_{A\cup B} = r_{A\cup B}$ and $m_{A\cap B} = r_{A\cap B}$. This implies for the associated entanglement entropies that $S_A + S_B \geq S_{A\cup B} + S_{A\cap B}$. (Source: [51])*

### Wald functional

The expression for holographic entanglement entropy (1.81) is very similar to the expression for the black hole entropy (1.1). In higher derivative non-Einstein gravity, the black holes entropy receives a correction to (1.1) given by the Wald functional. This suggests that we should also consider the Wald functional for the holographic entanglement entropy, modifying (1.81). Below we will discuss the Wald entropy, the Wald functional and its application to holographic entanglement entropy.

Wald showed that the black hole entropy is a conserved charge that corresponds to the symmetry generated by the Killing vector, for which the black hole event horizon is the (bifurcate) Killing horizon [53]. This statement remains valid for black holes in higher derivative gravity theories, but the associated entropy and conserved charge are given by the Wald functional [53–55]:

$$W = -2\pi \int_{\mathcal{H}} d^{d-1}x\sqrt{h}\frac{\delta\mathcal{L}}{\delta R^{ab}_{cd}}\epsilon^{ab}\epsilon_{cd}, \tag{1.86}$$

where $\mathcal{H}$ is the Killing horizon, $\epsilon^{ab}$ its bi-normal and

$$\begin{aligned}\frac{\delta\mathcal{L}}{\delta R_{abcd}} = \frac{\partial\mathcal{L}}{\partial R_{abcd}} - \nabla_{a_1}\frac{\partial\mathcal{L}}{\partial\nabla_{a_1}R_{abcd}} + \dots \\ + (-1)^n\nabla_{(a_1}\dots\nabla_{a_n)}\frac{\partial\mathcal{L}}{\partial\nabla_{(a_1}\dots\nabla_{a_n)}R_{abcd}} + \dots,\end{aligned} \tag{1.87}$$

where $\mathcal{L}$ is the gravitational Lagrangian.

A (bifurcate) Killing horizon is a special surface, since its extrinsic curvature vanishes by virtue of the Killing equation $\nabla_a\xi_b + \nabla_b\xi_a = 0$. For a minimal surface, the extrinsic curvature does generally not vanish completely, even though the trace of the extrinsic curvature does vanish [45]. It is not a priori clear that the Wald functional can be used for a generalization of the holographic entanglement entropy formula.

In [56] it was shown that the Wald functional needs to be modified in order to yield consistent answers for the holographic entanglement entropy. For Lovelock gravity, a modification of the Wald functional is proposed in [56]. A more general formula is given in [57].

Another difference with the black hole entropy is that the holographic entanglement entropy yields divergent answers, while the black hole entropy is finite, due to the fact that the area of the horizon is finite. Below we will describe the divergence structure of holographic entanglement entropy.

**Structure of divergences**

Holographic entanglement entropy is given by the area of a bulk surface that ends on the boundary (1.81). The bulk metric diverges near the asymptotic boundary. The area of the extremal surface must be regulated by implementing a bulk $IR$-cutoff. The leading divergence is proportional to the area of $\partial\mathcal{A}$:

$$S_{\mathcal{A}} \propto \frac{\partial\mathcal{A}}{\epsilon^{d-1}} + \dots + \gamma\log(\epsilon) + \dots \tag{1.88}$$

These divergences are consistent with field theory calculations. From the field theory point of view, the leading area term (1.88) can be associated to entanglement due to the short distance degrees of freedom, across the entanglement surface $\partial\mathcal{A}$. In the field theory calculation, a short distance or UV cut off must be used to regulate the divergences. The leading divergence is independent of the details of the background metric as long as the cutoff scale is much smaller then the curvature scale.

Power law divergences are generally cutoff dependent. For smooth surfaces $\partial\mathcal{A}$, in a field theory on a $d$-dimensional background, there is also a logarithmically

divergent term for even $d$. The coefficient of this logarithmically divergent term is universal for conformal field theories: it does not depend on the cutoff nor the state. The coefficient does depend on the geometry of the entanglement surface $\partial\mathcal{A}$. In $(3+1)$ dimensions, the coefficient of the logarithmically divergent part of the entanglement entropy is given by [58]

$$-\frac{a}{720\pi}\int_{\partial\mathcal{A}} R_{\partial\mathcal{A}} + \frac{c}{720\pi}\int_{\partial\mathcal{A}}\left(-K^a_{\mu\nu}K^{a\mu\nu} + \frac{1}{2}K_a K^a\right), \tag{1.89}$$

where $a$ and $c$ are the central charges of the theory. Note that these coefficients are invariant under boundary Weyl transformations $g_{\mu\nu} \to e^{2\omega} g_{\mu\nu}$.

**Example: the strip**

We consider the boundary region $\mathcal{A} = \{(\vec{x}, t) : |x_1| \leq \frac{w}{2} L_{\text{AdS}}^{-1}, t = 0\}$ for $d > 2$, with a pure AdS bulk metric in Poincaré coordinates (1.14,1.15).[5] The holographic entanglement entropy is given by (1.81). We need to minimize the area

$$\begin{aligned} A &= \int dx_1 \int_{-\frac{L_{\text{IR}}}{2L_{\text{AdS}}}}^{\frac{L_{\text{IR}}}{2L_{\text{AdS}}}} dx_2 ... dx_{d-1} \sqrt{\det \frac{\partial x^M}{\partial x^\alpha}\frac{\partial x^N}{\partial x^\beta} G^{ADS}_{MN}} \\ &= L_{\text{IR}}^{d-2} L_{\text{AdS}} \int dx_1 \sqrt{\left(\left(\frac{dz}{dx_1}\right)^2 \frac{1}{z^2} + \frac{1}{z^2}\right)\left(\frac{1}{z^2}\right)^{d-2}}, \end{aligned} \tag{1.90}$$

where $L_{\text{IR}}$ is a boundary IR-cutoff along the spatial coordinates orthogonal to $x_1$.

The Lagrangian does not explicitly depend on $x_1$

$$\mathcal{L} = \frac{1}{z^{d-1}}\sqrt{\left(\frac{dz}{dx_1}\right)^2 + 1}, \tag{1.91}$$

so the equation of motion for $z(x)$ can be written in terms of a "conserved quantity" $z_*$

$$\frac{\partial z}{\partial x} = \sqrt{\left(\frac{z_*}{z}\right)^{2(d-1)} - 1} \tag{1.92}$$

where $z_*$ is the "turning point" of the bulk surface: $\frac{dz}{dx_1}(z_*) = 0$.

Now we can solve for $z_*$ in terms of $w$:

$$\begin{aligned} \frac{w}{2L_{\text{AdS}}} &= \int_0^{\frac{w}{2L_{\text{AdS}}}} dx' = \int_0^{z_*} dz' \frac{dx}{dz'} = \int_0^{z_*} dz \frac{z^{d-1}}{\sqrt{z_*^{2(d-1)} - z^{2(d-1)}}} \\ &= z_* \int_0^1 dx \frac{x^{d-1}}{\sqrt{1 - x^{2(d-1)}}}. \end{aligned} \tag{1.93}$$

[5] Here we consider dimensionless coordinates $z \to \frac{z}{L_{\text{AdS}}}$, $x^i \to \frac{x^i}{L_{\text{AdS}}}$, for which the metric is still equal to (1.15).

The integral (1.93) can be done and gives

$$z_* = \frac{dw}{\sqrt{\pi} 2L_{\mathrm{AdS}}} \frac{\Gamma[\frac{2d-1}{2d-2}]}{\Gamma[\frac{3d-2}{2d-2}]}. \tag{1.94}$$

With $z_*$ (1.94) and the "equation of motion" (1.92) we can calculate the area:

$$\begin{aligned} A &= 2L_{\mathrm{AdS}}^{d-1} \int_{\frac{\epsilon}{L_{\mathrm{AdS}}}}^{\frac{w}{2L_{\mathrm{AdS}}}} dz \int_{-\frac{L_{\mathrm{IR}}}{2L_{\mathrm{AdS}}}}^{\frac{L_{\mathrm{IR}}}{2L_{\mathrm{AdS}}}} dx_2 ... dx_{d-1} \sqrt{\left( \left( \frac{dx_1}{dz} \right)^2 \frac{1}{z^2} + \frac{1}{z^2} \right) \left( \frac{1}{z^2} \right)^{d-2}} \\ &= \frac{2L_{\mathrm{AdS}}^{d-1}}{d-2} \left( \left( \frac{L_{\mathrm{IR}}}{\epsilon} \right)^{d-2} - \left( \frac{L_{\mathrm{IR}}}{w} \right)^{d-2} \frac{1}{2} \left( \frac{2\sqrt{\pi}\Gamma[\frac{d}{2(d-1)}]}{\Gamma[\frac{1}{2(d-1)}]} \right)^{d-1} \right) + O(\epsilon). \end{aligned} \tag{1.95}$$

The leading divergence is proportional to the area $\partial\mathcal{A}$, which is $2L_{\mathrm{IR}}^{d-2}$ for the strip. There is no logarithmically divergent term ($d > 2$), which is in agreement with (1.89), since both the intrinsic curvature and the extrinsic curvature of $\partial\mathcal{A}$ vanish everywhere on the strip.

# Chapter 2

# Shadows and holographic reconstruction

In this chapter we first give a non-exhaustive introduction of bulk reconstruction techniques: techniques that are used to reconstruct the bulk geometry, the bulk fields and the bulk dynamics from the boundary fields and dynamics. Then we describe the appearance of bulk regions where at least one of the reconstruction techniques fail. This does *not* mean that holography is wrong or incorrect; it is perfectly possible that we will be able to reconstruct all the bulk physics in the future, by discovering different "entries" in the holographic dictionary, or different techniques to make use of them. The necessity of discovering new bulk probes also motivates the study of *causal holographic information*, which we will discuss in chapter (3).

## 2.1 Holographic reconstruction

Holographic reconstruction is the construction of quantities on one side of the holographic duality with knowledge of the state and theory on the other side. The terminology of "holographic reconstruction" is mostly used in the context of reconstruction of bulk quantities with knowledge of the boundary theory and state. In this section we will give a non-exhaustive description of reconstruction techniques. Some of these reconstruction techniques already assume a semi-classical bulk geometry and attempt to reconstruct field values [59–62]. Other techniques are used to reconstruct the *dynamics* of the bulk fields [63–65]. The most funda-

mental reconstruction techniques do not even assume a spacetime a priori; a point of spacetime needs to be defined carefully [66].

Note that a subset of these techniques make extensive use of holographic entanglement entropy. One could hypothesize that the bulk is a representation or geometrization of the entanglement structure of the boundary theory. It is not immediately clear how this hypothesis relates to the interpretation of the radial direction as an RG-scale, which we discussed in section (1.2), but there are no apparent contradictions either.

We will first discuss the idea of subregion dualities. Then we will briefly present techniques that can be used to reconstruct bulk fields, bulk spacetime and bulk gravity.

### 2.1.1 Reconstruction & subregion duality

An important question in the context of the AdS/CFT-correspondence is whether a subregion duality exists. A subregion duality is a duality between a boundary subregion and a bulk subregion. Given the density matrix of a subregion, how much of the bulk can one generically reconstruct? This question has been analyzed in [67–69]. Below we discuss the two main candidates for such a subregion duality.

#### Causal wedge

The causal wedge $\blacklozenge_{\mathcal{A}}$ is a bulk subregion associated to a boundary subregion $\mathcal{A}$. Consider an asymptotically AdS manifold $\mathcal{M}$ with asymptotic boundary $\partial\mathcal{M}$. First we define the boundary causal diamond of $\mathcal{A}$; it is the union of the boundary future and past domains of dependence of $\mathcal{A}$:

$$\lozenge_{\mathcal{A}} = D^{+}_{\partial\mathcal{M}}(\mathcal{A}) \cup D^{-}_{\partial\mathcal{M}}(\mathcal{A}) \quad . \tag{2.1}$$

The so called causal wedge $\blacklozenge_{\mathcal{A}}$ of $\mathcal{A}$ is the intersection of the bulk future and past domains of influence of $\lozenge_{\mathcal{A}}$:

$$\blacklozenge_{\mathcal{A}} = J^{+}_{\mathcal{M}}(\lozenge_{\mathcal{A}}) \cap J^{-}_{\mathcal{M}}(\lozenge_{\mathcal{A}}). \tag{2.2}$$

In pure AdS spacetime, the causal wedge of a boundary ball on a constant time slice can be mapped to the AdS-Rindler spacetime. Even though there are difficulties in the construction of the smearing function, a subregion duality *is* thought to hold for the AdS-Rindler wedge, because the AdS-Rindler wedge can be mapped to the exterior of a hyperbolic black hole. The exterior of a black hole is expected to be reconstructable with the boundary data. Another argument for the proposition that there is a subregion duality between $\mathcal{A}$ and its causal wedge $\blacklozenge_{\mathcal{A}}$ is that

a boundary observer could send accelerated observers into the bulk, which could collect data from the causal wedge $\blacklozenge_{\mathcal{A}}$ and return to the boundary causal diamond $\Diamond_{\mathcal{A}}$. These arguments make a strong case for a subregion duality between a boundary subregion $\mathcal{A}$ and its causal wedge $\blacklozenge_{\mathcal{A}}$ and it is believed that the causal wedge $\blacklozenge_{\mathcal{A}}$ is the minimum subregion that is reconstructable with full knowledge of $\rho_{\mathcal{A}}$.

**Entanglement wedge**

Another candidate for a subregion duality is the boundary subregion $\mathcal{A}$ and its associated *entanglement wedge* [70]. Consider the boundary subregion $\mathcal{A}$ and the bulk extremal surface $\mathfrak{E}_{\mathcal{A}}$ which computes its entanglement entropy (1.81). There exists a spacelike surface $\mathcal{R}_{\mathcal{A}}$, that is part of a bulk Cauchy surface, such that $\partial\mathcal{R}_{\mathcal{A}} = \mathcal{A} \cup \mathfrak{E}_{\mathcal{A}}$. The entanglement wedge is the bulk causal diamond for this spacelike surface:

$$\mathcal{W}_{\mathcal{A}} = D^{+}_{\mathcal{R}_{\mathcal{A}}} \cup D^{-}_{\mathcal{R}_{\mathcal{A}}}, \tag{2.3}$$

where $D^{\pm}_{\mathcal{R}_{\mathcal{A}}}$ is the bulk future (past) domain of dependence of $\mathcal{R}_{\mathcal{A}}$. In [70] it was argued that this region should be reconstructable with the information of $\rho_{\mathcal{A}}$.[1]

## 2.1.2 Reconstruction of the fields

In section (1.1) we discussed the relation between a bulk scalar field $\Phi$ and its boundary dual $\mathcal{O}_{\Phi}$ and in particular the bulk to boundary propagator which allows the bulk scalar field $\Phi$ to be expressed in terms of the boundary source $\phi_{-}$.[2] Another approach is to reconstruct the *unsourced* bulk scalar field $\Phi$, in the semi-classical regime, with knowledge of all expectation values $\langle \mathcal{O}_{\Phi} \rangle$ of the boundary dual operator. This problem has been studied in [59–62], making use of a *smearing function*. Below we will briefly discuss the basics of this reconstruction method, which assumes both large $N$ and large t Hooft coupling.

A free scalar field $\Phi$ is taken to have normalizable fall-off near the boundary; in Poincaré coordinates (1.14,1.15)

$$\Phi(x, z) \sim z^{\Delta_+} \phi_+(x), \tag{2.4}$$

for small $z$. The approach here is slightly different from the approach in section (1.1), which goes under the name "differentiate", whereas the method that is presented here is called "extrapolate". These methods are shown to be equivalent [72].

[1] In [71] a more precise proposal was made.

[2] In a theory with bulk interactions the bulk to bulk propagator is also necessary.

The aim of [59] is to construct a *smearing function* $K$ such that

$$\Phi(x,z) = \int d^d x' K(x'|z,x)\mathcal{O}_\Phi(x'). \tag{2.5}$$

Several methods to explicitly construct the smearing function are presented in [59], but here we will only discuss the "mode-sum approach".

We can expand the field $\Phi$ and its normalizable mode $\phi_+$ (2.4) in modes labeled by quantum number $k$ and keep the dependence on the radial coordinate $z$:

$$\begin{aligned}\Phi(z,x) &= \int d^{d-1}k a_{\vec{k}} F_{\vec{k}}(z,x) + \text{c.c.} \\ \phi_+(x) &= \int d^{d-1}k a_{\vec{k}} f_{\vec{k}}(z,x) + \text{c.c.},\end{aligned} \tag{2.6}$$

with $F_{\vec{k}} = z^{\Delta_+} f_{\vec{k}}$, where $\vec{k}$ is typically associated to conserved quantities and the set of solutions $\{f_k\}$ is taken to be orthogonal:

$$\int d^{d-1}x f^*_{\vec{k}}(x) f_{\vec{k}'}(x) = N(\vec{k})\delta^{d-1}(\vec{k}-\vec{k}'). \tag{2.7}$$

We can determine the coefficients $\{a_{\vec{k}}\}$ by exploiting the orthogonality relations (2.7):

$$a_{\vec{k}} = \frac{1}{N(\vec{k})}\int d^{d-1}x f^*_{\vec{k}}(x)\phi_+(x). \tag{2.8}$$

Now we have, using (2.6) and (2.8)

$$\begin{aligned}\Phi(x,z) &= \int d^{d-1}k a_{\vec{k}} F_{\vec{k}}(x,z) + \text{c.c.} \\ &= \int d^{d-1}k \frac{1}{N(\vec{k})}\left(\int d^{d-1}x' f^*_{\vec{k}}(x')\phi_+(x')\right) F_{\vec{k}}(x,z) + \text{c.c.}\end{aligned} \tag{2.9}$$

If we can exchange the integrals over $x'$ and $k$ in (2.9) we obtain an expression for the smearing function:

$$\begin{aligned}\Phi(x,z) &= \int d^{d-1}x' \left(\int d^{d-1}k \frac{1}{N(\vec{k})} f^*_{\vec{k}}(x') F_{\vec{k}}(x,z)\right)\phi_+(x') + \text{c.c.} \\ &= \int d^{d-1}x' K(x'|z,x)\phi_+(x'),\end{aligned} \tag{2.10}$$

with

$$K(x'|z,x) = \int d^{d-1}k \frac{1}{N(\vec{k})} f^*_{\vec{k}}(x') F_{\vec{k}}(x,z) + \text{c.c.} \tag{2.11}$$

In both the Poincaré patch as well as global AdS, the smearing functions can be constructed. The smearing function is *not* unique. In global AdS patches, the

smearing functions $K(x'|z,x)$ constructed in [59, 60] have support on boundary points $\{x'\}$ spacelike separated from the bulk point $(z,x)$. In the Poincaré patch the smearing function has support on the whole boundary for $d$ even ($D$ odd).

An interesting question is whether a smearing function exists for AdS-Rindler space and other spacetimes. For pure AdS, corresponding to the vacuum state of the boundary CFT, the causal wedge associated to a boundary ball can be mapped to AdS-Rindler spacetime. In subsection (2.1.1) we argued that the causal wedge should be reconstructable with knowledge of the state on its associated boundary region. An expression in the form of (2.9) certainly exists for AdS-Rindler spacetime, but the integral over $k$ is not convergent after exchanging it with the integral over $x'$.[3] The construction of the smearing function in AdS-Rindler is thus at least problematic.

Reconstruction of the fields via the smearing function is possible for some bulk geometries, but not for every bulk geometry. In [73] it is argued that the smearing function does not exist when there are bulk normal modes with exponentially small boundary imprint. In [74] it is proposed that continuous bulk reconstruction is only possible when every null geodesic in a given bulk subregion has an endpoint on the associated boundary subregion. Note that the reconstuction of bulk fields using smearing functions has been extended to nonlinear level in [62] [61] and to gauge fields in [75].

### 2.1.3 Reconstruction of spacetime

Recently, reconstruction techniques have been developed using a quantity called *differential entropy* [66]. In this form of reconstruction, an attempt is made to *define* a point in spacetime. The discussion in [66] is limited to $AdS_{2+1}$ spacetime and quotients of $AdS_{2+1}$ (conical defect and BTZ geometries). At the moment of writing, it is not clear how to generalize the techniques presented in [66] to higher dimensional spacetimes [76, 77].

For static spacetimes we can introduce constant time slices. Let $\theta \in [0, 2\pi]$ be a coordinate on a constant timeslice of a compact boundary. To any value $\theta$, we can associate an interval $(\theta - \alpha(\theta), \theta + \alpha(\theta))$ on the (1+1)-dimensional boundary. The *differential entropy* is given by

$$E[\alpha] = \frac{1}{2}\int_0^{2\pi} d\theta \left.\frac{dS[\alpha]}{d\alpha}\right|_{\alpha=\alpha(\theta)}, \tag{2.12}$$

where $S[\alpha(\theta)]$ is the holographic entanglement entropy associated to an interval centered around $\theta$ with width $2\alpha(\theta)$. In [78] and [66] it is shown that for $-1 <$

[3] In [60] an attempt is made to cure this by complexifying the boundary.

$\alpha'(\theta) < 1$, (2.12) corresponds to the length of a closed bulk curve:

$$E[\alpha] = \frac{\text{circumference of closed curve associated to } \alpha}{4G}. \tag{2.13}$$

Roughly, a point in spacetime is defined in [66] as a function $\alpha$, where $\alpha$ is such that the corresponding closed bulk curve has zero circumference. Details can be found in [66], where a more precise definition of bulk points is given. Furthermore, a well behaved distance function on the set of bulk points is defined in [66]. The definition of points and relative distance allows the construction of the bulk manifold and coordinate charts.

The extension of these definitions to the conical defect spacetime and the BTZ black hole require more bulk probes than just the set of minimal surfaces; non-minimal extremal surfaces and surfaces spanning between both external regions of the BTZ black hole are required. Generally, the CFT interpretation of these surfaces is unclear. For certain $(2+1)$-dimensional conical defect bulk spacetimes, a CFT interpretation of non-minimal extremal surfaces is given in terms of a boundary quantity called "entwinement" [79].

### 2.1.4 Reconstruction of gravity

In order to reconstruct dynamics in the bulk, we must consider dynamics on the boundary, or in other words, we must consider perturbations of both the bulk and boundary state and find out how they are related. A different boundary states corresponds to a different bulk geometry, for example, the CFT vacuum corresponds to a pure AdS geometry. Another example is a thermal state in the CFT, which is dual to an AdS-black hole bulk geometry. Below we will briefly present the techniques used in [65] to construct gravitational dynamics in the bulk from dynamics in the boundary.

For small perturbations in the quantum state of the boundary, the first law of entanglement entropy (1.62) applies. Both sides of the equation (1.62) can be expressed in terms of bulk duals, which means that the first law of entanglement entropy gives a bulk condition for every boundary surface $\mathcal{A}$. A subset of these conditions is shown to be equivalent to the linearized Einstein equations [65] (see also [64] [63]).

The first law of entanglement entropy (1.62) holds to first order in a small change of the boundary state:

$$\delta\langle H\rangle = \delta S. \tag{2.14}$$

For boundary balls $B^{d-1}$ the density matrix and its modular Hamiltonian (1.60) are known; the modular Hamiltonian for the boundary ball $H_B$ is an integral of a

local operator [80]:

$$H_B = 2\pi \int_{B(R,x_0)} d^{d-1}x \ \frac{R^2 - |\vec{x} - \vec{x}_0|^2}{2R} \ T_{tt}. \tag{2.15}$$

The energy momentum tensor, appearing in (2.15), can be associated to the bulk metric via the holographic dictionary [81]:

$$T_{\mu\nu} = \frac{dL_{\text{AdS}}^{d-3}}{16\pi G} \, d_{\mu\nu}^{(d)} \tag{2.16}$$

where $g_{\mu\nu}^{(d)}$ is as in expansion (1.21). In higher derivative gravity [65] argues that expression (2.16) holds up to a different coefficient.

The change in entanglement entropy can be found by varying the holographic entanglement entropy of the sphere (1.81) with respect to the bulk metric. Both the bulk surface and the position of the bulk minimal surface change, but the latter effect is only at second order in the metric perturbation due to the extremality condition in its definition. The change in the entanglement entropy can hence be expressed as an integral over the original surface $\mathfrak{E}_{\mathcal{A}}$ (to first order in $\delta g_{\mu\nu} = h_{\mu\nu}$). For theories for which the entanglement entropy is given by the area of the minimal surface (1.81) [65],

$$\delta S = \frac{R L_{\text{AdS}}^{d-3}}{8G} \int_{|\vec{x}-\vec{x}_0|\leq R} d^{d-1}x \ z^{2-d} \left( \delta^{ij} - \frac{1}{R^2}(x^i - x_0^i)(x^j - x_0^j) \right) h_{ij}(z, t_0, \vec{x}) \ . \tag{2.17}$$

The holographic dictionary now relates bulk quantities (2.17) and (2.16) to the left and right hand side of (1.62), giving a constraint for each boundary ball $B^{d-1}(R)$ as well as for all boundary balls in boosted boundary frames. These constraints are show to be equivalent to the linearized gravitational equations around AdS, given certain boundary conditions [63, 65].

In [65], the first law of entanglement entropy (1.62) is shown to give the linearized gravitational equations of motion even for higher derivative gravity theories. An important step in this derivation is the observation that the bulk surface associated to the entanglement entropy of a boundary ball is the bifurcation two sphere of a Killing horizon. This is a special property of the entanglement entropy of a boundary ball with the CFT in the vacuum state (AdS). For general states and boundary subregions $\mathcal{A}$, the Ryu-Takayanagi surface (1.81) is *not* the bifurcation two sphere of a Killing horizon. This limits the potential of the techniques presented in [65]. At the moment of writing, it is unclear how the gravitational equations can be derived in more general settings and in particular in the "shadow regions" (see section 2.2) that some geometries exhibit.

## 2.2 Holographic shadows

In section (2.1) we discussed several reconstruction techniques and their limitations. Holographic entanglement entropy plays a central role in many recent reconstruction attempts. In [2] we quantified the ability of Ryu-Takayanagi surfaces to probe the bulk. We also analyzed the ability of Wilson loops to probe the bulk geometry. Regions that cannot be probed by bulk probes are called *shadows*. In this section, we present some general properties, terminology, and theorems that will prove useful in the analysis of *holographic shadows*. We will also illustrate the appearance of shadow regions with the example of the BTZ bulk geometry.

### 2.2.1 Minimal area surfaces

In section (1.3) we presented the well known holographic entanglement entropy formula (1.81). The bulk surfaces $\mathfrak{E}_{\mathcal{A}}$ associated to the entanglement entropy of a boundary subregion $\mathcal{A}$ play an important role in recent reconstruction techniques. In pure AdS spacetime, minimal surfaces associated to entanglement entropy of a certain boundary subregion pass through every point in every (spacelike) direction. However, in states corresponding to other geometries, like the AdS-Schwarzschild geometry, certain regions cannot be probed by minimal surfaces, or only partially. In this section we present the definition of two different degrees of "probe-ability". We only consider static spacetimes.

Let $\Sigma$ be a constant time slice of the bulk, with a natural extension $\partial\Sigma$ to the boundary.

**The Strong Coverage Property** (SCP):
$\forall x \in \Sigma,\ \forall v \in T_x\Sigma,\ \exists \mathcal{A} \subset \partial\Sigma$ whose dual minimal surface $\mathfrak{E}_{\mathcal{A}}$ intersects $x$ with tangent vector along $v$.

Intuitively, this says that the entire bulk and its tangent bundle are "scanned over" by the minimal surfaces $\mathfrak{E}_{\mathcal{A}}$ of all possible boundary regions $\mathcal{A}$. This is satisfied by empty AdS, and also holds up to small perturbations thereof. In $(2+1)$ dimensions, SCP is equivalent to the condition for boundary rigidity [82], which means that knowing the entanglement entropy for every boundary region $\mathcal{A}$ uniquely determines the bulk geometry. SCP is also a necessary condition for the "hole-ographic" reconstruction of [78] (see also [79]). However, the requirement that one covers the entire tangent bundle is quite strong, and is not *a priori* necessary for a successful reconstruction scheme. We will therefore also consider a weaker property:

**The Weak Coverage Property** (WCP):
$\forall x \in \Sigma$, $\exists \mathcal{A} \subset \partial\Sigma$ whose dual minimal surface $\mathfrak{E}_{\mathcal{A}}$ intersects $x$.

This simply means that every bulk point is covered by the minimal surface $\mathfrak{E}_{\mathcal{A}}$ of some boundary region $\mathcal{A}$, but not necessarily scanning over all orientations in its tangent space. Note that this is not sufficient for boundary rigidity in 2 dimensions, nor for the aforementioned "hole-ographic" reconstruction. Nevertheless, this should be a minimal requirement for any attempt to reconstruct the bulk using this particular geometric dual.

It is worth pointing out that in the case of a disjoint boundary region $\mathcal{A} = \bigcup_i \mathcal{A}_i$ with dual minimal surface $\mathfrak{E}_{\mathcal{A}} = \bigcup_j \mathcal{B}_j$ consisting of multiple components $\mathcal{B}_j$, there need not be a direct correspondence between $\mathcal{A}_i$ and $\mathcal{B}_j$. This is illustrated in the case of two disconnected boundary subregions in figure 2.1. There are two ways for the two bulk curves to end on the four boundary points that specify $\partial\mathcal{A}$ without crossing, so there are (at least) two different local minima of their total area. Since the Ryu-Takayanagi proposal specifies $\mathfrak{E}_{\mathcal{A}}$ as possessing the smallest area of all bulk surfaces with $\partial\mathfrak{E}_{\mathcal{A}} = \partial\mathcal{A}$, the choice of which of these two bulk possibilities to employ is determined by comparing their respective areas.

As illustrated in figure 2.1, as the boundary subregions $\mathcal{A}_i$ are continuously increased, the components of the bulk dual surface are pushed inwards until, at some critical point, there is a switchover to the other possible combination of $\mathcal{B}_j$, which are then pushed outwards towards the boundary as the $\mathcal{A}_i$ continue to grow. This provides a simple example of a key concept underlying holographic shadows: rather than mirror the continuous deformation of the boundary, the bulk dual surface may undergo a discontinuous switchover in order to be the global minimum. This is a phase transition from the boundary point of view [83], but here we will focus on the bulk implication. This switchover leaves out the middle region, and thereby limits the region of the bulk that can be probed.

### 2.2.2 Generalized minimal surfaces

Before proceeding, we shall first introduce a more general formulation of minimal bulk surfaces. In particular, one can formally take the Ryu-Takayanagi proposal as a special case of the following general prescription:

- Let $\mathcal{B} \subset \Sigma$ be an $(n < d)$-dimensional surface in the bulk, and define the geometric quantity

$$L(\mathcal{B}) = \int_{\mathcal{B}} \left| \mathrm{d}^n \vec{\mathcal{B}} \right| \; F(g_{\mu\nu}) \; . \tag{2.18}$$

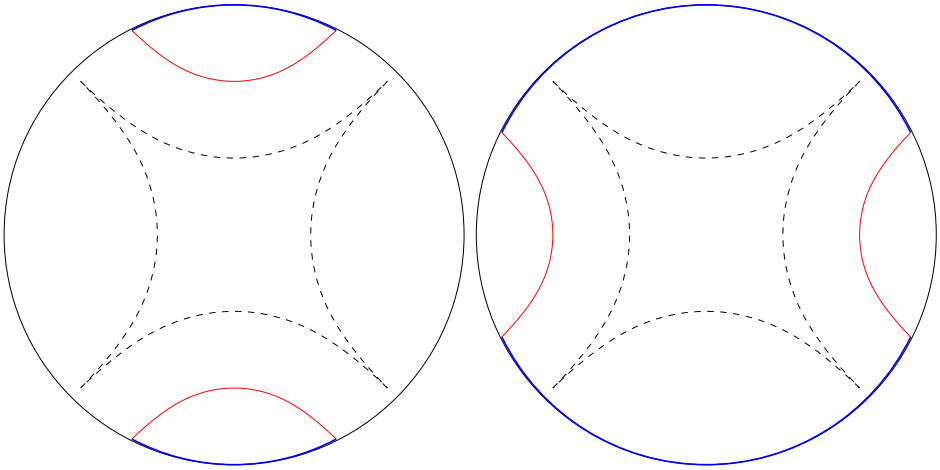

***Figure 2.1:*** *The left figure shows a disconnected boundary region $\mathcal{A} = \bigsqcup_i \mathcal{A}_i$ (blue) and the corresponding disjoint minimal surface $\mathfrak{E}_\mathcal{A} = \bigsqcup_j \mathcal{B}_j$ in the bulk (red). As the boundary region is continuously increased, the bulk surfaces $\mathcal{B}_j$ are pushed towards the dashed curve, at which point $\mathfrak{E}_\mathcal{A}$ discontinuously switches to the new global minimum $\mathfrak{E}_\mathcal{A} = \bigsqcup_j \mathcal{B}'_j$ shown in the right figure. The region inside the dashed curves cannot be probed with this particular choice of bulk dual.*

Over this surface, we integrate the area element and the function $F$ which only depends on the local geometry. This is then a very intuitive probe of the bulk geometry, as it does not care about the shape of $\mathcal{B}$, but rather only about how far $\mathcal{B}$ reaches into the bulk.

- For an $n$-dimensional boundary region $\mathcal{A}$ (or its boundary $\partial\mathcal{A}$), one finds an observable $Q$ associated with the minimal value of the above geometric quantity:

$$Q(\mathcal{A}) = \text{Min}[L(\mathcal{B})]\Big|_{\partial\mathcal{B}=\partial\mathcal{A}} . \tag{2.19}$$

When $n = (d-1)$ and $F = 1$, this reduces to the Ryu-Takayanagi proposal with $L =$ area and $Q =$ entanglement entropy. In addition, when $n = 1$ and $F = \sqrt{-g_{tt}}$, this reduces to the action of certain Wilson loops. Here, we will also limit ourselves to quantities with $F > 0$ and

$$\lim_{\mathcal{B}\to\mathcal{A}} L(\mathcal{B}) = \infty . \tag{2.20}$$

In other words, $L(\mathcal{B})$ is a positive definite quantity which diverges as one deforms $\mathcal{B}$ toward the boundary. It is therefore very natural to expect the minimal surface to reach into the bulk. This is related to boundary observables which have UV divergences and need to be regulated.

We can now study the failure of the coverage properties above, and the corresponding "holographic shadows," in a more general manner not limited to minimal area surfaces vis-à-vis Ryu-Takayanagi. Other holographic duals can suffer from exactly the same obstacle, namely that the bulk probes fail to cover the entire manifold, thus placing a geometric limit on such reconstruction efforts. Our generalization makes it easier to compare different holographic probes and see which one is better, in the sense of which probe casts the smallest shadow.

### 2.2.3 Seeking shadows

In this section, we will limit ourselves to $O(d)$ symmetric bulk geometries and $O(n)$ symmetric, simply connected boundary regions (disks). In such cases we can specify a bulk point $p$ by its radial distance to the origin (the "centre" of the bulk), $r_*$. This point will be the $O(n)$ fixed point of a unique, $O(n)$ symmetric $n$-dimensional surface $\mathcal{B}(r_*)$ (modulo the remaining $SO(d-n)$ rotation) such that the first order variation of (2.18) is zero.[4]

Proceeding from $r_*$, we follow the surface $\mathcal{B}(r_*)$ to the boundary at $r=\infty$ to find the $(n-1)$-dimensional boundary sphere $\mathcal{A}$ on which it ends, $\partial\mathcal{A}=\partial\mathcal{B}$. We define the interior of $\mathcal{A}$ to be the side closer to the initial bulk point $p$. In other words, one can deform from $\mathcal{B}$ to $\mathcal{A}$ without going through $r=0$. Denote the radius of this boundary ball $\mathcal{A}$ as $\theta_\infty(r_*)$.[5] We know two special values of this function: $\theta_\infty(\infty)=0$ and $\theta_\infty(0)=\pi/2$. The first is due to a surface $\mathcal{B}(\infty)$ that effectively never leaves the boundary, while the second comes from symmetry: it is basically the surface that cuts the bulk into two halves.

This function is straightforward to compute (at least numerically), and possesses a number of useful properties. First of all, there is a condition which guarantees that a holographic reconstruction scheme will work:

**Theorem 1:** *The set of all simply-connected, $O(n)$ symmetric boundary regions (balls) satisfies the Strong Coverage Property if $\theta_\infty(r_*)\in(0,\pi/2)$ is monotonic as $r_*$ goes from $0$ to $\infty$.*

Conversely, there is also a condition which guarantees that holographic reconstruction will fail:

[4] One might intuitively treat $r_*$ as the minimal radius reached by this critical surface, but there is no *a priori* reason for this identification to hold for an arbitrary positive function $F$ in (2.18). We will be very careful not to assume this identification in the proofs that follow.

[5] There might be cases where some critical surfaces $\mathcal{B}(r_*)$ do not reach the boundary, so $\theta_\infty$ is not well-defined. This is exactly what happens when there is a horizon, but such cases may be more general.

**Theorem 2:** *If* $\mathrm{d}\theta_\infty/\,\mathrm{d}r_* > 0$ *as* $r_* \to 0$*, then the weak coverage property fails for the set of all simply-connected,* $O(n)$ *symmetric boundary regions (balls).*

In appendix (2.A), we will prove these two theorems using the following lemmas:

**Lemma 1:** *For a boundary sphere* $\partial\mathcal{A}$*, the bulk surface* $\mathcal{B}$ *that minimizes* $L$ *in* (2.18) *with* $\partial\mathcal{B} = \partial\mathcal{A}$ *must be spherically symmetric.*

**Lemma 2:** *If the boundary anchors* $\partial\mathcal{B}$ *and* $\partial\mathcal{B}'$ *do not cross each other, but the corresponding bulk surfaces* $\mathcal{B}$ *and* $\mathcal{B}'$ *do, then* $\mathcal{B}$ *and* $\mathcal{B}'$ *cannot both be minimal surfaces.*

Proofs of these Lemmas will also be given in appendix (2.A).

## 2.3 Example: shadows for the BTZ metric

In [2] we analyze shadow regions for the AdS-Schwarzschild, the BTZ and AdS-star geometries. Here we will illustrate the occurrence of shadow regions with the example of the BTZ bulk metric, investigating its shadow regions for minimal surfaces and rectangular Wilson loops (1.2.4). Obviously, $\theta_\infty(r_*)$ is undefined if $r_*$ falls within the horizon radius of a black hole, hence from now on $r_* \geq r_H$ is always implied, where $r_H$ indicates the position of the horizon (see also page 12).

The homology condition in (1.81) is crucial for the behavior of minimal surfaces in singular spacetimes. In geometries with a black hole, there exist surfaces $\mathcal{B}$ such that $\partial\mathcal{B} = \partial A$ that are not continuously deformable to $\mathcal{A}$. Suppose $\mathfrak{E}_\mathcal{A}$ is the minimal surface homologous to $\mathcal{A}$. Then $\mathfrak{E}_\mathcal{A}$ satisfies $\partial\mathfrak{E}_\mathcal{A} = \partial\mathcal{A}^c$, where $\mathcal{A}^c$ is the complement of $A$ on a spatial slice of the boundary, but fails to be homologous to $\mathcal{A}^c$. We *can* add the horizon area to such a surface, such that *it is* homologous to a certain boundary subregion. By changing $\mathcal{A}$, there might be a transition from a minimal surface that does not include a component that covers the horizon, to a surface that *does*. This is another type of switchover, which will happen for boundary balls when

$$A(\theta_\infty) = A(\pi - \theta_\infty) + A_{\mathrm{BH}} \tag{2.21}$$

where $A_{\mathrm{BH}}$ is the area of the component that wraps the black hole horizon.

### 2.3.1 Minimal surfaces and shadows for the BTZ metric

A static BTZ black hole is described by the metric (see also section 1.2.1)

$$\mathrm{d}s^2 = -(r^2 - r_H^2)\,\mathrm{d}t^2 + \frac{\mathrm{d}r^2}{r^2 - r_H^2} + r^2\,\mathrm{d}\theta^2. \tag{2.22}$$

To determine the shadow region, it is sufficient to consider constant time slices.[6] In $d = 2$ the boundary is a circle, and the subsystem $\mathcal{A}$ an interval on the circle. The bulk extremal surface associated with the entanglement entropy (1.81) is then simply a geodesic anchored at the two-points that comprise $\partial\mathcal{A}$. We consider as a boundary region the interval $(-\theta_\infty, \theta_\infty)$, where the subscript $\infty$ indicates that the boundary corresponds to $r \to \infty$ in our coordinates (2.22).

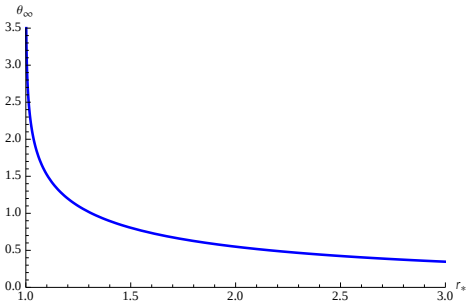


***Figure 2.2:*** *$\theta_\infty(r_*)$ for a static BTZ black hole with $r_H = 1$.*

The Lagrangian describing such a bulk extremal surface is given by

$$\mathcal{L} = \sqrt{\frac{r'^2}{r^2 - r_H^2} + r^2}\ , \qquad r' \equiv \frac{\mathrm{d}r}{\mathrm{d}\theta}\ . \tag{2.23}$$

Since the Lagrangian does not depend on $\theta$, there is a conserved momentum due to translation invariance in $\theta$. Hence:

$$\frac{\delta\mathcal{L}}{\delta r'} r' - \mathcal{L} = \text{constant}\ . \tag{2.24}$$

We may fix the constant by the demanding that the surface reaches its minimal value $r_*$ when $r' = 0$. This leads to the first-order equation of motion

$$\frac{\mathrm{d}r}{\mathrm{d}\theta} = \frac{r}{r_*}\sqrt{r^2 - r_*^2}\sqrt{r^2 - r_H^2} \tag{2.25}$$

[6] We generalize to $\mathrm{d}t \neq 0$ subregions in appendix 2.B and find that these suffer even larger entanglement shadows.

which may be integrated to obtain

$$\theta_\infty = \int_{r_*}^{\infty} \mathrm{d}r \frac{\mathrm{d}\theta}{\mathrm{d}r} = \frac{1}{2r_H} \cosh^{-1}\left(\frac{r_*^2 + r_H^2}{r_*^2 - r_H^2}\right) . \tag{2.26}$$

This curve is plotted in figure 2.2. Note that it diverges when $r_* \to r_H$, and decreases monotonically with increasing $r_*$.

We may invert (2.26) to obtain:

$$r_* = \frac{r_H}{\tanh\left(\theta_\infty r_H\right)}.. \tag{2.27}$$

For small enough $r_*$, $\theta_\infty$ becomes larger than $\pi$ (see figure 2.2), which means that the corresponding geodesic circles the black hole at least once. But a surface that intersects itself cannot correspond to a local minimum of the area functional (intuitively, the kinks in the intersection can be infinitesimally smoothed out to reduce the area). Thus for the purpose of identifying the appropriate bulk probe, we only care about the range $\theta_\infty \leq \pi$, since a switchover must occur before $\theta_\infty$ reaches this value. The alternative global minimum is then a surface with two disconnected components: a geodesic connecting the endpoints at $\pm\theta_\infty$ on the opposite side of the black hole, and a separate part that encircles the horizon; see figure 2.3.

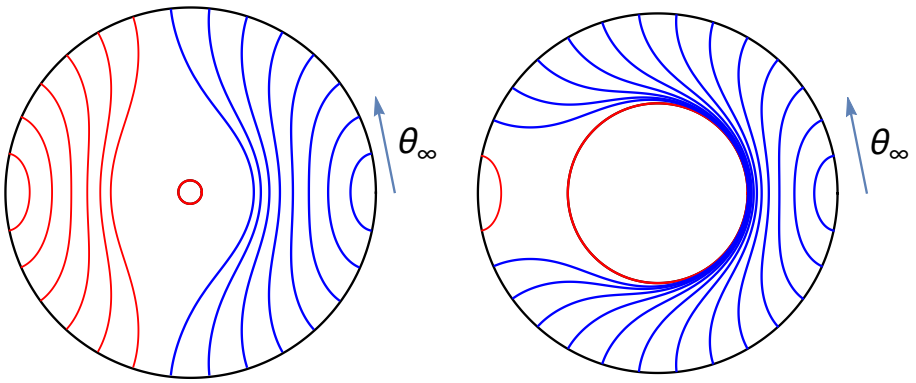


***Figure 2.3:*** *Minimal surfaces for boundary intervals of varying size $\theta_\infty$, for a black hole of radius (red circle) $r_H = 0.1 l_{\mathrm{AdS}}$ (left) and $r_H = l_{\mathrm{AdS}}$ (right). The switchover to the disconnected solution (red curves) takes place near $\theta_\infty = \pi/2$ for small black holes (left), and approaches $\pi$ for large black holes (right).*

We denote the critical angle at which this switchover happens by $\theta_{\mathrm{switch}}$, which is given by (2.21):

$$l(\theta_{\mathrm{switch}}) = l(\pi - \theta_{\mathrm{switch}}) + 2\pi r_H , \tag{2.28}$$

where $l(\theta_\infty)$ is the length of the geodesic connecting the boundary points $\pm\theta_\infty$ and $2\pi r_H$ is the length of the curve that wraps the horizon.

We can compute the length $l(\theta_\infty)$ by integrating the Lagrangian

$$l(\theta_\infty) = 2\int_{r_*}^{\infty} \sqrt{\frac{1}{r^2 - r_H^2} + r^2 \left(\frac{\mathrm{d}\theta}{\mathrm{d}r}\right)^2} = 2\int_{r_*}^{\infty} \frac{r\,\mathrm{d}r}{\sqrt{r^2 - r_H^2}\sqrt{r^2 - r_*^2}} \tag{2.29}$$

where we used (2.25), with $r_*$ given by (2.27). The integral is divergent, but the divergent parts on the left- and right-hand side of (2.28) cancel and the finite parts yield:

$$\theta_{\text{switch}} = \frac{\pi}{2} + \frac{1}{2r_H} \ln\left(\cosh(\pi r_H)\right) \ . \tag{2.30}$$

For small black holes ($r_H \ll l_{\text{AdS}}$) we have that $\theta_{\text{switch}} \approx \pi/2$, because the area contribution from the black hole in (2.28) is close to zero. Conversely, one sees that for large black holes ($r_H \gg l_{\text{AdS}}$), $\theta_{\text{switch}} \approx \pi$. See figure 2.3 for an explicit plot of both cases.

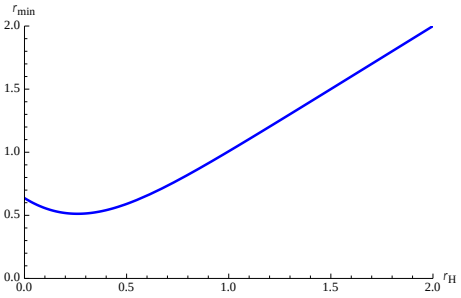


***Figure 2.4:*** *Shadow radius $r_{min}$ as a function of horizon radius $r_H$ for a static BTZ black hole.*

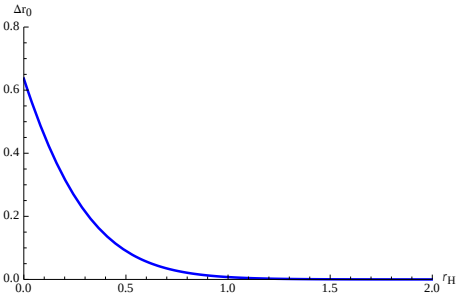


***Figure 2.5:*** *Relative shadow size $\Delta r_0$ as a function of horizon radius $r_H$ for a static BTZ black hole.*

The shadow radius $r_{\text{min}}$, within which no extremal surface associated to entanglement entropy can reach, is finally determined by substituting the value of $\theta_{\text{switch}}$ into (2.27):

$$r_{\text{min}} = \frac{r_H}{\tanh(\pi r_H)} + \frac{r_H e^{-\pi r_H}}{\sinh(\pi r_H)} \ . \tag{2.31}$$

This curve is plotted in figure 2.4. However, since the black hole is always within the shadow region, the shadow may be more conveniently expressed as

$$\Delta r_0 \equiv r_{\text{min}} - r_H = \frac{2r_H e^{-\pi r_H}}{\sinh\left(\pi r_H\right)} \tag{2.32}$$

which is plotted in figure 2.5. When referring to the "size" of the shadow, we shall implicitly mean the relative quantity (2.32) unless otherwise noted.

From either (2.32) or fig. 2.3, one sees that the shadow is exponentially small for large black holes, but remains an order one (AdS radius) distance from the horizon for small black holes. This behavior is easily explained by considering the switchover effect: a large black hole incurs a greater cost from the horizon component in the area condition (2.21), which allows the global minimum to remain on the original (connected) solution branch for larger values of $\theta_\infty$.

It may seem strange that that the shadow radius $r_{\min}$ does not go to zero for vanishing horizon radius. This is due to the mass gap in $AdS_3$: letting $r_H \to 0$ in the BTZ metric (2.22) will not yield the empty $AdS_3$ metric, but a conical defect geometry.

### 2.3.2 Wilson loops and shadows for the BTZ metric

Another type of bulk probe is given by the static world sheets arising from rectangular Wilson loops in the boundary CFT (see also section 1.2.4). The bulk dual of the expectation value of a Wilson loop $\mathcal{W}(\mathcal{C})$ evaluated in the supergravity limit is proposed to be [34]:

$$\mathcal{W}(\mathcal{C}) \sim e^{-S} \tag{2.33}$$

where $S$ is the proper area of a fundamental string ending on the boundary loop $\mathcal{C}$. To simplify our analysis, we will consider rectangular Wilson loops that extend far into the past and future time-directions. Such a Wilson loop with temporal "height" $T$ and spatial width $2\theta_\infty$ can be interpreted as the potential between a quark and an anti-quark [34, 84]. We assume sufficiently large $T$ that the world sheet may be considered invariant under time translations. The action for such a static world sheet is given by

$$S = 2T \int_0^{\theta_\infty} \mathrm{d}\theta \sqrt{(\partial_\theta r)^2 + r^2 f(r)} \ . \tag{2.34}$$

Note that in static spacetimes this quantity takes the standard form of (2.18) with $F \propto \sqrt{-g_{tt}}$, thus we may treat it as a holographic probe similar to minimal area surfaces.

The action (2.34) does not explicitly depend on $\theta$, so there is a conserved quantity that we shall use to write the equation of motion as a first order differential equation. We will find it convenient to distinguish two types of solutions to this equation:

**∪-shaped world sheets** are smooth world sheets anchored on the boundary that do not reach the black hole horizon, instead turning smoothly such that $\partial_\theta r|_{r=r_*} = 0$ at some finite $r_* > r_H$ (see figure 2.6).

**⊔-shaped world sheets** consist of two straight segments that extend from the boundary to the black hole, joined discontinuously by a third segment that partially wraps the horizon (see figure 2.6).

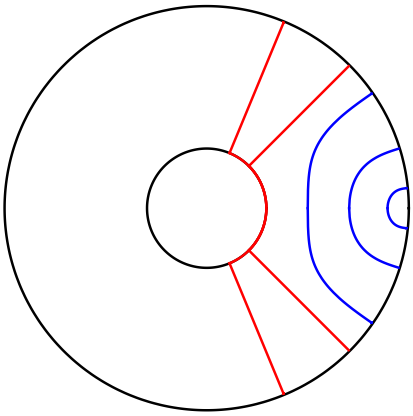

***Figure 2.6:*** *World sheets corresponding to different boundary angles for a BTZ black hole of radius $r_H = 0.5 l_{\mathrm{AdS}}$. The ∪-shaped world sheets are rendered in blue; ⊔-shaped, in red.*

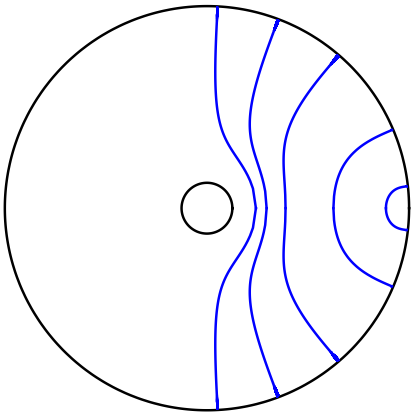

***Figure 2.7:*** *World sheets corresponding to different boundary angles for a BTZ black hole of radius $r_H = 0.2 l_{\mathrm{AdS}}$. Small black holes in $d = 2$ are special, because the ∪-shaped world sheet constitutes the leading saddle point for all values of $\theta_\infty$.*

For a given boundary angle $\theta_\infty$, multiple solutions to the equation of motion may exist. Evaluation of the area functional is therefore necessary to determine which world sheet constitutes the leading saddle point. Generally, we find that a switchover or phase transition occurs from ∪-shaped to ⊔-world sheets, as illustrated in fig. 2.6. We discuss this behavior in more detail below.

We first consider the smooth ∪-shaped solutions to the equation of motion. We can express the conserved charge in terms of the minimal/turning radius $r_*$. This allows us to find an implicit expression for $\theta_\infty$ in terms of $r_*$ by integrating the equation of motion:

$$\theta_\infty(r_*) = \int_{r_*}^{\infty} \mathrm{d}r \frac{1}{r\sqrt{f(r)}} \frac{1}{\sqrt{\frac{r^2 f(r)}{r_*^2 f(r_*)} - 1}}. \tag{2.35}$$

Note that this formula only depends on the number of dimensions via $f(r)$, which is given $f(r) = r^2 - r_H^2$ for the BTZ metric. $\theta_\infty(r_*)$ is plotted for the BTZ metric (cf. (2.22)) in figure 2.8. The function is characterized by a single maximum, and

decreases monotonically for large $r_*$. Near the horizon however, $\mathrm{d}\theta_\infty/\,\mathrm{d}r_* < 0$, and hence by Lemma 3 (see appendix 2.A) there cannot exist any local minima of the area functional in this range. The ∪-shaped world sheets thus suffer a shadow that extends some finite distance from the horizon, but we postpone further discussion of shadows until after considering ⊔-shaped solutions as well.

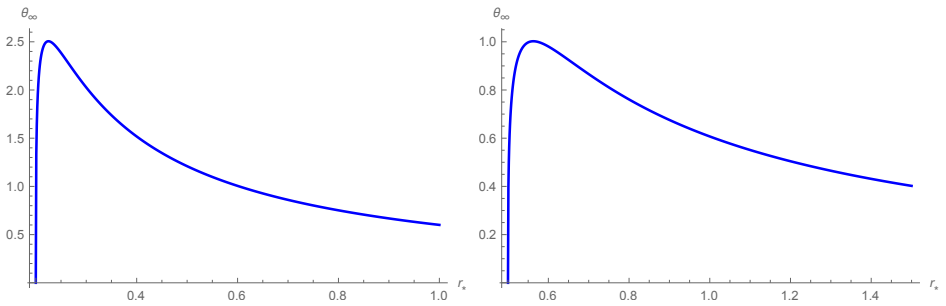


***Figure 2.8:*** *$\theta_\infty(r_*)$ for Wilson loops for a black hole of radius $r_H = 0.2 l_{\mathrm{AdS}}$ (left) and $r_h = 0.5 l_{\mathrm{AdS}}$ (right).*

As an aside, we note that for $d = 2$, $\theta_\infty$ can be much larger than $\pi/2$. Using the equivalence relations $\theta_\infty \sim \theta_\infty + n\pi$ and $\theta_\infty \sim \pi/2 - \theta_\infty$, we can map all values of $\theta_\infty > \frac{\pi}{2}$ into the range $[0, \pi/2]$; see figure 2.9. The solutions with $\theta_\infty > \pi/2$ correspond to strings that wind one or more times around the black hole (see figure 2.10). However, strings that cross themselves fail to be minimal, so we can discard these solutions in what follows.

We turn now to the ⊔-shaped solutions, which consist of two radial segments connecting the boundary and the horizon at $\pm\theta_\infty$ and a segment that wraps the horizon (see figure 2.6). The segment that wraps the horizon does not contribute to the area since the pullback of the metric vanishes. The radial segments have divergent area, which is associated to the unrenormalized self-energy of a quark-anti-quark pair. Thus the Wilson loops associated to these ⊔-shaped strings do not encode information about the bulk. Nonetheless, because these ⊔-shaped solutions exist for all boundary angles, evaluation of the area functional is necessary to determine when the ∪-shaped solutions constitute the global minimum.

We find that ∪-shaped solutions have minimal area up to some critical angle $\theta_{\mathrm{switch}}$, beyond which ⊔-shaped solutions dominate. In general, this switchover will always occur for sufficiently large $\theta_\infty < \frac{\pi}{2}$. The only only exception is a small BTZ black hole, for which the minimal area world sheets are ∪-shaped for all $\theta_\infty$.

Denote the smallest radius to which the ∪-shaped world sheets reach before the switchover by $r_{\mathrm{switch}}$. Then the switchover angle $\theta_{\mathrm{switch}}$ and associated switchover radius $r_{\mathrm{switch}}$ are determined by the equality of the areas of the ∪-shaped and

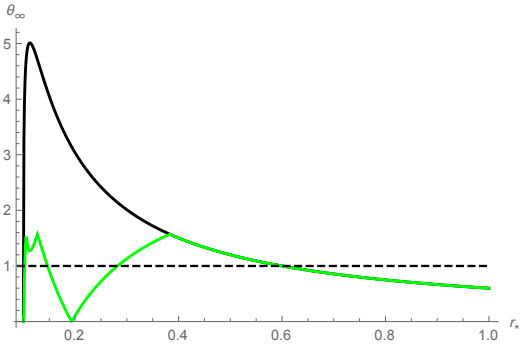


***Figure 2.9:*** *$\theta_\infty(r_*)$ for a BTZ black hole with radius $r_H = 0.1 l_{\mathrm{AdS}}$ (black). Solutions with $\theta_\infty > \pi/2$ are mapped to the range $[0, \pi/2]$ (green). The dashed line is at $\theta_\infty = 1$; every intersection with the green line corresponds to a solution to the equation of motion for this value of $\theta_\infty$. These world sheets are plotted in fig. 2.10.*

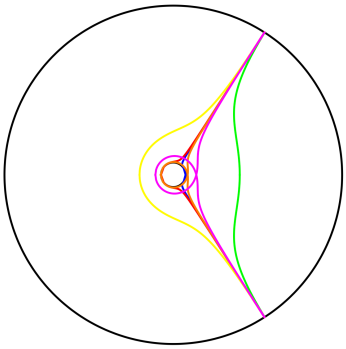

***Figure 2.10:*** *Extrema for $\theta_\infty = 1$ for a BTZ black hole with horizon radius $r_H = 0.1 l_{\mathrm{AdS}}$. Only one of these saddle points – that with zero winding number (green) – corresponds to a global minimum of the proper area of the world sheet.*

$\sqcup$-shaped solutions:

$$S_\cup(r_{\mathrm{switch}}) = S_\sqcup \ , \qquad \theta_\infty(r_{\mathrm{switch}}) \equiv \theta_{\mathrm{switch}} \ . \tag{2.36}$$

The $\cup$-shaped world sheet corresponding to the largest possible boundary angle $\theta_\infty$ penetrate deepest into the bulk. The switchover angle $\theta_{\mathrm{switch}}$ is the largest angle for which the $\cup$-shaped solutions have minimal area, so the shadow radius $r_{\mathrm{min}}$ is determined by:

$$r_{\mathrm{min}} = \mathrm{Max}\left[\theta_\infty^{-1}(\pi/2),\ r_{\mathrm{switch}}\right] \ . \tag{2.37}$$

We can solve for the value of $r_{\mathrm{switch}}$ by solving the area condition (2.36):

$$\begin{aligned} \int_{r_{\mathrm{switch}}}^{r_c} \frac{\mathrm{d}r}{\sqrt{1 - \frac{r_{\mathrm{switch}}^2}{r^2}\frac{f(r_{\mathrm{switch}})}{f(r)}}} &= \int_{r_H}^{r_c} \mathrm{d}r \\ \implies \int_{r_{\mathrm{switch}}}^{\infty} \mathrm{d}r \left( \frac{1}{\sqrt{1 - \frac{r_{\mathrm{switch}}^2}{r^2}\frac{f(r_{\mathrm{switch}})}{f(r)}}} - 1 \right) &= r_{\mathrm{s}} - r_H \ . \end{aligned} \tag{2.38}$$

where $r_c$ is a large radial cutoff, necessitated by the fact that both actions are linearly divergent. The dimensional dependence is encapsulated in $f(r)$. For the BTZ metric, we can solve (2.38) exactly by taking $r_{\text{switch}} = \lambda r_H$:

$$\lambda - 1 = \lambda \int_1^\infty \mathrm{d}x \left( \frac{1}{\sqrt{1 - \frac{1}{x^2}\frac{\lambda^2-1}{x^2\lambda^2-1}}} - 1 \right) , \tag{2.39}$$

which evaluates to $\lambda \approx 1.38$. We emphasize that the BTZ metric is exceptional in the sense that there is no switchover for small black holes $r_H \lesssim 0.26 l_{\text{AdS}}$. In [2] we show that this does not happen for $d \geq 3$. In this case the ⊔-shaped world sheets never constitute the leading saddle point of the area functional, even for $\theta_\infty > \pi/2$, and we find numerically that $r_{\min} \sim l_{\text{AdS}}$.

### 2.3.3 Shadows and holographic reconstruction

The BTZ geometry forms an example of a geometry with shadow regions for both minimal surfaces associated to entanglement entropy and world sheets associated to rectangular Wilson loops. In [2] we also analyze the shadow regions for the AdS-Schwarzschild geometry and an AdS-star geometry. In higher dimensions ($d \geq 3$), the boundary subregions $\mathcal{A}$ can have a complicated geometry, which makes the analysis of their corresponding bulk minimal surfaces much harder. In [2] we present evidence that these geometries also exhibit shadows in higher dimensions.

If the radial direction truly emerges as the realization of the entanglement structure of the boundary theory, then we have to address the issue of shadows. One strategy is to clarify the role of extremal, but not minimal surfaces, in the boundary theory. Alternatively, we need to discover other bulk probes in the holographic dictionary that *do* probe these regions. In the next chapter we will present a candidate bulk quantity, called the causal information surface, that is suspected to have a boundary dual quantity. We investigate its shadow region in section (3.4).

## 2.4 Summary & outlook

In this chapter we briefly described some bulk reconstruction methods. The known bulk reconstruction methods are still limited to specific cases and some of them assume a background bulk geometry in advance. We defined two properties, the weak and strong coverage properties, that qualitatively describe how well a bulk probe "covers" the bulk. We highlighted the limitations of known bulk probes to reach into the bulk, calling the regions that can not be probed "shadows".

There are nonetheless arguments that support the claim that reconstruction of the full bulk must be possible. This would mean that we need to discover new bulk probes and develop new techniques to use them for reconstruction. A first step in that direction was made in [79], in which a boundary interpretation was given to non-minimal extremal surfaces.

An interesting development in the field of bulk reconstruction techniques is the use of techniques from integral geometry. For example, in [85] the Radon transform, which we will not explain here, is used to reconstruct certain bulk quantities. In unpublished (at the moment of writing) work by Czech et al. the Crofton formula, which we will not explain here, is associated to differential entropy. The relevant feature about the Radon transform and the Crofton formula is that the strong coverage property seems to be relevant for these techniques.

In summary, we expect that new bulk probes will be identified in the near future, potentially casting light on our shadows. We also expect new reconstruction methods to arise from the application and adaption of methods from integral geometry to holography.

## 2.A Proofs

In this appendix, we present proofs of the two lemmas and the two theorems presented in section (2.2). Note that Lemma 1 is not limited to globally regular geometries, while the form of Lemma 2 in the main text is. However, we will prove a more general version of Lemma 2 that is applicable to geometries with horizons and/or singularities. We also introduce and prove a third lemma, from which the coverage properties are independent, but which finds utility in the main text.

### Lemma 1:

*For a boundary sphere $\partial\mathcal{A}$, the bulk surface $\mathcal{B}$ that minimizes $L$ in* (2.18) *with $\partial\mathcal{B} = \partial\mathcal{A}$ must be spherically symmetric.*

**Proof:**

If the minimal surface $\mathcal{B}$ is not spherically symmetric, one can rotate it to get a degenerate minimum $\mathcal{B}'$ of the same boundary region, with $\partial\mathcal{B} = \partial\mathcal{B}' = \partial\mathcal{A}$. As shown in the left panel of fig. 2.11, $\mathcal{B}$ and $\mathcal{B}'$ must intersect, but it follows from the uniqueness theorem that their normal vectors cannot agree at the intersection. Thus they must intersect with a "kink". We assume for simplicity that this kink

separates the surfaces into two regions each, but the generalization to multiple intersections is straightforward. Let $\mathcal{B}$ be separated into regions 1 and 2, and $\mathcal{B}'$ into 3 and 4 as depicted in fig. 2.11. By symmetry, regions 1 and 3 contribute the same amount to the geometric quantity $L$ in (2.18), which we denote $L_{13}$. Similarly, we denote the contribution from regions 2 and 4 by $L_{24}$.

If $L_{24} > L_{13}$, then we could construct a new surface from regions 1 and 3 with the same boundary, thereby contradicting the assumption that both $\mathcal{B}$ and $\mathcal{B}'$ are minima. Similarly for $L_{13} > L_{24}$. If instead $L_{13} = L_{24}$, then both of the newly constructed surfaces have the same $L$ as $\mathcal{B}$ and $\mathcal{B}'$. But these new surfaces will not be smooth due to the kink at the intersection, so neither can be a local minimum of $L$. This again contradicts our assumption. QED

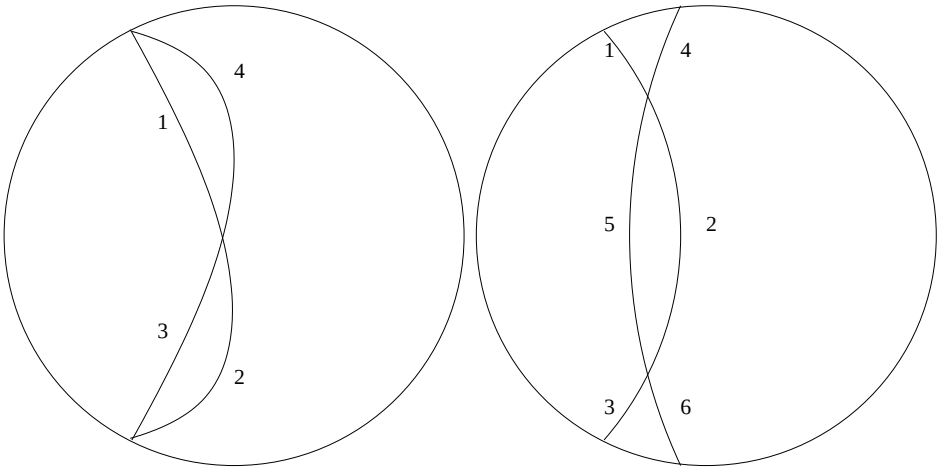


***Figure 2.11:*** *The left panel shows two non-spherically symmetric bulk surfaces, $b = (1 + 2)$ and $b' = (3 + 4)$, ending on the same spherical boundary, $\partial b = \partial b' = \partial a$. The right panel shows two intersecting bulk surfaces, $b = (1 + 2 + 3)$ and $b' = (4 + 5 + 6)$, whose corresponding boundary anchors do not intersect.*

## Lemma 2:

*If the boundary anchors $\partial\mathcal{B}$ and $\partial\mathcal{B}'$ do not cross each other, but the corresponding bulk surfaces $\mathcal{B}$ and $\mathcal{B}'$ do, and at least one connected region between $\mathcal{B}$ and $\mathcal{B}'$ does not contain a geometric obstruction, then $\mathcal{B}$ and $\mathcal{B}'$ cannot both be minimal surfaces.*

**Proof:**

For this proof, we define a geometric obstruction as any object, defined purely by the metric, through which a bulk surface cannot be deformed without leaving a disconnected piece that wraps the obstruction; this wrapping piece should furthermore have a nonzero contribution to $L$ in (2.18). (In other words, they are essentially generalizations of the black hole horizon in the case of minimal area surfaces.)

Refer to right panel of figure 2.11. Let $\mathcal{B} = (1+2+3)$, $\mathcal{B}' = (4+5+6)$, and assume there is no geometric obstruction within the volume enclosed between 2 and 5. We denote the contribution of region 5 as $L_5$, and the contribution of region 2 as $L_2$. If $L_2 > L_5$, then surface $(1+2+3)$ fails to be the minimum since surface $(1+5+3)$ has even smaller $L$. Similarly for $L_5 > L_2$. If $L_2 = L_5$, the uniqueness theorem again guarantees that the surface $(1+5+3)$ is not smooth, and thus we still arrive at a contradiction. Hence both $\mathcal{B}$ and $\mathcal{B}'$ cannot be global minima. QED

## Lemma 3:

*If* $\mathrm{d}\theta_\infty/\,\mathrm{d}r_* > 0$*, then the surface* $\mathcal{B}(r_*)$ *cannot be a local minimum.*

**Proof:**

By continuity, if $\mathcal{B}(r_*)$ is a local minimum, there must be an infinitesimal $\delta r$ such that $B(r_* + \delta r)$ is also a local minimum. Since $\mathrm{d}\theta_\infty/\,\mathrm{d}r_* > 0$, the corresponding boundary regions $\mathcal{A}(r_* + \delta r)$ and $\mathcal{A}(r_*)$ intersect exactly as in the right panel of fig. 2.11. Applying Lemma 2 to these two surfaces then implies that they cannot both be local minima. QED

## Proof of Theorem 1

**Theorem 1:** *The set of all simply-connected,* $O(n)$ *symmetric boundary regions (balls) satisfies the Strong Coverage Property if* $\theta_\infty(r_*) \in (0, \pi/2)$ *is monotonic as* $r_*$ *goes from* $0$ *to* $\infty$*.*

Monotonicity of the boundary angle implies that every $\mathcal{B}(r_*)$ is the unique global minimum for the boundary ball $\mathcal{A}$ of radius $\theta_\infty(r_*)$. Lemma 1 then implies that the bulk can be foliated by a family of non-intersecting minimal surfaces anchored on the corresponding family of concentric boundary spheres, as illustrated in fig. 2.12. Note that this is sufficient to satisfy WCP; for the strong coverage property, we need also demonstrate coverage of the bulk tangent bundle.

Consider a sphere with finite radius $R$ in the bulk. As shown in fig. 2.12, it intersects $\mathcal{B}(0)$ at an angle of $\pi/2$ between their normal vectors. As $r_*$ increases, $\mathcal{B}(r_*)$ will eventually stop intersecting this sphere. If we follow the intersection point during this process, the angle between the two normal vectors must continuously drop to 0. Thus $\mathcal{B}(r_*)$ can cover the full tangent space of a point at radius $R$. Since $R$ is arbitrary, we have covered the full tangent bundle. QED

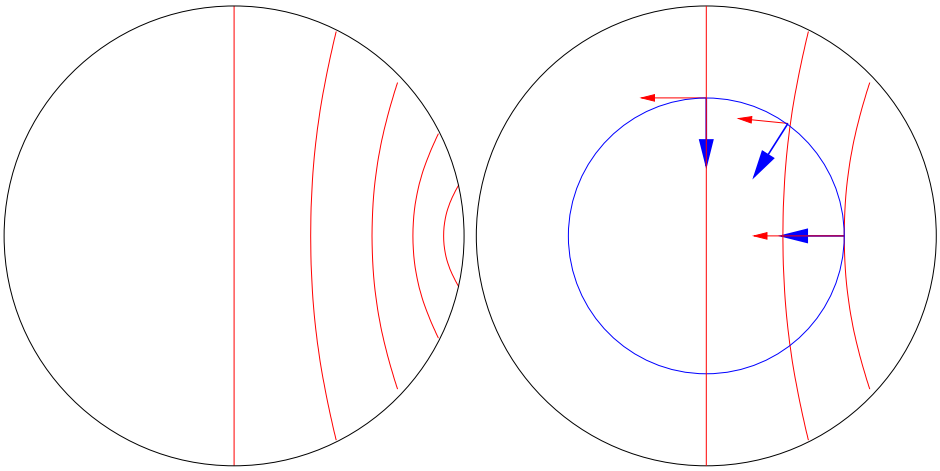

***Figure 2.12:*** *The left figure shows a continuous foliation of minimal $n$-dimensional surfaces (red) on an $(n+1)$-dimensional equatorial slice of the bulk. The right figure shows how the angle between an $n$-sphere (blue circle) in the bulk and the foliation surfaces changes continuously from 0 to $\pi/2$. Note that although the rightmost red surface is tangent to the blue circle at precisely $r_*$ in this plot, the proof does not rely on this.*

Note that the inverse of Theorem 1 is not generally true. That is, a non-monotonic $\theta_\infty(r_*)$ does not guarantee the violation of SCP.[7] But this is not so concerning. We have stipulated SCP as a *sufficient* condition for a successful holographic reconstruction scheme; violating SCP does not necessarily imply that all schemes will fail. Thus, the more physically meaningful "inverse" statement is rather our Theorem 2, about the violation of WCP. Insofar as WCP is a *necessary* condition, this indeed rules out holographic reconstruction (using the set of all boundary disks). Also note that Theorem 2 provides a sufficient condition to violate WCP. While WCP might be violated by other conditions, the condition Theorem 2 provides seems to be the most natural.

[7] The inverse of Theorem 1 can be proved if we use the additional assumption that $r_*$ is the minimal radius reached by the surface $\mathcal{B}(r_*)$, which happens to be true in many examples.

### Proof of Theorem 2

**Theorem 2:** *If* $\mathrm{d}\theta_\infty/\,\mathrm{d}r_* > 0$ *as* $r_* \to 0$*, then the weak coverage property fails for the set of all simply-connected,* $O(n)$ *symmetric boundary regions (balls).*

If $\mathrm{d}\theta_\infty/\,\mathrm{d}r_* > 0$ when $r_* \to 0$, then since $\theta_\infty(0) = \pi/2$ we can find some $r' > 0$ such that $\theta_\infty(r_*) \geq \pi/2$ for all $0 \leq r_* \leq r'$. According to Lemma 2, none of the critical surfaces $\mathcal{B}(r_*)$ in this range can be the global minimum of the corresponding boundary sphere $\partial\mathcal{B}$, because they always intersect their own mirror image.

If for all minimal surfaces $\mathcal{B}(r_*)$, $r_*$ is the minimal radius reached, then no minimal surfaces can probe the region $r < r'$. On the other hand, if a point $p \in \mathcal{B}(r_*)$ with radius $r_p < r_*$ is allowed, one still cannot allow $r_p \to 0$. As shown in fig. 2.13, such a surface can be pinched-off to one with smaller $L$, which contradicts the assumption that the original surface is a global minimum. Thus in this case there must be a lower bound $r''$ with $0 < r'' < r'$ beyond which these minimal surfaces cannot probe. QED

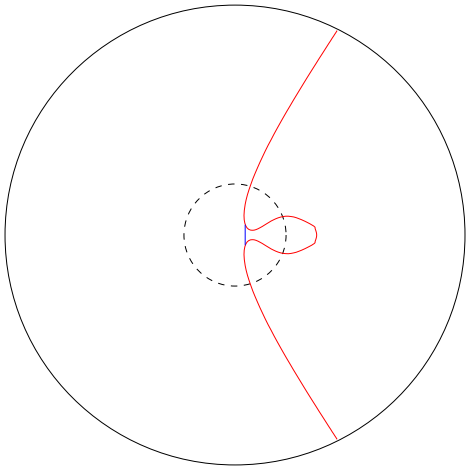

***Figure 2.13:*** *A minimal surface (red) with its symmetric point sitting at a finite radius* $r_*$ *cannot have other points approach arbitrarily close to* $r = 0$*. Otherwise, a pinched-off version (blue) will have even smaller area.*

## 2.B Entanglement surfaces for $\mathrm{d}t \neq 0$

In this appendix, we consider an entanglement surface with spacelike separated boundary points at $(-t_\infty, -\theta_\infty)$ and $(t_\infty, \theta_\infty)$. The bulk geodesics between these

endpoints are given by:

$$\begin{aligned} r^2(\theta) &= r_H^2 \left( \frac{\sinh^2(r_H\theta_\infty)}{\sinh^2(r_H\theta_\infty) - \sinh^2(r_H t_\infty)} \right) \\ &\quad \times \frac{\cosh^2(r_H\theta_\infty)}{\sinh^2(r_H\theta_\infty)\cosh^2(r_H\theta) - \sinh^2(r_H\theta)\cosh^2(r_H\theta_\infty)}, \\ r^2(t) &= r_H^2 \left( 1 + \frac{\cosh^2(r_H t_\infty)}{\sinh^2(r_H t_\infty)\cosh^2(r_H t) - \sinh^2(r_H t)\cosh^2(r_H t_\infty)} \right. \\ &\quad \left. \times \frac{\sinh^2(r_H t_\infty)}{\sinh^2(r_H\theta_\infty)\cosh^2(r_H t_\infty) - \sinh^2(r_H t_\infty)\cosh^2(r_H\theta_\infty)} \right). \end{aligned} \tag{2.40}$$

For a given boundary region, the minimal radius reached by this geodesic is given by:

$$r_*^2 = \frac{r_H^2 \cosh^2(r_H\theta_\infty)}{\sinh^2(r_H\theta_\infty) - \sinh^2(r_H t_\infty)}, \tag{2.41}$$

which clearly shows $r_*$ is smallest for $t_\infty = 0$.

The length of the geodesics (2.40) is given by:

$$l(\theta_\infty, t_\infty) = 2\ln\left(\frac{2r_c}{r_H}\right) + \ln\left(\sinh^2(r_H\theta_\infty) - \sinh^2(r_H t_\infty)\right) + O\left(r_c^{-2}\right) \ , \tag{2.42}$$

where $r_c$ is a radial cut off. As in the case of the constant-time slice analysis, we may determine the switchover angle $\theta_{\text{switch}}$ by the matching condition (2.28):

$$\theta_{\text{switch}} = \frac{\pi}{2} + \frac{1}{2r_H}\ln\left(\cosh(\pi r_H)\right) - \frac{1}{2r_H}\ln\left(\cosh(2r_H t_\infty)\right). \tag{2.43}$$

Thus $\theta_{\text{switch}}$ is indeed smallest for $t_\infty = 0$.

# Chapter 3

# Causal Holographic Information

In chapter (1) we introduced holography and elements of the holographic dictionary. In chapter (2) we discussed techniques to reconstruct the bulk geometry, fields and dynamics given the boundary description, emphasizing the limitations of the known techniques and the necessity to further explore the holographic dictionary. This sets the stage for the study of *causal holographic information*, a bulk quantity originally identified in [69]. In this chapter we will discuss causal holographic information and some of its properties. We also discuss possible boundary duals of causal holographic information.

In section (3.1) we give the (bulk) definition of causal holographic information and in section (3.2) we further motivate the reasons to study it. In section (3.3) we discuss some of its known properties. In section (3.4) we identify shadow regions of causal holographic information surfaces and compare these shadows to those of other bulk probes for the BTZ geometry. In section (3.5) we discuss the structure of divergences of causal holographic information. Finally, we discuss possible boundary duals for causal holographic information in section (3.6).

## 3.1 A bulk definition

Given a co-dimension one spacelike surface $\mathcal{A}$ on the boundary $\partial\mathcal{M}$ of an asymptotically AdS-spacetime $\mathcal{M}$, one can naturally associate it to two covariantly defined co-dimension two surfaces in the bulk $\mathcal{M}$. The first surface is the extremal surface

that ends on $\partial\mathcal{A}$ (1.81). The surface area is divergent, but can be regulated. The regulated surface area in Planck units of the extremal surface is proposed to be the dual quantity of the entanglement entropy (1.81):

$$S_{\mathcal{A}} = \frac{A_{\mathfrak{E}_{\mathcal{A}}}}{4G}. \tag{3.1}$$

The second covariantly defined co-dimension two bulk surface is the causal information surface.[1] First we define the boundary causal diamond of $\mathcal{A}$; it is the union of the boundary future and past domains of dependence (see also section 2.1):

$$\Diamond_{\mathcal{A}} = D^{+}_{\partial\mathcal{M}}(\mathcal{A}) \cup D^{-}_{\partial\mathcal{M}}(\mathcal{A}) \quad . \tag{3.2}$$

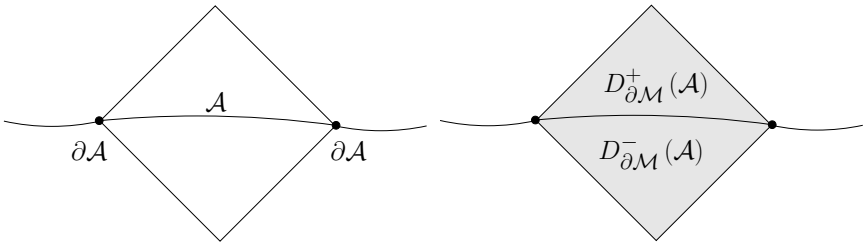


***Figure 3.1:*** *Visualization of the region $\mathcal{A}$ and the boundary $\partial\mathcal{A}$ (left) on a (1+1)-dimensional boundary and the construction of the causal diamond $\Diamond_{\mathcal{A}}$ (shaded area) consisting of the union of the future and past domains of dependence $D^{+}_{\partial\mathcal{M}}(\mathcal{A})$ and $D^{-}_{\partial\mathcal{M}}(\mathcal{A})$ (right).*

The causal diamond $\Diamond_{\mathcal{A}}$ of $\mathcal{A}$ is fully determined by $\partial\mathcal{A}$. We will refer to the set of points on the "top" and on the "bottom" of the causal diamond as $\mathcal{C}^{\pm}$ respectively. To be more precise, $\mathcal{C}^{+}$ is the set of points $p$ in $\Diamond_{\mathcal{A}}$ such that the intersection between the future lightcone of $p$ and $\Diamond_{\mathcal{A}}$ only includes $p$ itself. $\mathcal{C}^{-}$ is defined similarly. We will refer to points in $\mathcal{C}^{\pm}$ as future and past "caustics" respectively.

The so called causal wedge $\blacklozenge_{\mathcal{A}}$ of $\mathcal{A}$ is the intersection of the bulk future and past domains of influence of $\Diamond_{\mathcal{A}}$ (see also 2.2):

$$\blacklozenge_{\mathcal{A}} = J^{+}_{\mathcal{M}}(\Diamond_{\mathcal{A}}) \cap J^{-}_{\mathcal{M}}(\Diamond_{\mathcal{A}}). \tag{3.3}$$

The co-dimension two bulk surface we are interested in is the intersection of the bulk boundaries of the bulk future and past domains of influence of the causal

[1] In principle, there are more covariantly defined bulk surfaces associated to some boundary subregion $\mathcal{A}$. For example, one could extremize a different geometric quantity of the bulk surface. The extremal surface with minimal area is the simplest in this class.

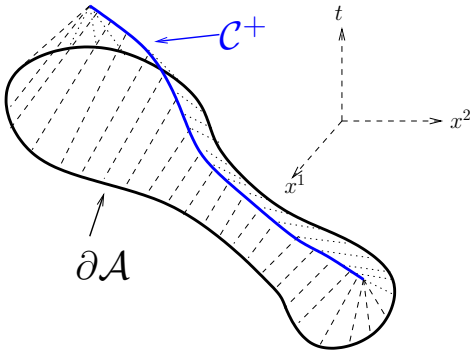


***Figure 3.2:*** *Visualization of the boundary causal diamond $\Diamond_{\mathcal{A}}$ in case of a (2+1)-dimensional boundary. The set of future "caustics" $\mathcal{C}^+$ is indicated by the blue line.*

diamond $\Diamond_{\mathcal{A}}$ (see figure 3.3):

$$\Xi_{\mathcal{A}} = \partial J^+_{\mathcal{M}}(\Diamond_{\mathcal{A}}) \cap \partial J^-_{\mathcal{M}}(\Diamond_{\mathcal{A}}). \tag{3.4}$$

Causal holographic information is defined in a way similar to the entanglement entropy (3.1):

$$\chi_{\mathcal{A}} = \frac{A_{\Xi_{\mathcal{A}}}}{4G}, \tag{3.5}$$

where $\Xi_{\mathcal{A}}$ is the causal information surface as defined in (3.4) [69].

The causal information surface has a surface area that is in general larger than or equal to the surface area of the extremal surface, when both surfaces are regularized in a consistent way. If the bulk spacetime is static and one picks $\mathcal{A}$ to be on a constant time slice, the extremal surface and the causal information surface both lie in the same bulk constant time slice. In this case the causal information surface either coincides with the minimal surface or it is located closer to the boundary [69].[2]

Causal holographic information does not satisfy the strong subadditivity property [69] whereas the holographic entanglement entropy does [51]. Also, for a pure state we can find examples with $\chi_{\mathcal{A}} \neq \chi_{\mathcal{A}^c}$ [69], where $\mathcal{A}^c$ is the boundary complement of $\mathcal{A}$.

[2]This does *not* mean that the minimal surface is bulk probe with a smaller shadow region than the causal information surface. For the analysis of shadow regions we must take into account switchover effects, as discussed in section (2.2). We will come back to the analysis of shadows for the causal information surface in section (3.4).

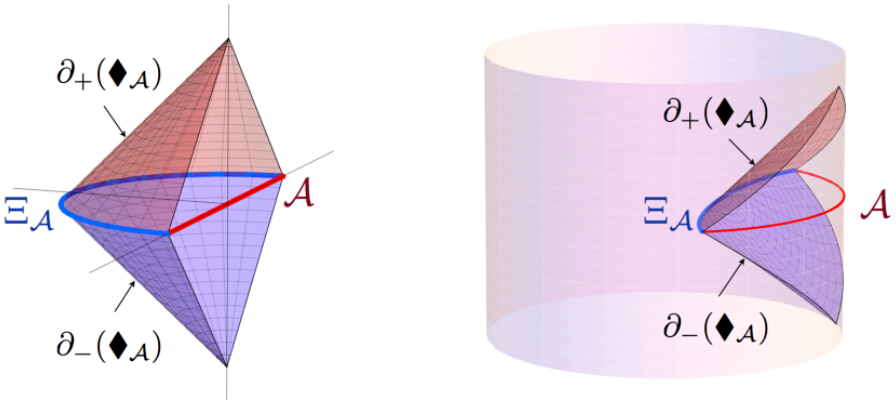


***Figure 3.3:*** *Left: the causal information surface $\Xi_{\mathcal{A}}$ (blue) for a boundary subregion $\mathcal{A}$ (red), in planar AdS. Right: the causal information surface $\Xi_{\mathcal{A}}$ (blue) for a boundary subregion $\mathcal{A}$ (red), in global AdS. Source: [86].*

## 3.2 Why causal holographic information is interesting

Why would one be interested in this co-dimension two bulk surface $\Xi_{\mathcal{A}}$? First of all, the causal holographic information surface $\Xi_{\mathcal{A}}$ is covariantly (coordinate independent) defined. The area of other covariantly defined co-dimension two surfaces like the minimal (extremal) surface $\mathfrak{E}_{\mathcal{A}}$ (1.81) and bifurcate Killing horizons in the bulk are associated to important boundary quantities. Secondly, light sheets play an important role in the so called Bousso bound (page 6) which is thought to be a deep statement underlying the principle of holography. Thirdly, for a complete reconstruction of the bulk minimal (extremal) surfaces do not seem to be sufficient (see section 2.2). The causal information surface has a smaller shadow region, which we will discuss in section (3.4). Lastly, it is believed that the causal wedge $\blacklozenge_{\mathcal{A}}$ associated to a boundary subregion $\mathcal{A}$ can be reconstructed with full knowledge of $\rho_{\mathcal{A}}$; it is thought to be the most conservative candidate for a subregion duality (see section 2.1).

## 3.3 Properties of the causal information surface

### 3.3.1 Topology of the causal information surface

The causal information surface $\Xi_{\mathcal{A}}$ can have a nontrivial topology. It can consist of disconnected pieces even if the boundary region $\mathcal{A}$ is connected. Examples of boundary regions which correspond to causal information surfaces that consist of disconnected pieces, can be found in the AdS-Schwarzschild bulk geometry [87] and soliton bulk geometries [88]. In this subsection we will illustrate the occurrence of causal information surfaces with nontrivial topology in the case of an AdS-Schwarzschild bulk geometry, as described in [87].

First we will heuristically motivate the occurrence of causal information that consist of different disconnected components. Consider pure AdS in global coordinates and a large boundary subregion $\mathcal{A}$ at $t = 0$ that almost completely covers the boundary. The intersection of the causal wedge $\blacklozenge_{\mathcal{A}}$ with the bulk $(t = 0)$-plane almost completely covers the $(t = 0)$-plane. Now introduce a *small* black hole in the centre $r_H \ll L_{\text{AdS}}$. The causal wedge cannot enter a black hole, because no causal curve can *leave* the black hole (per definition). However, the causal wedge is largely unaffected since the geometry is still close to the global AdS geometry further away $r \gg r_H$. Note that null rays can "bend" around a black hole and terminate on the "other" side of the black hole onto other null rays. This suggests that the causal information surface can split up into two disconnected parts: a part similar to the causal information surface in the global pure AdS metric, plus a part that encloses the black hole horizon.

Numerical analysis of the causal information surface for the BTZ and AdS-Schwarzschild geometries has been done by the authors of [87]. For the non-rotating BTZ black hole, the causal information surface remains connected, but for the AdS-Schwarzschild geometries it becomes indeed disconnected for large enough boundary regions (see figure 3.4).

The observation that the causal information surface becomes disconnected in some cases, puts constraints on the topology of Ryu-Takayanagi surfaces (1.81). In [50, 50] it is shown that the Ruy-Takayanagi surface $\mathfrak{E}_{\mathcal{A}}$ lies further away from $\mathcal{A}$ than the causal information surface $\Xi_A$. This implies that the Ruy Takayanagi must also become disconnected when parts of the causal information surface "pinch off", in the case of the AdS-Schwarzschild geometry and large enough boundary subregions $\mathcal{A}$.

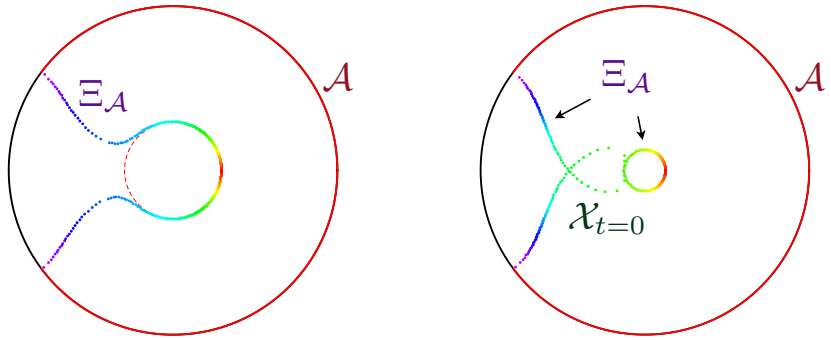


***Figure 3.4:*** *Causal information surfaces for boundary balls in the AdS-Schwarzschild geometry ($d > 2$). For large enough opening angle $\theta_\infty$, the causal information surface becomes disconnected (right). (Source: [87])*

### 3.3.2 Causal information surfaces in time dependent backgrounds

The causal information surface $\Xi$ has been studied in time-dependent situations in [86], of which we will give a short summary below. The behavior of the causal holographic information $\chi$ is found to be highly nontrivial in time-dependent geometries, which gives important restrictions on proposals for a boundary dual quantity of causal holographic information.

An example of a non-static, non-stationary time dependent asymptotically AdS geometry is the the Vaidya-AdS geometry. In [86], causal information surfaces and causal holographic information are studied in the context of the Vaidya-AdS geometry:

$$\begin{aligned} ds^2 &= 2\,dv\,dr - f(r,v)\,dv^2 + r^2\,d\mathbf{\Sigma}^2_{d-1,K}, \\ f(r,v) &= r^2\left(1 + \frac{K}{r^2} - \frac{m(v)}{r^d}\right), m(v) \qquad\qquad = m_0\,\theta(v - t_s)\ , \end{aligned} \tag{3.6}$$

where $d\mathbf{\Sigma}^2_{d-1,K}$ is the volume element of a spatial slice of the boundary. This metric describes the collapse of a thin spherical shell of "dust" which eventually forms an AdS-Schwarzschild black hole. The boundary state starts undergoing a transition from the vacuum state to a thermal state at $t = t_s$, which corresponds to bulk geometry with a shell that starts falling in at $t = t_s$. For boundary balls (strips) $\mathcal{A} = B^{d-1}$ with radius (width) $a$, the boundary causal diamond has past and future caustics with "height" $a$. When the boundary ball (strip) "sits" at $t = t_{\mathcal{A}}$, one can consider four qualitatively different cases:

| | | |
|---|---|---|
| **(1)** | $t_{\mathcal{A}} < t_s - a$ | $\blacklozenge_{\mathcal{A}}$ completely in AdS region |
| **(2)** | $t_s - a < t_{\mathcal{A}} < t_s$ | $\blacklozenge_{\mathcal{A}}$ both in AdS-Schwarzschild and AdS regions |
| **(3)** | $t_s < t_{\mathcal{A}} < t_s + a$ | $\blacklozenge_{\mathcal{A}}$ both in AdS-Schwarzschild and AdS regions |
| **(4)** | $t_s + a < t_{\mathcal{A}} < t_s - a$ | $\blacklozenge_{\mathcal{A}}$ completely in AdS-Schwarzschild region |

Cases 2 and 3 are interesting, because in both cases part of the boundary causal wedge $\blacklozenge_{\mathcal{A}}$ sits in the AdS regime of the bulk metric and part of $\blacklozenge_{\mathcal{A}}$ is in the AdS-Schwarzschild part of the metric, changing the geometry of the bulk causal wedge and the causal information surface non-trivially. In these cases we can expect the causal holographic information to be time dependent.

In [86] it is shown that for $d = 2$ the causal holographic information does not depend on time in regime 2, even though $\Xi_{\mathcal{A}}$ is modified compared to the pure AdS regime. In region 3, $\chi_{\mathcal{A}}$ *is* time dependent. For $d > 2$, the causal holographic information *does* depend on time even in regime 2, which means that the causal holographic information $\chi_{\mathcal{A}}$ "feels" the shell before it starts falling in. Causal holographic information is called "mildly teleological" because it only "senses" the change in the state an order $O(a)$ in advance, where $a$ is the typical length scale of $\mathcal{A}$.

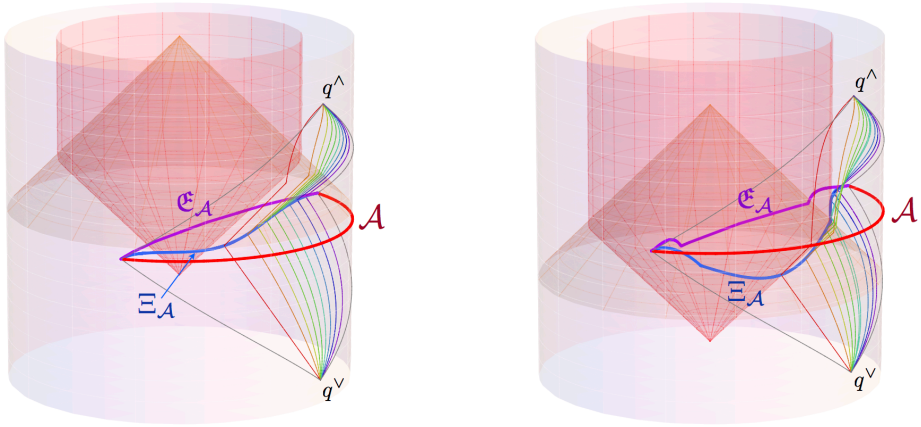


***Figure 3.5:*** *An in-falling shell forms a black hole. Left: $t_{\mathcal{A}} < t_s < t_{\mathcal{A}} + a$, so only the upper part of the causal wedge $\blacklozenge_{\mathcal{A}}$ gets deformed. Right: $t_{\mathcal{A}} - a < t_s < t_{\mathcal{A}}$, so the geodesics from the both the past and future caustic of $\blacklozenge_{\mathcal{A}}$ are affected by the shell encounter. (Source: [86])*

## 3.4 Causal information surfaces as bulk probe

In this section, we return to the point of "shadows" as discussed in chapter (2). Generally, the extremal surface $\mathfrak{E}_{\mathcal{A}}$ associated to the entanglement entropy of a given boundary region $\mathcal{A}$ reaches *deeper* into the bulk than the causal information surface $\Xi_{\mathcal{A}}$ [50, 69]. However, the extremal surface associated to entanglement entropy exhibits nontrivial "switchover behavior" (see chapter 2), such that the shadow region for causal information surfaces is *smaller* than the shadow region for the extremal surface associated to entanglement entropy. Below we analyze the shadow regions for causal information surfaces, in particular in the AdS-Schwarzschild geometry. Subsequently, we will compare the full and partial shadow regions of the causal information surface, the Wilson loops and the entanglement entropy for the BTZ geometry.

### 3.4.1 Causal information shadows

The causal information surface $\Xi_{\mathcal{A}}$ differs qualitatively from the extremal surfaces associated to entanglement entropy (1.81) and the string world sheets associated to Wilson loops in two ways. Firstly, its boundary CFT interpretation is unclear, although suggestions have been made (see section 3.6). Secondly, it does not take the general form we described in section 2.2.2 as a minimal geometric object. Nevertheless, it is still natural to define $\theta_\infty(r_*)$ for this probe. Thus we can study this probe alongside those above, and later make a comparison of their respective shadows.

Here we analyze the "full shadow" region for causal information surfaces in static, spherically symmetric spacetimes. In particular, we consider bulk geometries of the form

$$ds^2 = -f(r)dt^2 + \frac{dr^2}{f(r)} + r^2 d\Omega_{d-1}^2, \tag{3.7}$$

of which the AdS-Schwarzschild geometry is an example.

The boundary causal diamond $\Diamond_{\mathcal{A}}$ and the bulk causal wedge $\blacklozenge_{\mathcal{A}}$ for a ball $\mathcal{A}$ on the boundary are both generated by two caustics: a past and a future caustic. For a ball on a constant time slice ($t = 0$), the "height" of the caustic along the time direction is simply equal to the radius of the ball. The deepest bulk point to which a causal information surface reaches is determined by the intersection of the past and future directed radial null geodesics from the future and past caustics respectively. So given a boundary subregion with typical size $\theta_\infty$, we can identify a maximal penetration depth $r_*$.

Vice-versa, we can start from a point in the bulk at radial coordinate $r_*$, and construct the two radially outgoing light rays to the future and past. These will end on two boundary points, $p^{\pm}_{\mathcal{A}}$, past and future caustics that generate a boundary causal diamond $\Diamond_{r_*} = D^+(p^-_{\mathcal{A}}) \cup D^-(p^+_{\mathcal{A}})$. The waist of the diamond $\Diamond_{r_*}$ is exactly a boundary ball of radius $\theta_\infty$ that sits on the same timeslice as the initial bulk point. The width $\theta_\infty(r_*)$ can be determined by calculating the "height" of the causal diamond $\Diamond_{r_*}$, which we can do by following the radial null geodesics from the bulk point with $r = r_*$:

$$\theta_\infty(r_*) = \int_{r_*}^{\infty} \mathrm{d}r \left|\frac{dt}{dr}\right| = \int_{r_*}^{\infty} \mathrm{d}r \sqrt{-\frac{g_{rr}}{g_{tt}}} = \int_{r_*}^{\infty} \frac{\mathrm{d}r}{f(r)} \ . \tag{3.8}$$

For $\theta_\infty \geq \pi$, the boundary ball covers the entire asymptotic boundary, and its domain of dependence is the entire spacetime. For the AdS-Schwarzschild geometry, the causal information surface for a ball with $\theta_\infty \geq \pi$ would correspond to the black hole horizon. We are interested in the causal information surface corresponding to the largest possible ball that does not cover the whole boundary. This is the causal information surface which reaches deepest into the bulk and has $\theta_\infty = \pi - \epsilon$, for $\epsilon$ arbitrarily small.[3] The shadow radius is given by

$$r_{\min} = \theta_\infty^{-1}(\pi) \ , \tag{3.9}$$

if this inverse exists. Otherwise there is no shadow.

In spacetimes with a horizon at $r_H$, $f(r) \to 0$ linearly as $r \to r_H$, thus $\theta_\infty \to \infty$. Such spacetimes will always show shadows, since there are no probes for the part of the bulk that would correspond to boundary subregions with $\theta_\infty \in (\pi, \infty)$. For example, for the BTZ geometry with $f(r) = r^2 - r_H^2$, we have (3.8)

$$\pi = \int_{r_{\min}}^{\infty} \frac{\mathrm{d}r}{r^2 - r_H^2} = \frac{1}{r_H} \operatorname{arccoth}\left(\frac{r_{\min}}{r_H}\right) \implies r_{\min} = \frac{r_H}{\tanh(r_H \pi)} \ . \tag{3.10}$$

Note that this is precisely the first term of (2.31). In light of the earlier work by Hubeny [69], this similarity is not surprising. In the BTZ background, the causal information surface $\Xi_{\mathcal{A}}$ coincides with the extremal surface for a given boundary subregion. The only difference between their respective shadows is that the minimal area surfaces encounter a phase transition at some $\theta_\infty < \pi$ determined by the area matching condition (2.21). In particular, the phase transition for minimal area surfaces with a small black hole occurs when $\theta_\infty \sim \pi/2$, which makes a significant difference from the causal information surfaces. For large black holes, the minimal surface transition occurs at $\theta_\infty \lesssim \pi$, so these two probes agree with each other in this limit.

[3] For our purposes, we can simply take $\theta_\infty = \pi$.

The geometry of the causal information surfaces is more complicated in higher dimensions [87], but the minimal radius $r_{\min} = \min\{r_*\}$ can still be determined by (3.8) and (3.9). For $d \geq 3$ the integral in (3.8) is slightly more involved, but since we are primarily interested in knowing how close the surface gets to the black hole, a near-horizon approximation will suffice. Thus we assume $r_* - r_H \ll 1$ and expand the integrand of (3.8) in terms of $(r - r_H)$. For large black holes ($r_H \gg 1$), the near horizon contribution dominates the integral for $\theta_\infty = \pi$:

$$\pi \approx \int_{r_{\min}}^{r_{\min}+a} \frac{\mathrm{d}r}{f'(r_H)(r - r_H)} = \frac{1}{f'(r_H)} \ln\left(\frac{r_{\min} - r_H + a}{r_{\min} - r_H}\right) . \tag{3.11}$$

where $a \lesssim r_H$ is some constant, and $f(r)$ is given by

$$f(r) = r^2 + 1 - \frac{r_H^{d-2}}{r^{d-2}}(r_H^2 + 1) \tag{3.12}$$

for the AdS-Schwarzschild metric. Solving for $r_{\min}$, we find

$$r_{\min} \approx r_H + ae^{-d\pi r_H} . \tag{3.13}$$

Thus for large black holes, the causal information surfaces probe exponentially close to the horizon.

For small black holes ($r_H \ll 1$), there is also a contribution of approximately $\frac{\pi}{2}$ to the integral in (3.8) from the range where $f \approx f_{\mathrm{AdS}}$. The solution is then approximately:

$$r_{\min} \approx r_H + ae^{-\frac{\pi(d-2)}{2r_H}} . \tag{3.14}$$

Thus causal surfaces probe exponentially close to small black holes, which is dramatically better than minimal area surfaces in this limit [2]. In [2] we provided evidence for the statement that for small $r_H \ll 1$ minimal surfaces associated to entanglement entropy only reach upto an order $O(r_H)$ away from the horizon at $r = r_H$.

### 3.4.2 Comparison to other probes: the BTZ geometry

In section (2.3.1) of chapter (2) we analyzed the shadow regions for rectangular Wilson loops and the entanglement entropy of boundary intervals for the BTZ geometry. The analysis of shadows in $(2+1)$-dimensional geometries is simpler than that of higher dimensional geometries, because the subregions on the $(1+1)$-dimensional boundary can simply only be intervals. This simplification allows us to determine not only the region of full shadow, but for every bulk point we

can also determine the portion of the tangent space that can be probed. In this subsection we present these (numerical) results.

In figure 3.6 (left panel) $r_{\min}$ is plotted as function of the black hole radius $r_H$, for all three investigated probes. As noted earlier, the shadow persists even when $r_H = 0$ due to the mass gap in $AdS_{2+1}$. The horizon radius is related to the ADM mass by $r_H^2 = GM - 1$, so a vanishing horizon does not recover empty AdS. In the right panel of figure 3.6, we extend the parameter range below the mass gap to include the conical defect. Then as $GM \to 0$, all shadows indeed disappear.

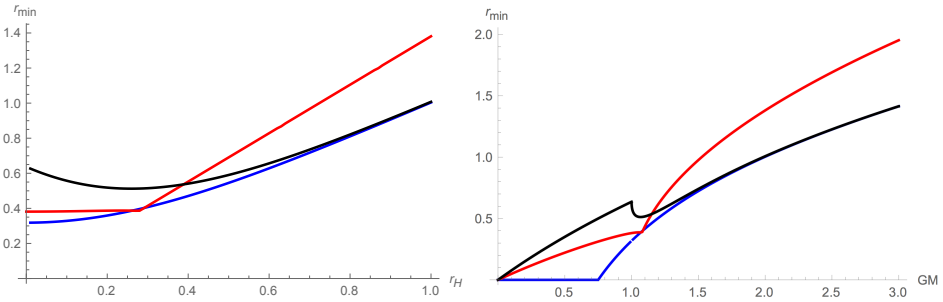


***Figure 3.6:*** *Shadow radius $r_{min}$ as a function of the black hole radius $r_H$ (left) and mass $GM$ (right) for the different bulk probes: entanglement entropy (black), Wilson loops (red), and causal information (blue). The kink in the Wilson loops curves are due to the transition from ∪-shaped to ⊔-shaped world sheets. The kink in the minimal area surface curve in the right panel is exactly at the horizon $r_H = 0$, at which point the phase transition angle becomes fixed at $\pi/2$.*

We can see clearly that causal information surfaces almost always leave the smallest shadow. This conclusion appears to hold in higher dimensions as well, as indicated by our numerical results and approximations for both small and large black holes as presented in [2].

It is interesting to note that for a point at radius $r_{\min}$, it may be that a given probe can only reach it with a specific orientation, implying a restriction on the accessibility of the bulk tangent space. Empty AdS space satisfies the Strong Coverage Property that the entire tangent space of any point is covered, and indeed this property is necessary for certain reconstruction schemes [78, 79]. It is thus interesting to ask how much of the tangent space once loses due to the presence of a black hole.

In the BTZ geometry, this question is easy to answer. The deepest probe in any particular family, $b(r_{\min})$, also passes through points with $r > r_{\min}$ at the steepest angle. Therefore, we need only calculate the slope of this surface to determine the coverage of the tangent space. These "partial shadows" are plotted in figure 3.7.

Somewhat surprisingly, although Wilson loops probe less deeply in general, they exhibit the smallest partial shadows throughout most of the bulk.

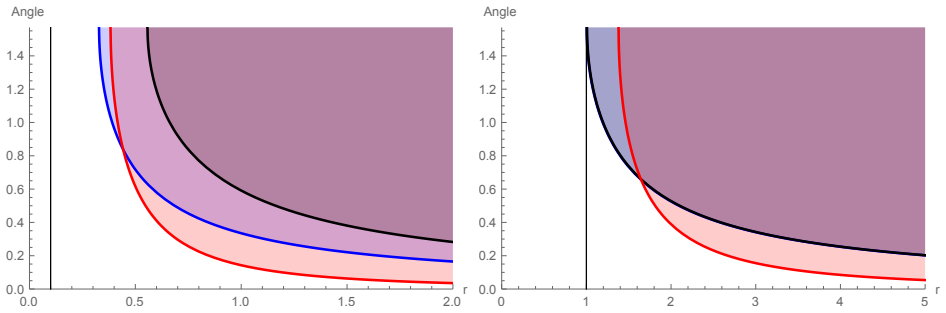


***Figure 3.7:*** *The shaded region above each curve represents the part of the tangent space accessible by the associated bulk probe (entanglement (black), Wilson (red), and causal (blue)) as a function of the radial coordinate $r$. $\pi/2$ is purely tangential, and 0 is purely radial. The horizon radius, $r_H = 0.1 l_{\text{AdS}}$ (left) and $r_H = l_{\text{AdS}}$ (right), is indicated by the vertical line. Note that in the right panel, the blue and black curves almost overlap, reflecting the agreement of minimal and causal information surfaces in the large black hole limit.*

## 3.5 Subleading divergences

### 3.5.1 Structure of divergences

Causal holographic information of a boundary subregion $\mathcal{A}$ is equal to the area of a bulk co-dimension two surface that ends on $\partial\mathcal{A}$, just like the extremal surface associated to entanglement entropy. To leading order, causal holographic information and entanglement entropy both exhibit an *area law*: the leading divergence is proportional to the area of $\partial\mathcal{A}$ ($d > 2$). The subleading divergences differ.

#### Example: the strip

Consider the boundary strip $\mathcal{A} = \{x : x_1 \leq \frac{w}{2}, t = 0\}$ in Poincaré coordinates (1.14,1.15) for pure AdS spacetime. The boundary causal diamond $\Diamond_{\mathcal{A}}$ has past and future caustics at $x_1 = 0, t = \pm\frac{w}{2}$. The causal information surface $\Xi_{\mathcal{A}}$ is then

given by $z^2 + x_1^2 = (\frac{w}{2})$ [69] and the area is given by

$$\begin{aligned} A_{\Xi_{\mathcal{A}}} &= \int_{-\frac{L_{\rm IR}}{2}}^{+\frac{L_{\rm IR}}{2}} d^{d-2}x \int_{\epsilon}^{\frac{w}{2}} dz \sqrt{\det \frac{\partial x^M}{\partial x^\alpha} \frac{\partial x^N}{\partial x^\beta} G^{ADS}_{MN}} \\ &= 2 \int_{-\frac{L_{\rm IR}}{2}}^{+\frac{L_{\rm IR}}{2}} d^{d-2}x \int_{\epsilon}^{\frac{w}{2}} dz \sqrt{\left( \left( \frac{dx_1}{dz} \right)^2 \frac{1}{z^2} + \frac{1}{z^2} \right) \left( \frac{1}{z^2} \right)^{d-2}} \\ &= \left( \frac{2L_{\rm IR}}{w} \right)^{d-2} \frac{2}{d-2} \sqrt{1 - \left( \frac{2\epsilon}{w} \right)^2} {}_2F_1 \left[ \frac{1}{2}, \frac{d}{2}, \frac{3}{2}, 1 - \left( \frac{2\epsilon}{w} \right)^2 \right]. \end{aligned} \tag{3.15}$$

For $d$ odd, (3.15) contains a logarithmically diverging term. For $d = 4$, we have

$$A = \left( \frac{2L_{\rm IR}}{w} \right)^2 \left( \frac{w^2}{8\epsilon^2} - \frac{1}{2} \log \frac{\epsilon}{w} + \dots \right). \tag{3.16}$$

Note that the causal holographic information for the strip has different subleading divergences from those of the holographic entanglement entropy (1.95). The leading divergences *do* correspond (1.95).

**Non-locality of subleading divergences** The example of the strip in $d = 4$ shows that the coefficient of the logarithmically divergent term of causal holographic information cannot be expressed as just an integral over $\partial\mathcal{A}$ of local geometric quantities. For $\mathcal{A}$ the strip in a flat background, both the intrinsic and extrinsic curvatures of $\partial\mathcal{A}$ vanish. The coefficient of the logarithmically divergent term of the causal holographic information for the strip (d=4) is proportional to $\frac{L_{IR}^2}{w^2}$ [69], where $L_{IR}$ is an IR-regulator in the directions $x^2$ and $x^3$. For the strip there is no local geometric quantity on $\partial\mathcal{A}$ (the two "plates" at $x^1 = \pm\frac{w}{2}$) that depends on the separation distance $w$. This means that we cannot write the coefficient of the logarithmically divergent term in $\chi_{\mathcal{A}}$ as the integral of a local quantity, which *is* possible for the coefficient of the logarithmically divergent term in entanglement entropy (1.89).

### 3.5.2 Causal holographic information for general surfaces

#### Caustics of the boundary causal diamond

The causal diamond $\Diamond_{\mathcal{A}}$ is generated by null rays emanating normally from $\partial\mathcal{A}$ [69]. For each point $x(\xi)$ on $\partial\mathcal{A}$ there are two unique null normal vectors (up to a sign). The inward-pointing null geodesics that emanate orthogonally from this point terminate in past and future caustics $x_{\vee} \in \mathcal{C}^-$ and $x_{\blacklozenge_{\mathcal{A}}} \in \mathcal{C}^+$ respectively. Given

a point on $\partial\mathcal{A}$, we need information about other points on $\partial\mathcal{A}$ to determine where the null geodesics will intersect for the first time with null geodesics emanating from another point on $\partial\mathcal{A}$. The location of this intersection point is determined by one or more other points on $\partial\mathcal{A}$.

**Entering the bulk**

We focus in our discussion on the case of $d = 4$ boundary dimensions; however, a logarithmically divergent term can be present in the causal holographic information whenever the number of boundary dimensions is even. For $d$ even and $d > 2$ the asymptotically AdS-metric can be put in Fefferman Graham form [24] [25]:

$$\begin{aligned} ds^2 &= G_{MN}dX^M dX^N \\ &= \frac{dz^2}{z^2} + \frac{1}{z^2}g_{\mu\nu}(z,x)dx^\mu dx^\nu \\ g_{\mu\nu}(z,x) &= g^{(0)}_{\mu\nu}(x) + z^2 g^{(2)}_{\mu\nu}(x) + ... + z^d\left(g^{(d)}_{\mu\nu}(x) + \log z\ h_{\mu\nu}(x)\right) + O(z^{d+1}). \end{aligned} \tag{3.17}$$

Here $g^{(0)}_{\mu\nu}(x)$ is the boundary metric, $g^{(2i)}_{\mu\nu}$ $(1 \leq i \leq \frac{d}{2} - 1)$ and $h_{\mu\nu}$ are determined by $g^{(0)}_{\mu\nu}$ and $g^{(d)}_{\mu\nu}$ encodes information about the state.

Close to the boundary, points on the causal information surface $\Xi_\mathcal{A}$ can be mapped to points on $\partial\mathcal{A}$. We expand the embedding function close to the boundary around points on $\partial\mathcal{A}$:

$$x^\mu_{bulk}(z,\xi_1,\xi_2) = x^\mu_{boundary}(\xi_1,\xi_2) + y^\mu(\xi_1,\xi_2)z^2 + O(z^4). \tag{3.18}$$

Generally, the component of $y^\mu$ that is tangent to $\partial\mathcal{A}$ does not give a contribution to the logarithmically diverging term in the area of the bulk surface. We can express the normal component of $y^\mu$ in terms of the boundary normal vectors $\{N^\mu_a\}$ of $\partial\mathcal{A}$:

$$y^\mu = y^\mu_\parallel + y^\mu_\perp \quad = y^\mu_\parallel + \lambda^a N^\mu_a. \tag{3.19}$$

For any such surface, the surface area that is regulated by a radial $z = \epsilon$ cutoff for an asymptotically AdS-space is:

$$\begin{aligned} A = &\frac{1}{2}\frac{A_{\partial\mathcal{A}}}{\epsilon^2} \\ &+ \log\left(\frac{1}{\epsilon}\right)\frac{1}{2}\int d^2\xi\sqrt{\tilde{g}}\left(4\lambda^a\lambda^b p_{ab} + 2\lambda^a K_a + h^{\mu\nu}g^{(2)}_{\mu\nu}\right) \\ &+ \text{finite}, \end{aligned} \tag{3.20}$$

where $N^\mu_a N^\nu_b g^{(0)}_{\mu\nu} = p_{ab}$, $h_{\mu\nu} = g^{(0)}_{\mu\nu} - N^a_\mu N^b_\nu p^{ab}$, $K^a$ is the trace of the extrinsic curvature, and an expression for $g^{(2)}_{\mu\nu}$ is given later (3.41).

### Smooth surfaces on a flat boundary

For entanglement entropy, the normal component of $y$ (3.18,3.19) is fixed by the extremality condition to $\lambda^a = -\frac{K^a}{4}$. For the causal information surface the $\lambda_a(x)$'s in the expansion (3.18,3.19) do not just depend on local geometric quantities of $\partial\mathcal{A}$, as can be seen in the example of the strip.

We first analyze the simpler case where the entangling surface lies on a constant time slice, then the more general case of an arbitrary spacelike surface embedded in flat Minkowski spacetime.

**Constant time slice case** In the case of a static spacetime with a flat boundary, the analysis is easier if we pick the surface $\partial\mathcal{A}$ to be on a constant time slice. Boundary normal null geodesics emanating from $\partial\mathcal{A}$ are simply straight null rays proportional to the null normal vectors of $\partial\mathcal{A}$. When $\partial\mathcal{A}$ is on a constant time slice $t = 0$, the causal information surface should also be on the $t = 0$ slice by symmetry considerations; both the bulk causal wedge and the boundary causal diamond are symmetric in the $t = 0$ plane. Points on the causal information surface are on the bulk boundaries of the bulk future and past domains of influence of the boundary causal diamond $\Diamond_{\mathcal{A}}$ (3.4).

The object $\mathcal{A}$ on the boundary will "shrink" as one moves deeper into the bulk along the radial coordinate. In appendix (3.A) we determine how this happens as a function of the radial Poincaré coordinate $z$.

If the future caustic that is separated from $x(\xi)$ on $\partial\mathcal{A}$ by the null normal emanating from $x(\xi)$ is located at $t = \tau$ and the spacelike normal vector in the $t = 0$[4] plane in $x(\xi)$ is given by $\hat{n}(\xi)$[5], then the embedding function can be written in terms of $\tau$ (Appendix 3.A):

$$\vec{x}_{bulk}(\xi, z) = \vec{x}_{\partial\mathcal{A}}(\xi) + \frac{z^2}{2\tau(\xi)}\hat{n}(\xi) - \frac{z^2}{2\tau(\xi)}b^\alpha \vec{T}_\alpha(\xi) + O(z^4). \tag{3.21}$$

Expression (3.20) simplifies in this case to

$$A = \frac{1}{2}\frac{A_{\partial\mathcal{A}}}{\epsilon^2} + \frac{1}{2}\int_{\partial\mathcal{A}} d^2\xi\sqrt{g_{\partial\mathcal{A}}}\left(\frac{1}{\tau^2} + \frac{K}{\tau}\right)\log\frac{1}{\epsilon} + \text{finite}. \tag{3.22}$$

[4]The quantity $\tau$ can be thought of as the affine parameter distance between a point on $\partial\mathcal{A}$ and its corresponding future (past) caustic. This explanation is clarified in for the more general case in section (3.5.2)

[5]We used $\hat{n}$ to be the inward pointing normal together with the conventions $K_{\mu\nu} = +h^\rho_\mu \nabla_\rho N_\nu$ and $K = +h^{\mu\nu}K_{\mu\nu}$ for extrinsic curvatures and expansions respectively, where $h$ is an induced metric and $N$ is a normal vector.

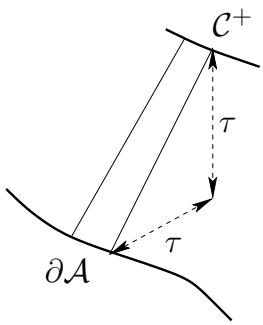


***Figure 3.8:*** *Visualization of the quantity $\tau$. Note that that for each point on $\partial\mathcal{A}$ there is a unique point on $\mathcal{C}^+$ separated by a vector that is proportional to the future directed inward pointing null normal vector. For a surface $\partial\mathcal{A}$ that does not lie on a constant time slice, a single function $\tau$ is not sufficient.*

**General spacelike region** Now dropping the assumption that $\partial\mathcal{A}$ lies on a constant timeslice, but remaining in Minkowski space, the separation in time of a point $p$ on $\partial\mathcal{A}$ and its caustics on the causal diamond may be different for the past and future caustics.

The past caustic $x^\mu_{\blacklozenge_\mathcal{A}}$ and the future caustic $x^\mu_\vee$ for a point $x^\mu(\xi)$ on $\partial\mathcal{A}$ are separated from $x^\mu(\xi)$ by null normal vectors:

$$\begin{aligned} x^\mu_{\blacklozenge_\mathcal{A}}(\xi) &= x^\mu(\xi) + \lambda_\uparrow(\xi) N^\mu_\uparrow(\xi) \\ x^\mu_\vee(\xi) &= x^\mu(\xi) + \lambda_\downarrow(\xi) N^\mu_\downarrow(\xi) \end{aligned} \tag{3.23}$$

where $N^\mu_\uparrow(\xi)$ and $N^\mu_\downarrow(\xi)$ are the null normal vectors in $x^\mu(\xi)$ where we choose to normalize them such that $N^\mu_\uparrow(\xi) N^\nu_\downarrow(\xi)\eta_{\mu\nu} = 1$. In appendix (3.B) we argue that we can still expand the embedding function similarly to (3.21):

$$x^\mu_{bulk}(z,\xi) = x^\mu(\xi) + \frac{z^2}{2}\left(\frac{N^\mu_\uparrow(\xi)}{\lambda_\downarrow(\xi)} + \frac{N^\mu_\downarrow(\xi)}{\lambda_\uparrow(\xi)}\right) + \frac{z^2}{2\lambda_\uparrow(\xi)} b^\alpha_i(\xi) T^\mu_\alpha + O(z^4) \tag{3.24}$$

The divergent part of the area is now simply:

$$A = \frac{1}{2}\frac{A_{\partial\mathcal{A}}}{\epsilon^2} + \frac{1}{2}\log\frac{1}{\epsilon}\int d^2\xi \sqrt{\det g_{\partial\mathcal{A}}}\left(\frac{2}{\lambda_\uparrow\lambda_\downarrow} + \frac{K_\uparrow}{\lambda_\downarrow} + \frac{K_\downarrow}{\lambda_\uparrow}\right) + finite. \tag{3.25}$$

Equation (3.23) defines $\lambda_\uparrow$ and $\lambda_\downarrow$, which can be thought of as being the affine parameter distances between $x(\xi)$ and $x^\mu_{\blacklozenge_\mathcal{A}}(\xi)$ and $x^\mu_\vee(\xi)$ respectively. The null

normal vectors can be scaled simultaneously with $\lambda_\uparrow$ and $\lambda_\downarrow$, subject to the condition $N_\uparrow \cdot N_\downarrow = 1$, but all terms in (3.25) are invariant under this rescaling. The absolute value of the distance between the future and past caustics related to a point $x(\xi)$ on $\partial\mathcal{A}$ by (3.23) is equal to $\sqrt{2\lambda_\uparrow(\xi)\lambda_\downarrow(\xi)}$.

### 3.5.3 Modification of the causal information formula

A candidate for the holographic entanglement entropy is obtained by applying the Wald entropy formula (1.86) to surfaces that end on the entanglement surface $\partial\mathcal{A}$. The entanglement entropy is then given by the surface that extremizes this quantity.

$$S_{\text{Wald}} = -2\pi \int_{horizon} d^{d-1}x\sqrt{h}\frac{\delta\mathcal{L}}{\delta R^{ab}{}_{cd}}\hat{\epsilon}^{ab}\hat{\epsilon}_{cd} \tag{3.26}$$

As discussed in section (1.3), a modification of the Wald functional (1.86) is necessary in the context of holographic entanglement entropy [56], due non-vanishing extrinsic curvature of a general minimal surface. For Lovelock gravity, a concrete modification is proposed in [56], where the modification can be written as a boundary term. A more general modification of the Wald functional is given in [57]. This modification does not affect the log-term, so for our purposes we propose to generalize causal holographic information by the evaluation of the Wald functional on the causal information surface, modulo some boundary terms. For causal holographic information in the context of Gauss-Bonnet gravity this becomes:

$$\chi_{\mathcal{A}} = \frac{1}{4G_N^{(5)}}\int_{\Xi_{\mathcal{A}}} d^{d-1}x\sqrt{\sigma_{\Xi_{\mathcal{A}}}}\left(1+\lambda L^2 R_{\Xi_{\mathcal{A}}}\right) + \text{boundary term}, \tag{3.27}$$

where $\sigma_{\Xi_{\mathcal{A}}}$ is the induced metric on the bulk surface $\Xi$ associated to $\mathcal{A}$ and $R_{\Xi_{\mathcal{A}}}$ is the intrinsic curvature.

The intrinsic curvature for a surface in an asymptotically AdS spacetime, for which the embedding function can be expanded as in (3.18) is given by:

$$R_{\Xi_{\mathcal{A}}} = -6 + z^2\left(R_{\partial\Sigma} + 2h^{\mu\nu}g^{(2)}_{\mu\nu} + 4\lambda^a K_a + 8\lambda^a\lambda_a\right) + O(z^4), \tag{3.28}$$

where $R_{\partial\mathcal{A}}$, $K^a$ and $h$ are boundary quantities.

The coefficient of the logarithmically diverging term is now proportional to:

$$a\int_{\partial\mathcal{A}} d^2\xi\sqrt{\tilde{g}}\left(-\frac{R_{\partial\mathcal{A}}}{4}\right) + c\int_{\partial\mathcal{A}} d^2\xi\sqrt{\tilde{g}}\left(\frac{R_{\partial\mathcal{A}}}{4} + \frac{1}{2}h^{\mu\nu}g^{(2)}_{\mu\nu} + \lambda^a K_a + 2\lambda^a\lambda_a\right). \tag{3.29}$$

We can evaluate this expression for the case of a static spacetime with a flat boundary. When $\partial\mathcal{A}$ is on a constant time slice, we can use (3.21) in order to get the coefficient of the logarithmically diverging term:

$$-\frac{a}{720\pi}\int d^2\xi\sqrt{\tilde{g}}R_{\partial\mathcal{A}}+\frac{c}{720\pi}\int d^2\xi\sqrt{\tilde{g}}\left(R_{\partial\mathcal{A}}+2\left(\frac{1}{\tau^2}+\frac{K}{\tau}\right)\right). \tag{3.30}$$

Now considering a spacelike surface $\partial\mathcal{A}$ that is not necessarily on a constant time slice, we can apply (3.24) and find for the coefficient of the logarithmically diverging term:

$$-\frac{a}{720\pi}\int d^2\xi\sqrt{\tilde{g}}R_{\partial\mathcal{A}}+\frac{c}{720\pi}\int d^2\xi\sqrt{\tilde{g}}\left(R_{\partial\mathcal{A}}+2\left(\frac{2}{\lambda_\uparrow\lambda_\downarrow}+\frac{K_\uparrow}{\lambda_\downarrow}+\frac{K_\downarrow}{\lambda_\uparrow}\right)\right). \tag{3.31}$$

### 3.5.4 Universality of the log-term

In this section, we show that the coefficient of the logarithmically divergent term, which we have focused on, is universal. It is independent of the regulator, and also independent of the state. Our result is more general than the particular causal information surface: the same will be true for *any* covariantly defined surface[6] The discussion will take place in a setting with a $(d = 4)$-dimensional boundary, but we believe similar arguments hold for $d = 2n$ with $n > 2$.

**Regulator independence** This subsection is to a large extent based on work from Schwimmer and Theisen [89,90]. We briefly review the relevant parts of their work and argue that any covariantly defined co-dimension two bulk surface that can be expanded as in (3.18) yields a universal log-divergence coefficient.

Our strategy for showing the regulator independence is to relate a change in regulator to a change of coordinates in the bulk that leaves the metric in Fefferman Graham form. The regulated area of the surface is computed up to a cutoff value of the new radial coordinate. Such a bulk change of coordinates acts as a conformal transformation on the boundary, so showing the regulator independence of the log term is equivalent to showing that it is Weyl invariant.

In more detail, to define the regulated area, one first puts the metric in Fefferman Graham form [24, 25]:

$$ds^2 = G_{MN}dX^M dX^N = \frac{d\rho^2}{4\rho^2}+\frac{1}{\rho}g_{\mu\nu}(\rho,x)dx^\mu dx^\nu \tag{3.32}$$

[6]It is important that the shape of the surface near the boundary allows an expansion like (3.18).

For $d$ even, we can expand $g_{\mu\nu}(\rho, x)$ as

$$g_{\mu\nu}(\rho, x) = g^{(0)}_{\mu\nu}(x) + \rho g^{(2)}_{\mu\nu}(x) + ... + \rho^{\frac{d}{2}} \left( g^{(\frac{d}{2})}_{\mu\nu}(x) + \log \rho \;\; h_{\mu\nu}(x) \right) + O(\rho^{\frac{d}{2}+1}). \tag{3.33}$$

One can take a finite cut off in the radial coordinate $\rho$ in order to regulate the surface area of a bulk surface that ends on $\partial\mathcal{A}$. The ambiguity in choice of cutoff arises because there is not a unique way to choose coordinates such that the bulk metric is in Fefferman Graham form.

To see how the area changes, consider an infinitesimal diffeomorphism that leaves the metric in the Fefferman Graham form. Such a transformation is parametrized by a vector field $(\xi^\rho, \xi^\mu)$ such that [89, 90]:

$$\begin{aligned} (\mathcal{L}_\xi G)_{\rho\mu} &= 0 \\ (\mathcal{L}_\xi G)_{\rho\rho} &= 0. \end{aligned} \tag{3.34}$$

Such a PBH-transformation (Penrose-Brown-Hennaux-transformation) corresponds to a Weyl transformation of the boundary metric $g^{(0)}_{\mu\nu}$ and can be parametrized by a function $\omega(x)$.

The infinitesimal coordinate transformation

$$\begin{aligned} \rho &= \tilde{\rho} e^{-2\omega(\tilde{x})} \simeq \tilde{\rho}\,(1 - 2\omega(\tilde{x})) \\ x^\mu &= \tilde{x}^\mu + a^\mu(\tilde{x}, \tilde{\rho}) \end{aligned} \tag{3.35}$$

corresponding to $\xi^\rho = -2\omega$ and $\xi^\mu = a^\mu$ satisfies the requirement (3.34) and the condition $a^\mu(\rho = 0) = 0$ if [90]:

$$\begin{aligned} \partial_\rho a^\mu &= \frac{1}{2} g^{(0)\mu\nu} \partial_\nu \omega \\ a^\mu(\rho, x) &= \frac{1}{2} \int_0^\rho d\tilde{\rho}\; g^{\mu\nu}(\tilde{\rho}, x) \partial_\nu \omega(x) + O(\omega^2) \\ &= \frac{\rho}{2} g^{(0)\mu\nu}(x) \partial_\nu \omega(x) + O(\rho^2) + O(\omega^2). \end{aligned} \tag{3.36}$$

If the embedding function of the causal information surface can be expanded as in (3.18);

$$x^\mu_{bulk}(\rho, \xi_1, \xi_2) = x^\mu_{boundary}(\xi_1, \xi_2) + y^\mu(\xi_1, \xi_2)\rho + ..., \tag{3.37}$$

we can make use of the covariant definition of the causal information surface by applying the coordinate transformation (3.35):

$$\tilde{x}^\mu_{bulk} + \frac{\tilde{\rho}}{2} g^{(0)\mu\nu} \partial_\nu \omega + ... = x^\mu_{boundary} + y^\mu \tilde{\rho}\,(1 - 2\omega) + ... \tag{3.38}$$

Collecting powers of $\tilde{\rho}$ we conclude that $y$ transforms in the following way:

$$\begin{aligned} \tilde{y}^\mu &= y^\mu - 2\omega y^\mu - \frac{1}{2} g^{(0)\mu\nu}(x)\partial_\nu \omega(x) + ... \\ \Rightarrow \tilde{y}^\mu &= e^{-2\omega}\left(y^\mu - \frac{1}{2} g^{(0)\mu\nu}\partial_\nu \omega\right). \end{aligned} \tag{3.39}$$

The normal components $\lambda_a = N_a^\mu y^\nu g^{(0)}_{\mu\nu}$ of $y$ transform as:

$$\tilde{\lambda}_a = e^{-\omega}\left(\lambda_a - \frac{1}{2} N_a \cdot \partial\omega\right). \tag{3.40}$$

The coefficients in the logarithmically diverging terms (3.20) and (3.29) are invariant under such a transformation, given that the other boundary quantities are subject to a conformal transformation. Taking a different cut off does not change these coefficients.

This shows that for *any* covariantly defined bulk surface with $d = 4$ boundary dimensions, the coefficient of the logarithmically divergent term is universal, as we expect from field theory intuition. It would be interesting to ask if there are any additional covariantly defined bulk surfaces associated to a region, since they would define new conformal invariants.

In $(d = 4)$ boundary dimensions (3.40) can be solved by $\lambda_a = -\frac{K^a}{4}$, where $K^a$ is the trace of the extrinsic curvature for the normal vector $N_a$. This corresponds to the result that is obtained by extremizing (3.20) with respect to $y$. The remarkable thing about the causal information surface is that the logarithmically divergent term cannot be constructed from just local geometric quantities as can be seen in the case of the strip.

Finally, it should be pointed out that one can use freedom to re-parametrize $\partial\mathcal{A}$ to gauge out the tangential part of $y$ [89]. In fact, we already partially fixed the freedom to re-parametrize the causal information surface $\Xi_\mathcal{A}$ by choosing one of the parameters to be $z$ (or equivalently $\rho$).

**State dependence** In expansion (3.33), the $g^{(n)}_{\mu\nu}(x)$ with $0 < n < d$ are fully determined in terms of $g^{(0)}_{\mu\nu}(x)$ [24,25]. Terms of order $O(\rho^{\frac{d}{2}})$ do not contribute to the logarithmically diverging term. The coefficient of the logarithmically diverging term is thus state independent since the $g^{(n)}_{\mu\nu}(x)$ with $0 < n < d$ do not depend on the state. In the case of a $(d = 4)$ dimensional boundary only $g^{(0)}_{\mu\nu}(x)$ and $g^{(2)}_{\mu\nu}(x)$ in expansion (3.33) are relevant for the coefficient of the logarithmically divergent term. The term $g^{(2)}_{\mu\nu}(x)$ is determined by the conformal structure of asymptotically

AdS-spacetime:

$$g^{(2)}_{\mu\nu}(x) = -\frac{1}{d-2}\left(R^{(0)}_{\mu\nu} - \frac{R^{(0)}g^{(0)}_{\mu\nu}}{2(d-1)}\right). \tag{3.41}$$

## 3.6 Dual CFT quantity

The motivation for considering the causal information surface was that it is a second covariantly defined co-dimension two surface that can be associated to spacelike co-dimension one boundary regions. The other natural co-dimension two surface that can be constructed given a spacelike co-dimension one boundary surface is the extremal surface that ends on $\partial\mathcal{A}$, whose area in Planck units is believed to be equal to the boundary entanglement entropy for the region $\mathcal{A}$. The question is hence: what is the boundary dual quantity of the causal holographic information?

Several boundary quantities have been proposed. In this section, we will discuss the current status of these proposals. In [4] it was proposed that causal holographic information of some region $\mathcal{A}$ is the entanglement of some coarse grained density matrix.

A candidate boundary dual quantity of causal holographic information of $\mathcal{A}$ should satisfy that:

1. it depends only on $\partial\mathcal{A}$ [69]
2. it violates strong subadditivity in certain cases [69]
3. it can violate $\chi_{\mathcal{A}} = \mathcal{A}^c$, even in pure states [69]
4. $\chi_{\mathcal{A}} \geq S_{\mathcal{A}}$
5. it should be teleological [86], that is, in certain cases it should be sensitive to changes to the state in the future of $\mathcal{A}$
6. the "mutual causal information" $\chi_{\mathcal{A}} + \chi_{\mathcal{B}} - \chi_{\mathcal{A}\cup\mathcal{B}}$ vanishes for spacelike separated $\mathcal{A}$ and $\mathcal{B}$ with $\mathcal{A}\cap\mathcal{B} = \emptyset$ [87]. In other words, causal holographic information satisfies additivity for non-overlapping spacelike separated $\mathcal{A}$ and $\mathcal{B}$
7. it satisfies subadditivity $\chi_{\mathcal{A}\cup\mathcal{B}} \leq \chi_{\mathcal{A}} + \chi_{\mathcal{B}}$ for $\mathcal{A}\cap\mathcal{B} \neq \emptyset$ [87].

We speculated about possible dual quantities in [4], discussing possible ways to construct a coarse grained density matrix. Below, we will discuss these proposals and their current status. Subsequently we will discuss a proposal by Kelly and Wall [91], which is at the moment of writing still uncontested.

### 3.6.1 Entanglement and Wilson loops

In non-Abelian gauge theories, there is more than one natural way to associate a spatial region $\mathcal{A}$ with a part of the whole Hilbert space. Non-Abelian gauge theories have non-local degrees of freedom associated to Wilson loops. In the case of an Abelian gauge field, large Wilson loops are equivalent to integrals of local operators, so we do not need to consider them separately. For non-Abelian theories, however, a large Wilson loop cannot be rewritten as a product of local, gauge-invariant operators.[7]

Because the gauge-invariant degrees of freedom include non-local operators, we have to decide what to do with these non-local excitations when we define the Hilbert space associated with a subregion $\mathcal{A}$. One natural choice, the bigger definition of $\mathcal{H}^B_{\mathcal{A}}$, is to include in $\mathcal{H}^B_{\mathcal{A}}$ open Wilson loops that end on $\partial\mathcal{A}$. With this definition, the full Hilbert space is a subset of $\mathcal{H}^B_{\mathcal{A}} \otimes \mathcal{H}^B_{\mathcal{A}^c}$, because both subsets allow open Wilson loops that end on $\partial\mathcal{A}$, while in the full Hilbert space these loops must be tied together into a closed Wilson loop. An excellent discussion of these subtleties in the context of lattice gauge theory is given by Donnelly [93]. To describe this definition more precisely, $\mathcal{H}^B_{\mathcal{A}}$ is defined by all gauge field configurations in $\mathcal{A}$ modulo gauge transformations that are trivial on $\partial\mathcal{A}$.

One could also make a different choice for how to treat Wilson loops that do not fit inside $\mathcal{A}$. The simplest possibility is not to allow Wilson loops to end on $\partial\mathcal{A}$; in other words, $\mathcal{H}^S_{\mathcal{A}}$ is defined to be gauge field configurations in $\mathcal{A}$ modulo all gauge transformations, with no requirement that the gauge transformations should act trivially on $\partial\mathcal{A}$. With this definition, the full Hilbert space of the theory is not contained in $\mathcal{H}^S_{\mathcal{A}} \otimes \mathcal{H}^S_{\mathcal{A}^c}$; the full Hilbert space also contains extra degrees of freedom associated to Wilson loops that do not fit in either side.

Since we are already thinking about what to do with large Wilson loops, there is another category of Wilson loops that could also be excluded from the Hilbert space associated with a region. These are Wilson loops that fit in $\mathcal{A}$, but cannot in principle be measured within the causal diamond associated with $\mathcal{A}$. In other words, these are loops with the property that no point within the causal diamond contains the loop in its backward lightcone. For spherical surfaces there are no such loops, but in general there are; for example, the strip contains long Wilson loops that are not in the backward lightcone of a single observer.

To summarize the above discussion, in non-Abelian gauge theories, there are sev-

[7] In conformal field theories, products of operators inserted at different points can be replaced by their OPE. Similarly one can attempt to construct OPE's for Wilson loops as in [92]. However, an OPE does not converge if other operators are inserted within its radius of convergence, so in general Wilson loops cannot be replaced by local operators.

eral simple candidates for how to associate a spatial region to a sub factor of the Hilbert space. Each of these definitions has an associated density matrix and entanglement entropy that may violate strong subadditivity or other properties a Von Neumann entropy would have. More generally, even in holographic dualities that do not involve gauge fields, the field theory always has non-local operators that encode what is happening in the bulk far from the boundary. The presence of these non-local operators will lead to ambiguity in defining the density matrix of a spatial region.

There are good reasons to believe that the above definitions of the "small" Hilbert space associated to a region are still not consistent with the geometric definition of $\chi$. For example, the "teleological" behavior of $\chi$ and the vanishing of the "mutual causal information" cannot be explained. Suppose we start with the vacuum state and add a source to the future of the surface $\mathcal{A}$ but inside the associated causal diamond. By construction, the source only changes the state inside its future lightcone, so it does not affect the state on $\mathcal{A}$. As long as the Hilbert space $\mathcal{H}^S_{\mathcal{A}}$ is defined in a state-independent way, as it is in all of the suggestions above, then the entanglement entropy of $\mathcal{A}$ must be independent of the source, because by construction it does not affect the density matrix on $\mathcal{A}$. But one can see from the bulk definition that such a source does in general change the area $\chi$.

Another argument against these proposals involving Wilson loops is that Wilson loops are associated to string world sheets in the bulk that reach outside the causal wedge $\blacklozenge_{\mathcal{A}}$. To be more precise, for some Wilson loops in a subregion $\mathcal{A}$, or in the causal development $\Diamond_{\mathcal{A}}$, the corresponding bulk world sheets reach further into the bulk than the causal information surface. As a consequence, these Wilson loops are sensitive to perturbations of the bulk metric outside the causal wedge $\blacklozenge_{\mathcal{A}}$, whereas causal holographic information is not sensitive to these kind of perturbations; this is an inconsistency.

### 3.6.2 Linear coarse-graining

Roughly, what we want to do is to do a coarse-graining where we identify states that cannot be distinguished by correlators of local, gauge-invariant operators. One method to do a coarse-graining is a linear transformation $\rho \to \tilde{\rho}$. Causal holographic information would then be the Von Neumann entropy of $\tilde{\rho}$. Linear maps $\rho \to \tilde{\rho}$ that are trace-preserving and completely positive can be written as [39]:

$$\tilde{\rho} = \sum_i M_i \rho M_i^\dagger, \tag{3.42}$$

where the $M_i$ satisfy $\sum_i M_i^\dagger M_i = \mathcal{I}$. One interesting case is a complete set of projection operators $\mathbb{P}_i$ that add up to the identity:

$$\sum_i \mathbb{P}_i = \mathcal{I}, \tag{3.43}$$

and given the full density matrix $\rho$, a density matrix $\tilde{\rho}$ can be defined by

$$\tilde{\rho} = \sum_i \mathbb{P}_i \rho \mathbb{P}_i. \tag{3.44}$$

This procedure ensures that the Von Neumann entropy of $\tilde{\rho}$ is greater than the Von Neumann entropy of $\rho$ [39], and this fits with the observation that the area of the causal information surface always has greater area than the extremal surface.

A second interesting implementation of a linear map (3.42), which we do not use here, is to consider a set of unitary operators:

$$\tilde{\rho} = \frac{1}{n} \sum_i^n U_i \rho U_i^\dagger. \tag{3.45}$$

This ensures that $S(\tilde{\rho}) \geq S(\rho)$ by concavity of Von Neumann entropy [39].

**Proposal for simple causal diamonds.** Suppose the boundary region $\mathcal{A}$ corresponds to a simple causal diamond, defined by one future caustic and one past caustic. Then there is a natural choice for the projection. Typically one can think of the projectors that project onto the eigenspaces of a particular hermitian operator. Since we want an operator associated to the causal development of the region $\mathcal{A}$, and we do not want it to depend on details of the theory, a natural choice is the time evolution operator $U$ that evolves the state from the "bottom" to the "top" of the causal diamond. The evolution operator $U$ is unitary, so it can be written as the exponential of a Hermitian operator $A$, $U = \exp(iA)$. The eigenvectors of $A$ naturally pick out a set of projection operators that can be used in the above construction (3.44).

There is one more encouraging observation that this construction may be on the right track, in addition to the above observation that the coarse-grained entanglement entropy is larger. In [69] it is analyzed in which cases the entanglement entropy and the causal holographic information coincide ($\chi = S$). The two quantities agree whenever the reduced density matrix is thermal. In this special case, the density matrix is already diagonal in the basis picked out by the Hamiltonian, so the coarse-graining (3.44) has no effect.[8]

[8] A subtlety is that the evolution from the bottom to the top requires $t \to \infty$.

**More complicated regions.** The simplest boundary causal diamond is one with just one future caustic and one past caustic, so that in flat space, $\partial\mathcal{A}$ is a sphere. However, for most choices of $\mathcal{A}$, the boundary region will be such that both $\mathcal{C}^+$ and $\mathcal{C}^-$ contain more than one-point. In this case, there is another natural procedure for throwing away non-local information. Starting from the full density matrix $\rho_{\mathcal{A}}$, define $\tilde{\rho}_{\mathcal{A}}$ to be the maximum entropy density matrix that correctly reproduces the measurements contained in *any* causal diamond contained within the boundary region.

This procedure is motivated by considering which bulk region should be described. It has the advantage that it defines a $\tilde{\rho}$ that agrees with another observation about $\chi$. Suppose $A$ and $B$ are two spacelike patches on a Cauchy-surface on the boundary and $A \cap B = 0$, then $\chi_A + \chi_B - \chi_{A\cup B} = 0$. This can be arranged iff the causal mutual information vanishes: $\tilde{\rho}_{A\cup B} = \tilde{\rho}_A \otimes \tilde{\rho}_B$. In this special case, one can show that the above procedure indeed leads to a density matrix that is a product.

An argument by Don Marolf [91] compromises the construction above, even for simple causal diamonds. The argument that the projection (3.44) removes off-diagonal elements in the density matrix with respect to the basis of projection operators and effectively takes a time average of the state:

$$\begin{aligned}\tilde{\rho} &= \sum_i P_i \rho P_i \\ &= \lim_{T\to\infty} \int_{-\frac{T}{2}}^{\frac{T}{2}} dt\ \rho(t),\end{aligned} \tag{3.46}$$

where $e^{-iHt}$ is the evolution operator in the boundary causal diamond $\Diamond_{\mathcal{A}}$. Now one could consider some matter, a particle, passing through "tip" of the original bulk causal wedge $\blacklozenge_{\mathcal{A}}$. The presence of bulk matter would cause null rays to focus, which changes the causal wedge. Due to the second law of horizons, the causal information will be smaller than its late time value. But the fact that the near boundary part of $\blacklozenge_{\mathcal{A}}$ is unchanged suggests that the state describing the corresponding boundary regions (bottom and top of the boundary causal diamond) is unchanged. The early and late time values of $\rho$ dominate (3.46), in contradiction to the fact that the causal holographic information *does* change. This argument suggests that this proposal can not be correct.

### 3.6.3 One-point entropy

Kelly and Wall [91] propose a different coarse-graining method, which we will explain below. This coarse-graining method makes use of a subset of operators, for

which there are several candidates. In this subsection we will discuss several subsets of operators that can be used with this coarse-graining method. A particular subset gives rise to the *one-point entropy*, which is proposed to be the boundary dual quantity for causal holographic information [91].

The coarse-graining method considered by Kelly and Wall [91] is the map $\rho \to \tilde{\rho}$ defined by:

$$\mathscr{S}_{\mathcal{A}}(\rho_{\mathcal{A}}) = \sup_{\tau_{\mathcal{A}} \in T_{\mathcal{A}}} [S_{\mathcal{A}}(\tau_{\mathcal{A}})] \tag{3.47}$$

where $\rho_{\mathcal{A}}$ is the reduced density matrix associated with $\mathcal{A}$, $S_{\mathcal{A}}(\tau_{\mathcal{A}})$ is the von Neumann entropy of $\tau_{\mathcal{A}}$, and $T_{\mathcal{A}}(\rho_{\mathcal{A}})$ is the set of all density matrices $\tau_{\mathcal{A}}$ which satisfy the constraints

$$\mathrm{Tr}\{\mathcal{O}_m \, \tau_{\mathcal{A}}] = \mathrm{Tr}[\mathcal{O}_m \rho_{\mathcal{A}}\} \tag{3.48}$$

for a set of operators $\{\mathcal{O}_m\}$.

It can be shown that $\tilde{\rho}$ defined by (3.47) is of the form

$$\tilde{\rho} = \frac{e^{-\sum_m \lambda_m \mathcal{O}_m}}{Z}, \tag{3.49}$$

where the $\lambda_m$ are the Lagrange multipliers of the constraint extremization [94].

**$\chi$-preserving coarse-grainings** Suppose there is a coarse-graining $\rho \to \tilde{\rho}$ such that

$$\chi_{\mathcal{A}} = S_{\tilde{\rho}\mathcal{A}}. \tag{3.50}$$

Further suppose that two density matrices $\rho_1, \rho_2$, that correspond to semi-classical bulk dual geometries, are mapped to the *same* coarse grained density matrix $\tilde{\rho}$. If $\mathscr{S}$ is dual to $\chi$, then we must have

$$\chi_{\rho_1} = \chi_{\rho_2} \tag{3.51}$$

for all such $\rho_1, \rho_2$. *Any* coarse-graining which maps any two density matrices $\rho_{1,2}$ to the same coarse-grained $\tilde{\rho}$, that also satisfies (3.51), is called $\chi$-preserving.

In principle, there could be more than one $\chi$-preserving coarse-graining. In [91] it is argued that $\chi$ must correspond to the "strongest" $\chi$-preserving coarse-graining. For details, see [91]. Note that in [91] it *is* assumed that the coarse-graining that corresponds to causal holographic information maps states with a semi-classical bulk dual geometry to states with a semi-classical bulk dual geometry.

For a coarse-graining associated to a boundary subregion $\mathcal{A}$, there are several natural options for the set of constraint operators $\{\mathcal{O}_m\}$ [91], which we will discuss below:

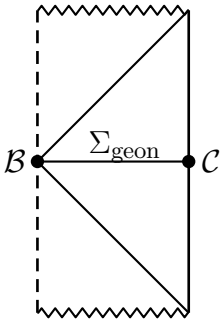


***Figure 3.9:*** *Penrose diagram of the geon-geometry. (Source: [91])*

1. The set of Wilson loops that can be measured in the causal diamond $\Diamond_{\mathcal{A}}$
2. The set of one-point functions, or local operators in $\mathcal{A}$
3. The set of one and two-point functions in $\mathcal{A}$
4. The set of one and two-point functions in $\mathcal{A}$ that can be measured within $\Diamond_{\mathcal{A}}$

**Wilson loops in $\mathcal{A}$** The set of Wilson loops that can be measured within the causal diamond $\Diamond_{\mathcal{A}}$ is not the most likely candidate, because Wilson loop operators correspond to minimal surfaces in the bulk that reach beyond the causal wedge.

**Two point functions in $\mathcal{A}$** In [91], it is argued that any set that includes two-point functions is also unlikely to correspond to causal holographic information. The so called *geon* geometry [95] is a central example in this argument. The geon-geometry is a modified AdS-Schwarzschild geometry, where the spacetime is cut in half and opposite points on the bifurcation two sphere are identified (see figure 3.9). Outside the horizon, the spacetime is isometric to the original AdS-Schwarzschild geometry. In [91] it is argued that the calculation of CFT two-point functions would yield different answers for these two geometries due to non-contractible Witten diagrams that wrap around the nontrivial topology of the geon-geometry. So if two-point functions would be in the set of constraints (3.48), then these two geometries would generically yield different $\mathscr{S}_{\mathcal{A}}$, whereas the $\chi_{\mathcal{A}}$ are equal. A similar argument is made for the set of one and two-point functions in $\mathcal{A}$ that can be measured within $\Diamond_{\mathcal{A}}$ [91].

**One point functions** The one-point entropy is the coarse grained entropy, with the set of one-point functions of all all gauge-invariant, local CFT operators with support on $\Diamond_{\mathcal{A}}$ as constraints (3.48).

In [91] it is argued that this is the "strongest" $4\chi$-preserving coarse-graining candidate. An important property of the one-point entropy is that it is equal to the entanglement entropy of a thermal state. To be more precise, when $\rho \propto e^{-\beta H}$ where $H$ is (the integral of) a local operator, the one-point entropy and the usual entanglement entropy are equal. The argument goes as follows: if $H$ is local, then $H \in \{\mathcal{O}_m\}$. The coarse grained density matrix $\tilde{\rho}$ must hence satisfy

$$\mathrm{Tr}\{H\tilde{\rho}\} = \mathrm{Tr}\{H\rho\}. \tag{3.52}$$

The original density matrix $\rho$ trivially solves (3.52) for all operators in $\{\mathcal{O}_m\}$. Since there are other constraints from other operators in $\{\mathcal{O}_m\}$, we must have

$$\mathscr{S}^{(1)}_{\mathcal{A}} \leq S_{\mathcal{A}}. \tag{3.53}$$

But we also have $\mathscr{S}^{(1)}_{\mathcal{A}} \geq S_{\mathcal{A}}$ by the extremality condition in the definition. Hence we conclude $\mathscr{S}^{(1)}_{\mathcal{A}} = S_{\mathcal{A}}$ and $\rho_{\mathcal{A}} = \tilde{\rho}_{\mathcal{A}}$. This observation corresponds with known examples where the holographic entanglement entropy is equal to the causal holographic information [69].

At the moment of writing, there is no definitive counter argument against the proposal (3.48).[9]

## 3.7 Summary & Outlook

In this chapter, we discussed causal holographic information. Causal holographic information is the area of a co-dimension two bulk surface associated to a boundary subregion. It has similarities with entanglement entropy, but there are also differences. Generally, it is larger than or equal to the entanglement entropy of a boundary subregion.

A boundary quantity dual to causal holographic information, which is defined in the bulk, is not identified yet, although several proposals have been made. All these proposals associate causal holographic information to the Von Neumann entropy of a coarse grained density matrix. The proposed "one-point entropy" is a particularly promising candidate.

[9] The one-point entropy cannot be equal to causal holographic information in case of boundary sources [91].

As a bulk probe, causal holographic information serves better than entanglement entropy and Wilson loops, at least for $d = 2$. For a higher number of dimensions, there is evidence for this statement as well.

Recently, the usefulness of causal holographic information has been discussed in the context of certain states that *are* pure, but are locally isometric to the geometry of a mixed state. To be more precise, one can think of geometries that correspond to a pure boundary state, that collapse into a black hole. Another example is the geon-geometry, discussed in section (3.6), which is isometric to AdS-Schwarzschild, but is topology different and corresponds to a pure boundary state. In [96] it is argued that a law similar to the first law of entanglement entropy (1.62) is valid for the one-point entropy, in certain cases.

If the one-point entropy proposal is correct, then the coarse-grained density matrix associated to causal holographic information would have a local modular Hamiltonian. It would be interesting to investigate whether it is possible to reconstruct the bulk gravitational equations using the dynamics of causal holographic information.

## 3.A Proof of formula for constant time slice

In this appendix we will derive the near boundary expansion of the embedding function of the causal information surface (3.4) for an entanglement surface $\partial\Sigma$ that lies on a constant time slice on a flat boundary, using a pure AdS bulk metric:

$$ds^2 = \frac{dz^2}{z^2} + \frac{1}{z^2}\eta_{\mu\nu}dx^\mu dx^\nu \tag{3.54}$$

For the boundary coordinates we will use the following notations interchangeably:

$$x^\mu = (t, \vec{x}). \tag{3.55}$$

For any point $x^\mu(\xi_1, \xi_2)$ on $\partial\Sigma$ there is a unique point on top- and on the bottom of the causal diamond, $x_\wedge(\xi)$ on $\mathcal{C}^+$ and $x_\vee(\xi)$ on $\mathcal{C}^-$ respectively. These points are separated from the base point $x^\mu(\xi)$ by boundary null geodesics that are normal to $\partial\Sigma$ in $x^\mu(\xi)$. The causal diamond $\Diamond_\Sigma$ is symmetric in the $t = 0$ plane, so if the future caustic $x_\wedge(\xi)$ is in the $t = \tau$ plane, the past caustic $x_\vee(\xi)$ is on the $t = -\tau$ plane. Since $\hat{t}$ is normal to $\partial\Sigma$, we can take the second normal vector $\hat{n}(\xi)$ to be in the $t = 0$ plane. This allows us to express $x^\mu_\wedge(\xi)$ in terms of $\hat{n}(\xi)$ and $\tau(\xi)$,

$$\begin{aligned} x^\mu_\wedge(\xi) &= \big(x^0_\wedge(\xi), \vec{x}_\wedge(\xi)\big) \\ &= (\tau(\xi), \vec{x}_{\partial\Sigma}(\xi) + \tau(\xi)\hat{n}(\xi)) \\ \vec{x}_\wedge(\xi) &= \vec{x}_{\partial\Sigma}(\xi) + \tau(\xi)\hat{n}(\xi), \end{aligned} \tag{3.56}$$

where $\hat{n}(\xi)$ is the unit normal vector in the $(t=0)$-plane and $\tau(\xi)$ depends (in general non-locally) on the geometry of $\partial\Sigma$. From now on we will not explicitly write that these are functions of $\xi$.

We parametrize the embedding function $x^M = (z, x^\mu_{bulk})$ of the causal information surface (3.4) with $z$ and $\xi^\alpha$ ($\alpha = 1, 2$). Given a point $x^M = (z, x^\mu_{bulk})$ on the causal information surface we would like to identify the point(s) $\vec{x}(\xi)$ on $\partial\Sigma$ such that a past directed bulk lightray emanating from $x^\mu_\wedge(\xi)$ and a future directed bulk lightray $x^\mu_\vee(\xi)$ intersect at $x^M = (z, x^\mu_{bulk})$. For small $z$, $x^\mu_{bulk}$ and a particular $x^\mu(\xi)$ are close together ($O(z^2)$). Since the causal information surface consists of points that are as far into the bulk as possible while still being intersected by at least one null ray emanating from $\mathcal{C}^+$ and $\mathcal{C}^-$. The point $\vec{x}(\xi)$ that generates the caustics (3.56) from which the bulk point $x^M = (z, x^\mu_{bulk})$ can be reached by null rays should be such that the distance between $x^\mu_{bulk}$ and $x^\mu_\wedge(\xi)$ is minimal. The set of future caustics $\mathcal{C}^+$ is piecewise smooth and we construct the normal plane for a point $x^\mu_\wedge(\xi)$ in $\mathcal{C}^+$. The point $\vec{x}(\xi)$ should be such that:

- $x^\mu_{bulk}$ lies in the intersection of the normal plane of $x^\mu_\wedge(\xi)$ and the $t = 0$ plane
- $|x_{bulk} - x_\wedge(\xi)|^2 = -z^2$.

One can construct two tangent vectors in $x_\wedge(\xi)$ (or $x_\vee(\xi)$) by taking derivatives with respect to the parameters $\xi^\alpha, \alpha = 1, 2$,

$$\begin{aligned} S^\mu_{\alpha\wedge} &= \partial_\alpha x^\mu_\wedge \\ &= (S^0_{\alpha\wedge}, \vec{S}_{\alpha\wedge}) \\ &= (\partial_\alpha\tau, \partial_\alpha\vec{x}_\wedge) \\ \vec{S}_{\alpha\wedge} &= \partial_\alpha\vec{x}_\wedge \\ &= \partial_\alpha\vec{x}_{\partial\Sigma} + (\partial_\alpha\tau)\hat{n} + \tau\partial_\alpha\hat{n} \\ &= \vec{T}_\alpha + (\partial_\alpha\tau)\hat{n} + \tau\partial_\alpha\hat{n} \end{aligned} \tag{3.57}$$

where $\vec{T}_\alpha = \partial_\alpha\vec{x}_{\partial\Sigma}$. One can construct $S_{\alpha\vee}$ similarly.

The space orthogonal to the tangent space $span\{S^\mu_{\alpha\wedge}\}$ in $x_\wedge \in \mathcal{C}^+$ is (in the most general case) two-dimensional and contains $(1, \hat{n})$. It is spanned by $(1, \hat{n})$ and by a second linearly independent vector. We construct such a vector $V^\mu_\wedge$ by demanding $V_\wedge \cdot S_{\alpha\wedge} = 0$ for $\alpha = 1, 2$.

$$\begin{aligned} V^\mu_\wedge &= (1, b^\alpha) \quad \text{(Ansatz)} \\ V_\wedge \cdot S_{\alpha\wedge} &= 0 \\ &= -\partial_\alpha\tau + b^\beta\vec{T}_\beta\vec{T}_\alpha + \tau b^\beta\vec{T}_\beta \cdot \partial_\alpha\hat{n} \\ &= -\partial_\alpha\tau + b^\beta\tilde{g}_{\beta\alpha} + \tau b^\beta K_{\alpha\beta} \end{aligned} \tag{3.58}$$

where $\tilde{g}_{\alpha\beta} = \vec{T}_\alpha \cdot \vec{T}_\beta$ is the induced metric on $\partial\Sigma$.

Equation (3.58) is solved by

$$b_\alpha = \frac{(\partial_\alpha \tau)(1+\tau K) - \tau K^\beta_\alpha (\partial_\beta \tau)}{1 + \tau K + \frac{\tau^2}{2}(K^2 - K_{\gamma\delta}K^{\gamma\delta})}. \tag{3.59}$$

Intersecting the $t = 0$ plane with the surface spanned by $(1, \hat{n}(\xi))$ and $V(\xi)$ identifies the point $\vec{x}(\xi)$ together with the condition that $|x_{bulk} - x_\wedge(\xi)|^2 = -z^2$.

$$\begin{aligned} x^\mu_{bulk} &= x^\mu_{\partial\Sigma} + a(0, \hat{n} - b^\alpha \vec{T}_\alpha)^\mu \\ x^\mu_\wedge &= x^\mu_{\partial\Sigma} + \tau(1, \hat{n})^\mu \\ |x^\mu_{bulk} - x^\mu_\wedge|^2 &= -z^2 \\ &= -\tau^2 + (a-\tau)^2 + b^\alpha b^\beta \tilde{g}_{\alpha\beta} \\ &= a^2(1+b^2) - 2a\tau. \end{aligned} \tag{3.60}$$

Solving for $a$ gives:

$$\begin{aligned} a &= \frac{\tau}{1+b^2} \pm \frac{\tau}{1+b^2}\sqrt{1 - \frac{z^2(1+b^2)}{\tau^2}} \\ &= \frac{z^2}{2\tau} + O(z^4) \quad \text{(Taking the minus solution).} \end{aligned} \tag{3.61}$$

Giving the near boundary expansion of the embedding function of the causal information surface:

$$\vec{x}_{bulk}(\xi, z) = \vec{x}_{\partial\Sigma}(\xi) + \frac{z^2}{2\tau(\xi)}\hat{n}(\xi) - \frac{z^2}{2\tau(\xi)} b^\alpha \vec{T}_\alpha(\xi) + O(z^4). \tag{3.62}$$

## 3.B Proof of the formula for a flat boundary

Allowing the entanglement surface $\partial\Sigma$ to be a general spacelike surface in the Minkowski background and a pure AdS dual removes the mirror symmetry of the causal diamond in the $t = 0$ plane we used in Appendix 3.A. Given a point $(z, x^\mu_{bulk})$ on the causal information surface, the past and future caustics from which the bulk null geodesics intersect at $(z, x^\mu_{bulk})$ might be related to different points on $\partial\Sigma$.

Now we have to find two-points $x^\mu_t = x^\mu(\xi^\alpha)$ and $x^\mu_b = x^\mu(\xi^\alpha + \Delta^\alpha)$ on $\partial\Sigma$ such that:

- $x^\mu_{bulk}$ lies in the plane through $x^\mu_\wedge(\xi)$ orthogonal to $\mathcal{C}^+$

- $x^\mu_{bulk}$ lies in the plane through $x^\mu_\vee(\xi+\Delta)$ orthogonal to $\mathcal{C}^-$
- $|x_{bulk} - x_\wedge(\xi)|^2 = -z^2$
- $|x_{bulk} - x_\vee(\xi+\Delta)|^2 = -z^2$,

using the definition (3.23).

From now we will interchangeably use the subscript $t$ for quantities that are evaluated at $\xi$ and the subscript $b$ for quantities that are evaluated at $\xi+\Delta$. So (3.23) can also be written as:

$$\begin{aligned} x^\mu_\wedge &= x^\mu_t + \lambda_{\uparrow t} N^\mu_{\uparrow t} \\ x^\mu_\vee &= x^\mu_b + \lambda_{\downarrow b} N^\mu_{\downarrow b}. \end{aligned} \tag{3.63}$$

In both $x_t$ and $x_b$ the two null normal vectors together with the two tangent vectors $T^\mu_\alpha = \partial_\alpha x^\mu$ constitute a basis and we can express $x^\mu_{bulk}$ in terms of these vectors:

$$\begin{aligned} x^\mu_{bulk} &= x^\mu_t + \alpha_{\uparrow t} N^\mu_{\uparrow t} + \alpha_{\downarrow t} N^\mu_{\downarrow t} + \alpha_{\downarrow t} b^\alpha_t T^\mu_{\alpha t} \\ &= x^\mu_b + \alpha_{\uparrow b} N^\mu_{\uparrow b} + \alpha_{\downarrow b} N^\mu_{\downarrow b} + \alpha_{\uparrow b} b^\alpha_b T^\mu_{\alpha b}, \end{aligned} \tag{3.64}$$

where $\alpha_{\uparrow t}$, $\alpha_{\uparrow b}$, $\alpha_{\downarrow t}$, $\alpha_{\downarrow b}$, $b^\alpha_t$ and $b^\alpha_b$ have to be determined by imposing the conditions listed above.

Imposing the condition that $x^\mu_{bulk}$ lies in the plane through $x^\mu_\wedge(\xi)$ orthogonal to $\mathcal{C}^+$ is equivalent to extremizing $|x_{bulk} - x_\wedge|$ by varying $x_t$:

$$\begin{aligned} 0 &= \partial_\alpha |x_{bulk} - x_\wedge|^2 \\ &= \partial_\alpha |x_{bulk} - x_t - \lambda_{\uparrow t} N_{\uparrow t}|^2 \\ &\Rightarrow (x^\mu_{bulk} - x^\mu_t)\eta_{\mu\nu}(T^\nu_{\alpha t} - \lambda_{\uparrow t}\partial_\alpha N^\nu_{\uparrow t} - (\partial_\alpha \lambda_{\uparrow t}) N^\mu_{\alpha t}). \end{aligned} \tag{3.65}$$

Similar for $|x_{bulk} - x_\vee|$.

Now using the expansion (3.64) we find equations for $b^\alpha_t, \alpha = 1, 2$.

$$0 = -(\partial_\alpha \lambda_{\uparrow t}) + b^\beta_t \tilde{g}_{\alpha\beta} - b^\beta_t K_{\uparrow t \alpha\beta} \lambda_{\uparrow t}, \tag{3.66}$$

where $\tilde{g}_{\alpha\beta} = \partial_\alpha x^\mu_t \partial_\beta x^\nu_t \eta_{\mu\nu}$.

This equation (3.66) (And similarly for $b_{\alpha b}$) is solved by:

$$b_{\alpha t} = \frac{-\left(1 + \lambda_{\uparrow t} K_{\uparrow t}\right)\partial_\alpha \lambda_{\uparrow t} - K^\beta_{\uparrow t\alpha}\partial_\beta \lambda_{\uparrow t}}{\left(1 + \lambda_{\uparrow t} K_{\uparrow t} + \frac{\lambda_{\uparrow t}\lambda_{\uparrow t}}{2}\left(K^2_{\uparrow t} - K_{\uparrow t\gamma\delta} K^{\gamma\delta}_{\uparrow t}\right)\right)}. \tag{3.67}$$

Another condition can be obtained by demanding:

$$\begin{aligned} |x_{bulk} - x_\wedge|^2 &= -z^2 \\ &= 2(\alpha_{\uparrow t} - \lambda_{\uparrow t})\alpha_{\downarrow t} + \alpha_{\downarrow t}^2 b_t^2 \\ &\Rightarrow \alpha_{\downarrow t} = \frac{z^2}{2\lambda_{\uparrow t}} + O(z^4). \end{aligned} \tag{3.68}$$

Similarly for $|x_{bulk} - x_\vee|$ giving a similar solution:

$$\alpha_{\uparrow b} = \frac{z^2}{2\lambda_{\downarrow b}} + O(z^4). \tag{3.69}$$

Now using (3.68) and (3.69) and implicitly using (3.67) we can re-express (3.64):

$$\begin{aligned} x_{bulk}^\mu &= x_t^\mu + \alpha_{\uparrow t} N_{\uparrow t}^\mu + \frac{z^2}{2\lambda_{\uparrow t}} N_{\downarrow t}^\mu + \frac{z^2}{2\lambda_{\uparrow t}} b_t^\alpha T_{\alpha t}^\mu + ... \\ &= x_b^\mu + \frac{z^2}{2\lambda_{\downarrow b}} N_{\uparrow t}^\mu + \alpha_{\downarrow b} N_{\downarrow b}^\mu + \frac{z^2}{2\lambda_{\downarrow b}} b_b^\alpha T_{\alpha b}^\mu. \end{aligned} \tag{3.70}$$

Now we can expand in $\Delta$ using that $\Delta^\alpha \partial_\alpha x^\mu$ is of order $O(z^2)$:

$$\begin{aligned} x_{bulk}^\mu &= x^\mu + \alpha_{\uparrow t} N_\uparrow^\mu + \frac{z^2}{2\lambda_\uparrow} N_\downarrow^\mu + \frac{z^2}{2\lambda_\uparrow} b_t^\alpha T_\alpha^\mu + ... \\ &= x^\mu + \Delta^\alpha \partial_\alpha x^\mu + \frac{z^2}{2\lambda_\downarrow} N_\uparrow^\mu + \alpha_{\downarrow b} N_\downarrow^\mu + \frac{z^2}{2\lambda_\downarrow} b_b^\alpha T_\alpha^\mu + ... \end{aligned} \tag{3.71}$$

We use linear independence to find equation for the coefficients of $T_\alpha^\mu$, $N_\uparrow^\mu$ and $N_\downarrow^\mu$:

$$\begin{aligned} \frac{z^2}{2\lambda_\uparrow} b_t^\alpha &= \Delta^\alpha + \frac{z^2}{2\lambda_\downarrow} b_b^\alpha + O(z^4) \\ \alpha_{\uparrow t} &= \frac{z^2}{2\lambda_\downarrow} + O(z^4) \\ \frac{z^2}{2\lambda_\uparrow} &= \alpha_{\downarrow b} + O(z^4). \end{aligned} \tag{3.72}$$

Now we can expand the embedding function using $x_t = x(\xi)$:

$$x_{bulk}^\mu(z, \xi) = x^\mu(\xi) + \frac{z^2}{2}\left(\frac{N_\uparrow^\mu}{\lambda_\downarrow} + \frac{N_\downarrow^\mu}{\lambda_\uparrow}\right) + \frac{z^2}{2\lambda_\uparrow} b_t^\alpha T_\alpha^\mu + O(z^4). \tag{3.73}$$

And for the relation between we find $x_t$ and $x_b$:

$$\begin{aligned} x_t^\mu &= x^\mu(\xi) \\ x_b^\mu &= x^\mu(\xi + \Delta) \\ &\Rightarrow \Delta^\alpha = \frac{z^2}{2}\left(\frac{b_t^\alpha}{\lambda_\uparrow} - \frac{b_b^\alpha}{\lambda_\downarrow}\right) + O(z^4). \end{aligned} \tag{3.74}$$

# Part II

# Cosmology

# Notes for the reader

## Conventions

| | |
|---|---|
| Planck units | $\hbar = c = 1$ |
| Minkowski metric | $\eta_{\mu\nu}$=diagonal(-1,+1,...,+1) |
| Reduced Planck mass set to one | $8\pi G = 1$ |
| Number of dimensions | 3+1 |

**The de Sitter radius $L_{\mathtt{ds}}$:** in chapter (4) we will consistently write $L_{\rm ds}$ where it is appropriate, since this is an introductory chapter. In chapters (5) and (6) we will also explicitly write $L_{\rm ds}$ except for section (5.2). In section (5.2) quantities with units of length should be considered in units of $L_{\rm ds} = H^{-1}$.

## Published work

This part of the thesis is based on (parts of) our work presented in the following articles:

[1] F.V. Dimitrakopoulos, L. Kabir, B. Mosk, M. Parikh and J.P. van der Schaar
*Vacua and correlators in hyperbolic de Sitter space*
JHEP **1506**, 095 (2015), arXiv:1502.00113 [hep-th].

[3] B. Mosk and J.P. van der Schaar
*Chaotic inflation limits for non-minimal models with a Starobinsky attractor*
JCAP **1412**, 022 (2014), arXiv:1407.4686 [hep-th].

In particular, elements of [1] will be presented in chapter (5). Elements of [3] can be found in chapter (6). Chapter (4) is introductory and does not contain products of our scientific endeavors.

# Chapter 4

# Introduction

In this chapter we present the basic concepts of cosmology necessary to present our work in chapters (5) and (6). In section (4.1) we will give a non-technical introduction into Big Bang cosmology and inflation. In section (4.2) we will introduce the concept of single field inflation, which will provide the framework for this part of the thesis. In section (4.3) we will present de Sitter spacetime, which is relevant for the description of our universe during inflation. We proceed with a more conceptual treatment of quantum field theory in curved spacetime in section (4.4), which forms the basis for chapter (5). Subsequently we give an extremely condensed summary of the derivation of the scalar power spectrum in section (4.5). The detailed derivation of the spectrum is outside the scope of this thesis and section (4.5) will be largely a summary of [97]. In section (4.6) we extract the most important parameters of the spectrum, which characterize models of inflation. These parameters serve an important role in chapter (6).

## 4.1 Cosmology: a brief history of the universe

This part of the thesis is about *inflation*, a period of accelerated expansion thought to have taken place just fractions after the Big Bang. We will briefly give a non-technical description of the Big Bang scenario and motivate the study of models of inflation.

Nowadays, the field of cosmology is dominated by the Big Bang scenario in combination with inflation. The Big Bang scenario emerged in the twentieth century. It was realized by Friedmann that general relativity allows for solutions that cor-

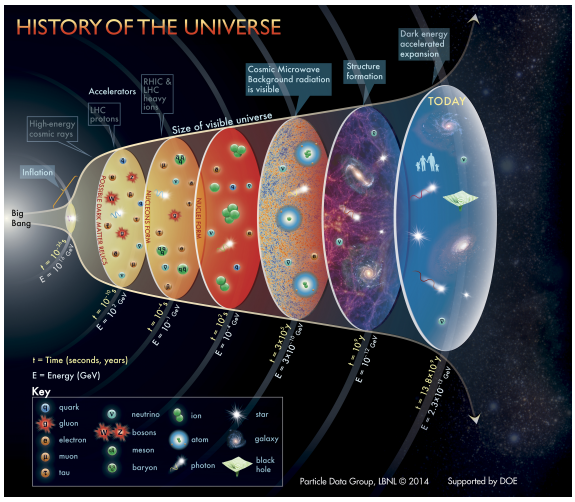


***Figure 4.1:*** *The history of our universe. Source: Particle Data Group.*

respond to an expanding universe. Another important observation was the recession of "spiral nebula" (galaxies), which was incurred from their Doppler shift. Lemaître proposed the idea that this Doppler shift is caused by the expansion of our universe. It was realized that if one winds back the clock and reverses this expansion, the matter in our universe would be extremely compact. The description of such a state with general relativity would yield a singularity, a point in spacetime where geometrical quantities "blow up".

In the course of the twentieth century a lot of evidence was found in support of the Big Bang scenario. For example, Hubble's measurements of galactic redshifts showed that galaxies are drifting apart. Another important observation was the measurement of the cosmic microwave background, which we will address later.

The Big Bang, which is thought to have happened some 13.8 billion years ago, is often referred to as a singularity. However, we do not really know how spacetime behaves under the conditions of extremely high energies and temperatures. As discussed in Part I, general relativity does not provide a good description at distances smaller than the Planck scale, where quantum effects become important.

Although we do not really know what happened during the Big Bang and what caused it, there is a more detailed model of the subsequent epochs. We will briefly describe a selection of events and epochs of the history of our universe, as far as they are relevant for this thesis (see also figure 4.1).[1]

[1] We will *not* discuss topics such as grand unification, dark matter, baryogenesis, electroweak unification, neutrino decoupling, Big Bang nucleosynthesis.

At a time-scale of $10^{-34}s$ after the Big Bang, the universe is thought to have been in a phase of *inflation*; accelerated expansion. In chapter (4) we give some motivation for the concept of inflation. Although there is a lot of evidence for an inflationary epoch, the mechanism behind it is still unclear. Single field inflation models have been very successful in explaining and predicting observations, such as the characteristics of the cosmic microwave background, which is described below.

After the Big Bang our universe was in an extreme high energy state, for which the physics is still poorly understood. Some $10^{-36}$ seconds after the Big Bang the universe enters the period of inflation, a period of accelerated expansion. Quantum fluctuations during the period of inflation are being "blown up" and constitute the seeds for the large scale structure of the universe at later times. The temperature drops dramatically, but at the end of inflation the universe reheats again as a consequence of the potential energy of the inflaton field being transferred to other particles. The universe is initially dominated by radiation, but it becomes matter-dominated as the temperature decreases. Radiation cannot propagate freely in a plasma with unbound electrons, so radiation cannot propagate until the energies are low enough for electrons and protons to form hydrogen. When protons and electrons form hydrogen, the photons *decouple*. This decoupling, some 380.000 years after the Big Bang allows photons to propagate freely, such that the first visible radiation is formed. This radiation is still "visible", but it is highly red-shifted to the microwave part of the spectrum. This cosmic microwave background (see figure 4.2) has an approximately thermal spectrum with $T \sim 2.73K$ and forms the most important footprint of the physics of inflation. It is also affected by post-inflationary physics, such as the baryon-acoustic oscillations. Other information about the early universe can be deduced from the relative abundance of particles, possibly by the measurement of gravitational waves and by observations of the large scale structure of the universe.

This thesis will not discuss topics in astroparticle physics or post-inflationary physics and will be theoretical in nature. In many cases, a simplified model of inflation will be used in order to study the effects of changing some basic assumptions. For example, in chapter (5) we analyze the effects of having a different initial quantum state. These effects can be discussed qualitatively in a simplified setup. The actual imprint on observable quantities is outside the scope of this thesis. In chapter (6) we consider different potentials for the field that describes a mechanism for inflation.

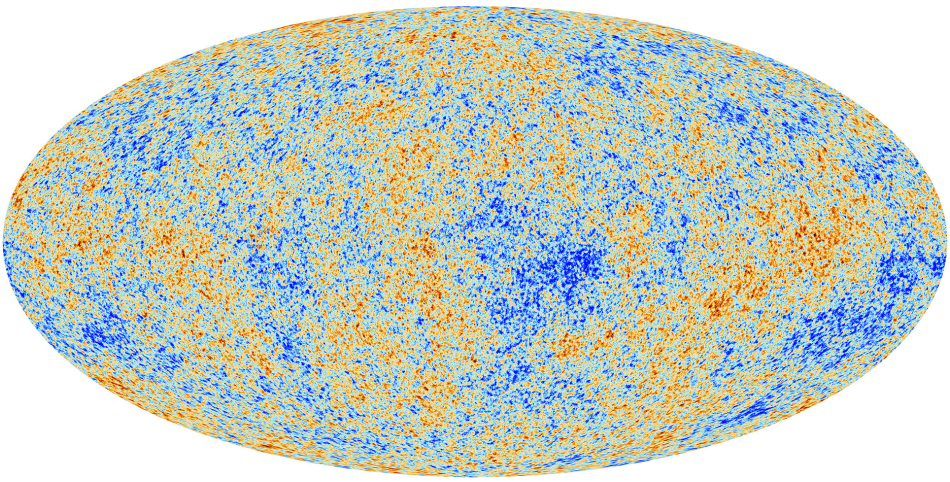

***Figure 4.2:*** *From ESA/Planck: The anisotropies of the Cosmic microwave background (CMB) as observed by Planck. The CMB is a snapshot of the oldest light in our Universe, imprinted on the sky when the Universe was just 380 000 years old. It shows tiny temperature fluctuations that correspond to regions of slightly different densities, representing the seeds of all future structure: the stars and galaxies of today. Source: ESA and the Planck Collaboration (Id 288792).*

## 4.2 Single field inflation

In this section we motivate the concept of inflation and introduce the single field inflation model. We only discuss the classical dynamics of inflation; the description of quantum effects will be postponed until section (4.5).

### 4.2.1 FLRW spacetimes

In order to make a model of the large scale development of the universe, one has to make a series of assumptions. At large scales, the spatial slices of our universe look surprisingly homogeneous in all directions and distances.

**Homogeneity** A manifold $\mathcal{M}$ is called homogeneous if for any $p, q \in \mathcal{M}$ there exists an isometry $f$ such that $f(p) = q$.

**Spatial homogeneity** A spacetime $(\mathcal{M}, g)$ is spatially homogeneous it there exists a group of isometries whose orbits are 3d spacelike surfaces.

A spacetime with spatial homogeneity has a set of preferred observers, called

*comoving observers*, whose velocity is perpendicular to the surfaces of spatial homogeneity. If these surfaces of spatial homogeneity look the same in all directions, then the space is called *isotropic*.

It can be shown that the metric of a spatially homogeneous and isotropic universe must be of the Friedmann Lemaître Robertson Walker (FRW or FLRW) type:

$$ds^2 = -dt^2 + a^2(t)\left(\frac{dr^2}{1-\kappa r^2} + r^2 d\Omega_2^2\right), \tag{4.1}$$

with $\kappa = 0, \pm 1$, corresponding to a flat, open or closed universe:

$$\kappa = \begin{cases} -1 & \text{open universe} \\ 0 & \text{flat universe} \\ 1 & \text{closed universe} \end{cases}. \tag{4.2}$$

Coordinates $r, \Omega$ are called *comoving coordinates*. Physical distances are obtained by multiplying the distance in comoving coordinates with the scale factor $a$. The physical velocity between two observers fixed at comoving coordinates, with a separation $\Delta x$ in comoving coordinates, is given by

$$\dot{d} = \frac{d}{dt}\left(a(t)\Delta x\right) = \frac{\dot{a}}{a}(a\Delta x) = Hd, \tag{4.3}$$

where $d = a\Delta x$ is the physical distance between the two comoving observers and $H$ is called the Hubble factor. The Hubble radius $H^{-1}$ is a physical distance and the comoving Hubble radius

$$\frac{1}{aH} \tag{4.4}$$

is a comoving scale. If the comoving distance between two observers is larger than the comoving Hubble radius, then they are out of causal contact by virtue of (4.3).

At large scales, the assumption that the universe can be modeled by a perfect fluid, is another good approximation. The Einstein equations describe the coupling between matter and the metric:[2]

$$G_{\mu\nu} = 8\pi G T_{\mu\nu}, \tag{4.5}$$

where $G_{\mu\nu} = R_{\mu\nu} - \frac{1}{2}Rg_{\mu\nu}$ is the Einstein tensor, $G$ is Newton's constant and $T_{\mu\nu}$ is the energy momentum tensor.

A perfect fluid can be modeled by a set of comoving observers with velocity $u$, such that $u^\mu u^\nu g_{\mu\nu} = -1$. The energy density $\rho$ and the pressure $p$ are given by:

$$\begin{aligned} \rho &= T_{\mu\nu}u^\mu u^\nu \\ p &= \frac{1}{3}T_{\mu\nu}\left(g^{\mu\nu} + u^\mu u^\nu\right). \end{aligned} \tag{4.6}$$

[2]From here on we will set $8\pi G = 1$, so that quantities with unit mass should be considered to be stated in units of the reduced Planck mass.

The simplest energy momentum tensor satisfying these properties is the energy momentum tensor of the perfect fluid

$$T_{\mu\nu} = \rho u_\mu u_\nu + p\left(g_{\mu\nu} + u_\mu u_\nu\right). \tag{4.7}$$

The Einstein equations (4.5) couple the energy momentum tensor (4.7) to the metric. Assuming a FRW metric (4.1), the Einstein equations give at a set of differential equations for $a(t)$ in terms of $\rho$ and $p$, called the Friedmann equations:

$$\left(\frac{\dot{a}}{a}\right)^2 = \frac{1}{3}\rho - \frac{\kappa}{a^2}, \tag{4.8}$$

$$\frac{\ddot{a}}{a} = -\frac{1}{6}\left(\rho + 3p\right), \tag{4.9}$$

where the dots indicate derivatives with respect to $t$.

One can combine the Friedmann equations to obtain the *continuity equation*:

$$\dot{\rho} + 3\frac{\dot{a}}{a}\left(\rho + p\right) = 0. \tag{4.10}$$

Another simplification can be made by assuming a linear equation of state:

$$p = w\rho. \tag{4.11}$$

For non relativistic matter $w = 0$, for relativistic matter (radiation) $w = \frac{1}{3}$ and for a cosmological constant $w = -1$.

### 4.2.2 Cosmological puzzles

Classical cosmology has been challenged to explain four (three) major problems: the homogeneity & the horizon problems, the flatness problem and the monopole problem. These problems were the main motivation to consider *inflation* (see subsection 4.2.3).We will briefly describe these problems in classical cosmology.[3]

#### Homogeneity & horizon problems

The cosmic microwave background radiation is surprisingly homogeneously distributed. A priori, there would be no reason for causally disconnected parts of the universe to show this level of homogeneity, because causally disconnected regions cannot equilibrate. Moreover, gravitational attraction is a long range force that

[3]By classical cosmology we mean a Big Bang model without subsequent accelerated expansion. In other words, $\ddot{a} \leq 0$.

magnifies instabilities, so one would expect the inhomogeneities to be even smaller at earlier times.

The analysis of causal regions in FLRW spacetimes is easiest done using *conformal time*, defined as[4]

$$\begin{aligned} \eta &= \int_0^t \frac{dt'}{a(t')} = \int_0^a d\ln\tilde{a}\frac{1}{\tilde{a}H}, \\ ds^2 &= a^2(\eta)\left(-d\eta^2 + \frac{dr^2}{1-\kappa r^2} + r^2 d\Omega_{d-1}^2\right) \end{aligned} \tag{4.12}$$

and is also called the comoving horizon or the comoving particle horizon, because particles whose comoving distance is larger than $\Delta\eta$ cannot have been in causal contact, whereas particles whose comoving distance is smaller than $\Delta\eta$ *can* have been in causal contact. In standard cosmology, the comoving Hubble radius $(aH)^{-1}$ is increasing, so from (4.12) we see that the causally connected areas were smaller in the past. Hence, standard cosmology does not explain the high level of homogeneity of the universe, because homogeneity is thought to result from an equilibration process which necessitates causal contact. This is called the horizon problem.

### Flatness problem

The universe is currently very close to flat ($\kappa = 0$) [98, 99]. Using the first Friedmann equation we can define the critical density $\rho_{\text{crit}}$ by

$$\begin{aligned} H^2(a) &= \frac{1}{3}\rho_{\text{crit}}(a), \\ &\Rightarrow \rho_{\text{crit}} = 3H^2(a), \end{aligned} \tag{4.13}$$

such that we have $\rho = \rho_{\text{crit}}$ for a flat universe ($\kappa = 0$). Rewriting the first Friedmann equation using (4.13) we have

$$1 - \Omega(a) = -\frac{\kappa}{3(aH)^2}, \tag{4.14}$$

where $\Omega(a) = \frac{\rho(a)}{\rho_{\text{crit}}(a)}$. From (4.14) it is clear that for a flat universe ($\kappa = 0$) we must have $\Omega(a) \approx 1$. In fact, initially $\Omega$ must be *very* close to one, because the comoving Hubble radius $(aH)^{-1}$ is increasing in standard cosmology: it requires extreme fine-tuning to obtain $\Omega = 1$ at late times.

[4] Here we write $t = 0$ as initial time, but later $t \to -\infty$ is more appropriate.

**Monopole problem**

In many models of a grand unified theory (GUT), in which the fundamental forces are unified in a single gauge group which is unbroken above a certain energy level, magnetic (GUT-) monopoles can be created [100], at least in the early universe [101–103]. Electric monopoles are well known. Electric charge in a volume $V$ is given by

$$Q_e^V = \frac{1}{4\pi}\int_{\partial V} \star F \tag{4.15}$$

where $\star$ is the Hodge dual and $F$ is the Maxwell field strength. Hodge duality exchanges $\star E = -B$ and $\star B = E$, so one could also define a "magnetic charge"

$$Q_m^V = \frac{1}{4\pi}\int_{\partial V} F. \tag{4.16}$$

For a magnetic monopole we would have $Q_m \neq 0$, or in other words, there would be a magnetic charge $\vec{\nabla}\cdot\vec{B} = \rho_m$. However, a magnetic monopole $Q_m \neq 0$ has never been observed. An important question in standard cosmology is hence: if monopoles can theoretically exist, why have we never seen one?

### 4.2.3 Inflation

In section 4.2.2 we described some problems with classical cosmology. In this subsection, we will explain how accelerated expansion in the early universe can solve these puzzles. We also briefly present the simplest mechanism that can explain accelerated expansion; single field slow roll inflation.

**Accelerated expansion**

A crucial insight from the seventies was that accelerated expansion,

$$\ddot{a} > 0, \tag{4.17}$$

where the dots represent derivatives with respect to $t$ (4.1), solves the cosmological puzzles. Firstly, from (4.17) it follows that the comoving Hubble radius $(aH)^{-1}$ decreases

$$\frac{d}{dt}\left(\frac{1}{aH}\right) < 0. \tag{4.18}$$

Returning to equation (4.14) we now see that the flat universe is in fact an *attractor*:

$$1 - \Omega(a) = -\frac{\kappa}{3(aH)^2}. \tag{4.19}$$

Also, the homogeneity & horizon problem is explained. In [104] it is explained as:

*If particles are separated by distances greater than $\eta$, they never could have communicated with one another; if they are separated by distances greater than $(aH)^{-1}$, they cannot talk to each other now! This distinction is crucial for the solution to the horizon problem which relies on the following: It is possible that $\eta$ is much larger than $(aH)^{-1}$ now, so that particles cannot communicate today but were in causal contact early on. From equation (4.12) we see that this might happen if the comoving Hubble radius in the early universe was much larger than it is now so that $\eta$ got most of its contribution from early times. Hence, we require a phase of decreasing Hubble radius. Since $H$ is approximately constant while $a$ grows exponentially during inflation we find that the comoving Hubble radius decreases during inflation just as advertised.*

The monopole problem can also be explained by accelerated expansion: even if monopoles would have been created in the early universe, they would be extremely diluted now, explaining the fact that they have never been observed.

**Voilating the strong energy condition**

From the second Friedmann equations (4.9) it follows that for an accelerating universe we have

$$\frac{\ddot{a}}{a} = -\frac{4\pi G}{3}(\rho + 3p) > 0 \quad \Rightarrow \quad \rho + 3p > 0. \tag{4.20}$$

This implies that the strong energy condition must be violated. The strong energy condition states that the energy momentum tensor obbeys, for any non-spacelike vector $k$

$$\left(T_{\mu\nu} - \frac{T}{2} g_{\mu\nu}\right) k^\mu k^\nu \geq 0. \tag{4.21}$$

One can check that for a perfect fluid energy momentum tensor (4.7) this implies $\rho + 3p > 0$, which is clearly violated by (4.20).

In the next subsection, we will present a simple mechanism that can explain the violation of the strong energy condition and the accelerated expansion of the universe.

### 4.2.4 Scalar field inflation

**Violating the strong energy condition**

Consider a scalar field $\phi$ with potential $V(\phi)$, for which the action is given by

$$\begin{aligned} S &= \int d^{d+1}x\sqrt{-g}\left(\frac{R}{2} + \mathcal{L}_{\text{matter}}\right), \\ \mathcal{L}_{\text{matter}} &= -\frac{1}{2}g^{\mu\nu}\partial_\mu\phi\partial_\nu\phi - \frac{1}{2}m^2\phi^2 - V(\phi). \end{aligned} \tag{4.22}$$

The energy momentum tensor is given by

$$T_{\mu\nu} = \frac{2}{\sqrt{g}}\frac{\delta S_{\text{matter}}}{\delta g^{\mu\nu}} \quad = \partial_\mu\phi\partial_\nu\phi - \frac{1}{2}g_{\mu\nu}\mathcal{L}_{\text{matter}}. \tag{4.23}$$

If we assume that $\phi = \phi(t)$, then it follows from (4.23) that:

$$\rho = T_{00} = \frac{\dot{\phi}^2}{2} + V(\phi), \quad p = \frac{1}{3}T_i^i = \frac{\dot{\phi}^2}{2} - V(\phi). \tag{4.24}$$

From the equation of state (4.11) it follows that

$$w = \frac{\frac{\dot{\phi}^2}{2} - V(\phi)}{\frac{\dot{\phi}^2}{2} + V(\phi)}, \tag{4.25}$$

so when the potential energy $V$ is much larger than the kinetic energy,

$$V \gg \dot{\phi}^2, \tag{4.26}$$

the strong energy condition can be violated ($w < -\frac{1}{3}$).

**Slow-roll parameters**

A scalar field can drive inflation if the kinetic energy is dominated by the potential energy (4.26). This condition must be satisfied throughout the period of inflation. The equation of motion of a scalar field in a FLRW spacetime (4.1) is given by

$$\ddot{\phi} + 3H\dot{\phi} - \frac{\delta V}{\delta\phi} = 0 \tag{4.27}$$

and with $p$ and $\rho$ given by (4.24) the first Friedmann equation becomes:

$$H^2 = \frac{1}{3}\left(\frac{\dot{\phi}^2}{2} + V\right). \tag{4.28}$$

From (4.25) we saw that inflation can only occur when the kinetic energy of the scalar field is dominated by the potential energy (4.26). Throughout inflation, the

kinetic term must remain sufficiently small. This requires the smallness of two parameters. These *slow-roll parameters*, given below, can be naturally expressed in terms of the number of e-folds during inflation, which is defined as

$$N \equiv \ln\left(\frac{a_{\rm end}}{a_{\rm begin}}\right). \tag{4.29}$$

Some useful equalities for $N$ are given by:

$$N = \int_{a_{\rm begin}}^{a_{\rm end}} \frac{da}{a} = \int_{t_{\rm begin}}^{t_{\rm end}} H(t)dt = -\int_{\phi_{\rm begin}}^{\phi_{\rm end}} \frac{H}{\dot{\phi}} d\phi \ . \tag{4.30}$$

From (4.8) we see that during inflation $H^2 \approx \frac{V}{3}$. Demanding that this remains true is equivalent to demanding that the relative change of $H$ per e-fold is small. A necessary condition is given by the smallness of a parameter $\epsilon$:

$$\epsilon = -\frac{d\ln H}{N} = -\frac{\dot{H}}{H^2}. \tag{4.31}$$

One can show, using the equation of motion, that we also have

$$\epsilon = \frac{1}{2}\frac{\dot{\phi}^2}{H^2}. \tag{4.32}$$

Smallness of $\epsilon$ ($\epsilon \ll 1$) is necessary but not sufficient. Another necessary condition is given by the requirement that $\epsilon \ll 1$ during all stages of inflation, or in other words, that the relative change of $\epsilon$ per e-fold is small. This is guaranteed by the smallness of

$$\eta = \epsilon - \frac{1}{2\epsilon}\frac{d\epsilon}{dN}. \tag{4.33}$$

Using the equation of motion and using $dN = Hdt$ (4.30), we can also write $\eta$ as:

$$\eta = \frac{-\ddot{\phi}}{H\dot{\phi}}. \tag{4.34}$$

The second slow roll parameter $\eta$ can also be negative, so the *slow-roll conditions* are given by:

$$\epsilon \ll 1, \quad |\eta| \ll 1. \tag{4.35}$$

The slow parameters $\epsilon$ and $\eta$ are given in terms of $H$ and $\phi$ and they are called the Hubble slow-roll parameters. It can be shown that a different set of parameters in terms of the potential $V$, the *potential slow-roll parameters*, are equivalent to the Hubble slow-roll parameters, in the slow-roll limit:

$$\epsilon_{\rm V} = \frac{1}{2}\left(\frac{V_{,\phi}}{V}\right)^2, \tag{4.36}$$

$$\eta_{\mathrm{V}} = \frac{V_{,\phi\phi}}{V}, \tag{4.37}$$

which are related to the Hubble slow-roll parameters by:

$$\epsilon \approx \epsilon_{\mathrm{V}}, \quad \eta \approx \eta_{\mathrm{V}} - \epsilon_{\mathrm{V}}. \tag{4.38}$$

A formalization of these slow roll parameters and a generalization to higher order parameters is given in [105].

**Perturbation theory**

Until now, we assumed the metric to be fixed to the FLRW-metric (4.1) and we assumed that $\phi = \phi(t)$. Such a simplified description describes the classical evolution of the scalar field. A next step to a more realistic model is to consider perturbations around this classical background evolution:

$$\begin{aligned} \phi(\vec{x}, t) &= \phi^{\text{background}}(t) + \delta\phi(\vec{x}, t) \\ g_{\mu\nu}(\vec{x}, t) &= g_{\mu\nu}^{\text{background}}(t) + \delta g_{\mu\nu}(\vec{x}, t). \end{aligned} \tag{4.39}$$

These perturbations can be quantized. A problem with considering perturbations around a background metric and scalar field is that there is not a unique way to split the metric and scalar field in a background part and a perturbation part as in (4.39). Different ways of making this cut are related to each other by "gauge transformations". There are however, certain gauge invariant quantities, that can be constructed with the ADM-formalism.

In [97] it is summarized how, in a particular gauge choice, the actions for the *comoving curvature perturbation* $\mathcal{R}$ and the tensor perturbation $h_{ij}$ can be derived. The result for the comoving curvature perturbation is given by:

$$S_{(2)} = \frac{1}{2} \int d^4x a^3 \frac{\dot{\phi}^2}{H^2} \left( \dot{\mathcal{R}}^2 - a^{-2} (\partial_i \mathcal{R})^2 \right). \tag{4.40}$$

The action for the tensor perturbation $h$ looks very similar and is effectively the action of two scalar degrees of freedom corresponding to the two polarizations of gravitational waves.

The action (4.40) can be simplified by introducing Mukhanov variables:

$$\begin{aligned} v &= z\mathcal{R} \qquad z^2 = \frac{a^2 \dot{\phi}^2}{H^2} = 2a^2\epsilon, \\ S_{(2)} &= \frac{1}{2} \int d\eta d^3x \, \left( (v')^2 + (\partial_i v)^2 + \frac{z''}{z} v^2 \right), \end{aligned} \tag{4.41}$$

where $\eta$ is conformal time (4.12) and primes denote derivatives with respect to $\eta$.

## 4.3 De Sitter spacetime

During inflation, the initial epoch of accelerated expansion, our universe has an approximate de Sitter geometry. In this section we will introduce de Sitter spacetime and several coordinate patches on de Sitter spacetime. These coordinate patches will be used extensively in later chapters.

### 4.3.1 Embedding

The (3+1)-dimensional de Sitter spacetime can be embedded in (4+1)-dimensional Minkowski spacetime. The embedding equation is given by:

$$-X_0^2 + \sum_{i=1}^{4} X_i^2 = L_{\rm dS}^2, \tag{4.42}$$

$$ds^2 = -dX_0^2 + \sum_{i=1}^{4} dX_i^2, \tag{4.43}$$

where $L_{\rm dS}$ is the de Sitter radius. The embedding equation (4.42) and the metric (4.43) are both manifestly invariant under $SO(1,4)$ transformations. The pullback of the Minkowski metric (4.43) on the hyperboloid (4.42) yields de Sitter spacetime.

De Sitter spacetime is also the maximally symmetric solution to Einsteins equations with positive cosmological constant. The Einstein Hilbert action with cosmological constant is given by:

$$S = \frac{1}{2}\int d^4x\sqrt{-g}\,(R-\Lambda)\,. \tag{4.44}$$

The Einstein equations that follow from extremizing the Einstein Hilbert action with cosmological constant (4.44) are given by

$$G_{\mu\nu} = R_{\mu\nu} - \frac{R}{2}g_{\mu\nu} = -\frac{\Lambda}{2}g_{\mu\nu}. \tag{4.45}$$

In a $3+1$ dimensional maximally symmetric spacetime, the Weyl tensor vanishes and the Riemann tensor obbeys:

$$R_{\mu\nu\rho\sigma} = \frac{R}{12}\left(g_{\mu\rho}g_{\nu\sigma} - g_{\mu\sigma}g_{\nu\rho}\right). \tag{4.46}$$

From the Einstein equations (4.45) it follows that

$$R = 2\Lambda. \tag{4.47}$$

The curvature in terms of $L_{\text{dS}}$ is given by

$$R = \frac{12}{L_{\text{dS}}^2}. \tag{4.48}$$

Below we discuss some coordinate charts for the de Sitter spacetime.

### 4.3.2 Coordinate patches on de Sitter

In chapters (5) and (6) we will use different coordinate patches on de Sitter spacetime. Below we will briefly introduce these coordinate patches and their Penrose diagrams.

#### Global coordinates

A set of global coordinates on de Sitter spacetime is defined by:

$$\begin{aligned} X_0 &= L_{\text{dS}} \sinh\left(\frac{t}{L_{\text{dS}}}\right), \\ \sum_{i=1}^{4} X_i^2 &= L_{\text{dS}}^2 \cosh^2\left(\frac{t}{L_{\text{dS}}}\right), \end{aligned} \tag{4.49}$$

where the last line in the equation implicitly defines three angular coordinates $\chi, \phi, \theta$ on the unit three-sphere. In these coordinates, the metric becomes:

$$ds^2 = -dt^2 + L_{\text{dS}}^2 \cosh^2 \frac{t}{L_{\text{dS}}} d\Omega_3^2. \tag{4.50}$$

These coordinates are called global because they cover all of the de Sitter spacetime. This is an example of a closed universe; the constant time slices have the geometry of a three-sphere.

A coordinate transformation shows that this metric is conformally $\mathbb{R} \times S^3$:

$$\begin{aligned} \eta &= 2 \arctan(e^{\frac{t}{L_{\text{dS}}}}), \\ ds^2 &= \frac{L_{\text{dS}}^2}{\sin^2 \eta} \left(-d\eta^2 + d\Omega_3^2\right), \end{aligned} \tag{4.51}$$

where $\eta \in [0, \pi]$ and $\chi \in [0, \pi]$. The Penrose diagram is given by the $(\eta, \chi)$-diagram, where every point represents an $S^2$ (figure 4.3).

#### Flat slicing

The flat slicing is a coordinate chart for which the constant time slices are flat. This coordinate chart does not cover the whole de Sitter spacetime, but a subsection

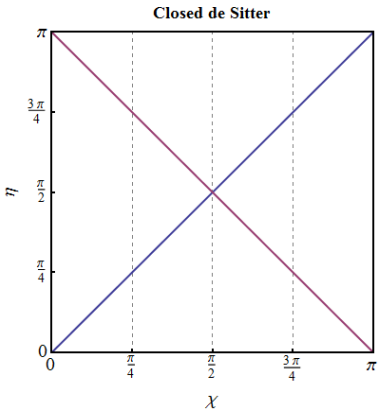


***Figure 4.3:*** *Penrose diagram of de Sitter spacetime. For an observer at $\chi = 0$, the comoving Hubble radius is indicated in blue. The comoving particle horizon is indicated in purple. Source: universeinproblems.com.*

which is called the planar patch (see figure 4.4). In terms of the embedding coordinates (4.43,4.42), a set of flat coordinates is given by:

$$\begin{aligned} X_0 &= L_{\text{dS}} \sinh\left(\frac{t}{L_{\text{dS}}}\right) + \frac{r^2 e^{\frac{t}{L_{\text{dS}}}}}{2L_{\text{dS}}} \\ X_4 &= L_{\text{dS}} \cosh\left(\frac{t}{L_{\text{dS}}}\right) - \frac{r^2 e^{\frac{t}{L_{\text{dS}}}}}{2L_{\text{dS}}} \\ X_i &= e^{\frac{t}{L_{\text{dS}}}} x_i, \text{ for } i = 1, \ldots, 3 \ . \end{aligned} \tag{4.52}$$

In these coordinates, the metric is given by:

$$ds^2 = -dt^2 + e^{2\frac{t}{L_{\text{dS}}}} d\vec{x}^2 = -dt^2 + e^{2Ht} d\vec{x}^2. \tag{4.53}$$

Alternatively, we can use spherical coordinates for the constant time slices:

$$ds^2 = -dt^2 + e^{2\frac{t}{L_{\text{dS}}}} \left(dr^2 + r^2 d\Omega_2^2\right). \tag{4.54}$$

### Hyperbolic slicing

The hyperbolic patch is yet another coordinate patch that does not cover the whole de Sitter spacetime (see figure 4.5). In fact, two hyperbolic patches can be

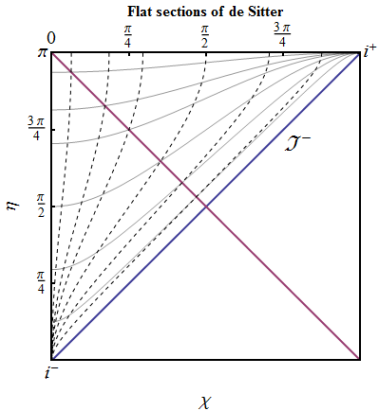


***Figure 4.4:*** *Planar patch of de Sitter spacetime. Source: universeinproblems.com.*

identified (see figure 5.3). A set of hyperbolic coordinates is defined by:

$$X_0 = L_{\mathrm{dS}} \sinh\left(\frac{t}{L_{\mathrm{dS}}}\right) \cosh r \tag{4.55}$$

$$X_4 = L_{\mathrm{dS}} \cosh\left(\frac{t}{L_{\mathrm{dS}}}\right) \tag{4.56}$$

$$\sum_{i=1}^{3} X_i^2 = L_{\mathrm{dS}}^2 \sinh^2\left(\frac{t}{L_{\mathrm{dS}}}\right) \sinh^2 r, \tag{4.57}$$

where the last line of the equation implicitly defines two angular coordinates. In these coordinates the metric is given by:

$$ds^2 = -dt^2 + L_{\mathrm{dS}}^2 \sinh^2\left(\frac{t}{L_{\mathrm{dS}}}\right) \left[dr^2 + \sinh^2 r \, d\Omega_2^2\right] \ . \tag{4.58}$$

In chapter (5) we will discuss the hyperbolic patches in more detail. We will also "derive" the hyperbolic coordinate set in a different manner and we will discuss a link between flat and hyperbolic coordinates. A hyperbolic coordinate set is sometimes called an *open slicing* of de Sitter spacetime, because the spatial slices are hyperbolic spaces.

### Static coordinates

The final coordinate set we will introduce is the static coordinate set. In figure (4.6) the region of de Sitter spacetime covered by these coordinates is indicated. There is a timelike Killing vector in the static patch. A set of coordinates covering

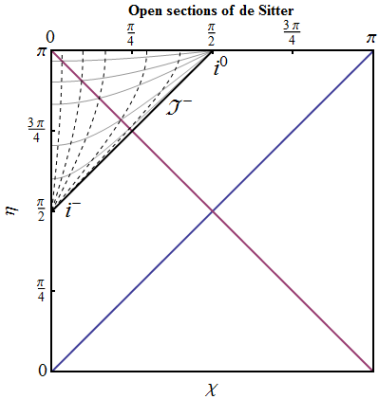


***Figure 4.5:*** *Hyperbolic patch of de Sitter. See also figure (5.3). Source: universeinproblems.com.*

the static patch is given by:

$$\begin{aligned} X_0 &= L_{\rm dS}\sqrt{1-\frac{r^2}{L_{\rm dS}^2}}\sinh\left(\frac{t}{L_{\rm dS}}\right) \\ X_4 &= L_{\rm dS}\sqrt{1-\frac{r^2}{L_{\rm dS}}}\cosh\left(\frac{t}{L_{\rm dS}}\right) \\ \sum_{i=1}^{3} X_i^2 &= r^2, \end{aligned} \tag{4.59}$$

where the last line implicitly defines two angular coordinates. In these coordinates, the metric is given by

$$ds^2 = -\left(1-\frac{r^2}{L_{\rm dS}^2}\right)dt^2 + \frac{dr^2}{\left(1-\frac{r^2}{L_{\rm dS}^2}\right)} + r^2 d\Omega_{d-1}^2. \tag{4.60}$$

The metric is singular as $r \to L_{\rm dS}$, but this is merely a coordinate singularity; the metric is smooth in lightcone coordinates. Note that $\partial_t$ is a timelike Killing vector. It is not a global Killing vector of de Sitter spacetime; the static coordinate set only covers part of de Sitter (see figure 4.6). The coordinate singularity at $r = L_{\rm dS}$ corresponds with the vanishing of the Killing vector and is hence a Killing horizon.

## 4.4 QFT in de Sitter spacetime

Quantum field theory in de Sitter spacetime, or curved spacetime in general, is more complicated than quantum field theory in Minkowski spacetime. Quantum

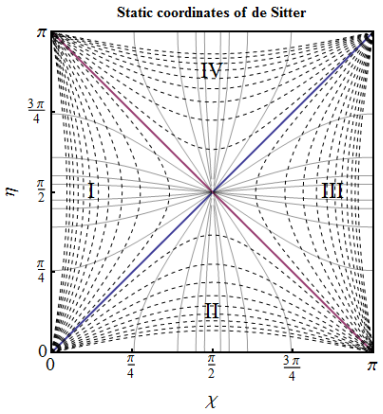


***Figure 4.6:*** *Static de Sitter patch. Region I and region III can be covered by static coordinates. Source: universeinproblems.com.*

effects are relevant for the explanation of the spectrum of the CMB, so a good understanding of quantum field theory in de Sitter spacetime is necessary. In this section, we will present techniques of quantum field theory in curved spacetime, that will be used in later chapters. The discussion is partially based on [106, 107].

### 4.4.1 QFT in curved spacetime

Consider a globally hyperbolic Lorentzian manifold $\mathcal{M}$ with metric $g$ and let $\Sigma$ be a Cauchy surface with future directed normal vector $\xi^\mu$. One can think of $\Sigma$ as a constant timeslice. Let $n \propto \xi$ be the future directed normal vector of $\Sigma$ ($n^2 = -1$) and let $h_{ab} = g_{ab} + n_a n_b$ be the induced metric on $\Sigma$. The conjugate variable to the scalar field $\phi$ is now defined as

$$\Pi = \sqrt{h} n^\mu \partial_\mu \phi. \tag{4.61}$$

Choose coordinates $\{\vec{x}\}$ on $\Sigma$, such that we can impose canonical commutation relations

$$[\phi(x), \Pi(y)] = i\delta(x,y), \qquad [\phi(x), \phi(y)] = 0, \qquad [\Pi(x), \Pi(y)] = 0, \tag{4.62}$$

where the delta function is defined such that $\int_\Sigma d^3x \delta(x,y) f(x) = f(y)$ for any function $f$ on $\Sigma$.

The scalar product or Klein Gordon product of two functions $f, g$ is given by

$$\langle f, g \rangle_\Sigma = -i \int_\Sigma d^3x \sqrt{h} n^\mu f(x) \overleftrightarrow{\partial}_\mu g^*(x) \tag{4.63}$$

If $f$ and $g$ satisfy the equation of motion, the Klein Gordon norm is conserved, which means that it does not depend on the choice of $\Sigma$. This allows us to construct a complete orthonormal set of solutions $\{\phi_i, \phi_i^*\}$ such that

$$\langle \phi_i, \phi_j \rangle = \delta_{ij}, \quad \langle \phi_i^*, \phi_j^* \rangle = -\delta_{ij}, \quad \langle \phi_i^*, \phi_j \rangle = \langle \phi_i, \phi_j^* \rangle = 0. \tag{4.64}$$

Note that when we have a continuous label for the mode functions, then the Kronecker delta becomes a delta Dirac function. The field $\phi$ can be expanded with respect to this basis and promoted to an operator

$$\phi = \sum_i \left( \hat{a}_i \phi_i + \hat{a}^\dagger \phi_i^* \right), \tag{4.65}$$

where the creation and annihilation operators satisfy

$$[\hat{a}_i, \hat{a}_j^\dagger] = \delta_{ij}, \qquad [\hat{a}_i, \hat{a}_j], \qquad \hat{a}_i^\dagger, \hat{a}_j^\dagger. \tag{4.66}$$

One can check that these commutation relations are guaranteed by the canonical commutation relations (4.62) and the Klein Gordon normalization of the mode functions (4.63,4.64).

The vacuum state can now be defined by:

$$\hat{a}_i |0\rangle = 0 \quad \forall i. \tag{4.67}$$

Unfortunately, the decomposition (4.65) in modes is not unique. One can check that a different set of modes $\{\tilde{\phi}_j, \tilde{\phi}_j^*\}$ also constitutes an orthonormalised basis as long as

$$\tilde{\phi}_i = \sum_j \left( A_i^j \phi_j + B_i^j \phi_j^* \right), \tag{4.68}$$

$$\delta_{ij} = \sum_k \left( A_i^k \bar{A}_j^k - B_i^k \bar{B}_j^k \right), \quad 0 = \sum_k \left( A_i^k B_j^k - B_i^k A_j^k \right), \tag{4.69}$$

or in matrix notation

$$AA^\dagger - BB^\dagger = \mathcal{I}, \qquad AB^T - BA^T = 0, \tag{4.70}$$

where the bar denotes complex conjugation.[5] The $A_i^j$ and $B_i^j$ are called Bogoliubov coefficients. As a consequence of this freedom to choose our orthonormal basis of modes, we can also associate a set of creation and annihilation operators $\{\tilde{a}_j, \tilde{a}_j^\dagger\}$ to the modes $\tilde{\phi}$ and define another vacuum state with respect to these operators. Hence, there generally is not a unique vacuum state in curved spacetime.

[5] Invertability of such a rotation of mode functions requires also that $A^\dagger A - B^T \bar{B} = \mathcal{I}$ and $A^\dagger B - B^T \bar{A} = 0$, as shown in [108] for example.

Even in Minkowski spacetime, one could take normalized linear combinations of the positive and negative frequency mode functions $e^{\pm i\omega_k t}$ and define an alternative vacuum with the creation and annihilation operators associated to these new mode functions. One way of selecting a unique vacuum is to demand that the mode functions correspond to plane waves at early times. In Minkowski spacetime this is equivalent to selecting the positive frequency mode functions. This choice also guarantees that the vacuum is an eigenstate of the Hamiltonian and the other conserved charges associated to the energy momentum tensor.

### 4.4.2 Wightman function

Generally, the vacuum state is not uniquely defined in curved spacetime. A way to characterize a vacuum state is to consider the Wightman function, a construct from axiomatic field theory. The Wightman function of a vacuum state $|\Omega\rangle$is given by:

$$W(x,y) = \langle\Omega|\phi(x)\phi(y)|\Omega\rangle. \tag{4.71}$$

If the field $\phi$ can be expanded as (4.65) and the vacuum is defined as (4.67), the Wightman can be written as:

$$W(x,y) = \sum_i \phi_i(x)\phi_i^*(y). \tag{4.72}$$

A vacuum state defined by creation and annihilation operators $\tilde{a}$, associated to a different set of mode functions (4.68), will result in a different Wightman function. A Bogoliubov transformation that is particularly relevant for this thesis, does not mix modes with different quantum numbers (it is diagonal), but mixes a mode function $\phi_k$ with its complex conjugate:

$$\tilde{\phi}_j = A\phi_k + B\phi_k^*, \qquad |A|^2 - |B|^2 \quad = 1. \tag{4.73}$$

The relation between the Wightman function $W$ for the vacuum state associated to the mode functions $\{\phi_k\}$ and the Wightman function $\tilde{W}$ for the vacuum associated to the mode functions $\{\tilde{\phi}_k\}$ defined by (4.73) is given by:

$$\begin{aligned}\tilde{W}(x,y) &= \langle\tilde{\Omega}|\phi(X)\phi(Y)|\tilde{\Omega}\rangle \\ &= |A|^2\sum_i \phi_i(X)\phi_i^*(Y) + |B|^2\sum_i \phi^*(X)\phi(Y) + \\ &+ AB^*\sum_i \phi_i(X)\phi_i(Y) + A^*B\sum_i \phi_i^*(X)\phi_i^*(Y).\end{aligned} \tag{4.74}$$

### 4.4.3 The Bunch-Davies state

In de Sitter spacetime, there *is* a special vacuum state which we will describe here. First we will describe the set of de Sitter invariant vacua, then we will further select one of them, the Bunch-Davies state.

**$\alpha$-vacua**

The Wightman function for a vacuum state $|\Omega\rangle$ is given by (4.71)

$$W(X,Y) = \langle\Omega|\phi(X)\phi(Y)|\Omega\rangle. \tag{4.75}$$

De Sitter spacetime is homogeneous, which means that different points are associated to each other by isometries. Hence, the de Sitter invariant vacuum state should yield a Wightman function which depends only on the de Sitter invariant distance between two points:[6]

$$W(X,Y) = W(Z(X,Y)). \tag{4.76}$$

In embedding space (4.43,4.42), the de Sitter invariant distance is given by[7]

$$Z(X,Y) = \frac{1}{L_{\text{dS}}^2} X^a Y^b \eta_{ab}. \tag{4.77}$$

The Wightman function should solve the equation of motion in each of it coordinate entries. In terms of $Z$ (4.77), the Klein Gordon equation for a massive scalar on $(3+1)$-dimensional de Sitter spacetime becomes:

$$\left(\left(Z^2-1\right)\partial_Z^2 + 4Z\partial_Z + m^2 L_{\text{dS}}^2\right) W(Z) = 0. \tag{4.78}$$

This equation has two solutions and is solved by hyper-geometric functions. One can take two solutions such that they are related by $Z \leftrightarrow -Z$ and such that one solution $f(Z)$ is singular in $Z=1$ and the other $f(-Z)$ in $Z=-1$.[8] Any linear combination of these solutions would solve the equation of motion (4.78) as well and can be associated to a vacuum state with its characterizing Wightman function:

$$W(X,Y) = af(Z) + bf(-Z). \tag{4.79}$$

The choice $b=0$ is special for the following reason. Euclidean de Sitter spacetime is simply a sphere. On the sphere, there *is* a unique Greens function and a unique

[6] Sometimes, the symmetrized Wightman function is used in this argument, for example see [109].

[7] The *geodesic distance is given by* $d(X,Y) = L_{dS} \arccos Z(X,Y)$.

[8] The transformation $Z \leftrightarrow -Z$ is called the antipodal transformation.

vacuum. Analytic continuation to Lorentzian de Sitter yields the Wightman function with $b = 0$ [110, 111]. This choice is also special because the Wightman function is not singular for $Z = -1$. It is called the Bunch-Davies state, or the Euclidean vacuum, due to its relation to the vacuum state on Euclideanized de Sitter (the sphere).

Associated to such a vacuum choice, there is a set of mode functions, $\{\phi_{k,\mathrm{BD}}\}$. The vacuum states corresponding to different choices of $a, b$ in 4.79 are associated by a Bogoliubov transformation of the Bunch-Davies mode functions $\{\phi_{k,\mathrm{BD}}\}$ of the type (4.73). A convenient parametrization is given by[9]

$$\tilde{\phi}_{k,\alpha} = \frac{1}{\sqrt{1 - e^{\alpha+\alpha^*}}}\phi_{k,\mathrm{BD}} + \frac{e^{\alpha}}{\sqrt{1 - e^{\alpha+\alpha^*}}}\phi^*_{k,\mathrm{BD}}, \tag{4.80}$$

and the associated vacua are called alpha or $\alpha$-vacua, where $\mathrm{Re}\{\alpha\} \to -\infty$ corresponds to the Bunch-Davies state.

Another frequently used parametrization of the $\alpha$-vacua is given by the two real parameters $(\alpha, \beta)$:

$$\tilde{\phi}_{k,\alpha} = \cosh(\alpha)\phi_{k,\mathrm{BD}} + \sinh(\alpha)e^{i\beta}\phi^*_{k,\mathrm{BD}}. \tag{4.81}$$

In [110] it is argued that $\beta = 0$ for states invariant under time reversal. The Bunch-Davies state corresponds to $\alpha = 0$. From different perspectives the non-Bunch-Davies $\alpha$-vacua seem to be non-physical: see for example [112, 113].

The Euclidean vacuum Wightman function in terms of the de Sitter invariant distance $Z(X, Y)$ is given by

$$W(X, Y) \propto {}_2F_1[h, 2 - h, \frac{3}{2}; \frac{1 + Z}{2}], \tag{4.82}$$

where $h$ is a solution of:

$$h(h - 2) + m^2 L^2_{\mathrm{dS}} = 0. \tag{4.83}$$

For the massless scalar field it is not clear that there exists a de Sitter invariant vacuum state. The Wightman function 4.79 becomes a constant as $m \to 0$ and $f(Z)$ and $f(-Z)$ are no longer independent solutions to (4.78). A second solution to (4.78) can be found, but the result is qualitatively different from the massive case. Strictly speaking, one could conclude that there is no de Sitter invariant vacuum state for the massless scalar [110]. This issue is a consequence of the shift symmetry $\phi \to \phi + c$ for the massless scalar field, which gives life to a *zero mode*.[10] Efforts have been made to construct a de Sitter invariant vacuum state

[9] See for example [112, 113]

[10] Some authors object to this interpretation, for example see [110]

for the massless scalar field nonetheless [114, 115]. A full discussion of these issues is outside the scope of this thesis. Below we will define the Bunch-Davies state for the massless scalar field in a different way, but strictly speaking it is not de Sitter invariant. We can think of the associated mode functions as being the small mass limit of the mode functions for the massive case.

### Positive frequency modes

In the previous paragraph we discussed the Bunch-Davies state, the de Sitter invariant vacuum state that can be associated to the unique Euclidean vacuum on the sphere. The Bunch-Davies state also appears as the natural vacuum of de Sitter spacetime in a different context. In the flat slicing (4.52) the Bunch-Davies mode functions can be associated to positive frequency or positive energy mode functions in the far past.

Consider first the example of Minkowski spacetime with coordinates $(t, \vec{x})$. Expanding a general solution in terms of momentum modes $\vec{p}$ yields the Klein Gordon equation

$$\left(\partial_t^2 + p^2 + m^2\right) \phi_{\vec{p}}(t) = 0, \tag{4.84}$$

which has general solution

$$\phi_{\vec{p}}(t) = \alpha e^{-i\omega_{\vec{p}} t} + \beta e^{+i\omega_{\vec{p}} t}, \qquad \omega_{\vec{p}} = \sqrt{p^2 + m^2}. \tag{4.85}$$

The solution with $\beta = 0$ is associated to plane waves with positive frequency $\omega_{\vec{p}}$. Particles are associated to (wave-packets of-) plane waves and a natural choice of mode functions and the associated vacuum in given by the choice $\beta = 0$.

In the flat slicing of de Sitter spacetime (4.52), using conformal time (4.12), we can construct eigenfunctions of the spatial Laplacian, with eigenvalues $\vec{p}$, the comoving momentum. In order to select a preferred set of mode functions we demand the following:

$$\lim_{\eta \to -\infty} \phi_p(\eta) \propto e^{-i\eta\omega_p}, \tag{4.86}$$

where $\omega_p = |p|$ for the massless scalar field. This selects a particular solution to the Klein Gordon equation with comoving momentum $|p|$, which can be associated to "positive frequency" excitations in the far past. It can be shown that this method, applied to the planar patch, selects the Bunch-Davies state. In chapter (5), we will also use this condition (4.86) to select a "natural vacuum" in the hyperbolic patch.

## 4.5 Inflationary power spectrum

In the introduction we explained how the cosmic microwave background (CMB) resulted from the decoupling of photons, constituting the first visible radiation in the universe. The CMB provides important observational data and a model of the early universe should be consistent with the power spectrum of the cosmic microwave background. Ideally, a model of inflation should explain features of the observed spectrum. Recombination[11] happened about 380.000 years after the Big Bang, whereas inflation occurred about $10^{-34}$ seconds after the Big Bang. This means that the CMB is heavily affected by post-inflationary physics, like the baryon acoustic oscillations. In this thesis we focus on the inflationary epoch and the effects of having different quantum states and different inflaton potentials. The post-inflationary physics is outside the scope of this thesis.

In section (4.2) we described how the classical description of a single scalar field model can explain the accelerated expansion of the primordial universe. Subsequently, we considered perturbations around the classical evolution, which lead to the quadratic action (4.41). These microscopic fluctuations are transformed into the seeds for the macroscopic structure of the universe at later times. A fluctuation on a certain comoving sub-horizon scale ($\lambda < (aH)^{-1}$) will eventually exit the comoving Hubble radius (4.4) and becomes super-horizon ($\lambda \gg (aH)^{-1}$). The super-horizon modes are frozen out; points separated by comoving distances $\Delta x \gg (aH)^{-1}$ are no longer in causal contact. Only after inflation, when the comoving Hubble radius increases again, these modes re-enter the horizon. Once they are subject to causal physics, gravity causes regions of higher density to become even denser. This process ultimately leads to the large scale structure of the universe. A full discussion of this process is outside the scope of this thesis, but details can be found in reviews like [97].

Here we will be concerned with the *spectrum* $\Delta_s^2(p)$ of the comoving curvature perturbation, which is defined by:

$$\langle \Omega_{\rm BD}|\mathcal{R}^2(\eta,\vec{x})|\Omega_{\rm BD}\rangle = \int d(\ln p)\Delta_s^2(p). \tag{4.87}$$

We can also write the two-point function in terms of comoving momenta:

$$\langle \Omega_{\rm BD}|\mathcal{R}^2(\eta,\vec{x})|\Omega_{\rm BD}\rangle = \int \frac{d^3p}{(2\pi)^3}\int \frac{d^3p'}{(2\pi)^3}\langle \Omega_{\rm BD}|\mathcal{R}_{\vec{p}}(\eta)\mathcal{R}_{\vec{p}'}(\eta)|\Omega_{\rm BD}\rangle e^{i(\vec{p}+\vec{p}')\dot{\vec{x}}}, \tag{4.88}$$

such that our task at hand is to calculate

$$\langle \mathcal{R}_p(x)\mathcal{R}_{p'}(x)\rangle. \tag{4.89}$$

[11] In fact, combination would be a more appropriate name.

Roughly speaking, the classical evolution of the inflaton field gives rise to a cosmological constant. The (quantum-) fluctuations locally change the cosmological constant, or local energy density, leaving their imprint on the structure of the universe and the CMB by the mechanisms described above.

In order to determine the spectrum (4.87), we must quantize the perturbations and determine the appropriate quantum state on which we should evaluate the field operators. We will give a simplified description of this procedure, taking the "de Sitter limit" $\epsilon_{\rm V} \to 0$ (4.36), which is equivalent to calculating the two-point function of a quantized scalar field on a fixed de Sitter geometry. This simplified calculation is sufficient for our analysis in chapter (6). Note that we gave a more conceptual treatment of quantum field theory in section (4.4), to which we will refer several times.

First, expand $v$ in terms of comoving momentum modes and promote the field to an operator:

$$v(\eta, \vec{x}) = \int \frac{d^3p}{(2\pi)^3} \left( \hat{a}_{\vec{p}} v_{\vec{p}}(\eta) e^{i\vec{p}\cdot\vec{p}} + \text{h.c.} \right), \tag{4.90}$$

where h.c. stands for hermitian conjugate. The mode functions $\{v_{\vec{p}}\}$ must satisfy the equation of motion

$$v''_{\vec{p}} + \left( p^2 - \frac{z''}{z} \right) v_{\vec{p}} = 0. \tag{4.91}$$

If the mode functions $\{v_{\vec{p}}\}$ are properly normalized (4.63), then the canonical commutation relations for $\hat{v}$ (4.62) and its conjugate variable imply the canonical commutation relations for the $\hat{a}_{\vec{k}}$ (4.66):

$$[\hat{a}_{\vec{p}}, \hat{a}^\dagger_{\vec{p}'}] = (2\pi)^3 \delta^3(\vec{p} - \vec{p'}), \quad [\hat{a}_{\vec{p}}, \hat{a}_{\vec{p}'}] = 0, \qquad [\hat{a}^\dagger_{\vec{p}}, \hat{a}^\dagger_{\vec{p}'}] = 0. \tag{4.92}$$

In the de Sitter limit, $\epsilon_{\rm V} \to 0$, we have $\frac{z''}{z} = \frac{a''}{a} = \frac{2}{\eta^2}$. We will consider this limit, in which the scalar density perturbation decouples and the action (4.41) becomes the action of a massless scalar field on a fixed de Sitter background. The general solution to the equation om motion is now given by

$$\begin{aligned} v_{\vec{k}}(\eta) = \alpha H \frac{e^{-i|p|\eta}}{\sqrt{2p}} \left( 1 - \frac{i}{|p|\eta} \right) \\ + \beta H \frac{e^{i|p|\eta}}{\sqrt{2p}} \left( 1 + \frac{i}{|p|\eta} \right), \end{aligned} \tag{4.93}$$

which is of the type (4.73). The normalization $|\alpha|^2 - |\beta|^2 = 1$ (4.73) guarantees that (4.92) is consistent with the canonical commutation relations for $\hat{v}$ (4.62).

To determine $\alpha, \beta$ for the "natural vacuum", we consider the limit $\eta \to -\infty$ (4.86):

$$\begin{aligned}\lim_{\eta\to-\infty} \alpha H\frac{e^{-i|p|\eta}}{\sqrt{2|p|}}\left(1-\frac{i}{|p|\eta}\right) \quad &+\beta H\frac{e^{i|p|\eta}}{\sqrt{2|p|}}\left(1+\frac{i}{|p|\eta}\right)\\ \sim \alpha H\frac{e^{(}-i|p|\eta)}{\sqrt{2|p|}} &+\beta H\frac{e^{+i|p|\eta}}{\sqrt{2|p|}},\end{aligned} \tag{4.94}$$

and we recognize that the choice $\alpha = 1, \beta = 0$ corresponds to positive frequency modes in the far past. With this choice, we define the vacuum, the Bunch-Davies state as in (4.67):

$$\hat{a}_{\vec{p}}|\Omega_{\rm BD}\rangle = 0 \quad \forall \vec{p}. \tag{4.95}$$

The two-point function is now given by

$$\begin{aligned}\langle\Omega_{\rm BD}|\mathcal{R}_{\vec{p}}(\eta)\mathcal{R}_{\vec{p}'}(\eta)|\Omega_{\rm BD}\rangle &= (2\pi)^3\delta^3(\vec{p}-\vec{p}')\frac{|v_{\vec{p}}|^2}{a^2}\\ &= (2\pi)^3\delta^3(\vec{p}-\vec{p}')\frac{H^2}{2|p|^3}\left(1+|p|^2\eta^2\right),\end{aligned} \tag{4.96}$$

or in position space

$$\begin{aligned}\langle\Omega_{\rm BD}|\mathcal{R}^2(\eta,\vec{x})|\Omega_{\rm BD}\rangle &= \int\frac{d^3p}{(2\pi)^3}\int\frac{d^3p'}{(2\pi)^3}\langle\Omega_{\rm BD}|\mathcal{R}_{\vec{p}}(\eta)\mathcal{R}_{\vec{p}'}(\eta)|\Omega_{\rm BD}\rangle e^{i(\vec{p}+\vec{p}')\dot{\vec{x}}}\\ &= \int\frac{d^3p}{(2\pi)^3}\frac{H^2}{2|p|^3}\left(1+|p|^2\eta^2\right)\\ &= \frac{H^2}{4\pi^2}\int_0^\infty d(\ln p)\left(1+p^2\eta^2\right).\end{aligned} \tag{4.97}$$

The *spectrum* $\Delta_s^2(p)$ is given by the integrand of (4.97):

$$\Delta_s^2(p) = \frac{H^2}{4\pi^2}\left(1+|p|^2|\eta|^2\right). \tag{4.98}$$

At late times, $|p\eta| \ll 1$ the spectrum of the scalar field is approximately

$$\Delta_s^2(k) = \frac{H^2}{4\pi^2}, \tag{4.99}$$

which is scale-invariant. However, we must not forget that we took the de Sitter limit as we went from the true two-point function of the comoving curvature perturbation to the two-point function of the scalar field in de Sitter. *If* the equation of motion is not changed to leading order, that is, if the approximation $\frac{z''}{z} \sim \frac{a''}{a}$ is still good, then we can use (4.99) and modify it in two ways: first we must multiply the result (4.99) by $\left(\frac{a}{z}\right)^2 = \left(\frac{H}{\dot{\phi}}\right)^2$. Secondly, the comoving curvature

perturbation remains constant outside the comoving horizon[12], so we evaluate the spectrum at horizon exit $p = aH$:

$$\Delta_s^2(p) = \left.\frac{H^2}{4\pi^2}\frac{H^2}{\dot{\phi}^2}\right|_{p=aH}. \tag{4.100}$$

This is the main result of this section. In the next section, we will use this result and relate it to two parameters that characterize an inflationary model.

## 4.6 Parameters of inflation

In section (4.5) presented a simplified derivation of the spectrum of comoving curvature perturbations. A similar derivation can be given for the tensor mode perturbations (see for example [97]). The spectrum depends on the inflationary potential ($V(\phi)$) via the first order slow-roll parameter $\epsilon$ (4.36). In fact, we can characterize an inflationary model by the two slow-roll parameters $\epsilon$ and $\eta$. Below we will describe how these parameters are related to the spectrum and how they are related to two other commonly used parameters that characterize a model of inflation; the scalar spectral index $n_s$ and the tensor to scalar ratio $r$. We will also discuss the possibility of having a non-zero *running* of these parameters.

From section (4.5) we have the main result (4.100). For the tensor fluctuations one can derive the spectrum in similar fashion; here we will state the result:

$$\Delta_t^2(p) = \left.\frac{2H^2}{\pi^2}\right|_{p=aH}. \tag{4.101}$$

The tensor to scalar ratio is defined as

$$r = \frac{\Delta_t^2}{\Delta_s^2} \tag{4.102}$$

and using (4.100) and (4.101) we find:

$$r = \left.16\epsilon\right|_{p=aH}. \tag{4.103}$$

The scalar spectral index $n_s$ is defined as:

$$n_s = 1 + \frac{d\ln\Delta_s^2}{d\ln p}. \tag{4.104}$$

[12]We did not discuss this here; it is outside the scope of this thesis. The fact that the comoving curvature perturbation is constant outside the horizon follows from the treatment of all perturbations and the construction of gauge invariant scalar perturbations in the ADM-formalism.

One can show that (using 4.100):

$$n_s = 1 + 2\eta\big|_{p=aH} - 4\epsilon\big|_{p=aH} \,. \tag{4.105}$$

In chapter (6) we will be interested in different potentials $V(\phi)$, so it is more convenient to write $n_s$ and $r$ in terms of the potential slow-roll parameters (4.36,4.37):[13]

$$\begin{aligned} n_s &= 1 + 2\eta_{\rm V} - 6\epsilon_{\rm V}, \\ &= 16\epsilon_{\rm V}. \end{aligned} \tag{4.106}$$

These expressions, together with the definitions (4.36,4.37) of the potential slow-roll parameters form the basis for chapter (6).

The scalar spectral index $n_s$ and the tensor to scalar ratio $r$ can be scale dependent. The "running" $\alpha_s$ is a measure of the scale dependence of $n_s$:

$$\alpha_s = \frac{dn_s}{d\ln k}. \tag{4.107}$$

A large running would spoil the scale-invariance of slow-roll inflation models. In single field inflation models, the running is an effect that appears at second order in the slow-roll parameters. If a large running would be measured, then this would cast doubt on at least some single field inflation models. In this thesis we do not analyze the running of parameters of the models under consideration.

[13] From now on we will drop the subscript $p = aH$.

# Chapter 5

# Vacua in hyperbolic de Sitter

In chapter (4) we introduced inflation and single field inflation models. We discussed how quantum fluctuations form the seeds of the large scale structures in the early universe and we derived an important characteristic: the scalar power spectrum. In section (4.5) we used flat coordinates (4.52,4.53) and assumed that the appropriate quantum state was given by the Bunch-Davies state (subsection 4.4.3). However, there are reasons to believe that our universe is actually best described by a hyperbolic patch (4.55,4.58).

In this chapter we investigate how the spectrum would be affected by considering the natural vacuum of the hyperbolic patch as the initial quantum state. We will work in a simplified model: we will just consider the two-point function of a scalar field on a fixed background and compare the Bunch-Davies state with the hyperbolic vacuum, which is defined below. Although this is a simplification, the effects of considering different initial states can be analyzed.

We attempt to determine whether we can distinguish the power spectra generated by these two states. The study of the hyperbolic patch is mainly motivated by the possibility that we live in a "bubble universe" (see section 5.1). A proper description of a bubble universe would involve the physics of its nucleation, which would certainly affect the quantum state. The Bunch-Davies State and the hyperbolic vacuum are *qualitatively different* from each other because from the point of view of the bubble, the Bunch-Davies state is mixed, or entangled, whereas the hyperbolic vacuum would be pure.

In section (5.1) we will motivate the study of the open universe and the hyperbolic de Sitter patch. In section (5.2) we will introduce a relationship between the planar patch of de Sitter spacetime and the hyperbolic patch of de Sitter spacetime. Subsequently, we will discuss the hyperbolic vacuum (section 5.3), the Bunch-Davies state (section 5.4) and the reduced density matrix associated to the hyperbolic patch in the Bunch-Davies state (section 5.5). In section (5.6) we calculate the power spectra in the two different states and in section (5.7) we analyze the difference of the energy-momentum tensor evaluated on these two vacua.

## 5.1 The universe as a hyperbolic patch of de Sitter

In this section we motivate the study of the hyperbolic patch of de Sitter spacetime and introduce coordinate charts. First we discuss the appearance of the open universe in the context of bubble universes. Subsequently, we discuss how we obtain coordinates on the hyperbolic patches by doing an analytic continuation from the Euclidean space. This discussion supplements the introduction of coordinates on the hyperbolic patch in section (4.3).

### 5.1.1 The universe as a bubble

Cosmological observations point to a primordial universe that can be effectively described by an approximate de Sitter phase. One scenario is that our universe is actually contained in a bubble which is embedded in a larger space. Pioneering work on such a scenario describes a single, minimally coupled scalar field with a potential with two local minima, of which only one is the true global vacuum [116]. The nucleation of a bubble can be interpreted as the tunneling of a region of space from the false vacuum to the true, global vacuum (see figure 5.1). Such a region expands approximately with the speed of light.

The probability per unit time per unit volume of a tunneling event is of the form

$$\frac{\Gamma}{V} \propto e^{-\frac{B}{\hbar}} \left(1 + O(\hbar)\right), \tag{5.1}$$

where $B \propto S_E$ and $S_E$ is the Euclidean action evaluated on the "bounce solution", the solution of the field $\phi$ that interpolates between the false vacuum and the true vacuum. The transition from the false vacuum to the true vacuum is a quantum tunneling effect, which can be seen by the appearance of $\hbar$ in (5.1).

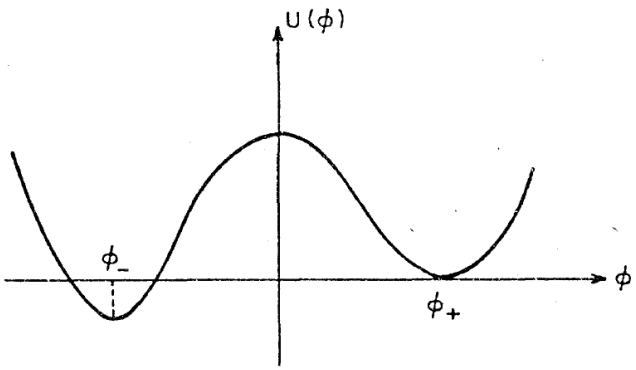


***Figure 5.1:*** *A potential with a true vacuum, associated to the field configuration $\phi = \phi_-$ and a false vacuum associated to the field configuration $\phi = \phi_+$. Source: [116].*

The original analysis by Coleman and De Luccia focused on the scenario of a Minkowski bubble in a de Sitter spacetime and that of an Anti de Sitter bubble in a Minkowski spacetime [116]. Later, other scenarios of an "open universe" bubble in de Sitter were studied [117]. In particular, scenarios in which the scalar field tunnels onto a slow-roll part of the potential were considered (see for example [118]), in which a first phase of inflation (old-inflation) corresponds to the false vacuum configuration of the scalar field and a second phase of inflation (new-inflation) occurs after tunneling to a slow-roll regime of the potential (see figure 5.2). The geometry of the bubble is usually of the FLRW-type (4.1), with hyperbolic spatial slices.

The possibility that our universe emerged as a bubble in a larger space also leads us to the idea that perhaps our universe is just one realization in a huge landscape of bubble universes that are continuously being produced as a consequence of a stochastically varying scalar field during a phase of eternal inflation [120, 121].

The general prediction that the spatial sections in our universe should be hyperbolic on the largest scales is hard, if not impossible, to verify because the primordial inflationary expansion typically redshifts the negative curvature scale far beyond the observable universe [122].

Recently, a rather generic consequence of a bubble universe has been explored [119, 123–125]. In the context of an inflationary landscape one would expect the initial vacuum state for quantum fluctuations in a single inflationary bubble to be entangled with the rest of the universe, leading to a mixed state inside the bubble. Since the Cosmic Microwave Background temperature anisotropies (as well as the large scale structure distribution) probe the statistics of these inflationary quantum

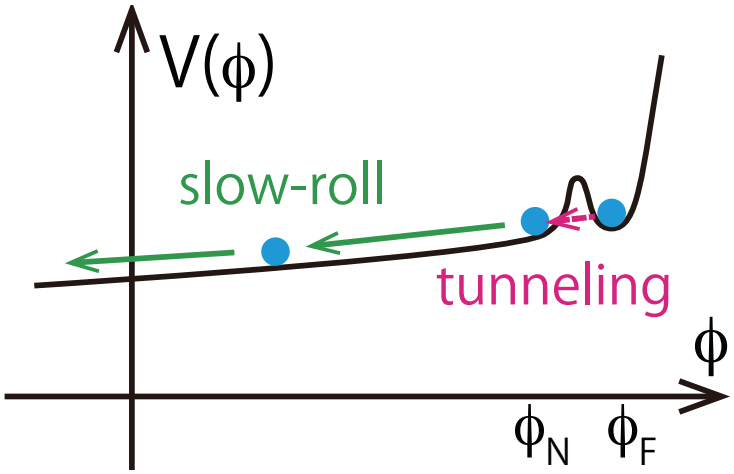


***Figure 5.2:*** *Potential for single-field open inflation. This scenario entails tunneling from the false vacuum field-configuration $\phi_F$ to a slow-roll regime of the potential with initial field configuration $\phi_N$. Source: [119].*

fluctuations, one could imagine uncovering evidence in favor of a mixed initial state that would support the idea that our universe originated from false vacuum decay. This idea warrants a careful study of the actual (observational) potential to constrain departures away from a standard pure initial state for inflationary quantum fluctuations and how these departures relate to the global vacuum state of eternal inflation.

In this chapter we present a first step, triggered by some recent work in this direction [125], in clarifying the connection between the vacuum state of the false, eternally inflating, vacuum and potential departures from the standard Bunch–Davies vacuum state in a hyperbolic bubble. We do not consider any bubble nucleation mechanism in particular, but instead consider a hyperbolic patch of de Sitter as a "toy bubble". In this setup, the difference between entangled and pure states of a scalar field in the bubble can be analyzed relatively easily.

### 5.1.2 Coordinates in hyperbolic patches

In this section we describe how can obtain coordinates on the hyperbolic patches by analytical continuation from Euclidean to Lorentzian signature in the embedding space. We follow [126]. Note that we already discussed the hyperbolic patch in section (4.3). Here we will show how we obtain two hyperbolic patches and a "center patch" (see figure 5.3).

Euclidean de Sitter spacetime is a four-sphere $S^4$ and is obtained from Lorentzian de Sitter by the analytic continuation $X_0 \to i\tilde{X}_0$, such that (4.43) and (4.42) become:

$$\begin{aligned} ds^2 &= d\tilde{X}_0^2 + \sum_{i=1}^{4} dX_i^2, \\ \tilde{X}_0^2 + \sum_{i=1}^{4} X_i^2 &= L_{\text{dS}}^2, \end{aligned} \tag{5.2}$$

which simply represents a four-sphere embedded in flat Euclidean spacetime.

We will use slightly unusual coordinates for the sphere and then consider the analytic continuation back to Lorentzian de Sitter. Consider the following coordinates:

$$\begin{aligned} \tilde{X}_0 &= L_{\text{dS}} \cos\tau \cos\rho \\ X_4 &= L_{\text{dS}} \sin\tau, \\ X_1 &= L_{\text{dS}} \cos\tau \sin\rho \cos\theta \\ X_2 &= L_{\text{dS}} \cos\tau \sin\rho \sin\theta \cos\varphi \\ X_3 &= L_{\text{dS}} \cos\tau \sin\rho \sin\theta \sin\varphi, \end{aligned} \tag{5.3}$$

with $\tau \in [-\frac{\pi}{2}, \frac{\pi}{2}]$ and $\rho \in [0, \pi]$. In these coordinates the metric is given by

$$d\tilde{s}^2 = L_{\text{dS}}^2 \left( d\tau^2 + \cos^2\tau (d\rho^2 + \sin^2\rho d\Omega^2) \right). \tag{5.4}$$

The analytic continuation back to Lorentzian de Sitter, $\tilde{X}^0 \to iX^0$, can be done in three different ways on the level of the intrinsic coordinates $\tau, \rho, \theta$ and $\varphi$, which corresponds to three different patches of de Sitter (see figure 5.3). These three regions will be referred to as $R$, $C$, and $L$, and their coordinates are related to the Euclidean coordinates by [126]:

$$\begin{aligned} &\begin{cases} t_{\text{R}} &= i(\tau - \pi/2), & (t_{\text{R}} \geq 0) \\ r_{\text{R}} &= i\rho, & (r_{\text{R}} \geq 0) \end{cases} \\ &\begin{cases} t_{\text{C}} &= \tau, & (\pi/2 \geq t_C \geq -\pi/2) \\ r_{\text{C}} &= i(\rho - \pi/2), & (\infty > r_{\text{C}} > -\infty) \end{cases} \\ &\begin{cases} t_{\text{L}} &= i(-\tau - \pi/2), & (t_{\text{L}} \geq 0) \\ r_{\text{L}} &= i\rho, & (r_{\text{L}} \geq 0) \end{cases} \end{aligned} \tag{5.5}$$

and their metrics are given by

$$ds_{\text{R}}^2 = L_{\text{dS}}^2 \left( -dt_{\text{R}}^2 + \sinh^2 t_{\text{R}} (dr_{\text{R}}^2 + \sinh^2 r_{\text{R}} d\Omega^2) \right), \tag{5.6}$$

$$ds_{\text{C}}^2 = L_{\text{dS}}^2 \left( dt_{\text{C}}^2 + \cos^2 t_{\text{C}} (-dr_{\text{C}}^2 + \cosh^2 r_{\text{C}} d\Omega^2) \right), \tag{5.7}$$

$$ds_{\text{L}}^2 = L_{\text{dS}}^2 \left( -dt_{\text{L}}^2 + \sinh^2 t_{\text{L}} (dr_{\text{L}}^2 + \sinh^2 r_{\text{L}} d\Omega^2) \right), \tag{5.8}$$

where $L_{\text{dS}}^{-1} = H$.

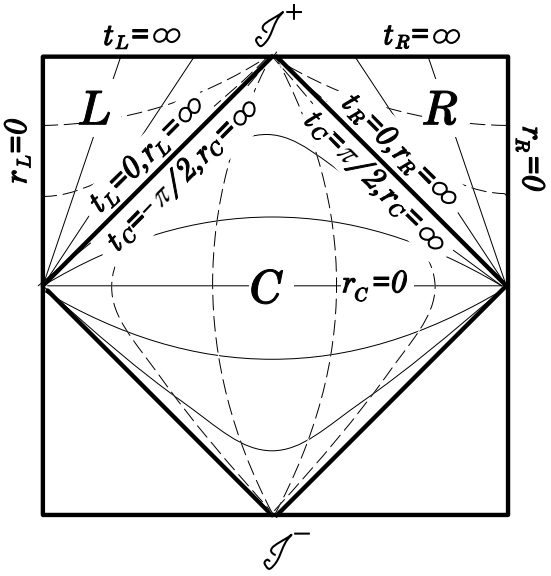


***Figure 5.3:*** *The left and right hyperbolic patches (5.8,5.6) and the center patch (5.7) on a Penrose diagram of de Sitter spacetime. Source: [126]*

## 5.2 A generalized hyperbolic embedding

In this section we will show a relation between the planar patch and the hyperbolic patches. Already in section (4.3) we noted that the embedding equation of de Sitter spacetime (4.42,4.43) is invariant under $O(1,4)$ transformations, corresponding to the isometry group of $dS_4$.[1] In this section we will show that an infinite boost in the $(X_0, X_4)$-plane, in combination with a coordinate transformation, relates a hyperbolic patch to the planar patch. This map allows us to compare mode-functions and the respective vacuum states on these different patches. Note that we set $L_{\rm dS} = 1$ in this section for notational convenience. We start by restating the definition of the planar and hyperbolic coordinate sets as discussed in section (4.3). The planar coordinates presented in (4.52,4.53) are defined by:

$$\begin{aligned} X_0 + X_4 &= e^{t_p} \\ X_0 - X_4 &= \left(r_p^2\, e^{2t_p} - 1\right) e^{-t_p} \\ \sum_{i=1}^{3} X_i^2 &= r_p^2\, e^{2t_p}\,. \end{aligned} \tag{5.9}$$

[1] From here we will only consider the continuous isometries of de Sitter, captured by $SO(1,4)$.

Note that we presented these coordinates in a slightly different way, making explicit that this patch covers only the part of the hyperboloid with $X_0 + X_4 \geq 0$. We also added a subscript $p$ (for planar) to distinguish the planar coordinates from the hyperbolic coordinates in what follows. In these coordinates the metric is given by (see also 4.53):

$$ds^2 = -dt_p^2 + e^{2t_p}\left[dr_p^2 + r_p^2\, d\Omega_2^2\right] \tag{5.10}$$

with $-\infty < t_p < +\infty$ and $r > 0$. Since $X_0 + X_4 \geq 0$ these coordinates only cover the upper half diagonal part in the $(X_0, X_4)$-plane. Besides the obvious $SO(3)$ isometries, the boost symmetries of the embedding space are realized on the planar metric as an isometry involving a particular combination of time translation and spatial scaling[2]. Because inflation redshifts away any existing spatial curvature present initially, this coordinate set should be an excellent approximation to derive the late-time effects of a sustained phase of cosmological inflation. Nevertheless, one could imagine a situation where our universe has originated from a tunneling event out of an eternally inflating false vacuum[3]. The nucleated bubble would have negatively curved spatial sections [116, 117], leading to the hyperbolic coordinate set (see also 4.55,4.58):

$$\begin{aligned} X_0 + X_4 &= \cosh t_h + \sinh t_h\, \cosh r_h \\ X_0 - X_4 &= -\cosh t_h + \sinh t_h\, \cosh r_h \\ \sum_{i=1}^{3} X_i^2 &= \sinh^2(t_h)\, \sinh^2(r_h)\,. \end{aligned} \tag{5.11}$$

In these coordinates, the de Sitter metric is given by:

$$ds^2 = -dt_h^2 + \sinh t_h{}^2\left[dr_h^2 + \sinh^2 r_h\, d\Omega_2^2\right] \tag{5.12}$$

where $0 \leq t_h < +\infty$ and $r_h > 0$. The coordinate singularity at $t_h = 0$ can be interpreted in the context of false vacuum decay as the creation of the open inflationary bubble. Note that $t_h = 0$ corresponds to $X_0 = 0$ (and $X_4 = 1$, $X_i = 0$ for $i = 1, 2, 3$): the bubble nucleation time from the point of view of the embedding space. The spatial sections correspond to constant negative curvature slices that exhibit an $SO(1,3)$ isometry. We will in fact be interested in a one-parameter generalization of this hyperbolic coordinate embedding, obtained by boosting in the $X_0$–$X_4$ plane of the 5–dimensional embedding space. Combined with rotations these transformation allow one to move the 'nucleation' time of the hyperbolic bubble to any specific point on the embedding surface. Just performing

[2] More precisely, it corresponds with the isometry $t \to t + \gamma$ and $r \to e^{-\gamma} r$ of the planar de Sitter metric.

[3] Moreover, in the nineties models of open inflation were of particular interest, independent of whether their origin was due to tunneling [118, 127].

a Lorentz boost in the $X_0$–$X_4$ plane will change the nucleation time (and position in $X_1$), which yields the following generalized hyperbolic coordinate set

$$\begin{aligned} X_0 + X_4 &= e^{-\gamma} \left[\cosh t_h + \sinh t_h \, \cosh r_h\right] \\ X_0 - X_4 &= e^{\gamma} \left[-\cosh t_h + \sinh t_h \, \cosh r_h\right] \\ \sum_{i=1}^{3} X_i^2 &= \sinh^2 t_h \, \sinh^2 r_h \end{aligned} \tag{5.13}$$

where $\gamma$ is the boost parameter. This generalized hyperbolic solution of the embedding equation will of course lead to the same induced metric, but the nucleation time and position of the associated bubble in the embedding space have now shifted to $X_0 = -\sinh\gamma$ and $X_4 = \cosh\gamma$ respectively. Moreover, since $t_h \geq 0$ one finds that $X_0 + X_4 \geq e^{-\gamma}$, restricting the hyperbolic section to the upper right diagonal part in the $(X_0, X_4)$-plane, which overlaps with, but for any finite $\gamma$ is smaller than, the part of de Sitter covered by planar coordinates. This is depicted in figure 5.4. One can verify that in the limit of infinite $\gamma$ the planar and hyperbolic coordinates cover the same region of de Sitter space, which is consistent with the observation that in this limit the hyperbolic nucleation time in the embedding space is shifted to $X_0 \to -\infty$.

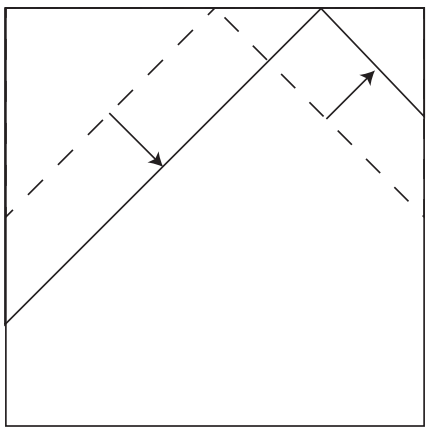

***Figure 5.4:*** *Conformal diagram of $dS_4$ with the left- and right-hyperbolic patch as the upper-left resp. upper-right triangles. The dashed line is the unboosted situation $\gamma = 0$. For finite $\gamma$ (solid line), we see that that nucleation time of the left bubble gets pushed to earlier times, and vice versa for the right bubble. In the limit of $\gamma \to \infty$, we can see that the left bubble will cover the entire upper-left triangle of the conformal diagram, coinciding with the planar patch.*

The generalization of the hyperbolic coordinate set introduced above allows us to explicitly relate the planar and hyperbolic sections of de Sitter space. Since the

two coordinate sets cover the same region in the $\gamma \to \infty$ limit, there should exist a one-to-one mapping between the coordinates in that limit. More precisely, we would like to introduce a new set of hyperbolic coordinates that are to be kept fixed in the limit $\gamma \to \infty$, and that in the limit exactly reproduce the planar coordinate embedding solution. Note that any (constant) shift or rescaling of the hyperbolic embedding coordinates is still a solution of the embedding equation, but will change the expression for the induced metric. Since we expect the range of the hyperbolic time coordinate to be extended to $-\infty$ and the negative curvature to be scaled away, we redefine

$$\tilde{t}_h \equiv t_h - \gamma \; ; \; \tilde{r}_h \equiv \frac{1}{2} r_h \, e^{\gamma} \, . \tag{5.14}$$

This leaves us with the following generalized hyperbolic solution to the embedding equation

$$\begin{aligned} X_0 + X_4 &= e^{-\gamma} \left[ \cosh\left(\tilde{t}_h + \gamma\right) + \sinh\left(\tilde{t}_h + \gamma\right) \cosh\left(2\tilde{r}_h \, e^{-\gamma}\right) \right] \\ X_0 - X_4 &= -e^{\gamma} \left[ \cosh\left(\tilde{t}_h + \gamma\right) - \sinh\left(\tilde{t}_h + \gamma\right) \cosh\left(2\tilde{r}_h \, e^{-\gamma}\right) \right] \\ \sum_{i=1}^{3} X_i^2 &= \sinh^2\left(\tilde{t}_h + \gamma\right) \sinh^2\left(2\tilde{r}_h \, e^{-\gamma}\right) \end{aligned} \tag{5.15}$$

where $-\gamma \leq \tilde{t}_h < +\infty$. For finite $\gamma$ the shift in hyperbolic time and the rescaling of the hyperbolic radius (or equivalently the inverse rescaling of hyperbolic momentum) does obviously not affect any hyperbolic patch observables, but it does allow one to analyze the infinite boost limit in a simple and useful way. The induced hyperbolic metric now reads

$$\begin{aligned} ds^2 &= -d\tilde{t}_h^2 + \sinh\left(\tilde{t}_h + \gamma\right)^2 \left[ 4e^{-2\gamma} \, d\tilde{r}_h^2 + \sinh\left(2\tilde{r}_h e^{-\gamma}\right)^2 d\Omega_2^2 \right] \\ &\overset{\gamma\to\infty}{=} -d\tilde{t}_h^2 + e^{2\tilde{t}_h} \left[ d\tilde{r}_h^2 + \tilde{r}_h^2 \, d\Omega_2^2 \right] + O(e^{-\gamma}) \, . \end{aligned} \tag{5.16}$$

In the second line we performed the limit $\gamma \to \infty$, keeping $\tilde{t}_h$ and $\tilde{r}_h$ fixed, showing that (5.15) exactly reduces to the planar embedding solution (5.9). Note that all the $\gamma$ dependence in the induced metric is removed and one is left with precisely the planar line-element (5.10) in terms of the coordinates $\tilde{t}_h$ and $\tilde{r}_h$.

For any finite boost parameter $\gamma$ global de Sitter space is covered by two (adjacent) hyperbolic sections, see figure 5.4. The other hyperbolic embedding can be obtained by changing the sign of $X_4$, resulting in the interchange of the expressions for $X_0 + X_4$ and $X_0 - X_4$ in (5.11). Acting with the same boost on this second hyperbolic embedding results in the opposite effect, moving the nucleation time to $X_0 \to +\infty$. The opposite minus infinity boost should instead reduce to another planar section (with $X_0 + X_4$ and $X_0 - X_4$ in (5.9) interchanged), suggesting that

the redefined coordinates in this case should read

$$\tilde{t}_h \equiv t_h + \gamma \; ; \; \tilde{r}_h \equiv \frac{1}{2} r_h \, e^{-\gamma} \, . \tag{5.17}$$

Putting this together we obtain for the adjacent hyperbolic section the following generalized embedding

$$\begin{aligned} X_0 + X_4 &= -e^{-\gamma} \left[ \cosh\left(\tilde{t}_h - \gamma\right) - \sinh\left(\tilde{t}_h - \gamma\right) \cosh\left(2\tilde{r}_h \, e^{\gamma}\right) \right] \\ X_0 - X_4 &= e^{\gamma} \left[ \cosh\left(\tilde{t}_h - \gamma\right) + \sinh\left(\tilde{t}_h - \gamma\right) \cosh\left(2\tilde{r}_h \, e^{\gamma}\right) \right] \\ \sum_{i=1}^{2} X_i^2 &= \sinh^2\left(\tilde{t}_h - \gamma\right) \sinh^2\left(2\tilde{r}_h \, e^{\gamma}\right) \end{aligned} \tag{5.18}$$

where now $\gamma \leq \tilde{t}_h < +\infty$. The induced hyperbolic metric in this case is obtained by just replacing $\gamma$ with $-\gamma$ in (5.16). By construction the limit $\gamma \to \infty$ should instead collapse and in a sense remove the adjacent hyperbolic section. Clearly, in the opposite $\gamma \to -\infty$ the roles of the two hyperbolic sections are reversed.

Having established this explicit relation between hyperbolic and planar coordinates, we can now use it to better understand and connect their respective vacua, which should be different for any finite value of $\gamma$. In particular, the planar Bunch–Davies state is known to be equivalent to the unique and de Sitter invariant Euclidean vacuum[4]. On the other hand, any pure hyperbolic vacuum state is defined on a negatively curved spatial slice that is not a de Sitter Cauchy surface. This means that the Bunch–Davies state in a single hyperbolic patch can only be described by an appropriately defined mixed state; see figures 5.5 and 5.6. The mixed state defined on one of the two (conjugate) hyperbolic sections reproducing the Bunch–Davies state was first constructed in [126] and was subsequently used in [128] to compute the reduced density matrix and the corresponding entanglement entropy for a single hyperbolic section (see also section 5.5).

One application of the one-parameter family of hyperbolic de Sitter foliations is that one can confirm that the natural choice for a hyperbolic vacuum reduces to the planar Bunch–Davies state in the limit $\gamma \to \infty$. Secondly, one could attempt to generalize the entangled expression for wave-functions of the Bunch–Davies state, with support on both the left and right hyperbolic section, and work out its dependence on the embedding boost parameter. In the $\gamma \to \infty$ limit this should reduce to the pure planar Bunch–Davies state, implying that the reduced density matrix carries some non-trivial $\gamma$ dependence to make sure the associated entanglement entropy vanishes in the strict $\gamma \to \infty$ limit (see also section 5.5).

[4]The invariance of the Bunch–Davies vacuum under de Sitter isometries strictly speaking fails for massless fields, but since this subtlety does not affect our results we will ignore it from now on.

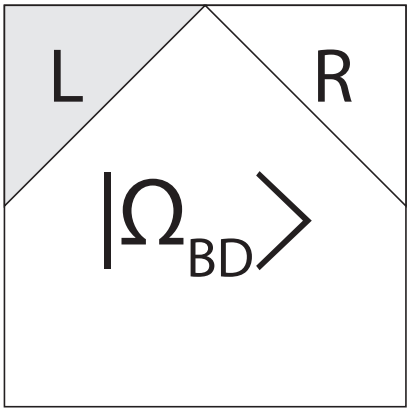


**Figure 5.5:** *Conformal diagram of $dS_4$ with the left- and right-hyperbolic patch shown. As neither patch contains a Cauchy slice of the full $dS_4$, restricting the Bunch-Davies vacuum to one of them will yield a mixed state.*

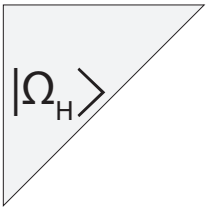


**Figure 5.6:** *An observer confined to live in the left-hyperbolic patch (a bubble universe) can define his own pure hyperbolic vacuum. This state will differ significantly from the mixed state resulting from a restriction of the Bunch-Davies state to this bubble.*

To summarize, we established that the infinite boost limit of a hyperbolic de Sitter patch (and as a consequence also its corresponding vacuum state) reduces to the planar de Sitter patch (and the Bunch–Davies vacuum). This appears to be similar to an observation made in [129] where the static vacuum, understood as the empty state for a corresponding free-falling observer, was also argued to reduce to the Bunch–Davies state in the infinite boost limit. Note that to each hyperbolic patch one can associate a free-falling observer in one of the two center regions in between the hyperbolic patches that never intersects either one of them. These time-like curves are indeed connected to each other by the same embedding space boosts [130]. To complete the argument one needs to confirm that the static vacuum state associated to this free-falling observer is connected to the hyperbolic vacuum state. Note that (for $\gamma = 0$) the center region in between the hyperbolic patches is usually covered by coordinates that are obtained from the hyperbolic coordinates as follows $t_h = i(t_{\rm C} - \frac{\pi}{2})$ and $r_h = r_{\rm C} + i\frac{\pi}{2}$, resulting in the following center region metric

$$ds^2 = dt_{\rm C}^2 + \cos t_{\rm C}{}^2 \left[-dr_{\rm C}^2 + \cosh r_{\rm C}{}^2 d\Omega^2\right] , \tag{5.19}$$

where $r_{\rm C}$ is now a time-like coordinate. Each of the two center regions clearly identifies a causal diamond belonging to the free-falling observer of interest (see

figures 5.3 and 4.6).

## 5.3 The hyperbolic vacuum

After having established a limit to obtain the planar embedding and coordinates, let us now remind the reader of the standard positive frequency modes on a single hyperbolic patch [126], as if it were the entire universe (see figure 5.6). The scalar wave equation for the hyperbolic patch of de Sitter (5.12) reads

$$\left[\frac{1}{\sinh^3 t}\partial_t \sinh^3 t\partial_t - \frac{1}{\sinh^2 t}\nabla^2_{\mathcal{H}^3} + m^2 L^2_{\rm dS}\right]\phi = 0 \tag{5.20}$$

where we defined the Laplacian on the three-hyperboloid

$$\nabla^2_{\mathcal{H}^3} = \frac{1}{\sinh^2 r}\partial_r(\sinh^2 r\partial_r) + \frac{1}{\sinh^2 r}\nabla^2_{\mathcal{S}^2}. \tag{5.21}$$

A natural set of solutions to the hyperbolic equations of motion (5.20) is given by

$$\frac{1}{\sinh(t)}P^{ip}_{\nu-\frac{1}{2}}(\cosh(t))\,Y_{plm}(r,\Omega) \tag{5.22}$$

where it is customary to define $\nu = \sqrt{\frac{9}{4} - \frac{m^2}{H^2}}$. The quantum numbers $l, m$ label the usual $SO(3)$ irreps, and together with the continuous quantum number $p$ it completely specifies the hyperbolic momentum. Furthermore, $P^{ip}_{\nu-\frac{1}{2}}$ are the associated Legendre functions of the second kind and the $Y_{plm}$ are the orthonormal eigenfunctions of the hyperbolic Laplacian (5.21)

$$\nabla^2_{\mathcal{H}^3}Y_{plm}(r,\Omega) = -(1+p^2)Y_{plm}(r,\Omega). \tag{5.23}$$

For $\nu > \frac{1}{2}$, there is in fact a supplementary set of solutions with $p = i(\nu - \frac{1}{2})$ [126]. These so-called "super-curvature modes" will not be of interest for the purposes that are considered here, where our main focus will be on potential signatures in the large ("sub-curvature) momentum limit. We refer to [131] for an interesting account on the role and interpretation of these super-curvature modes.

Switching to conformal time $\eta$ we can write the metric of the hyperbolic slice as

$$ds^2 = L^2_{\rm dS}\sinh^2(t(\eta))\left(-d\eta^2 + dr^2 + \sinh^2(r)d\Omega_2^2\right), \tag{5.24}$$

where $\eta = \ln(\tanh(\frac{t}{2}))$, or equivalently $\cosh t = -\frac{1}{\tanh\eta}$ and $-\infty < \eta < 0$. In terms of the conformal time $\eta$ we find that in the far past $\eta \to -\infty$ and in the limit of large momenta $p \gg 1$ one obtains

$$P^{ip}_1\left(-\frac{1}{\tanh\eta}\right) \propto e^{-ip\eta}\left(1 - \frac{i}{p\tanh\eta}\right) \to e^{-ip\eta}, \tag{5.25}$$

so we can identify these mode functions with the "natural hyperbolic vacuum": they define a state that is empty in the far past for large momenta (see also subsection 4.4.3). As expected, in the limit $\gamma \to \infty$ that we introduced in the previous section (5.17) the mode functions reduce to the standard Bunch–Davies mode functions in flat slicing, explicitly connecting the hyperbolic and planar patch vacua in this limit

$$\lim_{\gamma\to\infty} P_1^{ip}(\cosh(\tilde{t}+\gamma)) \propto e^{-i\tilde{p}\tilde{\eta}}\left(1-\frac{i}{\tilde{p}\tilde{\eta}}\right). \tag{5.26}$$

For all the details we refer the reader to the appendix 5.A.3, but it should be clear that the tildes on the coordinates in the above equation relate to the redefined hyperbolic coordinates that are kept fixed in the infinite boost limit. The mode functions (5.22) must of course be properly normalized, enforcing $[\hat{b}_{plm}, \hat{b}^\dagger_{plm}] = \delta_{ll'}\delta_{mm'}\delta(p-p')$, implying the following Klein-Gordon inner product (see also section 4.4)

$$\langle \phi_{plm}, \phi_{plm}\rangle_{\text{KG}} = \delta_{ll'}\delta_{mm'}\delta(p-p') \tag{5.27}$$

giving (see appendix 5.A.2)

$$\begin{aligned} N^2_{P^p} &\equiv \langle P^{ip}, P^{ip}\rangle_{\text{KG}} \\ &= \frac{1}{H^2}\frac{2\sinh(\pi p)}{\pi}. \end{aligned} \tag{5.28}$$

With the help of (5.28) we can now express the field operator in a single hyperbolic patch as (keeping in mind that we are ignoring super-curvature modes)

$$\phi(t,r,\Omega) = \int_0^\infty dp \sum_{l=0}^{\infty}\sum_{m=-l}^{l} \frac{1}{N_{P^p}}\frac{1}{\sinh(t)}\left(\hat{b}_{plm} P^{ip}_{\nu-\frac{1}{2}}(\cosh(t))\, Y_{plm}(r,\Omega) + \text{h.c.}\right) \tag{5.29}$$

defining the natural hyperbolic vacuum state $|\Omega_H\rangle$ as

$$\hat{b}_{plm}|\Omega_H\rangle = 0 \quad \forall p,l,m. \tag{5.30}$$

This hyperbolic vacuum state can be understood as a natural choice in an isolated (stand-alone) open inflationary universe, as described in subsection (4.4.3), as it is empty in the far past and reduces to the planar Bunch–Davies vacuum state in the infinite boost limit.

## 5.4 The Bunch-Davies vacuum

In subsection (4.4.3) we described the Bunch-Davies state. It is the de Sitter invariant vacuum that can be associated to the unique Euclidean vacuum. In

subsection (4.4.2) we described how the Wightman function (4.71) characterizes a vacuum state and how it can be expressed in terms of a sum of modes (4.72). In [126] the set of hyperbolic mode functions that correspond to the Bunch-Davies vacuum are identified by explicitly checking whether they reproduce the Bunch-Davies Wightman function (4.82). In this section we will review the results of [126]. More details can be found in those papers and in appendix 5.A.

The most important observation is that mode functions of one of the hyperbolic patches (5.22) do not correspond to regular mode functions on the full (Euclidean) de Sitter space. In [126] the hyperbolic mode functions are analytically continued to the other hyperbolic patch, allowing them to construct a set of regular mode functions that can cover all of de Sitter space as follows

$$\chi_p^{(R)} = \begin{cases} P^{ip}_{\nu-\frac{1}{2}}(z) & \text{for } z \in R \\ \frac{i\sin(\pi(\nu-\frac{1}{2}))}{\sinh(p\pi)} P^{ip}_{\nu-\frac{1}{2}}(z) + \frac{i\sin(\pi(ip+\nu-\frac{1}{2}))e}{\sinh(\pi p)} \frac{\Gamma[\nu+\frac{1}{2}+ip]}{\Gamma[\nu+\frac{1}{2}-ip]} P^{-ip}_{\nu-\frac{1}{2}}(z) & \text{for } z \in L \end{cases} \tag{5.31}$$

These mode functions do not yet describe the Euclidean or Bunch–Davies vacuum, which can for instance be concluded by the fact that they are not (anti-)symmetric under the transformation $R \leftrightarrow L$. It turns out that the linear combinations $\chi_{\mathrm{R}} \pm \chi_{\mathrm{L}}$ correspond to the proper mode functions associated with the Euclidean or Bunch–Davies vacuum, as was proved by computing the Wightman function [126]. The (still to be normalized) mode functions are linear combinations of the associated Legendre functions

$$\chi_{p,\sigma} = \begin{cases} \alpha^{\sigma}_{p,R} P^{ip}_{\nu-\frac{1}{2}}(z) + \beta^{\sigma}_{p,R} P^{-ip}_{\nu-\frac{1}{2}}(z) & \text{for } x \in R \\ \alpha^{\sigma}_{p,L} P^{ip}_{\nu-\frac{1}{2}}(z) + \beta^{\sigma}_{p,L} P^{-ip}_{\nu-\frac{1}{2}}(z) & \text{for } x \in L \end{cases} \tag{5.32}$$

where $\sigma = \pm 1$[5] and $z = \cosh(t)$; the expressions for the $\alpha$'s and $\beta$'s are given in (5.71). We stress that the associated Legendre functions $P$ in (5.32) do not have to be analytically continued any further[6]. The full field expansion, with creation and annihilation operators $\hat{a}_{\sigma plm}$ satisfying $[\hat{a}_{\sigma plm}, \hat{a}^{\dagger}_{\sigma' p' l' m'}] = \delta_{\sigma\sigma'}\delta_{ll'}\delta_{mm'}\delta(p-p')$, is given by:

$$\phi(t,r,\Omega) = \int dp \sum_{\sigma=\pm 1} \sum_{l,m} \frac{1}{N_{\chi^{p\sigma}}} \left(\hat{a}_{\sigma plm} \chi_{p,\sigma}(z) Y_{plm}(r,\Omega) + \text{h.c.}\right) \tag{5.33}$$

where $N_{\chi^{p\sigma}}$ is the Klein–Gordon norm consistent with the commutation relations[7].

[5] $\sigma = \pm 1$ is related to the combination $\chi_P^{(L)} \pm \chi_P^{(R)}$.

[6] They are constituents of $\chi_{\mathrm{L}}$ and $\chi_{\mathrm{R}}$, which are already regular everywhere. This is different from [125].

[7] Strictly speaking the expression (5.33) is incomplete, since we should also include the "zero mode". For our purposes this will however not affect the results.

In appendix 5.A.2 we show that the normalization $N_{\chi^{p\sigma}}$ is given by

$$\begin{aligned} N^2_{\chi^{p\sigma}} &\equiv \langle \chi_{p,\sigma} Y_{plm}, \chi_{p,\sigma} Y_{plm} \rangle_{\rm KG} \\ &= \sum_{q=L,R} \left( \alpha^\sigma_{p,q} \bar{\alpha}^\sigma_{p,q} - \beta^\sigma_{p,q} \bar{\beta}^\sigma_{p,q} \right) N^2_{Pp} \end{aligned} \tag{5.34}$$

where $\bar{\alpha}, \bar{\beta}$ denote the complex conjugates of $\alpha, \beta$. We conclude that the Bunch–Davies vacuum state, is defined as[8]

$$\hat{a}_{\sigma plm} |\Omega_{\rm BD}\rangle = 0 \quad \forall\, \sigma, p, l, m. \tag{5.35}$$

Now let us describe the relation between the creation and annihilation operators of the modes (5.32) and the creation and annihilation operators of hyperbolic modes (5.22). Both field expansions (5.33) and (5.29) are linear combinations of associated Legendre functions. We can find the relation between the $\hat{a}_{\sigma plm}$ and the $\hat{b}_{qplm}$ $(q = L, R)$ by comparing the coefficients

$$\hat{b}_{qplm} = \sum_{\sigma=\pm 1} \frac{N_{Pp}}{N_{\chi_{p,\sigma}}} \left( \alpha^\sigma_{p,q} \hat{a}_{\sigma plm} + \bar{\beta}^\sigma_{p,q} \hat{a}^\dagger_{\sigma pl-m} \right). \tag{5.36}$$

Given (5.34,5.36), they enforce

$$\begin{aligned} &\left[ \hat{a}_{\sigma plm}, \hat{a}^\dagger_{\sigma' p' l' m'} \right] = \delta(p-p') \delta_{\sigma\sigma'} \delta_{mm'} \delta_{ll'} \\ &[\hat{a}_{\sigma plm}, \hat{a}_{\sigma' p' l' m'}] = 0 \end{aligned} \Bigg\} \Leftrightarrow$$

$$\begin{cases} \left[ \hat{b}_{qplm}, \hat{b}^\dagger_{q' p' l' m'} \right] = \delta(p-p') \delta_{mm'} \delta_{ll'} \delta_{qq'} \\ \left[ \hat{b}_{qplm}, \hat{b}_{q' p' l' m'} \right] = 0 \end{cases}. \tag{5.37}$$

For more details we refer to [126] and the appendices. The above relationship confirms that the normalizations (5.28) and (5.34) are consistent and in particular that the right normalization for the hyperbolic mode functions is given by (5.28). This will be of importance when comparing the predictions for the power–spectrum of the two different states under consideration: the pure hyperbolic vacuum and the Bunch–Davies state (as we will do in section 5.6). The latter is a mixed state from the point of view of a single hyperbolic patch, due to the entanglement between the two hyperbolic patches in the Bunch–Davies vacuum.

Let us here remind the reader that we would like to compare the predictions for the expectation values of (scalar field) quantum fluctuations in the two different

[8] As before we ignore the super-curvature modes.

states that were introduced above. A priori different initial states give different predictions for the cosmic microwave background temperature anisotropies and the large scale structure distribution. We should stress that we are technically not considering an actual bubble nucleation event, where more intricate and model-dependent bubble wall physics could lead to additional effects [132, 133], see also [134]. Instead, we will work under the assumption that the two states that were introduced capture an essential difference that is generic: the entangled nature of the Bunch–Davies vacuum implies a mixed initial state, whereas the hyperbolic vacuum corresponds to a pure state on a single hyperbolic section.

We should add that one might anticipate the differences between the two states to only become visible at small hyperbolic momentum $p \lesssim 1$, i.e. scales comparable to the hyperbolic curvature. However, even small curvature suppressed changes in the initial state might be enhanced in the (nonlinear) bi–spectrum, as has been pointed out and analyzed in [135, 136] and for a certain generic type of mixed state in [123]. This motivates the computation of the bi–spectrum. In [1], we do consider the bi–spectrum, but the calculation of the bi-spectrum is *not* part of this thesis.

## 5.5 Pure and entangled states

In sections (5.3) and (5.4) we discussed the hyperbolic vacuum and the Bunch-Davies state respectively, and the mode functions associated with these states. From the point of view of a single hyperbolic patch, the Bunch-Davies state is mixed, entangled state. In this section we will derive the reduced density matrix for a hyperbolic patch in the Bunch-Davies state. This will be a summary of [128].

For a detailed introduction of entanglement entropy, see section (1.3) of Part I of the thesis. Here we will repeat the basics. If a quantum system can be divided into two parts, $A$ and $B$, such that the Hilbert space factorizes as

$$\mathcal{H} = \mathcal{H}_A \otimes \mathcal{H}_B, \tag{5.38}$$

then we can define a reduced density matrix. If the density matrix $\rho$ describes the full system $A \cup B$, then the reduced density matrix $\rho_A$ of $A$ is defined as:

$$\rho_A = \mathrm{Tr}_{\mathcal{H}_B}\{\rho\}, \tag{5.39}$$

where the trace is taken over the Hilbert space associated to subsystem $B$. The expectation values of operators that have support on $A$ and are trivial on $B$ can be calculated with $\rho_A$. The entanglement entropy, a measure of entanglement, is given by:

$$S_A = -\mathrm{Tr}_{\mathcal{H}_A}\{\rho_A \log \rho_A\}. \tag{5.40}$$

For our purposes, (spacelike Cauchy surfaces in-) the left (L) and right (R) hyperbolic patches serve as our "subsystems". If the state of the "full system" is the Bunch-Davies state, then the density matrix is given by:

$$\rho = |\Omega_{\rm BD}\rangle\langle\Omega_{\rm BD}|. \tag{5.41}$$

In order to determine the entanglement entropy, we must find a suitable basis of states to trace over. The hyperbolic vacuum (5.30) and its excitations constitute good bases for the left and right hyperbolic patches. Relation (5.36) allows us to write the state (5.41) with respect to these bases, which we will illustrate below. Here we will only consider the limited case of the massless scalar field, for which the analysis simplifies considerably. For a description of the entanglement entropy in the case of a massive scalar field, we direct the reader to [128]. Also note that we discard the super-curvature modes in this discussion, because there is no clear way to decompose their associated excitations as in (5.38).[9] The super-curvature mode corresponds to a particular imaginary value $p = i\nu'$ of the comoving momentum. The density matrix should respect the remaining $SO(1,3)$ symmetry of the hyperbolic patches, so it is diagonal in $p$ and the super-curvature mode will not be entangled with sub-curvature modes. Also note that the set of super-curvature modes, labeled by $p = i\nu'$ and $l, m$, has measure zero, compared to the continuous part of the spectrum with real valued $p$.

A natural basis to trace over in the left and right hyperbolic patches, are the "number states"

$$\begin{aligned} \{|n_{\rm L}\rangle\} \qquad &\text{with} \qquad |n_{\rm L}\rangle = \frac{\left(\hat{b}^\dagger_{\rm L}\right)^n}{\sqrt{n!}}|\Omega_{\rm H,L}\rangle, \\ \{|n_{\rm R}\rangle\} \qquad &\text{with} \qquad |n_{\rm R}\rangle = \frac{\left(\hat{b}^\dagger_{\rm R}\right)^n}{\sqrt{n!}}|\Omega_{\rm H,R}\rangle, \end{aligned} \tag{5.42}$$

where the subscripts $p, l, m$ are suppressed for simplicity. The full Hilbert space is the tensor product of these Fock spaces for the left and right hyperbolic patch (5.38). Before we can can trace out degrees of freedom, we need to know (5.41) in terms of these bases.

In [128] an ansatz is made for the Bunch-Davies state $|\Omega_{\rm BD}\rangle$ as an excitation of the left- and right hyperbolic vacua:

$$\begin{aligned} |\Omega_{\rm BD}\rangle &\propto e^{\frac{1}{2}m^{ij}\hat{b}^\dagger_i\hat{b}^\dagger_j}|\Omega_{\rm H,L}\rangle \otimes |\Omega_{\rm H,R}\rangle, \\ m^{ij}\hat{b}_i\hat{b}_j &= m^{\rm LL}\left(\hat{b}^\dagger_{\rm L}\right)^2 + m^{\rm RR}\left(\hat{b}^\dagger_{\rm R}\right)^2 + 2m^{\rm LR}\hat{b}^\dagger_{\rm L}\otimes\hat{b}^\dagger_{\rm R}. \end{aligned} \tag{5.43}$$

[9] In the context of bubble nucleation, it is argued that at least a subset of super-curvature modes correspond to pure gauge degrees of freedom [137, 138]. Here we consider a scalar field on a fixed background, so such an argument does not apply to our toy model of a bubble.

The coefficients $\{m^{ij}\}$ can be determined by demanding that the state is annihilated by the Bunch-Davies annihilation operators (5.35). We can use relation (5.36) between the Bunch-Davies creation and annihilation operators $\{\hat{a}^\dagger_\pm, \hat{a}_\pm\}$ and the hyperbolic creation and annihilation operators $\{\hat{b}^\dagger_{L/R}, \hat{b}_{L,R}\}$. In fact, this relation gives $\hat{b}_{L/R}$ in terms of the $\{\hat{a}^\dagger_\pm, \hat{a}_\pm\}$. The relation (5.36) needs to be inverted, which is equivalent to inverting a four by four matrix. This problem has a (linear-) solution,

$$\hat{a}_\pm = \hat{a}_\pm\left(\hat{b}^\dagger_{\rm L}, \hat{b}^\dagger_{\rm R}, \hat{b}_{\rm L}, \hat{b}_{\rm R}\right), \tag{5.44}$$

for which an explicit expression can be found in [128]. The general idea is that the coefficients $\{m^{ij}\}$ must solve the following equations:

$$\begin{aligned} 0 &= \hat{a}_\pm|\Omega_{\rm BD}\rangle \\ &= \hat{a}_\pm\left(\hat{b}^\dagger_{\rm L}, \hat{b}^\dagger_{\rm R}, \hat{b}_{\rm L}, \hat{b}_{\rm R}\right)|\Omega_{\rm BD}\rangle \\ &= \hat{a}_\pm\left(\hat{b}^\dagger_{\rm L}, \hat{b}^\dagger_{\rm R}, \hat{b}_{\rm L}, \hat{b}_{\rm R}\right) e^{\frac{1}{2}m^{ij}\hat{b}^\dagger_i\hat{b}^\dagger_j}|\Omega_{\rm H,L}\rangle\otimes|\Omega_{\rm H,R}\rangle. \end{aligned} \tag{5.45}$$

For the massless case, the matrix $\{m^{ij}\}$ simplifies to a diagonal matrix and Bunch-Davies state can be expressed as:

$$\begin{aligned} |\Omega_{\rm BD}\rangle &\propto e^{\gamma\hat{b}^\dagger_{\rm L}\otimes\hat{b}^\dagger_{\rm R}}|\Omega_{\rm H,L}\rangle\otimes|\Omega_{\rm H,R}\rangle \\ &= \sum_n \frac{\gamma^n}{n!}\left(\hat{b}^\dagger_{\rm L}\right)^n\otimes\left(\hat{b}^\dagger_{\rm R}\right)^n|\Omega_{\rm H,L}\rangle\otimes|\Omega_{\rm H,R}\rangle \\ &= \sum_n \gamma^n|n_{\rm L}\rangle\otimes|n_{\rm R}\rangle, \end{aligned} \tag{5.46}$$

where $\gamma$ depends on the comoving momentum $p$ and is given by:

$$\gamma_p = ie^{-\pi p}. \tag{5.47}$$

The reduced density matrix for the left hyperbolic patch can be found by tracing over the degrees of freedom in the right hyperbolic patch (5.39):

$$\begin{aligned} \rho_{\rm L} &\equiv {\rm Tr}_{\mathcal{H}_{\rm R}}\{\rho\} \\ &= \sum_{n_{\rm R}}\langle n_{\rm R}|\rho|n_{\rm R}\rangle \\ &\propto \sum_{n_{\rm R}}\langle n_{\rm R}|\left[e^{\gamma\hat{b}^\dagger_{\rm L}\otimes\hat{b}^\dagger_{\rm R}}|\Omega_{\rm H,L}\rangle\otimes|\Omega_{\rm H,R}\rangle\langle\Omega_{\rm H,L}|\otimes\langle\Omega_{\rm H,R}|e^{\gamma^*\hat{b}_{\rm L}\otimes\hat{b}_{\rm R}}\right]|n_{\rm R}\rangle \end{aligned} \tag{5.48}$$

Now we use the (5.46):

$$\begin{aligned} \rho_{\rm L} &\propto \sum_m\sum_l\sum_{n_{\rm R}}\langle n_{\rm R}|\gamma^m|m_{\rm L}\otimes m_{\rm R}\rangle\langle l_{\rm L}\otimes l_{\rm R}|(\gamma^*)^l|n_{\rm R}\rangle \\ &= \sum_m|\gamma|^{2m}|m_{\rm L}\rangle\langle m_{\rm L}|, \end{aligned} \tag{5.49}$$

where we remind the reader that we suppressed the label $p$ (and the labels $l, m$) in the above discussion. The full reduced density matrix $\rho_{\rm L}$ is diagonal in $p, l, m$. It is given by the tensor product:

$$\rho_{\rm L} \propto \otimes_{plm} \left( \sum_{n_{plm}} |\gamma|^{2n_{plm}} |n_{{\rm L},plm}\rangle\langle n_{{\rm L},plm}| \right) . \tag{5.50}$$

Alternatively, the density matrix with labels $(p, l, m)$ (5.49) can also be written as:

$$\begin{aligned} \rho_{{\rm L},plm} &= \frac{e^{2\ln|\gamma_p|^2 \hat{b}^\dagger_{{\rm L},plm}\hat{b}_{{\rm L},plm}}}{{\rm Tr}\rho_{{\rm L},plm}} \\ &= (1-e^{-2\pi p}) e^{-2\pi p \hat{b}^\dagger_{{\rm L},plm}\hat{b}_{{\rm L},plm}}. \end{aligned} \tag{5.51}$$

This density matrix looks "thermal" in comoving momentum space, with temperature $\frac{H}{2\pi}$ or $(2\pi L_{\rm dS})^{-1}$, but $p$ is *not* the energy associated to a timelike Killing vector.[10] A pure state has a density matrix with eigenvalue spectrum $\{1, 0, \dots\}$. Clearly, the density matrix (5.49,5.51) is not pure, it represents a mixed or entangled state: from the point of one hyperbolic patch, the Bunch-Davies state is an entangled state.

In [128], the entanglement entropy of one hyperbolic patch of de Sitter is calculated, given the Bunch-Davies state. The entanglement is divergent, which is a common feature of entanglement entropy in quantum field theory, as described in section (1.3) of part I. The leading divergence is usually proportional to the entanglement surface, a sphere in this case.

In section (5.6) we will use the density matrix to calculate the scalar field spectrum. In appendix (5.D) we construct the "inverse" of the density matrix; that is, we compute the components of $|\Omega_{\rm L}\otimes\Omega_{\rm R}\rangle\langle\Omega_{\rm L}\otimes\Omega_{\rm R}|$ in the basis of excitations of the Bunch-Davies state:

$$|\Omega_{\rm H,L}\rangle \otimes |\Omega_{\rm H,R}\rangle \propto e^{-|\gamma_p|\ \hat{a}^\dagger_+ \otimes\ \hat{a}^\dagger_-} |\Omega_{\rm BD}\rangle. \tag{5.52}$$

## 5.6 Correlators in hyperbolic de Sitter space

Making use of the previously established relations between the de Sitter invariant Bunch–Davies vacuum and the hyperbolic vacuum state, we will compute both the Bunch–Davies and the hyperbolic vacuum power–spectra of scalar field quantum fluctuations[11]. The Bunch–Davies result can also be calculated using a reduced

[10] For the massless scalar field, $p$ *is* associated to a conformal Killing vector.

[11] See [139] for related work on the response of Unruh detectors.

density matrix formalism in the hyperbolic patch. Let us from the outset emphasize that within our basic de Sitter set-up, even though the Bunch–Davies state is mixed from the hyperbolic patch perspective, all hyperbolic Bunch–Davies correlators should match the (hyperbolic coordinate transformed) planar Bunch–Davies correlators. As a consequence one can rule out large deviations of Bunch–Davies hyperbolic correlators at late time and large momenta (when the hyperbolic coordinates reduce to planar coordinates) as compared to the planar Bunch–Davies correlators. That leaves the (pure) hyperbolic vacuum as the potentially more interesting state to consider, as far as enhanced initial state effects compared to the planar Bunch–Davies state.

Let us start by pointing out that the field operator $\phi_p$ evaluated on points in the left hyperbolic patch is trivial in the right hyperbolic patch

$$\phi_p(x) = \phi_{L,p}(x) \otimes \mathbf{I}_{\mathrm{R}} \quad \text{for } x \in \mathrm{L}. \tag{5.53}$$

As a consequence, de Sitter $n$-point functions of fields $\phi_p$ in the Bunch–Davies state, evaluated on points in the left hyperbolic patch, can be calculated either using the full global description or by using a reduced density matrix $\hat{\rho}_{\mathrm{L}} = \mathrm{Tr}_{\mathcal{H}_{\mathrm{R}}}\{|\Omega_{\mathrm{BD}}\rangle\langle\Omega_{\Omega_{\mathrm{BD}}}|\}$, and their results should agree. This is shown explicitly in appendix 5.B.2. By defining the $\hat{b}_{qplm}$ as in (5.36), we can write the field operator for arbitrary values of $p, l, m$ as

$$\begin{aligned}\phi_{plm}(x) = \hat{b}_{Lplm} \frac{1}{N_{P^p}} P^{ip}_{\nu-\frac{1}{2},L} Y_{plm} + \mathrm{h.c.} \\ + \hat{b}_{Rplm} \frac{1}{N_{P^p}} P^{ip}_{\nu-\frac{1}{2},R} Y_{plm} + \mathrm{h.c.},\end{aligned} \tag{5.54}$$

where

$$P^{ip}_{\nu-\frac{1}{2},L} = \begin{cases} P^{ip}_{\nu-\frac{1}{2}}(t) & \text{for } t \in L \\ 0 & \text{for } t \in R \end{cases} \tag{5.55}$$

and vice versa for $P^{ip}_{\nu-\frac{1}{2},R}$. Although these functions are not mode functions on a full Cauchy slice covering the de Sitter space, we are allowed to express the field in terms of them. Note that the $\hat{b}_{\mathrm{L}}$ and $\hat{b}_{\mathrm{R}}$ operators mutually commute. To make explicit that the field operator decomposes in the left and right hyperbolic patches, we write

$$\begin{aligned}\phi_{plm}(x) = \left(\hat{b}_{Lplm} \frac{1}{N_{P^p}} P^{ip}_{\nu-\frac{1}{2},L} Y_{plm} + \mathrm{h.c.}\right) \otimes \mathbf{I}_{\mathrm{R}} \\ + \mathbf{I}_{\mathrm{L}} \otimes \left(\hat{b}_{Rplm} \frac{1}{N_{P^p}} P^{ip}_{\nu-\frac{1}{2},R} Y_{plm} + \mathrm{h.c.}\right).\end{aligned} \tag{5.56}$$

Note that the expansion of a scalar field in Minkowski spacetime in terms of left and right Rindler wedge modes is similar (see for instance [140]). The restriction of the operator (5.56) to points in the left hyperbolic patch is by definition equal

to the full operator evaluated on points in the left hyperbolic patch. Note that if the field operator evaluated on points in the left hyperbolic patch would also have support on the right hyperbolic patch, it would not make sense to do a density matrix calculation as done above.

Clearly therefore Bunch–Davies scalar field correlators should be the same, independent of whether one uses hyperbolic or planar coordinates. Of course, since the de Sitter invariant length is expressed differently in terms of planar or hyperbolic coordinates, the functional dependence of the equal (hyperbolic) time correlators will look different. Since the difference between planar and hyperbolic coordinates vanishes in the late time and large momentum limit, the planar and the hyperbolic Bunch–Davies correlators match in that limit and small modifications are suppressed in the hyperbolic curvature scale. We conclude that hyperbolic Bunch–Davies correlators can be computed either using a global de Sitter description (for which the Bunch–Davies state is a pure initial state) or by considering a single de Sitter hyperbolic patch (for which the Bunch–Davies state equals a mixed initial state).

After these important preliminaries let us now proceed by computing the power spectrum of a massless scalar field in a hyperbolic coordinate patch in the hyperbolic vacuum and Bunch–Davies initial state respectively, as a function of the hyperbolic momentum $p$.

### 5.6.1 Power–spectrum results

For most of the details we refer to the appendix 5.B. Here we will just quote the main results. For the two point function in the hyperbolic vacuum state we find

$$\langle \Omega_{\rm H}|\phi_p\phi'_p|\Omega_{\rm H}\rangle = \delta(p-p')\frac{H^2}{\sinh^2(t)}\frac{p}{4\pi^2}\frac{\cosh^2(t)+p^2}{p^2+1} \tag{5.57}$$

where we have used the completeness relation of the eigenfunctions of the hyperbolic Laplacian[12] and the commutation relations. At late times $t \to \infty$ this approaches

$$\langle \Omega_{\rm H}|\phi_p\phi'_p|\Omega_{\rm H}\rangle \to \frac{H^2 p}{4\pi^2(p^2+1)} \tag{5.58}$$

and the appropriately normalized power spectrum (at late times) equals

$$\Delta^2_{\phi,H}(p) = \frac{H^2}{4\pi^2}\frac{p^2}{p^2+1}. \tag{5.59}$$

[12] $\sum_{lm}|Y_{plm}|^2 = \frac{p^2}{2\pi^2}$.

The same (hyperbolic coordinate patch) two point function in the Bunch–Davies vacuum is instead found to be equal to

$$\langle\Omega_{\rm BD}|\phi_p\phi_{p'}|\Omega_{\rm BD}\rangle = \delta(p-p')\frac{H^2}{\sinh^2(t)}\frac{p}{4\pi^2}\frac{\cosh^2(t)+p^2}{p^2+1}\coth(\pi p). \tag{5.60}$$

This result can either be obtained from a direct calculation using the global Bunch–Davies vacuum construction and restricting to one of the hyperbolic coordinate patches [126], or from a (mixed) density matrix calculation in a single hyperbolic coordinate patch, using the explicit expression for the density matrix as reported in [128], as we confirm in appendix 5.B.2. As alluded to earlier, the reason for this expression to not exactly reproduce the scale-invariant planar coordinate result for the scalar field power spectrum in the Bunch–Davies vacuum is that different coordinates are used. As the hyperbolic and planar coordinates are the same at late times and for small distances, the late-time power spectra at large momentum should be the same as well. At late times $t \to \infty$ we find

$$\langle\Omega_{\rm BD}|\phi_p\phi_{p'}|\Omega_{\rm BD}\rangle \to \frac{H^2 p}{4\pi^2(p^2+1)}\coth(\pi p). \tag{5.61}$$

Correspondingly, the power spectrum (at late times) is given by

$$\Delta^2_{\phi,BD}(p) = \frac{H^2}{4\pi^2}\frac{p^2}{p^2+1}\coth(\pi p). \tag{5.62}$$

Looking at these power spectra we indeed find that for $p \gg 1$, when $\coth \pi p \approx 1$ and $p^2+1 \approx p^2$, the hyperbolic vacuum as well as the hyperbolic Bunch–Davies result matches the standard scale invariant planar Bunch–Davies result $\frac{H^2}{4\pi^2}$. They only start to differ from each other and the standard planar Bunch–Davies expression for sufficiently small momenta $p \lesssim 1$ (see figure (5.7)). Note that although the corresponding wavelengths are expected to lie far outside our observable window, given the fact that they correspond to length scales longer or comparable to the hyperbolic curvature scale, for both hyperbolic states the power is suppressed as compared to the standard planar Bunch–Davies result. As these departures from the standard planar result become evident, one should keep in mind that the difference found in the hyperbolic Bunch–Davies result can be attributed to a coordinate change, whereas (part of) the change in the hyperbolic vacuum power spectrum is related to an initial state modification.

We conclude that, independent of the particular initial state under consideration, any power–spectrum signatures of an open inflationary universe are confined to the curvature scale, which has to be several orders of magnitude larger than the largest observable length scale in the universe. Although the initial hyperbolic state is mixed when assuming a (globally defined) planar Bunch–Davies state, the

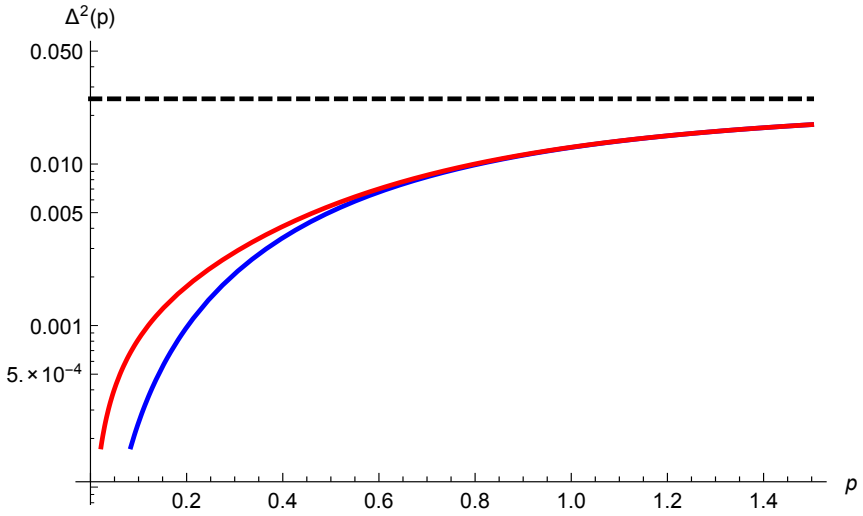


***Figure 5.7:*** *The power spectra (logarithmic scale) for the hyperbolic vacuum (blue) and the Bunch–Davies vacuum (red), as function of the hyperbolic momentum $p$ with $H = 1$. The dashed line indicates the scale–invariant planar Bunch–Davies result $\frac{H^2}{4\pi^2}$.*

power–spectrum results in this admittedly basic set-up in which all bubble wall physics is ignored, do not show large deviations, as should be expected. In fact, this statement is true for general hyperbolic $n$-point correlators in the Bunch–Davies vacuum. Potentially enhanced bi–spectrum results due to initial state excitations, as compared to the standard planar Bunch–Davies result, can therefore only be expected assuming the pure hyperbolic vacuum as the initial state in the hyperbolic patch.

In [1] we investigate the bi-spectrum. The study of the bi-spectrum in the Bunch-Davies state and the hyperbolic vacuum is not part of this thesis, but we will state the results. The bi–spectrum in the hyperbolic vacuum does not seem to produce interesting enhancements that make it distinguishable from the Bunch-Davies state. This conclusion is in fact corroborated by an approximate construction of the hyperbolic vacuum as an excited state on top of the (global) planar Bunch–Davies vacuum[13]. The relevant Bogoliubov coefficients are suppressed exponentially in momentum, ensuring that these effects will not be observable. Even though the hyperbolic vacuum can be effectively thought of as an excited state with respect to standard planar Bunch–Davies vacuum, it is not of a type that gives rise to large (enhanced) corrections in the bi–spectrum as compared to the

[13]Formally, the (reduced) Bunch Davies state and hyperbolic vacuum are not contained in the same Hilbert space. The Bunch Davies state is a Hadamard state whereas the hyperbolic vacuum is *not*; see appendix 5.D for details and discussion.

standard planar Bunch–Davies result.

## 5.7 Vacua and the energy momentum tensor

In this section we discuss the behavior of the energy momentum tensor. First we motivate why we expect to find something interesting, by comparing the hyperbolic patch of de Sitter spacetime to the Rindler wedge.

Note that for a flat Rindler wedge in lightcone coordinates $(u, v)$, there is a horizon at $u = 0$ and the Fulling-Rindler vacuum $|\Omega_{FR}\rangle$ corresponds to the empty state in a single wedge. In that case the $T_{uu}$ component of the energy momentum tensor (with the usual UV-divergence removed by subtracting the UV-divergent expectation value of $T_{uu}$ in the Minkowski vacuum $|0_M\rangle$) diverges as one approaches the horizon: $\langle T_{uu}\rangle_{FR} - \langle T_{uu}\rangle_M = -\frac{1}{48\pi}\frac{1}{u^2}$ in $(1+1)$ dimensions for $u > 0$ (for a nice derivation of this result see [140]).

A similar analysis can be done for the energy momentum tensor in the hyperbolic de Sitter patch, where the global de Sitter invariant vacuum state is now the Bunch-Davies vacuum $|\Omega_{\rm BD}\rangle$. The obvious difference with the Rindler wedge is the absence of a timelike Killing vector. In addition, the $t = 0$ surface is a (light-) cone, so a better analogy is with Milne space, to which the de Sitter hyperbolic section reduces for small $t$. In any case, we will use the same regularization procedure, restricting to the minimally coupled massless case $\nu = \frac{3}{2}$. The most convenient method to calculate components of the energy momentum tensor makes use of the Wightman function $G^+(x, x', t, t')$ and specifically we will look at the following contribution

$$\langle(\partial_\alpha\phi)^2(x,t)\rangle = \lim_{x',t'\to x,t} \partial_{\alpha'}\partial_\alpha G(x, x', t, t'). \tag{5.63}$$

The Wightman function for the Bunch-Davies state is well known, but here we use the expression in terms of an integral over the hyperbolic momentum $p$ as given in [126]. This allows us to consistently regulate the UV-divergence of $\langle T_{\mu\nu}\rangle$ in the two states of interest. In appendix 5.C we show that the difference $\langle T_{tt}\rangle_{\rm H} - \langle T_{tt}\rangle_{\rm BD}$ is UV-finite and diverges as $t \to 0$

$$\langle T_{tt}\rangle_{\rm H} - \langle T_{tt}\rangle_{\rm BD} = -\frac{11}{240\pi^2}\frac{1}{t^4} + O\left(\frac{1}{t^2}\right). \tag{5.64}$$

So we conclude that the hyperbolic vacuum $|\Omega_{\rm H}\rangle$ has singular properties that are completely analogous to the Minkowski Fulling-Rindler, Milne and de Sitter static vacuum, see also [139]. The energy momentum tensor diverges in the limit $t \to 0$, so infinite energy seems to be required to prepare the state at the (singular) origin. A complete description all the way until $t = 0$ is therefore obviously inconsistent,

but strictly speaking that does not need to be fatal in a cosmological setting, in the sense that in a stand-alone open universe this might be interpreted as the Big Bang singularity. Also, in a realistic setup, we should allow the scalar field to backreact on the geometry. An analysis of this situation would be an interesting topic for future study.

The problem of having divergent components of the energy momentum tensor at the boundary of a causal patch on a fixed background geometry, when one tries to define a pure, non-entangled state for this causal patch, has a remarkable interpretation in holography. If the entanglement between a boundary region and its complement is removed, then the corresponding bulk space tends to pinch of [5], since the corresponding Ryu-Takayanagi surface shrinks to zero size.

## 5.8 Conclusions and outlook

Before summarizing our results, let us remind the reader once more that our motivation was to carefully study the relation between the hyperbolic and planar coordinate patches and their corresponding states in (mostly) pure de Sitter space. We believe these results to be of interest, and partially applicable, in the context of de Sitter false vacuum decay, but it is also clear that in that case a more complete analysis should include (model-dependent) wall physics that will affect the details. Instead we concentrated on a general and qualitative difference between two examples of initial states on a hyperbolic section of de Sitter space: the pure hyperbolic vacuum and the (entangled) de Sitter invariant Bunch–Davies state, corresponding to a mixed state. We noted that the pure hyperbolic vacuum is formally inconsistent, due to the energy momentum tensor becoming singular at the null boundary of the hyperbolic section. This issue should plague all pure hyperbolic states.

We stressed that the hyperbolic vacuum can be approximated by an excitation of the Bunch–Davies vacuum. This is an effective description, because the Bunch Davies state and the hyperbolic vacuum do formally not live in the same Hilbert space. It can be used for the computation of the bi–spectrum and for the analysis of possibly enhanced features as compared to the standard Bunch-Davies results. Using the hyperbolic coordinate embedding we explicitly constructed a family of hyperbolic solutions that reduces to the planar coordinates in the infinite boost limit, as such providing a limiting relation between the hyperbolic vacuum and the planar Bunch–Davies vacuum. As a corollary we also argued that the hyperbolic vacuum can be mapped to a specific static vacuum, implying that the static vacuum should also reduce to (a sector of) the Bunch–Davies state in the infi-

nite boost limit, as was first noted in [129]. Again, this limiting behavior implies that in the late time and large momentum limit, the bi–spectrum results for the hyperbolic vacuum should agree with the standard planar Bunch–Davies result. Unfortunately, on the basis of our analysis here and in [1], we should conclude that no detectable signals of an open inflationary universe in the fluctuation statistics is expected on small sub-curvature scales.

To summarize the two hyperbolic states introduced, one of them mixed (Bunch–Davies) and the other one pure (hyperbolic vacuum), make almost identical predictions in the late time sub-curvature limit. In fact, in the infinite boost limit the states become formally identical to the planar Bunch–Davies vacuum. For the mixed Bunch–Davies state this seems to imply that the density matrix $\rho_{\rm BD}$ should depend on the boost parameter $\gamma$. Correspondingly, the associated von Neumann entropy $\mathrm{Tr}(-\rho_{\rm BD}\,\ln\rho_{\rm BD})$ of the mixed Bunch–Davies state on the hyperbolic section should depend on the boost parameter $\gamma$ to ensure that the entropy vanishes in the infinite boost limit.

It would be of interest to consider the generalization for non-zero boost parameter $\gamma$. Although one might think the density matrix and corresponding entropy to be boost invariant, this is not entirely obvious and the above observation does indeed suggest it might not be, perhaps in some subtle (singular) way. The dependence on the boost parameter should be such that it is invariant under $\gamma \to -\gamma$, effectively interchanging the two hyperbolic sections. Since the boost dependence can be implemented through a simple rescaling on the left hyperbolic momenta (and a time shift) 5.14 and the inverse rescaling on the right hyperbolic momenta (and a time shift) it should be possible to trace the boost dependence of the Bunch–Davies state in terms of the left and right hyperbolic modes. It should then be straightforward to construct the corresponding density matrix and confirm that the density matrix and corresponding entropy become trivial in the infinite boost limit.

# 5.A Mode functions

## 5.A.1 Solutions to the hyperbolic equation of motion

The metric for both the left and right hyperbolic patch is given by:

$$ds^2 = \frac{1}{H^2}\left(-dt^2 + \sinh^2 t\left(dr^2 + \sinh^2 r\; d\Omega_2^2\right)\right) \tag{5.65}$$

where the coordinates $t, r, \phi, \theta$ are dimensionless and $c = 1$. The action for a massive non-interacting minimally coupled scalar field $\phi$ is given by:

$$S = -\frac{1}{2}\int \sqrt{-g}\; d^4x \left(g^{\mu\nu}\partial_\mu\phi\partial_\nu\phi + m^2\phi^2\right). \tag{5.66}$$

The action of a conformally coupled scalar field can be written in the Einstein frame with effective mass $m^2 = 2H^2$. The equation of motion is given by

$$\begin{aligned} 0 &= \left(\frac{1}{\sinh^3(t)}\frac{\partial}{\partial t}\sinh^3(t)\frac{\partial}{\partial t} - \frac{1}{\sinh^2(t)}\nabla^2_{\mathcal{H}^3} + \frac{m^2}{H^2}\right)\phi \\ &= \left(\frac{1}{\sinh^3(t)}\frac{\partial}{\partial t}\sinh^3(t)\frac{\partial}{\partial t} - \frac{1}{\sinh^2(t)}\nabla^2_{\mathcal{H}^3} + \frac{9}{4} - \nu^2\right)\phi \end{aligned} \tag{5.67}$$

where $\nu$ is defined as $\nu = \sqrt{\frac{9}{4} - \frac{m^2}{H^2}}$ and $\nabla^2_{\mathcal{H}^3}$ is the Laplacian on the hyperboloid $\mathcal{H}^3$. We will use $\nu' = \nu - \frac{1}{2}$, consistent with [126], such that $\nu' = 1$ corresponds to the massless minimally coupled case and $\nu' = 0$ corresponds to the massless conformally coupled case for which the effective mass is $m^2 = 2H^2$.

The eigenfunctions $Y_{plm}$ of the Laplacian $\nabla^2_{\mathcal{H}^3}$ on the hyperboloid $\mathcal{H}^3$, that are regular in $r = 0$, are given by [126]:

$$\begin{aligned} -\nabla^2_{\mathcal{H}^3}Y_{plm} &= (p^2+1)Y_{plm} \\ Y_{plm}(r,\Omega) &= f_{pl}(r)Y_{lm}(\Omega) \\ f_{pl}(r) &= \frac{\Gamma(ip+l+1)}{\Gamma(ip+1)}\frac{p}{\sqrt{\sinh r}}P^{-l-1/2}_{ip-1/2}(\cosh r) \\ &= (-1)^l\sqrt{\frac{2}{\pi}}\frac{\Gamma(-ip+1)}{\Gamma(-ip+l+1)}\sinh^l r\frac{d^l}{d(\cosh r)^l}\left(\frac{\sin pr}{\sinh r}\right) \end{aligned} \tag{5.68}$$

where $Y_{lm}(\Omega)$ is the normalized spherical harmonic function on the unit two-sphere, $\Gamma(z)$ is the Gamma function and $P^\nu_\mu(z)$ is the associated Legendre function of the first kind [141].

The mode functions that correspond to the natural hyperbolic vacuum are given by:

$$\left\{ \begin{array}{ll} \frac{H}{\sinh t}P^{ip}_{\nu'}(\cosh t) & \text{positive energy modes} \\ \frac{H}{\sinh t}P^{-ip}_{\nu'}(\cosh t) & \text{negative energy modes} \end{array} : p \geq 0 \right\}. \tag{5.69}$$

Mode functions on a Cauchy slice of de Sitter, must be regular and consist of linear combinations of the hyperbolic mode functions in the left and right hyperbolic patches [126]. The mode functions that correspond to the Bunch–Davies state are

given in [126]:

$$\chi_{p,\sigma} = \begin{cases} \left( \dfrac{e^{\pi p} - \sigma e^{-i\pi\nu'}}{\Gamma(\nu' + ip + 1)} P^{ip}_{\nu'}(z) - \dfrac{e^{-\pi p} - \sigma e^{-i\pi\nu'}}{\Gamma(\nu' - ip + 1)} P^{-ip}_{\nu'}(z) \right) & \text{for } x \in R \\ \left( \dfrac{\sigma e^{\pi p} - e^{-i\pi\nu'}}{\Gamma(\nu' + ip + 1)} P^{ip}_{\nu'}(z) - \dfrac{\sigma e^{-\pi p} - e^{-i\pi\nu'}}{\Gamma(\nu' - ip + 1)} P^{-ip}_{\nu'}(z) \right) & \text{for } x \in L \end{cases}$$
$$= \begin{cases} \alpha^{\sigma}_{p,R} P^{ip}_{\nu'}(z) + \beta^{\sigma}_{p,R} P^{-ip}_{\nu'}(z) & \text{for } x \in R \\ \alpha^{\sigma}_{p,L} P^{ip}_{\nu'}(z) + \beta^{\sigma}_{p,L} P^{-ip}_{\nu'}(z) & \text{for } x \in L \end{cases} \tag{5.70}$$

where $z = \cosh t$ and the constants $\alpha^{\sigma}_{p,q}$ and $\beta^{\sigma}_{p,q}$ are defined as:

$$\begin{array}{ll} \alpha^{\sigma}_{p,L} = \sigma \frac{e^{\pi p} - \sigma e^{-i\pi\nu'}}{\Gamma(\nu' + ip + 1)} & \alpha^{\sigma}_{p,R} = \frac{e^{\pi p} - \sigma e^{-i\pi\nu'}}{\Gamma(\nu' + ip + 1)} \\ \beta^{\sigma}_{p,L} = -\sigma \frac{e^{-\pi p} - \sigma e^{-i\pi\nu'}}{\Gamma(\nu' - ip + 1)} & \beta^{\sigma}_{p,R} = -\frac{e^{-\pi p} - \sigma e^{-i\pi\nu'}}{\Gamma(\nu' - ip + 1)} \end{array} . \tag{5.71}$$

These mode functions must be normalized through the Klein–Gordon normalization (see section 5.A.2).

### 5.A.2 Klein–Gordon normalization

#### Hyperbolic modes

We normalize the hyperbolic modes on the hyperbolic patch using the variable $z = \cosh t$ and using the orthonormality of the $Y_{plm}$:

$$\begin{aligned} N^2_{Pp} &\equiv \langle \phi_{plm}, \phi_{plm} \rangle_{\mathrm{KG}} \\ &= i \int_{\Sigma} d\Sigma^{\mu} \left( \phi_{plm} \partial_{\mu} \phi^*_{plm} - \phi^*_{plm} \partial_{\mu} \phi_{plm} \right) \\ &= i \sinh^3 t \left( \frac{P^{ip}_{\nu'}(\cosh t)}{\sinh t} \partial_t \left( \frac{P^{-ip}_{\nu'}(\cosh t)}{\sinh t} \right) - \frac{P^{-ip}_{\nu'}(\cosh t)}{\sinh t} \partial_t \left( \frac{P^{ip}_{\nu'}(\cosh t)}{\sinh t} \right) \right) \\ &= i(z^2 - 1) \left( P^{ip}_{\nu'}(z) \partial_z P^{-ip}_{\nu'}(z) - P^{-ip}_{\nu'}(z) \partial_z P^{ip}_{\nu'}(z) \right). \end{aligned} \tag{5.72}$$

For the minimally coupled massless case $\nu' = 1$ we have:

$$\begin{aligned} N^2_{Pp} &= i(z^2 - 1) P^{ip}_1(z) P^{-ip}_1(z) \times \left( \begin{array}{c} \frac{1}{z - ip} + \frac{ip}{2} \frac{1}{1+z} + \frac{ip}{2} \frac{1}{1-z} - \\ \frac{1}{z + ip} + \frac{ip}{2} \frac{1}{1+z} + \frac{ip}{2} \frac{1}{1-z} \end{array} \right) \\ &= \frac{2p}{\left| \Gamma[1 + ip] \right|^2} \\ &= \frac{2 \sinh(\pi p)}{\pi}. \end{aligned} \tag{5.73}$$

In fact, for $\nu' \neq 1$ this normalization is also valid. In [126] it is shown that one can expand the mode functions in the $t \to 0$ regime:

$$\frac{1}{\sinh t} P^{ip}_{\nu'}(\cosh t) \approx \frac{2^{ip}}{\Gamma[1-ip]} t^{ip-1}. \tag{5.74}$$

Using this expansion in (5.72) also results into the normalization (5.73). This normalization is valid for any $t$ by the properties of the Klein–Gordon normalization.

**Bunch–Davies modes**

The Bunch–Davies modes are given in terms of linear combinations of the hyperbolic modes in (5.70). Schematically we have (using the orthogonality of the hyperbolic mode functions):

$$\begin{aligned} N^2_{\chi^{\sigma,p}} &= \langle \chi_{\sigma,p}, \chi_{\sigma,p} \rangle \\ &= \sum_{q=L,R} \sum_{q'=L,R} \langle \left(\alpha^\sigma_{p,q} P^{p,q} + \beta^\sigma_{p,q} \bar{P}^{p,q}\right), \left(\alpha^\sigma_{p,q'} P^{p,q'} + \beta^\sigma_{p,q'} \bar{P}^{p,q'}\right) \rangle_{KG} \\ &= \sum_{q,q'=L,R} \left( \begin{array}{l} \alpha^\sigma_{p,q} \bar{\alpha}^\sigma_{p,q'} \langle P^{p,q}, P^{p,q'} \rangle_{KG} + \alpha^\sigma_{p,q} \bar{\beta}^\sigma_{p,q'} \langle P^{p,q}, \bar{P}^{p,q'} \rangle_{KG} \\ + \bar{\alpha}^\sigma_{p,q'} \beta^\sigma_{p,q} \langle \bar{P}^{p,q}, P^{p,q'} \rangle_{KG} + \beta^\sigma_{p,q} \bar{\beta}^\sigma_{p,q'} \langle \bar{P}^{p,q}, \bar{P}^{p,q'} \rangle_{KG} \end{array} \right) \\ &= N^2_{P^p} \sum_{q=L,R} \left( \alpha^\sigma_{p,q} \bar{\alpha}^\sigma_{p,q} - \beta^\sigma_{p,q} \bar{\beta}^\sigma_{p,q} \right), \end{aligned} \tag{5.75}$$

where we used:

$$\begin{aligned} \langle P^{p,q}, P^{p,q'} \rangle_{KG} = -\langle \bar{P}^{p,q}, \bar{P}^{p,q'} \rangle_{KG} &= \delta_{qq'} N^2_{P^p}, \\ \langle P^{p,q}, \bar{P}^{p,q'} \rangle_{KG} = \langle \bar{P}^{p,q}, P^{p,q'} \rangle_{KG} &= 0. \end{aligned} \tag{5.76}$$

Using (5.71) we find:

$$\sum_{q=L,R} \left( \alpha^\sigma_{p,q} \bar{\alpha}^\sigma_{p,q} - \beta^\sigma_{p,q} \bar{\beta}^\sigma_{p,q} \right) = \frac{8 \sinh \pi p \left( \cosh \pi p - \sigma \cos \pi \nu' \right)}{\left| \Gamma[\nu' + ip + 1] \right|^2}. \tag{5.77}$$

So finally we can substitute (5.77) into (5.75):

$$\begin{aligned} N^2_{\chi^{\sigma,p}} &= N^2_{P^p} \sum_{q=L,R} \left( \alpha^\sigma_{p,q} \bar{\alpha}^\sigma_{p,q} - \beta^\sigma_{p,q} \bar{\beta}^\sigma_{p,q} \right) \\ &= \frac{2 \sinh \pi p}{\pi} \times \frac{8 \sinh \pi p \left( \cosh \pi p - \sigma \cos \pi \nu' \right)}{\left| \Gamma[\nu' + ip + 1] \right|^2} \\ &= \frac{16 \sinh^2 \pi p \left( \cosh \pi p - \sigma \cos \pi \nu' \right)}{\pi \left| \Gamma[\nu' + ip + 1] \right|^2}. \end{aligned} \tag{5.78}$$

This is consistent with [126], but note that we included an extra factor of $2 \sinh \pi p$ into the normalization, in order to simplify the expressions (5.71). The normalized mode functions are the same as in [126], of course.

### 5.A.3 Mode functions for the massless scalar field

Since we are mostly concerned with the massless minimally coupled scalar field ($\nu' = 1$), we state the normalized mode functions for that case explicitly in hyperbolic time coordinate $t$ and in conformal time $\eta = \ln\tanh\frac{t}{2}$:

$$\begin{aligned}\frac{1}{N_{Pp}}\frac{H}{\sinh t}P_1^{ip}(\cosh t) &= \frac{H}{\sqrt{2p(p^2+1)}}\left(\coth\frac{t}{2}\right)^{\frac{ip}{2}}(p\ \mathrm{csch}\ t + i\coth t)\\ &= \frac{H}{\sqrt{2p(p^2+1)}}e^{-ip\eta}\left(p\sinh\eta - i\cosh\eta\right),\end{aligned} \tag{5.79}$$

where we have chosen a convenient phase factor in the normalization, that does not affect the physics. The conformal time $\eta$ is defined as:

$$\begin{aligned}ds^2 &= \frac{1}{H^2}\left(-dt^2 + \sinh^2 t\left(dr^2 + \sinh^2 r d\Omega_2^2\right)\right)\\ &= \frac{\sinh^2(t(\eta))}{H^2}\left(-d\eta^2 + dr^2 + \sinh^2 r d\Omega_2^2\right)\\ \Rightarrow \eta &= \int\frac{dt}{\sinh t}\\ &= \ln\tanh\frac{t}{2}.\end{aligned} \tag{5.80}$$

Other useful relations between "hyperbolic" time $t$ and "conformal" time $\eta$ are:

$$\sinh t = -\frac{1}{\sinh\eta},\quad \cosh t = -\coth\eta. \tag{5.81}$$

At early times $\eta \to -\infty$ the mode function for the massless minimally coupled scalar field (5.79) behaves like a positive energy mode function:

$$\begin{aligned}\frac{H}{\sqrt{2p(p^2+1)}}e^{-ip\eta}\left(p\sinh\eta - i\cosh\eta\right) &= \sinh\eta\left(\frac{H(p+i)}{\sqrt{2p(p^2+1)}}e^{-ip\eta} + O(e^{2\eta})\right)\\ &\approx \sinh\eta\frac{H(p+i)}{\sqrt{2p(p^2+1)}}e^{-ip\eta}.\end{aligned} \tag{5.82}$$

The infinite boost limit $\gamma \to \infty$ (5.14) corresponds to the large $t$ (or small $\eta$) and large momentum limit. In particular in terms of conformal time, the rescaling for small $\eta$ reads $\eta \to \eta\, e^{-\gamma}$, implying that the combination $p\,\eta$ is invariant in the limit. This gives

$$\begin{aligned}e^{-ip\eta}\left(p\sinh\eta - i\cosh\eta\right) &= p\sinh\eta\, e^{-ip\eta}\left(1 - \frac{i}{p\eta} + O(\eta)\right)\\ &\approx e^{-ip\eta}\left(p\eta - i\right).\end{aligned} \tag{5.83}$$

This is exactly the mode function for a massless scalar field in the flat de Sitter slicing (up to the appropriate normalization).

# 5.B Power spectra for the massless field

## 5.B.1 Direct calculation

**Power spectrum in hyperbolic vacuum**
The power spectrum in the hyperbolic vacuum can be computed in a straightforward way

$$\begin{aligned}
\langle\Omega_{\rm H}|\phi_p\phi'_p|\Omega_{\rm H}\rangle &= \frac{H^2}{\sinh^2(t)}\sum_{lm}\sum_{l'm'}\frac{Y_{plm}Y^*_{p'l'm'}}{N_{P^p}N_{P^{p'}}} \\
&\times\langle\Omega_{\rm H}|\left(\hat{b}_{plm}P^{ip}_{\nu'}+\hat{b}^\dagger_{plm}P^{-ip}_{\nu'}\right)\left(\hat{b}_{p'l'm'}P^{ip'}_{\nu'}+\hat{b}^\dagger_{p'l'm'}P^{-ip'}_{\nu'}\right)|\Omega_{\rm H}\rangle \\
&= \frac{H^2}{\sinh^2(t)}\sum_{lm}\sum_{l'm'}Y_{plm}Y^*_{p'l'm'}\frac{P^{ip}_{\nu'}P^{-ip'}_{\nu'}}{N_{P^p}N_{P^{p'}}}\langle\Omega_{\rm H}|\hat{b}_{plm}\hat{b}^\dagger_{p'l'm'}|\Omega_{\rm H}\rangle \\
&= \delta(p-p')\frac{H^2}{\sinh^2(t)}\sum_{lm}|Y_{plm}|^2\frac{\left|P^{ip}_{\nu'}\right|^2}{N^2_{P^p}} \\
&= \delta(p-p')\frac{H^2}{\sinh^2(t)}\frac{p^2}{2\pi^2}\frac{\left|P^{ip}_{\nu'}\right|^2}{N^2_{P^p}},
\end{aligned} \tag{5.84}$$

where we used the completeness relation for the $Y_{plm}$ in the last step. For the massless minimally coupled case $\nu'=1$ we have:

$$\langle\Omega_{\rm H}|\phi_p\phi'_p|\Omega_{\rm H}\rangle = \delta(p-p')\frac{H^2}{\sinh^2(t)}\frac{p}{4\pi^2}\frac{\cosh^2(t)+p^2}{(p^2+1)}, \tag{5.85}$$

and for large $t\to\infty$

$$\langle\Omega_H|\phi_p\phi'_p|\Omega_{\rm H}\rangle \to \delta(p-p')\frac{H^2}{4\pi^2}\frac{p}{(p^2+1)}. \tag{5.86}$$

The power spectrum for the massless minimally coupled scalar field is given by:

$$\begin{aligned}
\langle\Omega_H|\phi^2|\Omega_{\rm H}\rangle &= \int dp\int dp'\langle\Omega_H|\phi_p\phi'_p|\Omega_{\rm H}\rangle \\
&= \int d\ln p\frac{H^2}{4\pi^2}\frac{p^2}{p^2+1} \\
\Rightarrow \Delta^2_{\phi,H}(p) &= \frac{H^2}{4\pi^2}\frac{p^2}{p^2+1}.
\end{aligned} \tag{5.87}$$

**Power spectrum in Bunch–Davies vacuum**
The computation is similar to the previous case:

$$\begin{aligned}
&\langle\Omega_{\rm BD}|\phi_p\phi_{p'}|\Omega_{\rm BD}\rangle \\
&= \frac{H^2}{\sinh^2 t}\sum_{lml'm'}\sum_{\sigma\sigma'}\frac{Y_{plm}Y^*_{p'l'm'}}{N_{\chi_{p,\sigma}}N_{\chi_{p',\sigma'}}} \\
&\times\langle\Omega_{\rm BD}|\left(\hat a_{\sigma plm}\chi_{p,\sigma}+\hat a^\dagger_{\sigma plm}\bar\chi_{p,\sigma}\right)\left(\hat a_{\sigma' p'l'm'}\chi_{p',\sigma'}+\hat a^\dagger_{\sigma' p'l'm'}\bar\chi_{p',\sigma'}\right)|\Omega_{\rm BD}\rangle \\
&= \frac{H^2}{\sinh^2 t}\sum_{lml'm'}Y_{plm}Y^*_{p'l'm'}\sum_{\sigma\sigma'}\frac{\chi_{p,\sigma}\bar\chi_{p',\sigma'}}{N_{\chi_{p,\sigma}}N_{\chi_{p',\sigma'}}}\langle\Omega_{\rm BD}|\hat a_{\sigma plm}\hat a^\dagger_{\sigma' p'l'm'}|\Omega_{\rm BD}\rangle \\
&= \delta(p-p')\frac{H^2}{\sinh^2 t}\sum_{lm}|Y_{plm}|^2\sum_\sigma\left|\frac{\chi_{p,\sigma}}{N_{\chi_{p,\sigma}}}\right|^2 \ \text{using}\ [\hat a_{\sigma plm},\hat a^\dagger_{\sigma' p'l'm'}] \\
&= \delta_{\sigma\sigma'}\delta_{ll'}\delta_{mm'}\delta(p-p') \\
&= \delta(p-p')\frac{H^2}{\sinh^2 t}\frac{p^2}{2\pi^2}\sum_\sigma\left(\begin{array}{l}\left(\frac{\alpha^\sigma_{p,L}\bar\alpha^\sigma_{p,L}}{N^2_{\chi^{p\sigma}}}+\frac{\beta^\sigma_{p,L}\bar\beta^\sigma_{p,L}}{N^2_{\chi^{p,\sigma}}}\right)\left|P^{ip}_{\nu'}\right|^2 \\ +\frac{\alpha^\sigma_{p,L}\bar\beta^\sigma_{p,L}}{N^2_{\chi^{p\sigma}}}P^{ip}_{\nu'}P^{ip}_{\nu'}+\frac{\bar\alpha^\sigma_{p,L}\beta^\sigma_{p,L}}{N^2_{\chi^{p\sigma}}}P^{-ip}_{\nu'}P^{-ip}_{\nu'}\end{array}\right).
\end{aligned} \tag{5.88}$$

In the last step we used the completeness relation for $Y_{plm}$ and the expansion of $\chi$ in terms of the associated Legendre polynomials (5.70,5.71). Here we will compute the spectrum for the massless scalar field ($\nu'=1$). For the massless minimally coupled scalar ($\nu'=1$) the cross terms involving $P^{ip}P^{ip}$ and $P^{-ip}P^{-ip}$ vanish:

$$\sum_\sigma\frac{\alpha^\sigma_{p,L}\bar\beta^\sigma_{p,L}}{N^2_{\chi^{p\sigma}}}\propto\sum_\sigma\frac{(e^{\pi p}+\sigma)(e^{-\pi p}+\sigma)}{\cosh\pi p+\sigma}\propto\sum_\sigma\sigma=0, \tag{5.89}$$

and similarly for the term involving $P^{-ip}P^{-ip}$. So for the massless minimally coupled case ($\nu'=1$) we have:

$$\begin{aligned}
&\langle\Omega_{\rm BD}|\phi_p\phi_{p'}|\Omega_{\rm BD}\rangle \\
&= \delta(p-p')\frac{H^2}{\sinh^2 t}\frac{p^2}{2\pi^2}\sum_\sigma\left(\frac{\alpha^\sigma_{p,L}\bar\alpha^\sigma_{p,L}+\beta^\sigma_{p,L}\bar\beta^\sigma_{p,L}}{N^2_{\chi^{p,\sigma}}}\right)\left|P^{ip}_1\right|^2 \\
&= \delta(p-p')\frac{H^2}{\sinh^2 t}\frac{p^2}{2\pi^2}\sum_\sigma\frac{\pi}{16\sinh^2\pi p}\frac{(e^{\pi p}+\sigma)^2+(e^{-\pi p}+\sigma)^2}{\cosh\pi p+\sigma}\left|P^{ip}_1\right|^2 \\
&= \delta(p-p')\frac{H^2}{\sinh^2 t}\frac{p^2}{2\pi^2}\frac{\pi\cosh(\pi p)}{2\sinh^2(\pi p)}\left|P^{ip}_1\right|^2 \\
&= \delta(p-p')\frac{H^2}{\sinh^2(t)}\frac{p(\cosh^2(t)+p^2)}{4\pi^2(p^2+1)}\coth(\pi p).
\end{aligned} \tag{5.90}$$

For large $t \to \infty$ we have:

$$\langle \Omega_{\rm BD}|\phi_p \phi_{p'}|\Omega_{\rm BD}\rangle = \delta(p-p')\frac{H^2}{4\pi^2}\frac{p\coth(\pi p)}{p^2+1} \tag{5.91}$$

and

$$\begin{aligned}\langle \Omega_{\rm BD}|\phi^2|\Omega_{\rm BD}\rangle &= \int dp \int dp' \langle \Omega_{\rm BD}|\phi_p\phi_{p'}|\Omega_{\rm BD}\rangle \\ &= \frac{H^2}{4\pi^2}\int dp \frac{p\coth\pi p}{p^2+1} + \text{super-curvature modes} \\ &= \frac{H^2}{4\pi^2}\int d\ln p \ \ \frac{p^2\coth\pi p}{p^2+1} + \text{super-curvature modes.}\end{aligned} \tag{5.92}$$

The power spectrum is given by

$$\Delta^2_{\phi,BD}(p) = \frac{H^2}{4\pi^2}\frac{p^2\coth\pi p}{p^2+1} \tag{5.93}$$

which reduces for $p \gg 1$ to an approximately scale invariant spectrum:

$$\Delta^2_{\phi}(p) \approx \frac{H^2}{4\pi^2}. \tag{5.94}$$

### 5.B.2 Reduced density matrix calculation

In this section we derive the power spectrum in the Bunch-Davies state using an alternative method. We consider the reduced density matrix that remains after having traced out the degrees of freedom in the right hyperbolic patch. We find the same answer as in the direct calculation (5.93,5.90). The reduced density matrix for the left hyperbolic patch has been calculated by Maldacena and Pimentel [128] and is given by:

$$\begin{aligned}\hat{\rho}_{{\rm L},plm} &= Tr_{H_{\rm R}}\left\{|\Omega_{\rm BD}\rangle\langle\Omega_{\rm BD}|\right\} \\ &= (1-|\gamma_p)|^2)\sum_{n=0}^{\infty}|\gamma_p|^{2n}|n;p,l,m\rangle\langle n;p,l,m|\end{aligned} \tag{5.95}$$

where for the *massless* scalar field $\gamma_p$ and $|n;p,l,m\rangle$ are given by[14]:

$$\begin{aligned}\gamma_p(m=0) &= ie^{-\pi p} \\ |n;p,l,m\rangle &= \frac{(\hat{b}^\dagger_{plm})^n}{\sqrt{n!}}|\Omega_H\rangle.\end{aligned} \tag{5.96}$$

[14]For the massive scalar field Maldacena and Pimentel apply a Bogoliubov transformation on the set of $\hat{b}_{plm}$ operators to bring $\hat{\rho}_{\rm L}$ in the form of (5.95).

For a point in the left hyperbolic wedge $x \in L$ the two point function is given by (5.29):

$$\begin{aligned}\langle\Omega_{\rm BD}|\phi_p\phi_{p'}|\Omega_{\rm BD}\rangle &= {\rm Tr}_{\mathcal{H}_{\rm L}}\{\phi_p\phi_{p'}\hat{\rho}_{\rm L}\}\\ &= \delta(p-p')\frac{H^2}{\sinh^2(t)}\sum_{lm}|Y_{plm}|^2\frac{|P_1^{ip}|^2}{N_{P^p}^2}\\ &\times(1-|\gamma_p|^2)\sum_n|\gamma_p|^{2n}(2n+1)\\ &= \delta(p-p')\frac{H^2}{\sinh^2(t)}\frac{p^2}{2\pi^2}\frac{\cosh^2(t)+p^2}{2p(p^2+1)}\frac{1+|\gamma_p|^2}{1-|\gamma_p|^2}\\ &= \delta(p-p')\frac{H^2}{\sinh^2(t)}\frac{p}{4\pi^2}\frac{\cosh^2(t)+p^2}{(p^2+1)}\coth(\pi p)\end{aligned} \tag{5.97}$$

which is equal to the result of the direct calculation (5.90).

## 5.C Divergence of the energy momentum tensor

As is the case in the Fulling-Rindler vacuum, the energy momentum tensor diverges at the null boundary of the hyperbolic patch. One could construct lightcone coordinates $u = \eta - r$ and $v = \eta + r$ in order to calculate $T_{uu}$. Equivalently, we consider the leading divergence of $T_{tt}$ in the $t \to 0$ limit, which is more convenient.

$$T_{tt} = (\partial_t\phi)^2 - \frac{1}{2}g_{tt}g^{\sigma\rho}(\partial_\sigma\phi)(\partial_\rho\phi) \tag{5.98}$$

For the massless case we have:

$$\langle T_{tt}\rangle = \frac{1}{2}\langle(\partial_t\phi)^2 + g^{rr}(\partial_r\phi)^2 + g^{\theta\theta}(\partial_\theta\phi)^2 + g^{\phi\phi}(\partial_{\phi\phi}\phi)^2\rangle. \tag{5.99}$$

One can calculate this directly using the hyperbolic mode functions (5.22) and the density matrix (5.95) for the Bunch-Davies expectation value $\langle T_{\mu\nu}\rangle_{\rm BD}$. Equivalently, for the leading order term we can use the Wightman functions $G^+(x,x')$ as given in [126]:

$$\langle(\partial_t\phi)^2\rangle = \lim_{t'\to t}\partial_t\partial_{t'}G^+(t,t'), \tag{5.100}$$

and similarly for the other coordinates. Note that the contribution of the super-curvature modes to the Wightman function only leads to subleading divergences[15].

[15] For $\nu' > 0$ the super-curvature mode contribution to the Wightman function is [126]:

$$G^+_*(t,t',\zeta) = \frac{H^2}{4\pi^{\frac{5}{2}}}\Gamma[-\nu'+1]\Gamma[\nu'+\frac{3}{2}]\frac{\sinh(\nu')\zeta}{\sinh\zeta}\left(\sinh t\sinh t'\right)^{\nu'-1}. \tag{5.101}$$

For the minimally coupled massless case $\nu = \frac{3}{2}$ the super-curvature mode becomes time-independent. The contribution to the energy momentum tensor is of subleading order.

The contribution of the sub-curvature modes to the Wightman function for the massless $\nu' = 1$ case is given by [126]:

$$\begin{aligned} G^+(t,t',\zeta) &= \frac{H^2}{\sinh t \sinh t'} \frac{1}{8\pi^2} \\ &\quad \times \int_{-\infty}^{\infty} dp \frac{\sin p\zeta}{\sinh \zeta} \frac{e^{\pi p}}{\sinh \pi p} \frac{(\cosh t + ip)(\cosh t' - ip)}{1+p^2} \left( \frac{\tanh \frac{t'}{2}}{\tanh \frac{t}{2}} \right)^{ip}, \\ \zeta &= \cosh r \cosh r' - \sinh r \sinh r' \left( \cos\theta \cos\theta' + \sin\theta \sin\theta' \cos(\phi - \phi') \right). \end{aligned} \tag{5.102}$$

One can check the following:

$$\begin{aligned} \langle (\partial_t \phi)^2 \rangle &= \lim_{t' \to t} \partial_t \partial_{t'} G^+(t,t',\zeta) = \frac{H^2}{4\pi^2} \int_0^{p_F} dp\ p(p^2+1) \coth(\pi p) \frac{1}{t^4} + O\left(\frac{1}{t^2}\right) \\ \langle (\partial_r \phi)^2 \rangle &= \lim_{r' \to r} \partial_r \partial_{r'} G^+(t,t,\zeta) = \frac{H^2}{4\pi^2} \int_0^{p_F} dp\ p(p^2+1) \coth(\pi p) \frac{1}{t^2} + O\left(t^0\right) \\ \langle (\partial_\theta \phi)^2 \rangle &= \lim_{\theta' \to \theta} \partial_\theta \partial_{\theta'} G^+(t,t,\zeta) \\ &= \sinh^2 r \frac{H^2}{4\pi^2} \int_0^{p_F} dp\ p(p^2+1) \coth(\pi p) \frac{1}{t^2} + O\left(t^0\right) \\ \langle (\partial_\phi \phi)^2 \rangle &= \lim_{\phi' \to \phi} \partial_\phi \partial_{\phi'} G^+(t,t,\zeta) \\ &= \sin^2\theta \sinh^2 r \frac{H^2}{4\pi^2} \int_0^{p_F} dp\ p(p^2+1) \coth(\pi p) \frac{1}{t^2} + O\left(t^0\right). \end{aligned} \tag{5.103}$$

Note that all these are divergent as $t \to 0$, but they also show the usual UV-divergence. The UV-divergence is regulated by a cutoff $p_F$. The difference $\langle T_{tt} \rangle_{\rm H} - \langle T_{tt} \rangle_{\rm BD}$ will be UV-finite. We combine the components (5.103) to obtain $\langle T_{tt} \rangle_{\rm BD}$. The expectation value $\langle T_{tt} \rangle_{\rm H}$ is obtained by replacing $\coth \pi p \to 1$, where we use the expectation value $\langle \hat{b}^\dagger_{plm} \hat{b}_{plm} + \mathbf{I} \rangle$ in the two different states [16]:

$$\begin{aligned} \langle \hat{b}^\dagger_{plm} \hat{b}_{plm} + \mathbf{I} \rangle_{\rm BD} &= \coth \pi p \\ \langle \hat{b}^\dagger_{plm} \hat{b}_{plm} + \mathbf{I} \rangle_{H} &= 1. \end{aligned} \tag{5.104}$$

Finally, we calculate the difference $\langle T_{tt} \rangle_{\rm H} - \langle T_{tt} \rangle_{\rm BD}$:

$$\begin{aligned} \langle T_{tt} \rangle_{\rm H} - \langle T_{tt} \rangle_{\rm BD} &= \frac{H^4}{2\pi^2} \int_0^{\infty} dp\ p(p^2+1) \left(1 - \coth \pi p\right) \frac{1}{t^4} + O\left(\frac{1}{t^2}\right) \\ &= -\frac{11}{240\pi} \frac{1}{t^4} + O\left(\frac{1}{t^2}\right). \end{aligned} \tag{5.105}$$

Note that we took the cutoff $p_F$ to infinity and obtain a UV-finite integral.

[16] We can calculate $\langle \hat{b}^\dagger_{plm} \hat{b}_{plm} + \mathbf{I} \rangle$ by using the density matrix (5.95)

An important observation is that (5.105) is divergent on the past horizon of the hyperbolic patch. This is indicative of the fact the hyperbolic vacuum is a non-Hadamard state. The (reduced) Bunch-Davies state *does* satisfy the Hadamard condition (see [142] for a discussion of the Hadamard condition), which we will not discuss here. Formally, one could argue that the hyperbolic vacuum and the (reduced) Bunch-Davies state are *not* in the same Hilbert space.

## 5.D The hyperbolic vacuum embedded in the Bunch–Davies state

From [128] we have for the massless case $\nu' = 1$:

$$|\Omega_{\rm BD}\rangle = \left(\otimes_{plm} e^{\gamma_p \hat{b}^\dagger_{Lplm}\otimes \hat{b}^\dagger_{Rplm}}\right)|\Omega_{\rm H,L}\rangle \otimes |\Omega_{\rm H,R}\rangle \tag{5.106}$$

or suppressing the indices $p, l, m$:

$$|\Omega_{\rm BD}\rangle = e^{\gamma \hat{b}^\dagger_{\rm L}\otimes \hat{b}^\dagger_{\rm R}}|\Omega_{\rm H,L}\rangle \otimes |\Omega_{\rm H,R}\rangle \tag{5.107}$$

with $\gamma = ie^{-\pi p}$. The left hyperbolic vacuum $|\Omega_{\rm H,L}\rangle$ is not a state of the full system; we need information about the state in the right hyperbolic patch as well. The simplest way to embed the left hyperbolic vacuum in the full Hilbert space, we can consider the simple and symmetric state $|\Omega_{\rm H,L}\rangle \otimes |\Omega_{\rm H,R}\rangle$. This state is *not* the natural vacuum state (the Bunch–Davies state) for the full de Sitter space. Also keep in mind that the hyperbolic vacuum and the Bunch-Davies state are formally not part of the same Hilbert space. However, for an effective description and comparison of the power spectra and bi–spectra a purification of the hyperbolic vacuum can be described as an excitation of the Bunch-Davies state.

**Proposition:**

$$|\Omega_{\rm H,L}\rangle \otimes |\Omega_{\rm H,R}\rangle \propto e^{-|\gamma_p|\ \hat{a}^\dagger_+ \otimes\ \hat{a}^\dagger_-}|\Omega_{\rm BD}\rangle. \tag{5.108}$$

**Proof:**

We will show that the right hand side of (5.108) vanishes when we act with any of the $\hat{b}_{Llpm}$ annihilation operators. We use the expression for the hyperbolic annihilation operator $\hat{b}_{Llpm}$ in terms of the creation and annihilation for Bunch-Davies modes (5.36), suppressing from now on the labels $p, l, m$:

$$\hat{b}_{\rm L} = \sum_\sigma \frac{N_P}{N_{\chi_\sigma}}\left(\alpha^\sigma_{\rm L}\hat{a}_\sigma + \bar{\beta}^\sigma_{\rm L}\hat{a}^\dagger_\sigma\right). \tag{5.109}$$

We want to show that $\hat{b}_{\rm L}$ acting on the RHS of (5.108) vanishes:

$$\sum_\sigma \frac{N_P}{N_{\chi_\sigma}}\left(\alpha^\sigma_{\rm L}\hat{a}_\sigma + \bar{\beta}^\sigma_{\rm L}\hat{a}^\dagger_\sigma\right) e^{-|\gamma_p|\hat{a}^\dagger_+\otimes\hat{a}^\dagger_-}|\Omega_{\rm BD}\rangle \stackrel{?}{=} 0. \tag{5.110}$$

Consider the annihilation operator $\hat{a}_\sigma$ acting on (5.108):

$$\begin{aligned}\hat{a}_\pm e^{-|\gamma_p|\hat{a}_+^\dagger\hat{a}_-^\dagger}|\Omega_{\rm BD}\rangle &= \left[\hat{a}_\pm\ ,\ e^{-|\gamma_p|\hat{a}_+^\dagger\hat{a}_-^\dagger}\right]|\Omega_{\rm BD}\rangle \\ &= -\left[\hat{a}_\pm\ ,\ |\gamma_p|\hat{a}_+^\dagger\hat{a}_-^\dagger\right]e^{-|\gamma_p|\hat{a}_+^\dagger\hat{a}_-^\dagger}|\Omega_{\rm BD}\rangle \\ &= -|\gamma_p|\hat{a}_\mp^\dagger e^{-|\gamma_p|\hat{a}_+^\dagger\hat{a}_-^\dagger}|\Omega_{\rm BD}\rangle.\end{aligned} \tag{5.111}$$

Substituting this result in (5.110) gives:

$$\begin{aligned}&\sum_\sigma \frac{N_P}{N_{\chi_\sigma}}\left(\alpha_{\rm L}^\sigma\hat{a}_\sigma + \bar{\beta}_{\rm L}^\sigma\hat{a}_\sigma^\dagger\right)e^{-|\gamma_p|\hat{a}_+^\dagger\otimes\hat{a}_-^\dagger}|\Omega_{\rm BD}\rangle \\ &= N_P\sum_\sigma\left(-\frac{\alpha_{\rm L}^{-\sigma}}{N_{\chi_{-\sigma}}}|\gamma| + \frac{\bar{\beta}_{\rm L}^\sigma}{N_{\chi_\sigma}}\right)\hat{a}_\sigma^\dagger e^{-|\gamma_p|\hat{a}_+^\dagger\otimes\hat{a}_-^\dagger}|\Omega_{\rm BD}\rangle.\end{aligned} \tag{5.112}$$

It is easy to check that the quantity between brackets on the RHS of (5.112) vanishes for both $\sigma = \pm 1$. This finalizes the proof:

$$\hat{b}_{\rm L}e^{-|\gamma|\hat{a}_+^\dagger\otimes\hat{a}_-^\dagger}|\Omega_{\rm BD}\rangle = 0 \qquad \forall p,l,m. \tag{5.113}$$

The state (5.108) is pure. Note that the symmetric and antisymmetric modes corresponding to $\sigma = \pm 1$ are entangled with each other and their reduced density matrices are thermal. We reiterate that the hyperbolic vacuum does not satisfy the Hadamard condition and formally speaking the hyperbolic vacuum and the (reduced) Bunch-Davies state do not live in the same Hilbert space.

# Chapter 6

# Inflationary potentials & non-minimal coupling

There are many single field inflation models and it would be helpful if we could make progress towards *reducing* the number of models, or at least organize them in an insightful way. In this chapter we will analyze single field inflation models with non-minimal coupling to gravity, with the purpose of finding *special* models, that appear as attractors in the inflationary landscape. An attractor model is a model that appears as a limiting case of a class of models; we will make this idea more precise below. In recent work it has been shown that the Starobinsky inflation model appears as an attractor in several seemingly unrelated classes of models. We try to explain this from the perspective of general non-minimally coupled single scalar field models.

In section (6.1) we introduce the Starobinsky and chaotic inflation models, which appear as attractor models in later sections. We also discuss how non-minimally coupled models can be written in the Einstein frame, the frame in which the scalar field *is* minimally coupled to gravity. In section (6.2) we present a non-exhaustive overview of recently discovered attractor mechanisms. In section (6.3) we try to generalize the non-minimally coupled attractor mechanisms presented in section (6.2). We describe which conditions suffice for attractor behavior and we give a different perspective on the "fine-tuning" problem. We show, that under certain conditions, the well known Starobinsky and chaotic inflation models appear in the opposite strong and weak limits of the non-minimal coupling. We also discuss the nature of the attractor points.

## 6.1 Introducing the attractors

### 6.1.1 A zoo of models

Many single field inflation models are in accordance with observational data. Planck data favor models with $n_s = 0.968 \pm 0.006$ and with an upper limit $r < 0.11$ on the tensor-scalar ratio at 95% confidence level [98,99]. In [143] results emerged suggesting a large amplitude for the tensor mode fluctuations ($r \sim 0.2$), but these results were later revoked after a joint analysis of BICEP2, Keck Array and Planck Data [144].

Countless inflationary models have been developed; an "encyclopedia" of a subset of them can be found in [145]. Inflationary models can be (partially-) characterized by their position in the $(n_s, r)$ plane. Clearly, it would be helpful if we could make progress towards *reducing* the number of models, or at least organize them in an insightful way.

A second issue with many of these models is the "fine-tuning problem". In an effective field theory description one generally writes down a potential of the form:

$$V(\phi) = \sum_n \lambda_n \phi^n. \tag{6.1}$$

One argues that terms with $n > 4$ are *irrelevant*; their coupling is small at low energies, or in other words, the higher order terms in the expansion (6.1) are suppressed. But in many such models, for example chaotic inflation, the change of the field value exceeds the Planck mass over the course of inflation: $\Delta\phi > M_{pl}$. In these cases, there is no reason to assume that these terms are small and the assumption they *are* is a form of fine-tuning. Generally, the fewer parameters that need to be fine-tuned, the more natural they are. This provides a second motivation for investigating non-minimally coupled models; how does the fine-tuning in the minimally coupled description translate to the non-minimally coupled description?

In this chapter, we will discuss the emergence of attractor points in the $(n_s, r)$ plane in the context of non-minimally coupled inflation models. Attractor points correspond to *special* points in the $(n_s, r)$ plane and appear as a limiting case of a class of models. We will see that one particular model, Starobinsky inflation, appears as a limit of several different classes of models.

Below, we briefly describe the Starobinsky model and the chaotic inflation model. Both these models appear as attractor points in sections (6.2) and (6.3). Subsequently, we discuss the relation between the Jordan and Einstein frames for scalar field Lagrangians.

### 6.1.2 Starobinsky inflation

Starobinsky inflation was one of the earliest models of inflation [146]. It arises naturally in the context of $f(R)$-gravity. The degrees of freedom of $f(R)$-gravity can be decomposed into normal Einstein gravity plus a scalar degree of freedom. For certain $f(R)$-models, this scalar degree of freedom has a potential that allows for inflation to happen. Below, we will briefly illustrate how $f(R)$-gravity gives rise to the Starobinsky model.

Consider the gravitational action

$$S = \frac{1}{2}\int d^4x\sqrt{-g}f(R), \tag{6.2}$$

where $f(R)$ is a polynomial of the curvature scalar $R$. We introduce an auxiliary field $\chi$

$$S = \frac{1}{2}\int d^4x\sqrt{-g}\left(f(\chi) + f_{,\chi}(\chi)\left(R-\chi\right)\right), \tag{6.3}$$

such that (6.3) corresponds to (6.2) when $\chi$ is on shell. Now consider the field redefinition

$$\begin{aligned}\psi &= f_{,\chi}(\chi),\\ \chi &= \chi(\psi).\end{aligned} \tag{6.4}$$

In terms of $\psi$, we now have a scalar field action with non-minimal coupling to Einstein gravity:

$$\begin{aligned}S &= \int d^4x\sqrt{-g}\left(\frac{\psi R}{2} - U(\psi)\right),\\ U(\psi) &= \frac{1}{2}\left(\psi\chi(\psi) - f(\chi(\psi))\right).\end{aligned} \tag{6.5}$$

In subsection 6.1.4 we describe how we can write an action of the type (6.5) in the Einstein frame, with canonically normalized kinetic energy term, by doing a Weyl transformation $g_{\mu\nu} \to \psi^{-1}g_{\mu\nu}$ followed by a field redefinition. Here we simply state the result:

$$\begin{aligned}S &= \int d^4x\sqrt{-g}\left(\frac{R}{2} - \frac{1}{2}(\partial\phi)^2 - V(\phi)\right),\\ V(\phi) &= \left[\frac{U(\psi)}{\psi^2}\right]_{\psi=e^{\sqrt{\frac{2}{3}}\phi}}.\end{aligned} \tag{6.6}$$

So far we have seen how $f(R)$-gravity can be decomposed into Einstein gravity plus a scalar degree of freedom, with a scalar potential given by (6.5,6.6). One might wonder which types of $f(R)$-gravity lead to viable single field inflation models.

Inspection of the first order potential slow-roll parameter $\epsilon_{\rm V}$ (4.36), which can be expressed in terms of $f$, shows that:

$$\begin{aligned}\epsilon_{\rm V} &= \frac{1}{2}\left(\frac{V_{,\phi}}{V}\right)^2 \\ &= \frac{1}{3}\left(\frac{\chi(\psi)f_{,\chi}(\chi(\psi)) - 2f(\chi(\psi))}{\chi(\psi)f_{,\chi}(\chi(\psi)) - f(\chi(\psi))}\right)^2\Bigg|_{\psi=e\sqrt{\frac{2}{3}}\phi}.\end{aligned} \tag{6.7}$$

Smallness of (6.7) puts a condition on the polynomial $f(R)$. The first slow-roll condition ($\epsilon_{\rm V} \ll 1$) can be satisfied by having a large coefficient of the $R^2$ term in $f$. In fact, the model originally proposed by Starobinsky is given by:

$$f(R) = R + \alpha R^2. \tag{6.8}$$

The Einstein frame potential (6.6) for this model is given by:

$$V(\phi) = \frac{1}{8\alpha}\left(1 - e^{-\sqrt{\frac{2}{3}}\phi}\right)^2. \tag{6.9}$$

To leading order in $N^{-1}$, where $N$ is the number of e-folds (4.29,4.30), the scalar spectral index (4.104) and the tensor to scalar ratio (4.102) of the Starobinsky-model are given by:

$$\begin{aligned} n_s &\approx 1 - \frac{2}{N} \\ r &\approx \frac{12}{N^2}. \end{aligned} \tag{6.10}$$

The Starobinsky model lies in the "sweet-spot" of the Planck data [98, 99, 147] (see figure 6.1). An estimate of the energy scale of inflation depends on the value of the slow-roll parameter $\epsilon$, but the COBE normalization indicates an order of magnitude $V^{\frac{1}{4}} \sim 10^{-3} M_{pl}$, which corresponds to large $\alpha$.

### 6.1.3 Chaotic inflation

Chaotic inflation was proposed in [148]. It is an example of a *large field* inflation model, where the difference between the final and initial value of the scalar field is large in units of Planck's mass ($\Delta\phi > M_{pl}$). In chaotic inflation, the scalar field is minimally coupled to gravity and has monomial potential

$$V(\phi) = \lambda_{2n}\phi^{2n}, \tag{6.11}$$

where $\lambda_{2n}$ is a coupling constant. The number of e-folds is given by (4.29,4.30):

$$N \approx -\int_{\phi_N}^{\phi_{\rm end}} \frac{1}{\sqrt{2\epsilon_{\rm V}}} d\phi = -\int_{\phi_N}^{\phi_{\rm end}} \frac{V}{V_{,\phi}} d\phi = -\frac{\phi^2}{4n}\Big|_{\phi_N}^{\phi_{\rm end}} \approx \frac{\phi_N^2}{4n}. \tag{6.12}$$

In terms of $N$ (6.12), the first two slow roll parameters are given by

$$\epsilon_{\rm V} \approx \frac{n}{2N}, \qquad \eta_V \approx \frac{2n-1}{2N}. \tag{6.13}$$

This corresponds to a scalar index and tensor to scalar ratio[1]

$$\begin{aligned} n_s &= 1 + \frac{3-5n}{N} \quad &&\approx 0.967 \quad \text{for } n = 1, \\ r &= \frac{8n}{N} &&\approx 0.133 \quad \text{for } n = 1, \end{aligned} \tag{6.14}$$

where the tensor to scalar ratio is considered to be large, like the tensor to scalar ratio of other large field inflation models. Such a large tensor to scalar ratio is not in the "sweet-spot" of the Planck data (see figure 6.1). Interest in chaotic inflation models rose after a report of a large tensor to scalar ratio, but a more elaborate analysis did not confirm this conclusion [143, 144].

### 6.1.4 Switching frames

A general scalar field Lagrangian can have non-minimally coupling to gravity and a kinetic energy terms that is not canonically normalized. Below we show how we can rewrite such a general scalar field Lagrangian in terms of a Lagrangian with minimal coupling to gravity and with a canonically normalized kinetic energy term (the *Einstein frame*). This can be accomplished by doing a Weyl transformation followed by a field redefinition. The purpose of considering a scalar field Lagrangian in the non-minimally coupled *Jordan frame* is that a Lagrangian might look very simple in one frame and very complicated in the other. For example, fine-tuning in one frame might have a different interpretation in another frame. However, the physics should be frame-independent.

A general Lagrangian of a theory with a non-minimally coupled scalar field can be written as:

$$\mathcal{L} = \sqrt{-g}\left(\frac{1}{2}\Omega(\phi)R - \frac{K(\phi)}{2}(\partial\phi)^2 - U(\phi)\right). \tag{6.15}$$

One could do a field redefinition $\phi \to \chi$ to make the kinetic term canonically normalized. Such a field redefinition must satisfy $\tilde{K}(\chi)\left(\frac{\delta\chi}{\delta\phi}\right)^2 = K(\phi)$.

A Weyl transformation $g_{ab} \to \Omega^{-1} g_{ab}$ can be used to bring the Lagrangian (6.15) into the Einstein frame. The curvature scalar in four spacetime dimensions transforms as follows:

$$R \to \Omega\left(R + 3\Box \ln(\Omega) - \frac{3}{2}(\partial \ln(\Omega))^2\right). \tag{6.16}$$

[1] We take $N = 60$ here.

The second term in 6.16 will result into a boundary term in the Lagrangian. If we discard this term, the Lagrangian in the Einstein frame is given by:

$$\mathcal{L} = \sqrt{-g}\left(\frac{R}{2} - \left(\frac{K}{\Omega} + \frac{3}{2}\frac{\Omega'^2}{\Omega^2}\right)\frac{1}{2}(\partial\phi)^2 - \frac{U}{\Omega^2}\right). \tag{6.17}$$

A field redefinition $\chi = \chi(\phi)$ can be done such that the kinetic energy term is canonically normalized:

$$\left(\frac{\delta\chi}{\delta\phi}\right)^2 = \frac{K}{\Omega} + \frac{3}{2}\frac{\Omega'^2}{\Omega^2}. \tag{6.18}$$

In terms of the field $\chi(\phi)$, of which the explicit expression can be found by solving (6.18), the Lagrangian takes a simple form

$$\mathcal{L} = \sqrt{-g}\left(\frac{R}{2} - \frac{1}{2}(\partial\chi)^2 - V(\chi)\right), \tag{6.19}$$

where $V(\chi)$ is given by

$$V(\chi) = \frac{U(\phi(\chi))}{\Omega^2(\phi(\chi))}. \tag{6.20}$$

The possibility to switch between the Jordan and Einstein frames will be extensively used in sections (6.2) and (6.3).

## 6.2 Attractor models

In this section we will present a non-exhaustive overview of attractor mechanisms that recently appeared in the literature. The first two examples we will discuss, the universal attractor model and the induced inflation model, form a subset of the class of non-minimally coupled models. It is this class of non-minimally coupled models that we describe and generalize in section (6.3). Here we will focus on their "Starobinsky attractor point" and in section (6.3) we will discuss their "chaotic attractor points". The third and fourth examples of attractor models, the (multifield-) conformal attractor model and the $\alpha$-attractor model are to some degree qualitatively different from universal attractor inflation and induced inflation. For completeness we briefly describe them here. Their relation to non-minimally coupled attractor models is described in [149].

### 6.2.1 Universal attractor inflation

Universal attractor inflation is a non-minimally coupled model. The model was proposed in [150], of which we will give a brief summary. In the universal attractor model, the coupling of the scalar field to the curvature is regulated by a

dimensionless parameter $\xi$. In the large $\xi$ limit, this model reduces to Starobinsky inflation.

The action of the universal attractor model is given by:

$$S = \int d^4x\sqrt{-g}\left(\frac{1}{2}\Omega(\phi)R - \frac{1}{2}g^{\mu\nu}\partial_\mu\phi\partial_\nu\phi - V_J(\phi)\right), \tag{6.21}$$

with

$$\begin{aligned}\Omega(\phi) &= 1 + \xi f(\phi),\\ V_J(\phi) &= \lambda f^2(\phi),\end{aligned} \tag{6.22}$$

where $\xi$ and $\lambda$ are dimensionless couplings and $f(\phi)$ is a function of the field.

A Weyl transformation $g_{\mu\nu} \to \Omega(\phi)^{-1}g_{\mu\nu}$ brings the action in the Einstein frame (6.17):

$$S = \int d^4x\sqrt{-g}\left(\frac{R}{2} - \frac{1}{2}\left(\frac{1}{\Omega(\phi)} + \frac{3}{2}\frac{\Omega'(\phi)^2}{\Omega(\phi)^2}\right)(\partial\phi)^2 - \frac{V_J(\phi)}{\Omega^2(\phi)}\right). \tag{6.23}$$

For large $\xi$, the kinetic term is dominated by the second part:

$$\frac{1}{\Omega(\phi)} \ll \frac{3}{2}\frac{\Omega'(\phi)^2}{\Omega(\phi)^2}. \tag{6.24}$$

The field redefinition $\chi = \chi(\phi)$ that gives the kinetic energy term canonical normalization is, using (6.24), approximately:

$$\sqrt{\frac{3}{2}}\frac{\Omega'(\phi)}{\Omega(\phi)} = \frac{\delta\chi}{\delta\phi} \tag{6.25}$$

The potential for $\chi$ can be recognized as the Starobinsky model (6.9):

$$V_E(\chi) = \frac{\lambda}{\xi^2}\left(1 - e^{-\sqrt{\frac{2}{3}}\chi}\right)^2. \tag{6.26}$$

At strong (non-minimal) coupling, the universal attractor model is equivalent to Starobinsky inflation. Note that this argument does not depend on the specific form of $f(\phi)$. In [151] it is shown that the weak coupling limit effectively yields chaotic inflation for monomial $f$.

### 6.2.2 Induced inflation

Induced inflation is a different non-minimally coupled model. The model is called induced inflation, because in the Jordan frame the Planck mass is determined by the expectation value of the scalar field. It was proposed in [152], of which

we will give a brief summary. In the induced inflation model, the coupling to the curvature is regulated by a dimensionless parameter $\xi$. In the large $\xi$ limit, this model resembles Starobinsky inflation. It was proposed in the context of a general search for non-minimally coupled models that give rise to Starobinsky-like inflation.

In [152], the starting point is a general Lagrangian of the form (6.15), with the assumptions that $U \to 0$ and $\Omega \to 1$ at the end of inflation (when $\phi = \phi_{\text{end}}$). It is argued that any Jordan frame potential $U$ of the form

$$U = \lambda(\Omega(\phi) - 1)^2 \tag{6.27}$$

leads to Starobinsky-like inflation as long as

$$K(\phi) \ll \frac{\Omega'(\phi)^2}{\Omega(\phi)} \tag{6.28}$$

during inflation. Note that universal attractor inflation at strong coupling is a realization of this mechanism. In [152] a model similar to universal attractor inflation is proposed, with

$$\Omega(\phi) = \xi f(\phi). \tag{6.29}$$

This model is motivated by the fact that it is perturbatively unitary, which means that the Einstein frame potential $\frac{U}{\Omega^2}$ does not include an expansion in positive powers of the large coupling $\frac{\xi^2}{\lambda}$.

This model is a Starobinsky attractor at strong coupling, but in [151] it is shown that it is a $\phi^2$-chaotic inflation attractor in the weak coupling limit $\xi \to 0$. This observation motivated our research: which non-minimally coupled models have Starobinsky attractors and which of them have chaotic inflation attractors? These questions and a more thorough treatment of the weak coupling limit of induced inflation can be found in section (6.3).

### 6.2.3 Conformal attractors

The (multifield-) conformal attractor model provides a mechanism that naturally favors Starobinsky-like inflation. It was proposed in [153, 154] and further developed in [155–158]. We will briefly present the main concepts.

The starting point is a Lagrangian with two fields:

$$\mathcal{L} = \sqrt{-g}\left[\frac{1}{2}\partial_\mu\chi\partial^\mu\chi + \frac{\chi^2}{12}R(g) - \frac{1}{2}\partial_\mu\phi\partial^\mu\phi - \frac{\phi^2}{12}R(g) - \frac{\lambda}{36}F\left[\frac{\phi}{\chi}\right](\phi^2 - \chi^2)^2\right]. \tag{6.30}$$

This theory is locally conformal invariant under the following transformations:

$$\tilde{g}_{\mu\nu} = e^{-2\sigma(x)} g_{\mu\nu}\,, \qquad \tilde{\chi} = e^{\sigma(x)}\chi\,, \qquad \tilde{\phi} = e^{\sigma(x)}\phi\,. \tag{6.31}$$

This allows for a "gauge choice" $\chi^2 + \phi^2 = 6$. The remaining physical degrees of freedom can be parametrized by writing:

$$\begin{aligned} \chi &= \sqrt{6}\cosh\frac{\varphi}{\sqrt{6}}, \\ \phi &= \sqrt{6}\sinh\frac{\varphi}{\sqrt{6}}, \end{aligned} \tag{6.32}$$

which brings the Lagrangian in the following form:

$$\mathcal{L} = \sqrt{-g}\left[\frac{1}{2}R - \frac{1}{2}\partial_\mu\varphi\partial^\mu\varphi - F[\tanh\frac{\varphi}{\sqrt{6}}]\right]. \tag{6.33}$$

The point is that the potential $F[\tanh\frac{\varphi}{\sqrt{6}}]$ admits slow-roll inflation for a wide choice of potentials $F$. In particular, for $F[x] = \lambda_{2n}x^{2n}$ one finds $n_s \approx 1 - \frac{2}{N}$ and $r \approx \frac{12}{N^2}$, which resembles the Starobinsky model. In fact, the choice $F[x] = \frac{x^2}{(1+x)^2}$ is exactly equivalent to the Starobinsky model, as shown in [153,154]. In summary, a wide range of potentials $F$ give rise to inflation at the Starobinsky point in the $(n_s, r)$-plane.

The $\alpha$-attractor models emerged in the analysis of (multifield-) conformal attractor models, by considering modifications or generalizations of its supergravity embedding [157,158]. The Lagrangian at single field level is given by:

$$\mathcal{L} = \sqrt{-g}\left(\frac{R}{2} - \frac{1}{(1-\frac{\phi^2}{6\alpha})^2}(\partial\phi)^2 - F\left[\frac{\phi}{\sqrt{6\alpha}}\right]\right) \tag{6.34}$$

Note that this Lagrangian has non-canonically normalized kinetic energy term. For $\alpha = 1$ this Lagrangian is equal to (6.33), which can be seen by doing a field redefinition.

In [157,158] the behavior of these models is analyzed for different values of $\alpha$. For large $\alpha$, chaotic inflation attractor point are found. For $\alpha = 1$, Starobinsky-like inflation is found, as described above. For $\alpha < 1$, the models are characterized by $n_s \approx 1 - \frac{2}{N}$ and $r \approx \frac{12\alpha}{N^2}$ (see figure 6.1). Note that there are model dependent corrections in higher orders of $\frac{1}{N}$ for all these parameters $(n_s, r)$.

## 6.3 Non-minimally coupled models

In this section we describe the framework of single scalar field models with non-minimal coupling to Einstein gravity. It has been realized for quite some time that

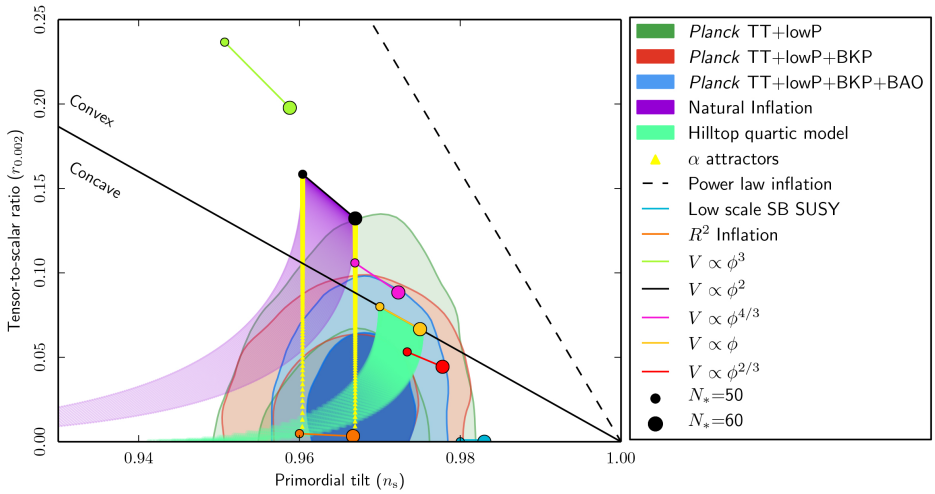


***Figure 6.1:*** Caption from [98]: *Marginalized joint 68 % and 95 % CL regions for $n_s$ and $r_{0.002}$ from Planck alone and in combination with its cross-correlation with BICEP2/Keck Array and/or BAO data compared with the theoretical predictions of selected inflationary models. Source: [98].*

with the introduction of non-minimal couplings the space of phenomenologically acceptable theories of inflation can be expanded considerably [159–162], typically in fact ameliorating the required degree of fine-tuning [163, 164]. We will try to generalize the appearance of attractor points as described by the non-minimally coupled models of universal attractor inflation and induced inflation (see section 6.2).

In subsection (6.3.1) we define the 'flat' and 'steep' conformal limits in the context of single scalar field models that are non-minimally coupled to Einstein gravity. In subsection (6.3.2), we identify under which conditions the flat conformal factor limit leads to slow-roll inflation and we explicitly show the appearance of chaotic models of inflation in this limit. In subsection (6.3.3) we show that the weak coupling limit of a subset of induced inflation models effectively yields $\phi^2$-chaotic inflation. In subsection (6.3.4) we further generalize and identify another set attractor points that correspond to $\phi^{2n}$-chaotic inflation.

### 6.3.1 Non-minimal coupling and its limits

The Lagrangian for a non-minimally coupled scalar field is given by:

$$\mathcal{L} = \sqrt{-g}\left(\frac{1}{2}\Omega(\phi)R - \frac{K(\phi)}{2}(\partial\phi)^2 - U(\phi)\right), \tag{6.35}$$

where we require that at the vacuum configuration $\Omega \to 1$ and $U \to 0$[2].

One can write (6.35) in the Einstein frame with a canonically normalized kinetic energy term, by performing a Weyl transformation followed by a field redefinition. In appendix (6.A) we give expressions for the Einstein frame potential slow-roll parameters in terms of the Jordan frame quantities $\Omega$ and $U$. These expressions greatly simplify if $K = \Omega$, which can be accomplished by doing an initial field redefinition. However, we will choose $K = 1$, just to be consistent with the formulation of induced inflation in [152]. After performing a Weyl transformation $g_{ab} \to \Omega^{-1} g_{ab}$, the Lagrangian reads:

$$\mathcal{L} = \sqrt{-g}\left(\frac{R}{2} - \frac{1}{2}\left(\frac{1}{\Omega} + \frac{3}{2}\left(\frac{\Omega'}{\Omega}\right)^2\right)(\partial\phi)^2 - \frac{U}{\Omega^2}\right), \tag{6.36}$$

where the prime denotes differentiation with respect to the scalar $\phi$. The kinetic energy term can be canonically normalized by performing a field redefinition $\chi(\phi)$ such that

$$\left(\frac{\delta\chi}{\delta\phi}\right)^2 = \frac{1}{\Omega} + \frac{3}{2}\left(\frac{\Omega'}{\Omega}\right)^2. \tag{6.37}$$

We will analyze these non-minimally coupled models in two limits, in which one of the two contributions to the Einstein frame kinetic term dominates (6.36). We will suggestively call these the *flat* and *steep* conformal factor limits respectively:

*flat limit*

$$\frac{3}{2}\frac{\Omega'^2}{\Omega} \ll 1 \tag{6.38}$$

*steep limit*

$$\frac{3}{2}\frac{\Omega'^2}{\Omega} \gg 1. \tag{6.39}$$

In these limits, starting from the usual Einstein frame definitions for the inflationary slow-roll parameters [105](see appendix 6.A.1), the expressions for the inflationary slow-roll parameter $\epsilon$ and $\eta$, in terms of $U$ and $\Omega$ (6.63,6.64), simplify considerably. For the first order slow-roll parameter $\epsilon$ one arrives at the following expressions

*flat limit*

$$\epsilon \approx \frac{\Omega}{2}\left(\frac{U'}{U} - 2\frac{\Omega'}{\Omega}\right)^2 \tag{6.40}$$

*steep limit*

$$\epsilon \approx \frac{\Omega^2}{3\Omega'^2}\left(\frac{U'}{U} - 2\frac{\Omega'}{\Omega}\right)^2. \tag{6.41}$$

The slow-roll conditions can be naturally satisfied by Jordan frame potentials $U$ that are proportional to $\Omega^2$ up to terms higher order in the slow-roll approximation, for both the flat and steep limits. Requiring the inflationary model to

[2]We have set the reduced Planck mass to one. The vanishing of the potential $U$ corresponds to a small cosmological constant.

be Starobinsky-like in the steep limit in fact determines the Jordan frame potential [152]

$$U = \lambda \left(\Omega - 1\right)^2 . \tag{6.42}$$

We will refer to these models as *asymptotic Starobinsky models*. This particular relation between the conformal factor and the Jordan frame potential allows a further simplification of the slow-roll parameters in the flat and steep conformal factor limits

*flat limit*

$$\epsilon \approx 2 \left(\frac{\Omega'^2}{\Omega}\right) \frac{1}{\left(\Omega - 1\right)^2} \tag{6.43}$$

*steep limit*

$$\epsilon \approx \frac{4}{3} \frac{1}{\left(\Omega - 1\right)^2} . \tag{6.44}$$

It is important to note, as should also be clear from the above expressions, that the flat or steep conformal factor limits do not necessarily imply the slow-roll conditions. They do seem to be sufficient to allow for regions in field space where the slow-roll conditions are met. From now on we will mostly be interested in considering the (opposite) flat conformal factor limit of the asymptotic Starobinsky models. First we identify sufficient conditions for the conformal factor such that a slow-roll inflationary regime exists in the flat conformal factor limit and, if the flat limit exists, to what type of inflationary model this leads.

### 6.3.2 The flat conformal factor limit

In this section we will investigate the flat conformal factor limit of asymptotic Starobinsky models. We will show that a generic power law implementation of the flat conformal factor limit is sufficient to make sure that a slow-roll limit can be satisfied in some region of field space. If we are interested in considering a flat conformal factor limit (6.38) that can be satisfied over a large enough field range, a natural procedure would be to constrain all derivatives of $\Omega$ around the vacuum field value $\phi_{\rm vac}$ to be sufficiently small. Note that for the asymptotic Starobinsky models that we are considering the vacuum field value is defined by $U(\phi_{\rm vac}) = 0$. It is straightforward to check that this imposes the following condition on the derivatives of $\Omega$ at $\phi_{\rm vac}$, denoted by $\Omega^{(n)}_{\rm vac}$

$$\Omega^{(n)}_{\rm vac} = O\left((\alpha)^n\right) , \tag{6.45}$$

for some small parameter $\alpha$, such that $\alpha(\phi - \phi_{\rm vac}) \ll 1$, with $\phi_{\rm vac} < \phi < \phi_N$ where $\phi_N$ denotes the field value to allow for $N$ e-folds of slow-roll inflation. In general it is useful to perform a shift to the field variable $\tilde{\phi}$ defined as $\tilde{\phi} = \phi - \phi_{\rm vac}$. After the

shift the same conditions (6.45) apply, with $\phi$ replaced by $\tilde{\phi}$ and $\tilde{\phi}_{\rm vac} = 0$. These conditions on the derivatives of $\Omega$ at $\phi_{\rm vac}$ resemble the slow-roll conditions and as such could be considered as fine-tuning. When we discuss specific examples of the flat conformal factor limit we will come back to this point.

An expansion of the Einstein frame potential in terms of the canonically normalized field $\chi$ (6.37) around $\chi_{\rm vac} = 0$ explicitly shows the relation between the flat conformal factor condition (6.45) and the suppression of higher order powers of $\chi$, for the asymptotic Starobinsky model $U = \lambda(\Omega - 1)^2$

$$\begin{aligned}\left.\frac{U}{\Omega^2}\right|_{\phi=\phi(\chi)} &= \lambda\Omega'^2_{\rm vac}\chi^2 + \lambda\left(\Omega'_{\rm vac}\Omega''_{\rm vac} - \frac{3}{2}\Omega'^3_{\rm vac}\right)\chi^3 + \\ &+ \frac{\lambda}{24}\left(-50\Omega'^2_{\rm vac}\Omega''_{\rm vac} + \frac{75}{2}\Omega'^4 + 6\Omega''^2_{\rm vac} + 8\Omega'_{\rm vac}\Omega'''_{\rm vac}\right)\chi^4 + \dots ,\end{aligned} \tag{6.46}$$

where it should be understood that the dots not only include higher powers of $\chi$ but also corrections to the coefficients higher order in the flat conformal factor limit (6.A.2). So we conclude that the leading term in the power law expansion is the $\chi^2$-term, as long as $\Omega'_{\rm vac} \neq 0$. This is of course recognized as the potential for (quadratic) chaotic inflation. Note that the slow-roll conditions are violated for small $\chi$, so the field range where the slow-roll conditions apply is smaller than the field range where the flat conformal factor conditions apply. Higher order terms are polynomially suppressed by virtue of the flat conformal factor condition (6.45) on the higher order derivatives of $\Omega$. Smallness of the higher order terms in the Einstein frame potential of a $\chi^2$-chaotic inflation model can be interpreted as the smallness of the variation of the conformal factor $\Omega$ in the Jordan frame of a Lagrangian (6.35).

From the above expansion we also see that when $\Omega'_{\rm vac} = 0$, but $\Omega''_{\rm vac} \neq 0$, then the first nonzero term in expansion (6.46) is the $\chi^4$-term. The higher order terms are again suppressed by virtue of the flat conformal factor condition (6.45). The first non-zero derivative of $\Omega$ therefore determines the (higher-order) model of chaotic inflation. Note that although the coefficients are different for different $\Omega$ (and $\lambda$), the slow-roll parameters for chaotic models do not depend on the coefficients and as such the predictions in the $n_s$ versus $r$ plane will be the same, as we will soon show explicitly. Of course, the scale of inflation is related to the specific value of the coefficient. To agree with observational constraints, for quadratic chaotic inflation the COBE normalisation implies that the mass parameter should roughly equal $10^{-5}$ (in natural units). For a given $\lambda$ this further constrains the first derivative of the conformal factor. So although these models all give the same predictions for $n_s$ and $r$, they are observationally distinguished in their prediction for the magnitude of the density perturbations. This is different from the steep conformal factor limit, where the scale of inflation is uniquely determined by the parameter $\lambda$. This

perhaps favors fixing $\lambda$ to a value that agrees with the COBE normalisation in the Starobinsky limit, but as should be clear from the above discussion this will then not reproduce the COBE normalisation in the weak non-minimal coupling limit.

After this general discussion, let us now move on to the general expressions for the slow-roll parameters in this limit and provide some specific examples in which a non-minimal coupling parameter governs a flow between the flat and steep conformal factor limits.

### 6.3.3 Chaotic fixed points for asymptotic Starobinsky models

In the previous section we saw that in general, when the flat conformal factor condition is satisfied, the Einstein frame potential will be that of chaotic inflation. Here we will first determine the consequences of this general result for the first and second slow-roll parameters, explicitly using the flat conformal factor condition (6.45). Subsequently we give some specific examples in which this behavior is realized.

If the conformal factor $\Omega$ satisfies the flat conformal factor limit (6.45), we can expand $\Omega$ as

$$\Omega = 1 + \sum_{m=1} \Omega_m \alpha^m \tilde{\phi}^m, \tag{6.47}$$

where we extracted the coefficients $\Omega_m$ that are of order $O(1)$ and again introduced the small parameter $\alpha$ that should satisfy $\alpha\tilde{\phi} \ll 1$ for $0 < \tilde{\phi} < \tilde{\phi}_N$.

In appendix (6.A.1) we compute the slow-roll parameters for several different cases. If $\Omega_1 \neq 0$, we find (6.75 with $n = 1$):

$$\epsilon = \frac{2}{\tilde{\phi}^2} + O\left(\alpha\tilde{\phi}\right), \quad \eta = \frac{2}{\tilde{\phi}^2} + O\left(\alpha\tilde{\phi}\right), \tag{6.48}$$

which indeed corresponds to leading order to the results of $\phi^2$-chaotic inflation. One could imagine imposing the condition that $\Omega$ is an even function. In that case, for $\Omega_2 \neq 0$, we find (6.76 with $n = 1$)

$$\epsilon = \frac{8}{\tilde{\phi}^2} + O\left((\alpha\tilde{\phi})^2\right), \qquad \eta = \frac{12}{\tilde{\phi}^2} + O\left((\alpha\tilde{\phi})^2\right), \tag{6.49}$$

which corresponds to leading order to the results of $\phi^4$-chaotic inflation. The explicit expressions for the subleading parts can be found in appendix (6.A.1).

To illustrate this further and relate the flat and steep conformal limits to a continuous non-minimal coupling parameter to be able to consider the flow behavior

as a function of this non-minimal coupling, let us give two examples where the conformal factor naturally satisfies the flatness limit (6.45). In the first example we analyze induced inflation models. This agrees with the analysis done in [151].

**Example 6.3.1. Induced inflation**

*Induced inflation*[3] is a particular subset of asymptotic Starobinsky models, with $\Omega(\phi) = \xi f(\phi)$ and $f(0) = 0$, where $\xi$ is a coupling parameter.

**Monomial:** $\Omega = \xi\phi^m$

Since we demand that $\Omega(\phi_{\text{vac}}) = 1$, we find $\phi_{\text{vac}} = \xi^{-\frac{1}{m}}$. Defining $\tilde{\phi} = \phi - \xi^{-\frac{1}{m}}$ one can write the following expansion of $\Omega$ in terms of $\tilde{\phi}$:

$$\begin{aligned}\Omega &= \xi\phi^m \\ &= \xi\left(\tilde{\phi} + \xi^{-\frac{1}{m}}\right)^m \\ &= 1 + \sum_{i=1}^{m} \tilde{\phi}^i \xi^{\frac{i}{m}} \binom{m}{i}.\end{aligned} \tag{6.50}$$

Expansion (6.50) explicitly shows that induced inflation with $f = \phi^m$ provides a realization of the flat conformal factor limit (6.45) with the identification $\alpha \sim \xi^{\frac{1}{m}}$ for small $\xi$. Induced inflation with a monomial conformal factor *also* guarantees that $\Omega'_{\text{vac}} \neq 0$. This means that (6.50) is of the form (6.47) with $\Omega_1 = m$ and $\Omega_2 = \binom{m}{2}$ and identifying $\xi^{\frac{1}{m}} \sim \alpha$ (see also example 6.A.1). Hence for small $\xi$ the result (6.48) applies; to leading order this model corresponds to quadratic chaotic inflation. We can verify this directly by computing the Einstein frame potential $V(\chi)$

$$V = \lambda m^2 \xi^{\frac{2}{m}} \chi^2 + O(\xi^{\frac{3}{m}}). \tag{6.51}$$

The slow-roll parameters are independent of the mass parameter $M^2 = 2\lambda\, m^2\, \xi^{\frac{2}{m}}$ of this chaotic inflationary potential, but the mass does determine the magnitude of the density perturbations, which in natural units should roughly equal $10^{-5}$ to be in agreement with the COBE normalisation. The coupling $\xi$ parametrizes a trajectory in the $(n_s, r)$-plane, connecting the Starobinsky attractor point with the chaotic attractor point (see figure 6.2). If one fixes the parameter $\lambda$ along the flow, then the prediction for the magnitude of the (scalar) density perturbations will not be in agreement with observation in the strict weak (non-minimal) coupling limit $\xi \to 0$. Alternatively, one could introduce a rescaled coupling $\tilde{\lambda}$ killing off the $\xi$ dependence. However, one would then have a similar problem in the strong

[3] Originally these models were studied as examples where the spontaneous symmetry breaking in (non-minimal) induced gravity models would allow for slow-roll inflation [159]. More recently it was pointed out that the Einstein frame potential does not include power series in terms of $\xi$ in the large $\xi$ limit. Hence perturbative unitarity is not violated before reaching the Planck scale in models of induced inflation [152].

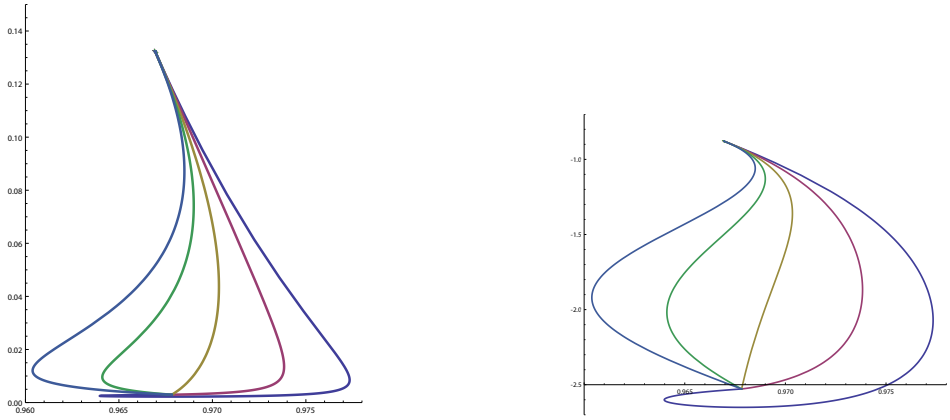


***Figure 6.2:*** *$(n_s, r)$-plane with linear and $\log_{10}$-scale on the vertical $r$-axis, for monomial induced inflation (6.50) with $m = 0.5, 1, 2,\ 4,\ 8$, from right to left.*

coupling limit and moreover, the required rescaling would be different for different values of $m$. In contrast, the normalisation in the opposite strong coupling limit is independent of the power $m$ of the monomial.

In addition to the properties of the fixed points, in figure 6.2 the flow as a function of the non-minimal coupling $\xi$ is plotted. A notable feature, in contrast to the strong coupling Starobinsky attractor, is that the approach to the weak coupling chaotic fixed point is clearly seen to be universal (independent of $m$), as can be analytically confirmed by determining the first order corrections in $\xi$ around the chaotic fixed point.

**Finite polynomial:** $\Omega = \xi\,(\cdots + \phi^m)$

A minimal extension of the monomial conformal factor is to consider the case where $f$ is a polynomial in $\phi$ with a finite number of terms. In this case, the highest power of $\phi$ determines the vacuum value of the field $\phi_{\text{vac}}$; if $f(\phi) = \cdots + \phi^m$, where the dots indicate lower powers of $\phi$, then the previous analysis goes through, with

$$\begin{aligned} \phi_{\text{vac}} &= \xi^{-\frac{1}{m}} + O(\xi^0) \\ \Omega &= 1 + m\xi^{\frac{1}{m}}\tilde{\phi} + O(\xi^{\frac{2}{m}}) \end{aligned} \tag{6.52}$$

and we arrive at the same conclusion: the weak coupling limit is described by quadratic chaotic inflation. Lower powers of $\phi$ in the polynomial do affect the subleading terms in expansion (6.52). The coupling parameter $\xi$ parametrizes a curve in the $(n_s, r)$-plane, connecting the strong coupling Starobinsky attractor point with the weak coupling chaotic attractor point.

In an infinite series expansion of the conformal factor (as could be generated by

quantum corrections) this sensitivity to the highest order term might be considered problematic. Neglecting that for now, it does imply that *all induced inflation models with a finite number of powers of the field* $\phi$ reduce to chaotic inflation in the weak coupling limit.

**Exponential:** $\Omega = \xi f = \xi\left(e^{\beta\phi} - 1\right)$
In the previous example we observed that $\Omega$ is sensitive to the highest power in the expansion of $f$, in the weak coupling limit. In this example we investigate whether the weak coupling limit of induced inflation still leads to $\phi^2$-chaotic inflation if $f$ is an infinite series in $\phi$. If $f = \left(e^{\beta\phi} - 1\right)$, then $\phi_{\rm vac} = \frac{1}{\beta}\ln\left(1 + \frac{1}{\xi}\right)$ and $\Omega = e^{\beta\tilde{\phi}}(\xi + 1) - \xi$. For large $\xi$ this model *will* satisfy the steep limit (6.39) and hence have the Starobinsky model as a strong coupling attractor point. For very small $\xi$ this model does generally not satisfy the flat limit (6.38), unless $\beta$ is tuned for this purpose. So in general the $\xi \to 0$ limit does *not* correspond to quadratic chaotic inflation.

In fact the above conclusion that exponential functions generically do not feature chaotic inflation attractors can be changed by making a different identification of the coupling parameter. Below we briefly present this case as another example.

**Example 6.3.2.** $\Omega = e^{\xi\phi^m}$ **in weak coupling limit**

The conformal factor $\Omega = e^{\xi\phi^m}$ naturally satisfies the flat conformal factor condition (6.45) for small $\xi$[4]. We require that in the vacuum configuration, $\Omega = 1$; this means that $\phi_{\rm vac} = 0$. In the $\xi \to 0$ limit we expand $\Omega$ in orders of $\xi$:

$$\begin{aligned}\Omega &= e^{\xi\phi^m} \\ &= 1 + \xi\phi^m + O(\xi^2)\end{aligned} \tag{6.53}$$

If $m = 1$, then $\Omega_1 \neq 0$ and we directly recover the result (6.48), corresponding to $\phi^2$-chaotic inflation in the $\xi \to 0$ limit. For general $m$, we find (see example 6.A.4):

$$\begin{aligned}N &= \frac{\phi_N^2}{4m} + O(\xi) \\ \epsilon &= \frac{2m^2}{\phi_N^2} + O(\xi) && \approx \frac{m}{2N} \\ \eta &= \frac{2m(2m-1)}{\phi_N^2} + O(\xi) && \approx \frac{2m-1}{2N}\end{aligned} \tag{6.54}$$

[4] An expansion of the kinetic term in the Einstein frame, at strong coupling, suggests that perturbative unitarity is violated before reaching the Planck scale for $m > 1$, unlike induced inflation.

These results correspond to those of $\phi^{2m}$-chaotic inflation.[5]

To conclude, we have confirmed that the weak coupling limit of some, but not all, models of induced inflation imply the flat conformal factor limit (6.45), yielding chaotic inflation attractor points. We also explicitly confirmed that the Einstein frame potential in this limit depends on the details of the conformal factor, implying that although the predictions for the spectral index and tensor-to-scalar ratio are the same for all these models and as such denote a fixed point, the magnitude of the density perturbations will depend on the details of the function $\Omega$ under consideration. In the opposite strong coupling limit, for the Starobinsky attractor, the magnitude of the density perturbations is instead independent of the details of the function $\Omega$, which can be used to uniquely fix $\lambda$ to agree with the COBE normalisation in the Starobinsky fixed point. In that sense the strong coupling Starobinsky fixed point can be considered more universal.

### 6.3.4 Generalized asymptotic Starobinsky models

A straightforward extension of the asymptotic Starobinsky models (6.42) with $U \propto \Omega^2(1-\Omega^{-1})^2$ is given by the set of Jordan frame potentials:

$$U = \lambda\Omega^2(1-\frac{1}{\Omega})^{2n}. \tag{6.55}$$

We will show that the steep conformal factor limit again corresponds to Starobinsky inflation, to leading order. We will also point out that the flat conformal factor limit corresponds to $\phi^{2n}$-chaotic inflation [6].

**Steep conformal factor limit** In this limit (6.39) the field redefinition(6.37) simplifies to:

$$\left(\frac{\delta\chi}{\delta\phi}\right)^2 = \frac{3}{2}\left(\frac{\Omega'}{\Omega}\right)^2 \quad \Rightarrow \Omega(\phi(\chi)) = e^{\pm\sqrt{\frac{2}{3}}\chi}. \tag{6.56}$$

The Einstein frame potential that corresponds to the potential (6.55) in terms of $\chi$ now reads

$$V(\chi) = \lambda\left(1-e^{-\sqrt{\frac{2}{3}}\chi}\right)^{2n}. \tag{6.57}$$

[5] Adding extra terms in the exponent, e.g. $e^{\xi(\phi^n+\beta\phi^{n+m})}$ would explicitly violate the flat conformal factor condition (6.45).

[6] In this subsection we will assume $\Omega'_{\rm vac} \neq 0$ for simplicity

For $n = 1$, we recognize the Starobinsky potential. For general $n$ we have a generalized Starobinsky model which also has, to leading order in $N$, for *all* $n$[7]:

$$\epsilon \approx \frac{3}{4N^2}, \quad \eta \approx -\frac{1}{N}, \tag{6.58}$$

similar to the standard Starobinsky model. In terms of the position in the $(n_s, r)$-plane of the strong coupling limit of these models, the attractor point coincides with that of Starobinsky inflation for all $n$, at least to leading order in $N$. The parameter $\lambda$ should be fixed to agree with the COBE normalisation. Requiring 60 e-folds implies that $\epsilon \sim 10^{-3}$ and as a consequence $\lambda$ is fixed to roughly equal $10^{-10}$ (in natural units), i.e. a very small number. A value for $\lambda$ this small causes an obvious problem in the opposite weak coupling limit, where the potential depends on the non-minimal coupling $\xi$ and $\lambda$ and as a consequence, for small $\xi$, the predicted magnitude for scalar density perturbations will be too small.

**The flat conformal factor limit** In this limit (6.38), the first and second order slow-roll parameters are given by (see appendix 6.A.1):

$$\begin{aligned} \epsilon &\approx 2n^2 \frac{\Omega'^2}{\Omega} \frac{1}{(\Omega-1)^2} \\ \eta &\approx \frac{\Omega'^2}{\Omega} \frac{2n(2n-1)}{(\Omega-1)^2} + \frac{2n}{\Omega-1}\left(\frac{\Omega''}{\Omega} - \frac{3}{2}\frac{\Omega'^2}{\Omega}\right). \end{aligned} \tag{6.59}$$

Given that $\Omega$ satisfies condition (6.45), we find to leading order in $N$

$$\epsilon \approx \frac{2n^2}{\tilde{\phi^2}_N} \approx \frac{n}{2N} \tag{6.60}$$

$$\eta \approx \frac{2n(2n-1)}{\tilde{\phi}^2_N} \approx \frac{2n-1}{2N}. \tag{6.61}$$

Indeed, for $n = 1$ we recover $\phi^2$-chaotic inflation. In fact, these results correspond to $\phi^{2n}$-chaotic inflation for all $n$ (see figure 6.3). Chaotic inflation models are fixed points for flat $\Omega$, whereas Starobinsky inflation is obtained in the opposite steep conformal factor limit. Looking at figure 6.3, where the flow between fixed points in the $(n_s, r)$ plane is plotted for different values of the parameters $m$ and $n$, with $\Omega = \xi\phi^m$.

**Approaching the chaotic attractor point** If the flat and steep limits can be controlled by a single flow parameter $\alpha$, like in examples (6.3.1,6.3.2), then $\alpha$

[7]For large $n$ of order $N$ the slow-roll conditions can be violated.

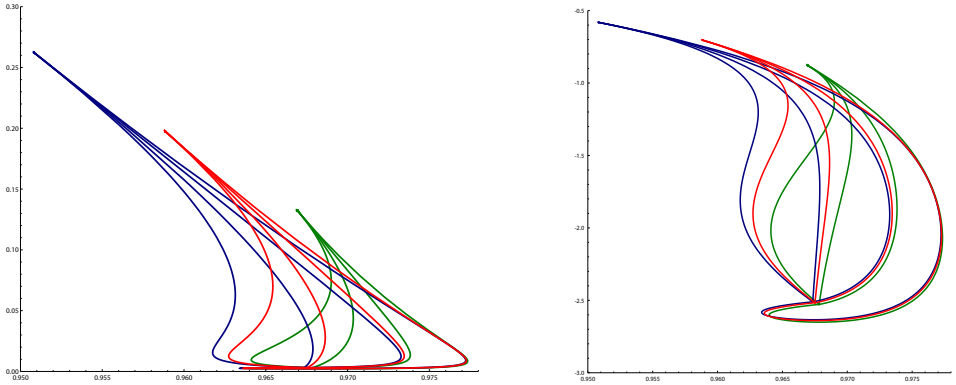

***Figure 6.3:*** *$(n_s, r)$-plane with linear and $\log_{10}$-scale on the vertical $r$-axis, for generalized asymptotic Starobinsky models (6.55) with $n = 1,\ 1.5,\ 2$ and $\Omega = \xi\phi^m$ (6.50) with $m = 0.5, 1, 2,\ 4$ for each $n$, from right to left. The weak coupling limit corresponds to $\phi^2, \phi^3$ and $\phi^4$-chaotic inflation respectively.*

parametrizes a trajectory in the $(n_s, r)$-plane, connecting the Starobinsky attractor point with the chaotic attractor point. The analysis of induced inflation (see figures 6.2 and 6.3) suggests that the approach of the chaotic attractor point is well behaved and along a certain universal angle, whereas the approach of the Starobinsky attractor point is more chaotic. The slope of the line in the $(n_s, r)$-plane close to the chaotic attractor point can be determined analytically by dividing $\frac{dr}{d\alpha}$ by $\frac{dn_s}{d\alpha}$. For polynomial induced inflation and polynomial universal attractor inflation, we find a slope of $\frac{-16}{2-\frac{1}{n}}$ for generalized asymptotically Starobinsky models (6.55)[8]. This suggests that the slope does not depend on the details of $\Omega$, and only on the number $n$ in the potential (6.55). However, there are explicit counter examples[9].

## 6.4 Conclusions

We studied non-minimally coupled single scalar field inflation models with a Starobinsky attractor point in the strong coupling limit. We have identified the relevant conditions on the conformal factor, corresponding to the flat and steep conformal factor limits, and shown how these can be obtained introducing a continuous coupling parameter, for instance in the context of induced inflation models. General (sufficient) conditions were determined that produce chaotic models of inflation in the flat conformal factor limit. Employing these general results we have confirmed

[8] This is in agreement with [150], where $(n = 1)$

[9] For example, consider $\Omega = 1 + \xi^2\phi^2 + \xi^3\phi^3$

the existence of chaotic fixed points for a subset of models that are asymptotically Starobinsky. As long as the first derivative of the conformal factor is non-zero the fixed point corresponds to the simplest quadratic model of chaotic inflation. The fine tuning of higher order powers in the potential of chaotic inflation was shown to be directly related to the flatness condition of the conformal factor. We also introduced and studied a straightforward generalization of asymptotic Starobinsky models, parametrized by a power $n$, that reduces at weak coupling to a chaotic inflation fixed point of order $n$ (the leading power of the canonical Einstein scalar field $\chi$).

One important observation is that this fixed point behavior differs from the Starobinsky fixed point at strong coupling due to the explicit dependence of the mass (or the couplings in higher order chaotic models) on the details of the model under consideration. This means it should be considered less universal in the sense that different models in this class, although they all reduce to the same (chaotic) slow-roll parameters in the weak coupling limit, predict different scales of inflation. A related consequence is that the COBE normalisation cannot be matched in both fixed points at the same time. This observation is best illustrated in a three-dimensional flow plot that would include the predicted magnitude of density perturbations as a function of the non-minimal coupling $\xi$. By appropriately rescaling the coupling $\lambda$ to allow for a finite magnitude in the weak coupling limit, one would find that the weak coupling limit is not a fixed point in this 3-dimensional space of inflationary parameters, whereas the strong coupling Starobinsky attractor remains a true fixed point.

An important and interesting avenue for future work would be to better understand the UV embedding and (effective field theoretical) consistency of these classes of non-minimally coupled models, in particular from the point of view of string theory.

# 6.A From Jordan frame to Einstein frame

## 6.A.1 Slow-roll parameters in the Einstein frame

In this subsection we express the Einstein frame potential slow-roll parameters in terms of the Jordan frame quantities $U$ and $\Omega$. We only use potential slow-roll parameters[10]. The potential slow-roll parameters $\epsilon$ and $\eta$ in terms of the Einstein

[10]Since we only use potential slow-roll parameters, we will write $\epsilon$ and $\eta$ instead of $\epsilon_{\rm V}$ and $\eta_{\rm V}$ for the first and second potential slow-roll parameters

frame potential (6.20) are given by[11]:

$$\epsilon = \frac{1}{2}\left(\frac{V_{,\chi}}{V}\right)^2, \eta \quad = \frac{V_{,\chi\chi}}{V} \tag{6.62}$$

We can also express the slow-roll parameters in terms of the Jordan frame potential $U(\phi)$, the conformal factor $\Omega(\phi)$, using the relation between the Jordan frame potential and the Einstein frame potential (6.20), and the field redefinition (6.18). The first order potential slow-roll parameter $\epsilon$ is given by:

$$\begin{aligned}\epsilon &= \frac{1}{2}\left(\frac{V_{,\chi}}{V}\right)^2 \\ &= \frac{1}{2}\left(\frac{\delta\phi}{\delta\chi}\right)^2\left(\frac{\frac{d}{d\phi}\left(\frac{U}{\Omega^2}\right)}{\left(\frac{U}{\Omega^2}\right)}\right)^2 \\ &= 2\frac{1}{\frac{K}{\Omega}+\frac{3}{2}\frac{\Omega'^2}{\Omega^2}}\left(\frac{U'}{U}-2\frac{\Omega'}{\Omega}\right)^2.\end{aligned} \tag{6.63}$$

The second order potential slow-roll parameter $\eta$ is given by:

$$\begin{aligned}\eta &= \frac{V_{,\chi\chi}}{V} \\ &= \frac{1}{V}\frac{\delta\phi}{\delta\chi}\frac{\partial}{\partial\phi}\frac{\delta\phi}{\delta\chi}\frac{\partial}{\partial\phi}V \\ &= \frac{\Omega^2}{U}\frac{1}{\sqrt{\frac{K}{\Omega}+\frac{3}{2}\frac{\Omega'^2}{\Omega^2}}}\frac{\partial}{\partial\phi}\frac{1}{\sqrt{\frac{K}{\Omega}+\frac{3}{2}\frac{\Omega'^2}{\Omega^2}}}\frac{\partial}{\partial\phi}\frac{U}{\Omega^2} \\ &= \frac{1}{\left(\frac{K}{\Omega}+\frac{3}{2}\frac{\Omega'^2}{\Omega^2}\right)}\left[\left(\frac{U''}{U}-4\frac{U'\Omega'}{U\Omega}-2\frac{\Omega''}{\Omega}+6\frac{\Omega'^2}{\Omega^2}\right)\right] \\ &+ \frac{1}{\left(\frac{K}{\Omega}+\frac{3}{2}\frac{\Omega'^2}{\Omega^2}\right)^2}\left[\left(\frac{U'}{U}-2\frac{\Omega'}{\Omega}\right)\left(-\frac{1}{2}\right)\left(\frac{K'}{\Omega}-\frac{K}{\Omega}\frac{\Omega'}{\Omega}+3\frac{\Omega''}{\Omega}\frac{\Omega'}{\Omega}-3\frac{\Omega'^3}{\Omega^3}\right)\right],\end{aligned} \tag{6.64}$$

where primes denote derivatives with respect to $\phi$.
Related to our expression for $\epsilon$, we find for the number of e-folds $N$:

$$\begin{aligned}N &= \int_{\chi_{\rm end}}^{\chi_N} d\chi\frac{V}{V_{,\chi}} \\ &= \int_{\phi_{\rm end}}^{\phi_N} d\phi\left(\frac{\delta\chi}{\delta\phi}\right)^2\frac{V}{V_{,\phi}} \\ &= \int_{\phi_{\rm end}}^{\phi_N} d\phi\left(\frac{K(\phi)}{\Omega(\phi)}+\frac{3}{2}\frac{\Omega'^2(\phi)}{\Omega^2(\phi)}\right)\frac{1}{\left(\frac{U'}{U}-2\frac{\Omega'}{\Omega}\right)}\end{aligned} \tag{6.65}$$

[11] In the expressions of slow-roll parameters, the reduced Planck mass has been set to one (e.g. $\epsilon = \frac{m_{pl}^2}{16\pi}\left(\frac{V,\chi}{V}\right)^2 \to \frac{1}{2}\left(\frac{V,\chi}{V}\right)^2$)

### 6.A.2 Expansion of the Einstein frame potential

For the asymptotic Starobinsky model we have the Jordan frame potential $U = \lambda(\Omega-1)^2$. The Einstein frame potential $V$ is given by (6.20)

$$V(\chi) = \frac{U(\phi(\chi))}{\Omega^2(\phi(\chi))}. \tag{6.66}$$

where $\chi$ is the canonically normalized field defined by the field redefinition (6.37)

$$\left(\frac{\delta\chi}{\delta\phi}\right)^2 = \frac{1}{\Omega} + \frac{3}{2}\frac{\Omega'^2}{\Omega^2}. \tag{6.67}$$

These two relations allow us to expand $V$ in terms of $\chi$ around the vacuum value $\chi_{\rm vac} = 0$:

$$V(\chi) = \sum_n c_n \chi^n, \tag{6.68}$$

where $c_n = \frac{1}{n!}\left.\frac{\delta^n V}{\delta\chi^n}\right|_{\chi_{\rm vac}}$. Using the field redefinition (6.37) we find:

$$\begin{aligned}
c_0 &= 0\\
c_1 &= 0\\
c_2 &= \frac{\lambda\Omega'^2_{\rm vac}}{1+\frac{3}{2}\Omega'^2_{\rm vac}}\\
c_3 &= \lambda\frac{\left(\Omega''_{\rm vac}\Omega'_{\rm vac} - \frac{3}{2}\Omega'^3_{\rm vac} - \frac{3}{2}\Omega'^5_{\rm vac}\right)}{\left(1+\frac{3}{2}\Omega'^2_{\rm vac}\right)^{\frac{5}{2}}}\\
c_4 &= \frac{1}{\left(1+\frac{3}{2}\Omega'^2_{\rm vac}\right)^4}\frac{\lambda}{48}\left[\begin{array}{c}12\Omega''^2_{\rm vac} + 63\Omega'^8_{\rm vac} + 126\Omega'^6_{\rm vac} + 24\Omega^{(3)}_{\rm vac}\Omega'^3_{\rm vac} + 16\Omega^{(3)}_{\rm vac}\Omega'_{\rm vac} + \\ \Omega'^4_{\rm vac}(75 - 36\Omega''_{\rm vac}) - 4\Omega'^2_{\rm vac}\Omega''_{\rm vac}(24\Omega''_{\rm vac} + 25)\end{array}\right]
\end{aligned} \tag{6.69}$$

For $\Omega'^2_{\rm vac} \ll 1$ we therefore obtain

$$\begin{aligned}
V(\chi) \approx{}& \lambda\Omega'^2_{\rm vac}\chi^2 + \lambda\left(\Omega''_{\rm vac}\Omega'_{\rm vac} - \frac{3}{2}\Omega'^3_{\rm vac}\right)\chi^3 + \\
&+ \frac{\lambda}{24}\left(-50\Omega'^2_{\rm vac}\Omega''_{\rm vac} + \frac{75}{2}\Omega'^4 + 6\Omega''^2_{\rm vac} + 8\Omega'_{\rm vac}\Omega'''_{\rm vac}\right)\chi^4 + \dots
\end{aligned} \tag{6.70}$$

### 6.A.3 Generalized asymptotic Starobinsky models

We consider the Jordan frame potential $U = \lambda\Omega^2(1-\Omega^{-1})^{2n}$. In the steep conformal limit this potential corresponds to the Einstein frame potential $V$ in terms of the canonically normalized field $\chi$

$$V(\chi) = \lambda\left(1 - e^{-\sqrt{\frac{2}{3}}\chi}\right)^{2n}, \tag{6.71}$$

which is called a generalized Starobinsky model.

The Einstein frame slow-roll parameters and the number of e-folds $N$ can be expressed in terms of $\Omega$ and its derivatives:

$$\epsilon = \frac{2n^2}{\Omega + \frac{3}{2}\Omega'^2}\left(\frac{\Omega'}{\Omega - 1}\right)^2 \tag{6.72a}$$

$$\eta = \frac{2n(2n-1)}{\Omega + \frac{3}{2}\Omega'^2}\left(\frac{\Omega'}{\Omega - 1}\right)^2 + \frac{2n}{\left(\Omega + \frac{3}{2}\Omega'^2\right)^2}\frac{\Omega'}{\Omega - 1}\left(-\frac{3}{2}\Omega'\Omega - \frac{3}{2}\Omega'^3 + \frac{\Omega''}{\Omega'}\Omega^2\right) \tag{6.72b}$$

$$N = \frac{1}{n}\int^{\phi_N} d\phi \left(1 + \frac{3}{2}\frac{\Omega'^2}{\Omega}\right)\left(\frac{\Omega - 1}{2\Omega'}\right) \tag{6.72c}$$

**Flat limit**

In the flat limit $1 \gg \frac{3}{2}\frac{\Omega'^2}{\Omega}$, (6.72a), (6.72b) and (6.72c) simplify to:

$$\epsilon \approx 2n^2 \frac{\Omega'^2}{\Omega}\frac{1}{(\Omega - 1)^2} \tag{6.73a}$$

$$\eta \approx 2n(2n-1)\frac{1}{(\Omega - 1)^2}\frac{\Omega'^2}{\Omega} + 2n\frac{1}{\Omega - 1}\left(\Omega'' - \frac{3}{2}\frac{\Omega'^2}{\Omega}\right) \tag{6.73b}$$

$$N \approx \frac{1}{n}\int_{\phi_{\text{end}}}^{\phi_N} \frac{\Omega - 1}{2\Omega'} d\phi \tag{6.73c}$$

**Flat conformal factor condition**

If $\Omega$ satisfies the flat conformal factor condition (6.45), $\Omega$ has the following form, for $\tilde{\phi} = \phi - \phi_{\text{vac}}$:

$$\Omega = 1 + \sum_{m=1} \Omega_m \alpha^m \tilde{\phi}^m, \tag{6.74}$$

where the $\Omega_m$ are of order $O(1)$ and $\alpha\tilde{\phi} \ll 1$ for $0 < \tilde{\phi} < \tilde{\phi}_N$. This form allows us to evaluate (6.72a,6.72b,6.72c) in orders of $\alpha$.

**Example 6.A.1.** $\Omega_1 \neq 0, \Omega_2 \neq 0$**:**

$$\epsilon = \frac{2n^2}{\tilde{\phi}^2} + (\alpha\tilde{\phi})\frac{2n^2}{\tilde{\phi}^2}\left(2\frac{\Omega_2}{\Omega_1} - \Omega_1\right) + O\left((\alpha\tilde{\phi})^2\right) \tag{6.75a}$$

$$\eta = \frac{2n(2n-1)}{\tilde{\phi}^2} + (\alpha\tilde{\phi})\frac{2n}{\tilde{\phi}^2}\left(4n\frac{\Omega_2}{\Omega_1} - (2n + \frac{1}{2})\Omega_1\right) + O((\alpha\tilde{\phi})^2) \tag{6.75b}$$

$$N = \frac{\tilde{\phi}_N^2}{4n} - \frac{(\alpha\tilde{\phi}_N)}{6n}\frac{\Omega_2}{\Omega_1}\tilde{\phi}_N^2 + O\left((\alpha\tilde{\phi}_N)^2\right) \tag{6.75c}$$

This example illustrates that for generic $\Omega$ with non vanishing $\Omega_1$, the flat conformal factor attractor point of generalized asymptotic Starobinsky model of degree $2n$ corresponds to $\phi^{2n}$-chaotic inflation.

**Example 6.A.2.** $\Omega_1 = \Omega_3 = 0$**,** $\Omega_2 \neq 0, \Omega_4 \neq 0$

If we impose $\Omega$ to be an even function of $\tilde{\phi}$, we find $\Omega_i = 0$ for $i$ odd.

$$\epsilon = \frac{2(2n)^2}{\tilde{\phi}^2} + (\alpha\tilde{\phi})^2 \frac{2(2n)^2}{\tilde{\phi}^2}\left(2\frac{\Omega_4}{\Omega_2} - \Omega_2\right) + O\left((\alpha\tilde{\phi})^4\right) \tag{6.76a}$$

$$\eta = \frac{4n(4n-1)}{\tilde{\phi}^2} + \alpha^2\left(\frac{\Omega_4}{\Omega_2}4n(8n+1) - \Omega_2 4n(4n+1)\right) + O\left((\alpha\tilde{\phi})^4\right) \tag{6.76b}$$

$$N = \frac{\tilde{\phi}_N^2}{8n} - \frac{1}{16n}\frac{\Omega_4}{\Omega_2}(\alpha\tilde{\phi}_N)^2\tilde{\phi}_N^2 + O\left((\alpha\tilde{\phi})^4\right) \tag{6.76c}$$

**Example 6.A.3.** $\Omega_1 = m, \Omega_2 = \binom{m}{2}$ **(induced inflation with monomial)**

In example (6.3.1) we have shown that we can expand the monomial induced inflation model $\Omega = \xi\phi^m$ in terms of $\tilde{\phi} = \phi - \phi_{\text{vac}}$ with $\Omega_1 = m, \Omega_2 = \binom{m}{2}$. For the generalized asymptotic Starobinsky (6.55) model we find:

$$\epsilon = \frac{2n^2}{\tilde{\phi}^2} - (\alpha\tilde{\phi})\frac{2n^2}{\tilde{\phi}^2} + O((\alpha\tilde{\phi})^2) \tag{6.77a}$$

$$\eta = \frac{2n(2n-1)}{\tilde{\phi}^2} - (\alpha\tilde{\phi})\frac{2n^2}{\tilde{\phi}^2}\left(2 + \frac{1}{2}\frac{m}{n}\right) + O((\alpha\tilde{\phi})^2) \tag{6.77b}$$

$$N = \frac{\tilde{\phi}_N^2}{4n} - \frac{(m-1)}{12n}(\alpha\tilde{\phi}_N)\tilde{\phi}_N^2 + O\left((\alpha\tilde{\phi}_N)^2\right) \tag{6.77c}$$

**Example 6.A.4.** $\Omega = 1 + \alpha\phi^m$ **(universal attractor inflation with monomial)**

Universal attractor inflation [150] is a class of asymptotic Starobinsky models with $\Omega(\phi) = 1 + \xi f(\phi)$. We consider the monomial case $f(\phi) = \phi^m$, for which $\phi_{\text{vac}} = 0$ and extend the discussion to *generalized* asymptotic Starobinsky models (6.55). We find:

$$\epsilon = \frac{2(nm)^2}{\phi^2} - (\alpha\phi^m)\frac{2(nm)^2}{\phi^2} + O(\alpha^2\phi^{2m}) \tag{6.78a}$$

$$\eta = \frac{2(nm)(nm-1)}{\phi^2} - (\alpha\phi^m)\frac{m^2n(4n+1)}{\phi^2} + O((\alpha^2\phi^{2m})) \tag{6.78b}$$

$$N = \frac{\phi_N^2}{4mn} + O((\alpha^2\phi^{2m})). \tag{6.78c}$$

These results correspond to leading order to $\phi^{2mn}$-chaotic inflation. This illustrates that if $\Omega$ satisfies the flat conformal factor condition (6.45), but with the first $m-1$ derivatives vanishing, the generalized asymptotic Starobinsky model of order $2n$ will lead to $\phi^{2mn}$-chaotic inflation, to leading order.

### 6.A.4 Beyond the asymptotic Starobinsky paradigm

If $\Omega$ satisfies the flat conformal factor condition (6.45), the generalized asymptotic Starobinsky models (6.55) have a chaotic inflation attractor point. We could also consider the much more general class of models satisfying that $U \to 0$ and $\Omega \to 1$ in the vacuum configuration:

$$U = \sum_{n \neq 0} a_n \left(\Omega - 1\right)^n , \tag{6.79}$$

for a set of coefficients $\{a_n\}$. One can check that these general potentials are *not* Starobinsky-like in the steep limit (6.39). They *can* correspond to chaotic inflation if $\Omega$ satisfies the flat conformal factor condition (6.45). If $a_n = 0$ for $n < m$ and $a_m \neq 0$, than these models correspond to leading order to $\phi^{km}$-chaotic inflation, where $k$ is the first nonzero derivative of $\Omega$ in the vacuum.

# Bibliography


[1] Fotios V. Dimitrakopoulos, Laurens Kabir, Benjamin Mosk, Maulik Parikh, and Jan Pieter van der Schaar. Vacua and correlators in hyperbolic de Sitter space. *JHEP*, 06:095, 2015.

[2] Ben Freivogel, Robert Alan Jefferson, Laurens Kabir, Benjamin Mosk, and I-Sheng Yang. Casting Shadows on Holographic Reconstruction. *Phys. Rev.*, D91(8):086013, 2015.

[3] Benjamin Mosk and Jan Pieter van der Schaar. Chaotic inflation limits for non-minimal models with a Starobinsky attractor. *JCAP*, 1412(12):022, 2014.

[4] Ben Freivogel and Benjamin Mosk. Properties of Causal Holographic Information. *JHEP*, 1309:100, 2013.

[5] Mark Van Raamsdonk. Building up spacetime with quantum entanglement. *Gen.Rel.Grav.*, 42:2323–2329, 2010.

[6] James M. Bardeen, B. Carter, and S.W. Hawking. The Four laws of black hole mechanics. *Commun.Math.Phys.*, 31:161–170, 1973.

[7] S.W. Hawking. Particle Creation by Black Holes. *Commun.Math.Phys.*, 43:199–220, 1975.

[8] S.W. Hawking. Black hole explosions. *Nature*, 248:30–31, 1974.

[9] J.D. Bekenstein. Extraction of energy and charge from a black hole. *Phys.Rev.*, D7:949–953, 1973.

[10] J.D. Bekenstein. Black holes and the second law. *Lett.Nuovo Cim.*, 4:737–740, 1972.

[11] Jacob D. Bekenstein. Black holes and entropy. *Phys.Rev.*, D7:2333–2346, 1973.

[12] Jacob D. Bekenstein. Generalized second law of thermodynamics in black hole physics. *Phys.Rev.*, D9:3292–3300, 1974.

[13] Jacob D. Bekenstein. A Universal Upper Bound on the Entropy to Energy Ratio for Bounded Systems. *Phys.Rev.*, D23:287, 1981.

[14] Leonard Susskind. The World as a hologram. *J.Math.Phys.*, 36:6377–6396, 1995.

[15] Raphael Bousso. A Covariant entropy conjecture. *JHEP*, 9907:004, 1999.

[16] Raphael Bousso. The Holographic principle. *Rev.Mod.Phys.*, 74:825–874, 2002.

[17] Juan Martin Maldacena. The Large N limit of superconformal field theories and supergravity. *Int.J.Theor.Phys.*, 38:1113–1133, 1999.

[18] Joseph Polchinski. Dirichlet Branes and Ramond-Ramond charges. *Phys.Rev.Lett.*, 75:4724–4727, 1995.

[19] Joseph Polchinski. Tasi lectures on D-branes. pages 293–356, 1996.

[20] Joseph Polchinski, Shyamoli Chaudhuri, and Clifford V. Johnson. Notes on D-branes. 1996.

[21] Mark Van Raamsdonk. Comments on quantum gravity and entanglement. 2009.

[22] A. Ashtekar and A. Magnon. Asymptotically anti-de Sitter space-times. *Class.Quant.Grav.*, 1:L39–L44, 1984.

[23] Kostas Skenderis. Lecture notes on holographic renormalization. *Class.Quant.Grav.*, 19:5849–5876, 2002.

[24] C. Fefferman and C.R. Graham. Conformal Invariants. *Elie Cartan et les Mathématiques d'Aujourd'hui*, 95, 1985.

[25] Charles Fefferman and C. Robin Graham. The ambient metric. 2007.

[26] Maximo Banados, Claudio Teitelboim, and Jorge Zanelli. The Black hole in three-dimensional space-time. *Phys.Rev.Lett.*, 69:1849–1851, 1992.

[27] Jan de Boer, Erik P. Verlinde, and Herman L. Verlinde. On the holographic renormalization group. *JHEP*, 0008:003, 2000.

[28] Emil T. Akhmedov. A Remark on the AdS / CFT correspondence and the renormalization group flow. *Phys.Lett.*, B442:152–158, 1998.

[29] Vijay Balasubramanian and Per Kraus. Space-time and the holographic renormalization group. *Phys.Rev.Lett.*, 83:3605–3608, 1999.

[30] Massimo Bianchi, Daniel Z. Freedman, and Kostas Skenderis. Holographic renormalization. *Nucl.Phys.*, B631:159–194, 2002.

[31] Igor R. Klebanov and Edward Witten. AdS / CFT correspondence and symmetry breaking. *Nucl.Phys.*, B556:89–114, 1999.

[32] Edward Witten. Anti-de Sitter space and holography. *Adv.Theor.Math.Phys.*, 2:253–291, 1998.

[33] S.S. Gubser, Igor R. Klebanov, and Alexander M. Polyakov. Gauge theory correlators from noncritical string theory. *Phys.Lett.*, B428:105–114, 1998.

[34] J. M. Maldacena. Wilson loops in large N field theories. *Phys. Rev. Lett.*, 80, 1998. arXiv:hep-th/9803002.

[35] Soo-Jong Rey and Jung-Tay Yee. Macroscopic strings as heavy quarks in large N gauge theory and anti-de Sitter supergravity. *Eur.Phys.J.*, C22:379–394, 2001.

[36] Stefano I. Finazzo and Jorge Noronha. Estimates for the Thermal Width of Heavy Quarkonia in Strongly Coupled Plasmas from Holography. *JHEP*, 1311:042, 2013.

[37] Michael A. Nielsen and Isaac L. Chuang. *Quantum computation and quantum information*. Cambridge University Press, 2000.

[38] M. M. Wolf, F. Verstraete, M. B. Hastings, and J. I. Cirac. Area Laws in Quantum Systems: Mutual Information and Correlations. *Physical Review Letters*, 100(7):070502, February 2008.

[39] Michael A. Nielsen and Isaac L. Chuang. *Quantum computation and quantum information*. Cambridge University Press, 2000.

[40] Jyotirmoy Bhattacharya, Masahiro Nozaki, Tadashi Takayanagi, and Tomonori Ugajin. Thermodynamical Property of Entanglement Entropy for Excited States. *Phys.Rev.Lett.*, 110(9):091602, 2013.

[41] Jr. Callan, Curtis G. and Frank Wilczek. On geometric entropy. *Phys.Lett.*, B333:55–61, 1994.

[42] Pasquale Calabrese and John L. Cardy. Entanglement entropy and quantum field theory. *J.Stat.Mech.*, 0406:P06002, 2004.

[43] Shinsei Ryu and Tadashi Takayanagi. Aspects of Holographic Entanglement Entropy. *JHEP*, 0608:045, 2006.

[44] Shinsei Ryu and Tadashi Takayanagi. Holographic derivation of entanglement entropy from AdS/CFT. *Phys.Rev.Lett.*, 96:181602, 2006.

[45] Veronika E. Hubeny, Mukund Rangamani, and Tadashi Takayanagi. A Covariant holographic entanglement entropy proposal. *JHEP*, 0707:062, 2007.

[46] Aitor Lewkowycz and Juan Maldacena. Generalized gravitational entropy. *JHEP*, 1308:090, 2013.

[47] Dmitri V. Fursaev. Proof of the holographic formula for entanglement entropy. *JHEP*, 0609:018, 2006.

[48] Matthew Headrick. Entanglement Renyi entropies in holographic theories. *Phys.Rev.*, D82:126010, 2010.

[49] Thomas Faulkner, Aitor Lewkowycz, and Juan Maldacena. Quantum corrections to holographic entanglement entropy. *JHEP*, 1311:074, 2013.

[50] Netta Engelhardt and Aron C. Wall. Quantum Extremal Surfaces: Holographic Entanglement Entropy beyond the Classical Regime. *JHEP*, 1501:073, 2015.

[51] Matthew Headrick and Tadashi Takayanagi. A Holographic proof of the strong subadditivity of entanglement entropy. *Phys.Rev.*, D76:106013, 2007.

[52] Robert Callan, Jian-Yang He, and Matthew Headrick. Strong subadditivity and the covariant holographic entanglement entropy formula. *JHEP*, 1206:081, 2012.

[53] Robert M. Wald. Black hole entropy is the Noether charge. *Phys.Rev.*, D48:3427–3431, 1993.

[54] Vivek Iyer and Robert M. Wald. Some properties of Noether charge and a proposal for dynamical black hole entropy. *Phys.Rev.*, D50:846–864, 1994.

[55] Ted Jacobson, Gungwon Kang, and Robert C. Myers. On black hole entropy. *Phys.Rev.*, D49:6587–6598, 1994.

[56] Ling-Yan Hung, Robert C. Myers, and Michael Smolkin. On Holographic Entanglement Entropy and Higher Curvature Gravity. *JHEP*, 1104:025, 2011.

[57] Xi Dong. Holographic Entanglement Entropy for General Higher Derivative Gravity. *JHEP*, 1401:044, 2014.

[58] Sergey N. Solodukhin. Entanglement entropy, conformal invariance and extrinsic geometry. *Phys.Lett.*, B665:305–309, 2008.

[59] Alex Hamilton, Daniel N. Kabat, Gilad Lifschytz, and David A. Lowe. Local bulk operators in AdS/CFT: A Boundary view of horizons and locality. *Phys.Rev.*, D73:086003, 2006.

[60] Alex Hamilton, Daniel N. Kabat, Gilad Lifschytz, and David A. Lowe. Holographic representation of local bulk operators. *Phys.Rev.*, D74:066009, 2006.

[61] Daniel Kabat, Gilad Lifschytz, and David A. Lowe. Constructing local bulk observables in interacting AdS/CFT. *Phys.Rev.*, D83:106009, 2011.

[62] Idse Heemskerk, Donald Marolf, Joseph Polchinski, and James Sully. Bulk and Transhorizon Measurements in AdS/CFT. *JHEP*, 1210:165, 2012.

[63] N. Lashkari, M. B. McDermott, and M. van Raamsdonk. Gravitational dynamics from entanglement "thermodynamics". *JHEP*, 1404, 2013. arXiv:1308.3716.

[64] Masahiro Nozaki, Tokiro Numasawa, Andrea Prudenziati, and Tadashi Takayanagi. Dynamics of Entanglement Entropy from Einstein Equation. *Phys.Rev.*, D88(2):026012, 2013.

[65] Thomas Faulkner, Monica Guica, Thomas Hartman, Robert C. Myers, and Mark Van Raamsdonk. Gravitation from Entanglement in Holographic CFTs. *JHEP*, 1403:051, 2014.

[66] Bartomiej Czech and Lampros Lamprou. Holographic definition of points and distances. *Phys.Rev.*, D90(10):106005, 2014.

[67] Bartlomiej Czech, Joanna L. Karczmarek, Fernando Nogueira, and Mark Van Raamsdonk. The Gravity Dual of a Density Matrix. *Class.Quant.Grav.*, 29:155009, 2012.

[68] Raphael Bousso, Stefan Leichenauer, and Vladimir Rosenhaus. Light-sheets and AdS/CFT. *Phys.Rev.*, D86:046009, 2012.

[69] Veronika E. Hubeny and Mukund Rangamani. Causal Holographic Information. *JHEP*, 1206:114, 2012.

[70] Matthew Headrick, Veronika E. Hubeny, Albion Lawrence, and Mukund Rangamani. Causality & holographic entanglement entropy. *JHEP*, 1412:162, 2014.

[71] Ahmed Almheiri, Xi Dong, and Daniel Harlow. Bulk Locality and Quantum Error Correction in AdS/CFT. 2014.

[72] Daniel Harlow and Douglas Stanford. Operator Dictionaries and Wave Functions in AdS/CFT and dS/CFT. 2011.

[73] Stefan Leichenauer and Vladimir Rosenhaus. AdS black holes, the bulk-boundary dictionary, and smearing functions. *Phys.Rev.*, D88(2):026003, 2013.

[74] Raphael Bousso, Ben Freivogel, Stefan Leichenauer, Vladimir Rosenhaus, and Claire Zukowski. Null Geodesics, Local CFT Operators and AdS/CFT for Subregions. *Phys.Rev.*, D88:064057, 2013.

[75] Daniel Kabat, Gilad Lifschytz, Shubho Roy, and Debajyoti Sarkar. Holographic representation of bulk fields with spin in AdS/CFT. *Phys.Rev.*, D86:026004, 2012.

[76] Robert C. Myers, Junjie Rao, and Sotaro Sugishita. Holographic Holes in Higher Dimensions. *JHEP*, 1406:044, 2014.

[77] Bartlomiej Czech, Xi Dong, and James Sully. Holographic Reconstruction of General Bulk Surfaces. *JHEP*, 1411:015, 2014.

[78] Vijay Balasubramanian, Borun D. Chowdhury, Bartlomiej Czech, Jan de Boer, and Michal P. Heller. Bulk curves from boundary data in holography. *Phys.Rev.*, D89(8):086004, 2014.

[79] Vijay Balasubramanian, Borun D. Chowdhury, Bartlomiej Czech, and Jan de Boer. Entwinement and the emergence of spacetime. *JHEP*, 1501:048, 2015.

[80] Horacio Casini, Marina Huerta, and Robert C. Myers. Towards a derivation of holographic entanglement entropy. *JHEP*, 1105:036, 2011.

[81] Kostas Skenderis. Asymptotically Anti-de Sitter space-times and their stress energy tensor. *Int.J.Mod.Phys.*, A16:740–749, 2001.

[82] L. Pestov and G. Uhlmann. Two dimensional compact simple Riemannian manifolds are boundary distance rigid. *Ann. Math.*, 161(2), 2003. arXiv:math/0305280.

[83] S. Hartnoll. Holographic mutual information and distinguishability of Wilson loop and defect operators. 2014. arXiv:1407.8191.

[84] A. Brandhuber et al. Wilson loops in the large N limit at finite temperature. *Phys. Lett. B*, 434, 1998. arXiv:hep-th/9803137.

[85] Jennifer Lin, Matilde Marcolli, Hirosi Ooguri, and Bogdan Stoica. Tomography from Entanglement. 2014.

[86] Veronika E. Hubeny, Mukund Rangamani, and Erik Tonni. Thermalization of Causal Holographic Information. *JHEP*, 1305:136, 2013.

[87] Veronika E. Hubeny, Mukund Rangamani, and Erik Tonni. Global properties of causal wedges in asymptotically AdS spacetimes. *JHEP*, 1310:059, 2013.

[88] Simon A. Gentle and Mukund Rangamani. Holographic entanglement and causal information in coherent states. *JHEP*, 1401:120, 2014.

[89] A. Schwimmer and S. Theisen. Entanglement Entropy, Trace Anomalies and Holography. *Nucl.Phys.*, B801:1–24, 2008.

[90] C. Imbimbo, A. Schwimmer, S. Theisen, and S. Yankielowicz. Diffeomorphisms and holographic anomalies. *Class.Quant.Grav.*, 17:1129–1138, 2000.

[91] William R. Kelly and Aron C. Wall. Coarse-grained entropy and causal holographic information in AdS/CFT. *JHEP*, 1403:118, 2014.

[92] David Eliecer Berenstein, Richard Corrado, Willy Fischler, and Juan Martin Maldacena. The Operator product expansion for Wilson loops and surfaces in the large N limit. *Phys.Rev.*, D59:105023, 1999.

[93] William Donnelly. Decomposition of entanglement entropy in lattice gauge theory. *Phys.Rev.*, D85:085004, 2012.

[94] Murray Gell-Mann and James Hartle. Quasiclassical Coarse Graining and Thermodynamic Entropy. *Phys.Rev.*, A76:022104, 2007.

[95] Peter G. Bergmann and Venzo De Sabbata. *Topological Properties and Global Structure of Space-Time*. Springer US, 1986.

[96] William R. Kelly. Deriving the First Law of Black Hole Thermodynamics without Entanglement. *JHEP*, 1410:192, 2014.

[97] Daniel Baumann. TASI Lectures on Inflation. 2009.

[98] P.A.R. Ade et al. Planck 2015 results. XX. Constraints on inflation. 2015.

[99] P.A.R. Ade et al. Planck 2015 results. XIII. Cosmological parameters. 2015.

[100] Gerard 't Hooft. Magnetic Monopoles in Unified Gauge Theories. *Nucl.Phys.*, B79:276–284, 1974.

[101] Alan H. Guth and S.H.H. Tye. Phase Transitions and Magnetic Monopole Production in the Very Early Universe. *Phys.Rev.Lett.*, 44:631, 1980.

[102] Martin B. Einhorn, D.L. Stein, and Doug Toussaint. Are Grand Unified Theories Compatible with Standard Cosmology? *Phys.Rev.*, D21:3295, 1980.

[103] John Preskill. Cosmological Production of Superheavy Magnetic Monopoles. *Phys.Rev.Lett.*, 43:1365, 1979.

[104] S. Dodelson. *Modern Cosmology*. Academic Press. Academic Press, 2003. ISBN: 9780122191411.

[105] Andrew R. Liddle, Paul Parsons, and John D. Barrow. Formalizing the slow roll approximation in inflation. *Phys.Rev.*, D50:7222–7232, 1994.

[106] Ted Jacobson. Introduction to quantum fields in curved space-time and the Hawking effect. pages 39–89, 2003.

[107] Marcus Spradlin, Andrew Strominger, and Anastasia Volovich. Les Houches lectures on de Sitter space. pages 423–453, 2001.

[108] P.K. Townsend. Black holes: Lecture notes. 1997.

[109] Jan de Boer, Vishnu Jejjala, and Djordje Minic. Alpha-states in de Sitter space. *Phys.Rev.*, D71:044013, 2005.

[110] Bruce Allen. Vacuum states in de sitter space. *Phys. Rev. D*, 32:3136–3149, Dec 1985.

[111] J. S. Dowker and Raymond Crichley. Scalar effective lagrangian in de sitter space. *Phys. Rev. D*, 13:224–234, Jan 1976.

[112] Ulf H. Danielsson. On the consistency of de Sitter vacua. *JHEP*, 0212:025, 2002.

[113] Nemanja Kaloper, Matthew Kleban, Albion Lawrence, Stephen Shenker, and Leonard Susskind. Initial conditions for inflation. *JHEP*, 0211:037, 2002.

[114] Don N. Page and Xing Wu. Massless Scalar Field Vacuum in de Sitter Spacetime. *JCAP*, 1211:051, 2012.

[115] Marco Bertola, Francesco Corbetta, and Ugo Moschella. Massless scalar field in a two-dimensional de sitter universe. In AnneBoutet de Monvel, Detlef Buchholz, Daniel Iagolnitzer, and Ugo Moschella, editors, *Rigorous Quantum Field Theory*, volume 251 of *Progress in Mathematics*, pages 27–38. Birkhuser Basel, 2007.

[116] Sidney R. Coleman and Frank De Luccia. Gravitational Effects on and of Vacuum Decay. *Phys.Rev.*, D21:3305, 1980.

[117] J.R. Gott. Creation of Open Universes from de Sitter Space. *Nature*, 295:304–307, 1982.

[118] Martin Bucher, Alfred S. Goldhaber, and Neil Turok. An open universe from inflation. *Phys.Rev.*, D52:3314–3337, 1995.

[119] Kazuyuki Sugimura and Eiichiro Komatsu. Bispectrum from open inflation. *JCAP*, 1311:065, 2013.

[120] Alexander Vilenkin. The Birth of Inflationary Universes. *Phys.Rev.*, D27:2848, 1983.

[121] Leonard Susskind. The Anthropic landscape of string theory. 2003.

[122] Alan H. Guth and Yasunori Nomura. What can the observation of nonzero curvature tell us? *Phys.Rev.*, D86:023534, 2012.

[123] Ivan Agullo and Leonard Parker. Non-gaussianities and the Stimulated creation of quanta in the inflationary universe. *Phys.Rev.*, D83:063526, 2011.

[124] Andreas Albrecht, Nadia Bolis, and R. Holman. Cosmological Consequences of Initial State Entanglement. *JHEP*, 1411:093, 2014.

[125] Sugumi Kanno. Impact of quantum entanglement on spectrum of cosmological fluctuations. *JCAP*, 1407:029, 2014.

[126] Misao Sasaki, Takahiro Tanaka, and Kazuhiro Yamamoto. Euclidean vacuum mode functions for a scalar field on open de Sitter space. *Phys.Rev.*, D51:2979–2995, 1995.

[127] David H. Lyth and Ewan D. Stewart. Inflationary density perturbations with Omega¡ 1. *Phys.Lett.*, B252:336–342, 1990.

[128] Juan Maldacena and Guilherme L. Pimentel. Entanglement entropy in de Sitter space. *JHEP*, 1302:038, 2013.

[129] Brian Greene, Maulik Parikh, and Jan Pieter van der Schaar. Universal correction to the inflationary vacuum. *JHEP*, 0604:057, 2006.

[130] Maulik K. Parikh and Erik P. Verlinde. De Sitter holography with a finite number of states. *JHEP*, 0501:054, 2005.

[131] J.D. Cohn and David I. Kaiser. Where do the supercurvature modes go? *Phys.Rev.*, D58:083515, 1998.

[132] Kazuhiro Yamamoto, Misao Sasaki, and Takahiro Tanaka. Quantum fluctuations and CMB anisotropies in one bubble open inflation models. *Phys.Rev.*, D54:5031–5048, 1996.

[133] Jaume Garriga, Xavier Montes, Misao Sasaki, and Takahiro Tanaka. Spectrum of cosmological perturbations in the one bubble open universe. *Nucl.Phys.*, B551:317–373, 1999.

[134] S.W. Hawking, Thomas Hertog, and Neil Turok. Gravitational waves in open de Sitter space. *Phys.Rev.*, D62:063502, 2000.

[135] R. Holman and Andrew J. Tolley. Enhanced Non-Gaussianity from Excited Initial States. *JCAP*, 0805:001, 2008.

[136] Pieter Daniel Meerburg, Jan Pieter van der Schaar, and Pier Stefano Corasaniti. Signatures of Initial State Modifications on Bispectrum Statistics. *JCAP*, 0905:018, 2009.

[137] Takahiro Tanaka and Misao Sasaki. No supercritical supercurvature mode conjecture in one bubble open inflation. *Phys.Rev.*, D59:023506, 1999.

[138] Jaume Garriga and Viatcheslav F. Mukhanov. On classical anisotropies in models of open inflation. *Phys.Rev.*, D56:2439–2441, 1997.

[139] Slava Emelyanov. Local thermal observables in spatially open FRW spaces. 2014.

[140] Renaud Parentani. The Energy momentum tensor in Fulling-Rindler vacuum. *Class.Quant.Grav.*, 10:1409–1416, 1993.

[141] Wilhelm Magnus, Fritz Oberhettinger, and Raj Pal Soni. *Formulas and theorems for the special functions of mathematical physics*. Third edition, 1966.

[142] Stefan Hollands and Robert M. Wald. Quantum fields in curved spacetime. *Phys.Rept.*, 574:1–35, 2015.

[143] P.A.R. Ade et al. Detection of $B$-Mode Polarization at Degree Angular Scales by BICEP2. *Phys.Rev.Lett.*, 112(24):241101, 2014.

[144] P.A.R. Ade et al. Joint Analysis of BICEP2/$KeckArray$ and $Planck$ Data. *Phys.Rev.Lett.*, 114(10):101301, 2015.

[145] Jerome Martin, Christophe Ringeval, and Vincent Vennin. Encyclopdia Inflationaris. *Phys.Dark Univ.*, 2014.

[146] Alexei A. Starobinsky. A New Type of Isotropic Cosmological Models Without Singularity. *Phys.Lett.*, B91:99–102, 1980.

[147] P.A.R. Ade et al. Planck 2013 results. XXII. Constraints on inflation. *Astron.Astrophys.*, 571:A22, 2014.

[148] Andrei D. Linde. Chaotic Inflation. *Phys.Lett.*, B129:177–181, 1983.

[149] Mario Galante, Renata Kallosh, Andrei Linde, and Diederik Roest. The Unity of Cosmological Attractors. *Phys.Rev.Lett.*, 114:141302, 2015.

[150] Renata Kallosh, Andrei Linde, and Diederik Roest. Universal Attractor for Inflation at Strong Coupling. *Phys.Rev.Lett.*, 112(1):011303, 2014.

[151] Renata Kallosh, Andrei Linde, and Diederik Roest. The double attractor behavior of induced inflation. *JHEP*, 1409:062, 2014.

[152] Gian F. Giudice and Hyun Min Lee. Starobinsky-like inflation from induced gravity. *Phys.Lett.*, B733:58–62, 2014.

[153] Renata Kallosh and Andrei Linde. Universality Class in Conformal Inflation. *JCAP*, 1307:002, 2013.

[154] Renata Kallosh and Andrei Linde. Superconformal generalizations of the Starobinsky model. *JCAP*, 1306:028, 2013.

[155] Renata Kallosh and Andrei Linde. Multi-field Conformal Cosmological Attractors. *JCAP*, 1312:006, 2013.

[156] Renata Kallosh and Andrei Linde. Non-minimal Inflationary Attractors. *JCAP*, 1310:033, 2013.

[157] Renata Kallosh, Andrei Linde, and Diederik Roest. Superconformal Inflationary $\alpha$-Attractors. *JHEP*, 1311:198, 2013.

[158] Renata Kallosh, Andrei Linde, and Diederik Roest. Large field inflation and double $\alpha$-attractors. *JHEP*, 1408:052, 2014.

[159] Frank S. Accetta, David J. Zoller, and Michael S. Turner. Induced Gravity Inflation. *Phys.Rev.*, D31:3046, 1985.

[160] D.S. Salopek, J.R. Bond, and James M. Bardeen. Designing Density Fluctuation Spectra in Inflation. *Phys.Rev.*, D40:1753, 1989.

[161] Fedor L. Bezrukov and Mikhail Shaposhnikov. The Standard Model Higgs boson as the inflaton. *Phys.Lett.*, B659:703–706, 2008.

[162] B.L. Spokoiny. INFLATION AND GENERATION OF PERTURBATIONS IN BROKEN SYMMETRIC THEORY OF GRAVITY. *Phys.Lett.*, B147:39–43, 1984.

[163] R. Fakir and W.G. Unruh. Improvement on cosmological chaotic inflation through nonminimal coupling. *Phys.Rev.*, D41:1783–1791, 1990.

[164] David I. Kaiser. Constraints in the context of induced gravity inflation. *Phys.Rev.*, D49:6347–6353, 1994.

# Contributions to Publications

Below I will describe my personal contributions to the publications on which this thesis is based. Note that in theoretical high energy physics, the order of the list of authors is alphabetical, so it does not reflect the contribution of the individual authors.

[1] F. V. Dimitrakopoulos, L. Kabir, B. Mosk, M. Parikh and J.P. van der Schaar
*Vacua and correlators in hyperbolic de Sitter space*
Journal of High Energy Physics **1506**, 095 (2015),
arXiv:1502.00113 [hep-th].

*I was responsible for (sub) sections 2.2, 2.3, 3.1 and the appendices of the original paper. In particular, I calculated the power spectra, analyzed the divergence of the energy momentum tensor and constructed the expression for the tensor product of the hyperbolic vacua in terms of the Bunch Davies state. J.P. van der Schaar and F. V. Dimitrakopoulos were the main contributors to the calculation of the bi-spectrum and J.P. van der Schaar and L. Kabir were the main contributors to section 2.1 on the mapping between the hyperbolic patch and the planar patch. I contributed in conceptual discussions to all parts and topics discussed in the paper.*

[2] B. Freivogel, R. A. Jefferson, L. Kabir, B. Mosk and I. S. Yang
*Casting Shadows on Holographic Reconstruction*
Physical Review D **D 91**, 086013 (2015), arXiv:1412.5175 [hep-th].

*I was responsible for (sub) sections 4.1, 4.3, 5, 6 and appendices B and C of the original paper. I also did the calculations for section 3.1. I proposed to analyze Wilson loops and causal information surfaces as bulk probes. I-Sheng Yang was the main contributor to (sub) sections 2, 3.2 and appendix A. L.Kabir was the main contributor to (sub) sections 4.2. R. A. Jefferson was the main contributor to (sub) section 3.1. B.W. Freivogel was leading the project and was a major contributor to conceptual discussions. I contributed in conceptual discussions to all parts and topics discussed in the paper.*

[3] B. Mosk and J.P. van der Schaar
*Chaotic inflation limits for non-minimal models with a Starobinsky attractor*
Journal of Cosmology and Astroparticle Physics **1412**, 022 (2014),
arXiv:1407.4686 [hep-th].

*I was responsible for all calculations in this article. The intellectual content originated from discussions between the authors.*

[4] B. Freivogel and B. Mosk
*Properties of Causal Holographic Information*
Journal of High Energy Physics **1309**, 100 (2013), arXiv:1304.7229 [hep-th].

*I was responsible for all calculations in this article. The intellectual content originated from discussions between the authors.*

# Summary

## THE ENTANGLED UNIVERSE

### Context

In the beginning of the $20^{\text{th}}$ century, two fundamentally new concepts in physics changed our understanding of the universe. The first revolution came with the advent of Einstein's theory of general relativity in 1915, which replaced Newton's universal law of gravity. General relativity profoundly changed our understanding of space and time, especially at large scales. The second revolution came with the conception of quantum mechanics, which changed our understanding of physics at small scales.

These new ideas gave an enormous boost to the fields of cosmology and particle physics. General relativity gave insight in the description of the geometry of our universe. The observation of cosmological redshifts and the theoretical description of an expanding universe with general relativity formed the basis for the Big Bang model and the concept of cosmological inflation. The standard model of particle physics was developed using the concepts of quantum mechanics and special relativity, resulting in the prediction and discovery of many new particles, such as recently the Higgs boson.

Although the standard model of particle physics and the theory of cosmological inflation are extremely successful in predicting and explaining observations, several questions remain unanswered. Firstly, attempts to reconcile quantum mechanics and general relativity in a UV-complete theory have been largely unsuccessful. Secondly, there are many models of cosmological inflation, but which one describes our universe? Obviously, there are other important open questions that are not addressed in this thesis, such as the quest for the nature and origin of dark matter and dark energy.

## Motivation of research

### Holography

String theory is an attempt to reconcile quantum mechanics and general relativity; it is like a marriage between gravity and quantum mechanics. In string theory, particles can be seen as vibrations on strings. Even though it is questionable whether string theory describes our universe, it did give birth to a concrete realization of the concept of holography; the idea that the degrees of freedom in a volume of space can be described by a model on a holographic screen with one dimension less.

The peculiar thing about holography is that the model on the holographic screen, the boundary, does not include gravity, whereas the volume of space it describes, the bulk, *does* include gravity. This means that a description of gravity can be given in terms of a non-gravitational quantum model, at least under certain circumstances. This opens the door to studying gravity from a completely different perspective; the perspective of the description on the "holographic screen".

Holography gives rise to a duality; the exact equivalence of two models in physics, in this case the bulk model and the boundary model. Models that are dual to each other might look very different, but they are related by a dictionary that translates quantities and laws of physics in one model to those in the other model. The holographic dictionary has not been decoded completely (yet).

The reconstruction of bulk physics, given laws of physics and physical quantities of the boundary model, is the subject of study in the field of *holographic reconstruction*. Part I of this thesis discusses the limitations of known reconstruction techniques and a possibly "new word" in the holographic dictionary: causal holographic information.

### Cosmology

Observations suggest that our universe went through a phase of accelerated expansion, inflation, during the first fractions after the Big Bang. The cosmic microwave background (CMB) gives an important observational clue and can be seen as a footprint of inflation. A successful model of inflation should reproduce the measured CMB power spectrum.

The classical evolution of the metric and a scalar field, dubbed the inflaton field, effectively provides a mechanism for inflation. Quantum fluctuations of the degrees of freedom described by the metric and the inflaton field successfully describe the observed power spectrum of the cosmic microwave background.

There are several problems with the theory of cosmological inflation. There are hundreds of different models that explain inflation. Many of them cannot be excluded by current observational data, although they have been based on different assumptions. This prompts the question: how can we distinguish different models with different assumptions in the available observational data? And can we at least organize these models in a useful way?

## Results

### Holography

In chapter 2 we discussed bulk reconstruction techniques and their limitations. We introduced two different qualitative characterizations of a bulk probe's ability to cover the bulk: the strong and weak coverage properties. For a subset of bulk probes, we proved a number of lemmas and theorems, casting light on their ability to probe bulk regions. We proceeded with the analysis of several bulk probes for the example of the BTZ-metric, showing that the weak and strong coverage properties are not satisfied. This implies that at least with these known bulk probes and techniques, a non-perturbative bulk reconstruction is not possible in certain regions, which we called "shadows".

As mentioned above, the holographic dictionary is incomplete and our failure to fully reconstruct bulk physics is one practical motivation to search for "new words" in the holographic dictionary. In chapter (3) we discussed properties of causal holographic information, a bulk construct for which the boundary dual is unknown. Our most important contribution is that we noted that the subleading divergences of causal holographic information are generally non-local; they cannot be written as integrals of local quantities. Secondly, we showed that the coefficient of the logarithmically divergent term (if present) is universal; it does not depend on the state or the cutoff procedure. Thirdly, we proposed several dual boundary quantities, which are all associated to the Von Neumann entropy of a coarse grained density matrix. An improved proposal of this form was subsequently made by A. C. Wall and W. R. Kelly.

### Cosmology

In chapter (5) we considered the hyperbolic patch of de Sitter spacetime, which served as a toy model for a "bubble universe". We compared two different quantum states and their associated power spectra. We also analyzed the behavior of the energy-momentum tensor. Our main result is firstly that the power spectrum for the scalar field in the Bunch Davies must correspond to the power spectrum

calculated with the reduced density matrix associated to the Bunch Davies state, clarifying earlier work by S. Kanno. Also, we noted that the difference between the power spectra associated to these two states is not observable. Subsequently, we presented a mapping between the hyperbolic and planar patches of de Sitter spacetime, confirming that the natural hyperbolic vacuum is mapped to the Bunch-Davies state. Finally we showed that the difference between the expectation values of the energy momentum tensor in these states is typically UV-finite, but divergent near the boundary of the hyperbolic patch.

In chapter (6) we came back to the problem of having so many different models of cosmological inflation. We took a different point of view on the set of single field inflation models, by considering them in the non-minimally coupled Jordan-frame. Firstly, we concluded that two types of models appear naturally as attractor points. In the limits of a flat and steep conformal factor, or weak and strong non-minimal coupling, these models correspond to chaotic and Starobinsky inflation respectively. Secondly, we noted that the fine-tuning problem for chaotic inflation can directly be interpreted in terms of the flat conformal factor limit. Thirdly, we showed that the Starobinsky attractor is a more universal attractor in the sense that the energy scale of inflation does not depend on the particular conformal factor under consideration, as long as the steep conformal factor limit is satisfied. For the chaotic attractor points, the scale of inflation does depend on the particular form of the conformal factor under consideration.

## Outlook

The quest for new holographic reconstruction techniques continues and promising results have recently been obtained using methods of integral geometry and quantum information. We hope that we can contribute to the effort of shedding light on our shadow-regions in future work, with the identification of new bulk probes and reconstruction techniques.

In the field of cosmology, the interest in chaotic attractor points diminished after a joint analysis of the BICEP2/Keck Array and Planck groups, which points to a small tensor to scalar ratio, which is not consistent with chaotic inflation models. The Starobinsky attractor point is in the sweet spot of models favored by observations by the Planck satellite. More precise measurements of the tensor to scalar ratio and of non-Gaussianities in the CMB are crucial to develop a more accurate model of inflation.

# Samenvatting

## THE ENTANGLED UNIVERSE

### Context

In het begin van de 20$^{ste}$ eeuw veranderden twee fundamenteel nieuwe concepten in de natuurkunde ons begrip van het universum. De eerste revolutie werd ingezet met de komst van Einsteins algemene relativiteitstheorie in 1915, waarmee Newtons universele wet van de zwaartekracht werd vervangen. De algemene relativiteitstheorie veranderde ons begrip van ruimte en tijd. De relativiteitstheorie geeft een goede beschrijving op grote schalen. De tweede revolutie vloeide voort uit de ontdekking van de kwantummechanica. De kwantummechanica geeft een goede beschrijving van de natuurkunde op kleine schalen.

Deze nieuwe ideeën gaven een enorme impuls aan het gebied van de kosmologie en dat van de deeltjesfysica. De algemene relativiteitstheorie gaf inzicht in de beschrijving van de geometrie van ons universum. Het waarnemen van de kosmologische roodverschuiving, in combinatie met het ontdekken van de theoretische beschrijving van een uitdijend heelal met de algemene relativiteitstheorie vormden de basis voor de modellen van de Oerknal en kosmologische inflatie. Het standaardmodel van de deeltjesfysica werd ontwikkeld met behulp van de concepten uit de kwantummechanica en de speciale relativiteitstheorie en resulteerde in de voorspelling en de ontdekking van vele nieuwe deeltjes, zoals recentelijk nog het Higgs boson.

Hoewel het standaardmodel van de deeltjesfysica en de theorie van kosmologische inflatie zeer succesvol zijn in het voorspellen en verklaren van observaties, blijft een aantal vragen onbeantwoord. In de eerste plaats is het verzoenen van de kwantummechanica en de algemene relativiteitstheorie problematisch. Ten tweede zijn er vele modellen van kosmologische inflatie, maar welk model geeft een juiste

beschrijving van ons universum? Daarnaast zijn er nog vele andere open vragen die niet in dit proefschrift worden behandeld, zoals de zoektocht naar de aard en herkomst van donkere materie en donkere energie.

## Motivatie van het onderzoek

### Holografie

Met de ontwikkeling van de snaartheorie is een poging gedaan om de kwantummechanica en de algemene relativiteitstheorie met elkaar te verzoenen; de theorie is als een huwelijk tussen de zwaartekracht en de kwantummechanica. In de snaartheorie kunnen deeltjes worden gezien als trillingen op snaren. Ook al is het twijfelachtig of de snaartheorie de natuurverschijnselen in ons universum verklaart, de theorie bracht een concrete realisatie voort van het concept van holografie; het idee dat de vrijheidsgraden in een volume van ruimte kunnen worden beschreven met een model op een holografisch scherm met één dimensie minder.

Het eigenaardige van holografie is dat het model op het holografische scherm, de "rand", geen zwaartekracht kent, terwijl de beschrijving van het volume van ruimte, de "bulk", wél zwaartekracht kent. Dit betekent dat een beschrijving van de zwaartekracht mogelijk is in termen van een quantum mechanisch model zónder zwaartekracht, althans onder bepaalde omstandigheden. Dit opent de deur om de zwaartekracht te bestuderen vanuit een heel ander perspectief: het perspectief van de beschrijving op een "holografisch scherm".

Holografie geeft een voorbeeld van een dualiteit: een exacte equivalentie van twee modellen in de natuurkunde. In dit geval betreft het de twee modellen van de bulk en de rand. Modellen die duaal zijn zien er misschien heel anders uit, maar er is een woordenboek dat de grootheden en natuurwetten in één model vertaald naar grootheden en natuurwetten in het andere model. Het holografische woordenboek is nog incompleet.

Bij een échte dualiteit moet het mogelijk zijn het woordenboek tussen de twee modellen volledig te ontrafelen. *Holografische reconstructie* is het vakgebied van de reconstructie van de bulk fysica, waarbij de natuurwetten en grootheden van het model op de rand gegeven zijn. In deel I van dit proefschrift wordt ingegaan op de beperkingen van de bekende reconstructietechnieken en een eventueel "nieuw woord" in het holografische woordenboek, namelijk de "causale holografische informatie".

### Kosmologie

Waarnemingen suggereren dat ons universum een fractie na de Oerknal een fase van versnelde uitdijing (inflatie) doormaakte. De kosmische achtergrondstraling kan gezien worden als een voetafdruk van de kosmologische inflatie. Het verklaren van het spectrum van de kosmische achtergrondstraling is dan ook een belangrijke eigenschap waaraan een model van inflatie moet voldoen.

Een model gebaseerd op de klassieke evolutie van de metriek en een scalair veld, genaamd het inflaton-veld, voorziet in een effectieve beschrijving van het mechanisme achter inflatie. Quantum fluctuaties verklaren de vorm van het waargenomen spectrum van de kosmische achtergrondstraling verbazingwekkend goed.

Er zijn verscheidene problemen met de theorie van kosmologische inflatie. Zo zijn er bijvoorbeeld honderden verschillende modellen die inflatie kunnen verklaren. Vele van deze modellen kunnen niet worden uitgesloten op basis van waarnemingen. Desalniettemin zijn die modellen vaak gebaseerd op verschillende aannames. Dit roept de volgende vraag op: hoe kunnen we verschillende modellen met verschillende aannames onderscheiden in de (toekomstige) waarnemingen? En kunnen we op zijn minst deze modellen op een nuttige manier organiseren of ordenen?

## Resultaten

### Holografie

In hoofdstuk 2 werd een aantal bulk-reconstructietechnieken besproken. Bulk-reconstructie technieken maken gebruik van bulk-sondes; dat zijn objecten in de bulk, waarvan we idealiter ook weten wat de representatie is in het model op de rand. Er werden twee verschillende begrippen geïntroduceerd die kwalitatief aangeven wat het vermogen van een bulk-sonde is om de bulk te reconstrueren: de sterke- en zwakke bedekkingseigenschappen. Voor een deelverzameling van bulk-sondes bewezen we een aantal lemma's en stellingen, die inzichtelijk maken hoe "goed" een bulk-sonde is in de context van bulk-reconstructie. Vervolgens illustreerden wij de beperkingen van bulk-sondes door te kijken naar het voorbeeld van de BTZ-metriek, waaruit blijkt dat niet aan de sterke bedekkingseigenschap wordt voldaan. Dit betekent dat we met de bekende bulk-sondes en bulk-reconstructietechnieken niet in staat zijn de bulk op een niet-perturbatieve wijze te reconstrueren. De gebieden waar een niet-perturbatieve reconstructie niet mogelijk is noemen we "schaduwen". Zoals hierboven al is beschreven, is het holografische woordenboek onvolledig. Het feit dat men op dit moment niet in staat is de bulk helemaal te reconstrueren, motiveert de zoektocht naar "nieuwe woorden" in het holografische woordenboek.

In hoofdstuk (3) bespraken we eigenschappen van de causale holografische informatie, een bulk-sonde waarvan niet duidelijk is wat het corresponderende object is in het duale model op de rand. Onze belangrijkste bijdrage is dat we hebben ontdekt dat de niet-leidende divergenties van causale holografische informatie in het algemeen niet-lokaal zijn; ze kunnen niet worden uitgedrukt in termen van integralen van lokale grootheden. Ten tweede hebben we laten zien dat de coëfficiënt van de logaritmisch divergerende term (indien aanwezig) universeel is; deze coéfficiënt is niet afhankelijk van de kwantum-toestand, of de procedure waarmee de divergentie wordt gereguleerd. Ten derde hebben we gespeculeerd over de mogelijke kandidaten voor een duale representatie van causale holografische informatie in het model op de rand. Onze voorstellen worden gekenmerkt door het feit dat zij allemaal de Von Neumann entropie van een grofkorrelige dichtheidsmatrix zijn. Volgend op onze initiële suggesties, is er recentelijk een verbeterd voorstel van deze aard gedaan door A. C. Wall en W. R. Kelly.

**Kosmologie**

In hoofdstuk (5) beschouwden we de hyperbolische sectie van de Sitter ruimtetijd, die als model diende voor een "bubbel universum". We vergeleken twee verschillende kwantumtoestanden en de bijbehorende spectra. Ook analyseerden we het gedrag van de energie-momentum tensor. Ons belangrijkste resultaat is in de eerste plaats dat het spectrum van het scalaire veld in de Bunch-Davies toestand overeenkomt met het spectrum dat volgt uit de berekening met de gereduceerde dichtheidsmatrix van de Bunch-Davies toestand. In principe is dat logisch, maar in recent werk van S. Kanno werd gesuggereerd dat deze twee berekeningen verschillende resultaten geven. Verder concludeerden we dat de Bunch-Davies toestand en het hyperbolische vacüum niet resulteren in *waarneembare* verschillen in het spectrum.

Ook presenteerden we een afbeelding tussen de hyperbolische en vlakke secties van de Sitter ruimtetijd. Met deze afbeelding laten we zien dat het natuurlijke hyperbolische vacuüm wordt afgebeeld op de Bunch-Davies toestand van de vlakke sectie. Vervolgens toonden we aan dat het verschil tussen de energie-momentum tensoren in deze toestanden UV-eindig is, maar divergeert nabij de horizon van de hyperbolische sectie.

In hoofdstuk (6) kwamen we terug op het probleem van het grote aantal modellen van kosmologische inflatie. We namen een ander perspectief op de verzameling van inflatiemodellen met één scalar veld, door ze in het niet-minimaal gekoppelde Jordan-raamwerk te bekijken. Ten eerste hebben wij geconcludeerd dat er twee typen modellen *speciaal* zijn vanuit dit perspectief; dat zijn zogenaamde aantrekkingspunten. In de limiet van een vlakke- en steile conforme factor, ofwel de

zwakke- en sterke niet-minimale koppeling, reduceren deze modellen respectievelijk tot de chaotische- en Starobinsky-inflatiemodellen. Ten tweede zagen we dat het fijn-afstelingsprobleem ("fine-tuning") bij chaotische inflatie kan worden geïnterpreteerd als de vlakke conforme factor limiet. Ten derde toonden we aan dat het Starobinsky-aantrekkingspunt een universeler karakter heeft dan de chaotische aantrekkingspunten, omdat de energie-schaal van inflatie bij het Starobinsky-aantrekkingspunt niet afhangt van de precieze vorm van de conforme factor, zolang aan de steile conforme factor limiet wordt voldaan. Voor de chaotische aantrekkingspunten hangt de schaal van de inflatie wel af van de specifieke vorm van de conforme factor.

## Vooruitblik

In de zoektocht naar nieuwe technieken in het veld van de holografische reconstructie zijn recentelijk veelbelovende resultaten verkregen door methoden uit de integraal-geometrie en de kwantuminformatietheorie te gebruiken. We hopen dat we in de toekomst een bijdrage kunnen leveren aan het belichten van mogelijkheden om de holografische schaduwgebieden in de bulk te reconstrueren, door nieuwe bulk-sondes en reconstructietechnieken te identificeren.

Op het gebied van de kosmologie is de interesse in de chaotische aantrekkingspunten afgenomen na een gezamenlijke analyse van de BICEP2/Keck Array en Planck groepen, die wijst op een kleinere tensor-scalar verhouding dan oorspronkelijk geopperd door de BICEP2-groep, wat inconsistent is met chaotische inflatiemodellen. Het Starobinsky-aantrekkingspunt is juist consistent met de waarnemingen van de Planck-satelliet. Meer nauwkeurige metingen van de tensor-scalar verhouding en van de niet-Gaussische afwijkingen in het spectrum van de kosmische microgolf achtergrond zijn cruciaal om tot een juister model van inflatie te komen.